PROTEOMICS ANALYSIS OF BT-474 AND SKOV-3 CANCER CELL LINES TREATED WITH PURIFIED COMPOUNDS FROM BEE POLLEN AND CERUMEN

Mr. Teeranai Ittiudomrak

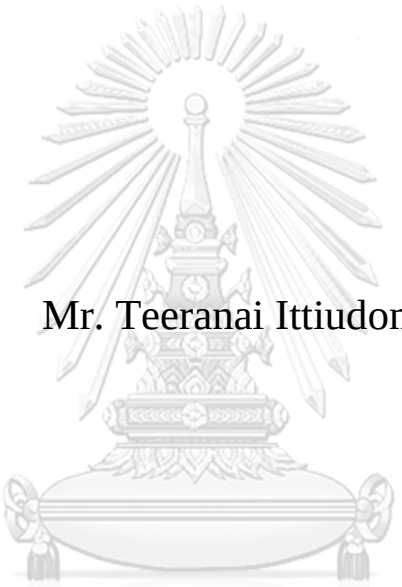

A Dissertation Submitted in Partial Fulfillment of the Requirements
for the Degree of Doctor of Philosophy in Biotechnology
Common Course
FACULTY OF SCIENCE
Chulalongkorn University
Academic Year 2021

การวิเคราะห์โปรติโอมิกส์ของเซลล์มะเร็ง BT-474 และ SKOV-3 เมื่อได้รับสารประกอบบริสุทธิ์จากเกสรผึ้งและซีรูเมน

นายธีรนัย อิทธิอุดมรักษ์

วิทยานิพนธ์นี้เป็นส่วนหนึ่งของการศึกษาตามหลักสูตรปริญญาวิทยาศาสตรดุษฎีบัณฑิต
สาขาวิชาเทคโนโลยีชีวภาพ ไม่สังกัดภาควิชา/เทียบเท่า
คณะวิทยาศาสตร์ จุฬาลงกรณ์มหาวิทยาลัย
ปีการศึกษา 2564

Thesis Title	PROTEOMICS ANALYSIS OF BT-474 AND SKOV-3 CANCER CELL LINES TREATED WITH PURIFIED COMPOUNDS FROM BEE POLLEN AND CERUMEN
By	Mr. Teeranai Ittiudomrak
Field of Study	Biotechnology
Thesis Advisor	Professor Dr. Chanpen Chanchao
Thesis Co Advisor	Dr. Sittiruk Roytrakul

Accepted by the FACULTY OF SCIENCE, Chulalongkorn University in Partial Fulfillment of the Requirement for the Doctor of Philosophy

..... Dean of the FACULTY OF SCIENCE
(Professor Dr. POLKIT SANGVANICH)

DISSERTATION COMMITTEE

..... Chairman
(Associate Professor Dr. KUAKARUN KRUSONG)

..... Thesis Advisor
(Professor Dr. Chanpen Chanchao)

..... Thesis Co-Advisor
(Dr. Sittiruk Roytrakul)

..... Examiner
(Associate Professor Dr. APHICHART KARNCHANATAT)

..... Examiner
(Professor Dr. TANAPAT PALAGA)

..... External Examiner
(Dr. Wittaya Pimtong)

..... External Examiner
(Dr. Aditi Kanhere)

..... External Examiner
(Assistant Professor Dr. Teeraphan Laomettachit)

ธีรนัย อิทธิอุดมรักษ์ : การวิเคราะห์โปรติโอมิกส์ของเซลล์มะเร็ง BT-474 และ SKOV-3 เมื่อได้รับสารประกอบบริสุทธิ์จากเกสรผึ้งและซีรูเมน. (PROTEOMICS ANALYSIS OF BT-474 AND SKOV-3 CANCER CELL LINES TREATED WITH PURIFIED COMPOUNDS FROM BEE POLLEN AND CERUMEN) อ.ที่ปรึกษาหลัก : ศ. ดร.จันทร์เพ็ญ จันทร์เจ้า, อ.ที่ปรึกษาร่วม : ดร.สิทธิรักษ์ รอยตระกูล

มะเร็งเต้านมและมะเร็งทางนรีเวชเป็นสาเหตุหลักของการเสียชีวิตด้วยโรคมะเร็งในผู้หญิงทั่วโลก จนกระทั่งปัจจุบันมีการค้นพบสารประกอบหลายชนิดจากส่วนประกอบยาแผนโบราณและผลิตภัณฑ์จากธรรมชาติที่พบว่ามีฤทธิ์ต้านมะเร็ง ก่อนหน้านี้มีรายงานว่าสามารถสกัดแยก alpha-mangostin (alpha-MG) และ apigenin (APG) ให้บริสุทธิ์ได้จาก cerumen ของชันโรง (*Tetragonula laeviceps*) และเกสรผึ้งของผึ้งพันธุ์ (*Apis mellifera*) ตามลำดับ จากการศึกษาเบื้องต้นพบว่าสารทั้งสองชนิดนี้แสดงฤทธิ์ต้านการเพิ่มจำนวนของเซลล์มะเร็งได้หลายชนิด ในการศึกษานี้ ได้ทำการตรวจสอบ alpha-MG และ APG ที่มีต่อผลการต้านการเพิ่มจำนวนของเซลล์มะเร็งเต้านม BT-474 และเซลล์มะเร็งรังไข่ SKOV-3 โดยใช้วิธี MTT การย้อมด้วยฟลูออเรสเซนต์ควบคู่กับการวิเคราะห์ด้วย flow cytometry การตรวจวัดกิจกรรมของเอนไซม์ caspase และการหาปริมาณของยีนที่น่าสนใจด้วยวิธีการ real-time PCR, จากผลการศึกษาของเซลล์ BT-474 พบว่าสารประกอบทั้งสองทำให้เซลล์เกิดการตายแบบ necrosis โดยการชักนำให้เกิดการอักเสบ ซึ่งเกี่ยวข้องกับการเพิ่มการแสดงออกของยีน COX2 ในกรณีของเซลล์ SKOV-3 พบว่า APG ชักนำให้เกิดการตายของเซลล์แบบ apoptosis ด้วยกระบวนการ intrinsic pathway ในขณะที่ alpha-MG นำเซลล์ไปสู่การตายแบบ necrosis ซึ่งเกี่ยวข้องกับการแสดงออกของยีน COX2 ที่เพิ่มขึ้น ทั้งนี้สารประกอบทั้งสองทำให้เซลล์หยุดการเจริญเติบโตในระยะ G_2/M อีกด้วย นอกจากนี้ยังพบว่าความเข้มข้นที่ออกฤทธิ์ยับยั้งการเจริญเติบโตได้ 50% (IC_{50}) ของสารประกอบทั้งสองชนิดในเซลล์ปกติสูงกว่าในเซลล์มะเร็ง ซึ่งแสดงให้เห็นถึงความเป็นพิษที่มีต่อเซลล์ปกติที่น้อยกว่า จากผลต้านการเพิ่มจำนวนเซลล์ในเซลล์ SKOV-3 ของ APG จึงทำให้เกิดความสนใจว่า APG ควบคุมกลไกระดับเซลล์เพื่อยับยั้งการเพิ่มจำนวนเซลล์อย่างไร เพื่อตอบข้อสงสัยนี้ จึงทำการศึกษาผลแบบองค์รวมของการเปลี่ยนแปลงของ phosphoproteins อย่างรวดเร็วหลังจากเติมสาร APG ด้วยวิธีการ phosphoproteomics อาศัยการติดฉลากตัวอย่างด้วย 11-plex TMT และจากการวิเคราะห์ gene set enrichment ปรากฏว่า APG สามารถเปลี่ยนแปลงการควบคุมการถอดรหัส DNA ผ่าน epigenetics, histone modifications และ histone organisation ที่เกี่ยวข้องกับกระบวนการ demethylation รวมถึงสามารถกระตุ้นวิถีการส่งสัญญาณภายในเซลล์ที่หลากหลาย โดยเฉพาะอย่างยิ่งการส่งสัญญาณผ่าน mitogen-activated protein kinase (MAPK) นอกจากนี้จากการวิเคราะห์ด้วย NetworKIN และ Kinase set enrichment (KSEA), APG ยับยั้งกิจกรรมของ cyclin-dependent kinase 1, 2 และ 4 (CDK1, CDK2 และ CDK4) และกระตุ้นการตอบสนองต่อสภาวะเครียดต่อเซลล์และสัญญาณเพื่อการอยู่รอดของเซลล์ เป็นสิ่งที่น่าสังเกตอย่างยิ่งว่าการยับยั้งกิจกรรมของ pyruvate dehydrogenase complex โดยการกระตุ้นกิจกรรมของ pyruvate dehydrogenase kinase (PDK1 และ PDK2) ทำให้สันนิษฐานได้ว่าเกิดการเปลี่ยนแปลงของกระบวนการสร้างพลังงานและ aerobic glycolysis ภายในเซลล์ SKOV-3 เมื่อได้รับ APG โดยสรุป a-MG และ APG แสดงฤทธิ์ต้านการเพิ่มจำนวนของเซลล์ด้วยกลไกที่แตกต่างกันและองค์ความรู้จากการศึกษานี้ก่อให้เกิดความเข้าใจที่ดีขึ้นเกี่ยวกับการตอบสนองของเซลล์ต่อสารประกอบที่อาจถูกนำไปใช้เป็นยารักษาโรคหรือการบำบัดร่วมสำหรับการรักษามะเร็ง

สาขาวิชา	เทคโนโลยีชีวภาพ	ลายมือชื่อนิสิต .....
ปีการศึกษา	2564	ลายมือชื่อ อ.ที่ปรึกษาหลัก .....
		ลายมือชื่อ อ.ที่ปรึกษาร่วม .....

5872815123 : MAJOR BIOTECHNOLOGY
KEYWORD: α-Mangostin, Apigenin, Anticancer, Gene set enrichment analysis, Kinase set enrichment analysis, phosphoproteomics

Teeranai Ittiudomrak : PROTEOMICS ANALYSIS OF BT-474 AND SKOV-3 CANCER CELL LINES TREATED WITH PURIFIED COMPOUNDS FROM BEE POLLEN AND CERUMEN. Advisor: Prof. Dr. Chanpen Chanchao Co-advisor: Dr. Sittiruk Roytrakul

Breast and gynaecological cancers are the main causes of global cancer death in females. So far, several compounds have been identified from traditional medicine components and natural products that exhibited anticancer activity. Previously, α-mangostin (α-MG) and apigenin (APG) had been extracted and purified from cerumen of *Tetragonula laeviceps* and bee pollen of *Apis mellifera* respectively. Preliminary studies reported that these compounds express antiproliferative activity in several cancer cell lines. In this study, α-MG and APG were investigated for antiproliferation effect in breast cancer cell line BT-474 and ovarian adenocarcinoma cell line SKOV-3 using MTT assay, fluorescent staining coupled with flow cytometry analysis, caspase activity assay, and quantitative real-time PCR of interest genes. From BT-474 cell line result, both compounds caused necrotic death by induction of inflammation, as observation of COX2 gene upregulation. In SKOV-3 cell line, APG induced apoptosis via an intrinsic pathway while α-MG led to necrosis that was associated with upregulation of COX2 gene expression. Both compounds arrested cell progression at G_2/M phase. In addition, the half proximal inhibition concentration (IC_{50}) of both compounds in normal cell lines was higher than cancer cell lines representing less cytotoxicity on normal cells. Regarding the antiproliferation effect of APG in SKOV-3, it is interesting how APG regulated cellular mechanisms to suppress cell proliferation. To clarify this question, 11-plex TMT labelling phosphoproteomics was performed at an early response time to observe the global changes of phosphoproteins after APG exposure. Gene set enrichment analysis appeared that APG treatment altered regulation of transcription via epigenetics, histone modification, and organisation associated with demethylation, and activated various signalling pathways especially signalling through mitogen-activated protein kinase (MAPK). APG inhibited cyclin-dependent kinase 1, 2, and 4 (CDK1, CDK2, and CDK4) activities, and activated stress response and cell survival signalling from NetworKIN and Kinase set enrichment analysis (KSEA). Notably, inhibition of pyruvate dehydrogenase complex activity by enhancing activities of pyruvate dehydrogenase kinase (PDK1 and PDK2) presumed that conversion of energy metabolism and aerobic glycolysis occurred in SKOV-3 cells after exposure with APG. Taken together, α-MG and APG exhibit antiproliferative activity on a different mechanism and knowledge from this study provide a better understanding of cellular response to the compounds that could become useful as a therapeutic or co-treatment agent for cancer medication.

Field of Study:	Biotechnology	Student's Signature .....
Academic Year:	2021	Advisor's Signature .....
		Co-advisor's Signature .....

ACKNOWLEDGEMENTS

As a part of dual degree reward, I would like to share my foremost deepest gratitude and appreciation towards Professor Dr. Chanpen Chanchao, my advisor at Chulalongkorn University, and Dr. Philipp Anctzak, my primary supervisor at the University of Liverpool. Prof. Dr. Chanpen has been and is still very supportive in my Ph.D. life both physically and mentally. She kindly provides opportunities for overseas experience and warmly opens for listening to my desire in both experiment goal and life. Similarly, Dr. Philipp has been taking great care of me especially in guiding me in a direction for being a better scientist and man. Both of them contribute a lot in encouraging me during the difficult time of my study and I cannot deny that they were a big part of this project.

I would like to share my deep appreciation for those who have been associated with my project and shared their knowledge in various ways. I would like to thank Prof. Dr. Andy Jones for taking care of me during settling in at UoL and giving valuable advice for the project. This appreciation extends to staff in Computational Biology Facility for a warm welcome and being helpful and to Dr. Catarina De Matos Ferraz Franco assisting in phosphoproteomics at the Centre of Proteome Research. I would to thank Dr. Sittiruk Roytrakul and the staff at Proteome Research Laboratory for providing me with a chance to work in the proteomics facility and kindly suggest some great ideas to move on with the study. I would to present my gratitude to Prof.Dr. Tanapat Palaga and his lab members in sharing their facility for flow cytometry analysis and RT-qPCR experiment. I deeply appreciated Ms. Songchan Puthong and members of the Antibody production laboratory at IBGE, Chulalongkorn University for providing cell culture facilities and helping me through the experiments. Thanks to Dr. Wittaya Pimtong for sharing the machine and equipment for the western blotting study.

I acknowledge The 100th Anniversary Chulalongkorn University for Doctoral Scholarship and Overseas Research Experience Scholarship for Graduate Student for financial support my study. Moreover, I would like to show my gratitude to The 90th Anniversary of Chulalongkorn University Scholarship and the University of Liverpool Technology Directorate Voucher Scheme on financial support for antiproliferative effect and phosphoproteomics studies, respectively. Last but not least, I appreciated members of the molecular biology research laboratory and my family for their support.

Teeranai Ittiudomrak

TABLE OF CONTENTS

Page

LIST OF TABLES

Page

LIST OF FIGURES

Page

LIST OF ABBREVATIONS

A560	Absorbance at 560 nanometres
ACN	acetonitrile
ATF-3	activating transcription factor 3
AMPK	Adenosine monophosphate-activated protein kinase
AAs	amino acids
ANOVA	analysis of variance
AMP	antimicrobial peptide
APG	apigenin
ATM	Ataxia-telangiectasia mutated
ABCG2	ATP-binding cassette drug transporter
AGC	automatic gain control
Atg13	autophagy-related protein 13
Bcl2	B-cell lymphoma 2
BCE	before common era
BSA	bovine serum albumin
BRCA	breast cancer gene
CAPE	caffeic acid phenethyl ester
CaCl2	calcium chloride
CO2	carbon dioxide
CK2α	casein kinase 2 alpha
CASP	caspase
CAD	caspase-activated DNase
CTNNB1	Catenin Beta 1
CTSB	Cathepsin B
CDKi	CDK inhibitors
CAK	CDK-activating kinase
cIAP	cellular inhibitor of apoptosis protein
CHK	checkpoint kinase
ChIP-Seq	Chromatin immunoprecipitation sequencing
JNK	c-Jun N-terminal kinase
JNK1/2	c-Jun N-terminal kinase 1 and 2
CTTN	cortactin
CDK	cyclin-dependent kinase
COX2	Cyclooxygenase-2
CYLD	cylindromatosis
DD	death domain
DR5	death receptor protein 5
DISC	death-inducing signalling complex
°C	degree Celsius
DNA	deoxyribonucleotide
DMSO	dimethyl sulfoxide
DNMT	DNA methyltransferase

Topo-I, -II	DNA topoisomerase I and II
Dox	Doxorubicin
DMEM/F12	Dulbecco's modified Eagle medium and Ham's F-12 medium
MEM	Eagle's Minimum Essential medium
ETD	electron transfer dissociation
ECL	enhanced chemiluminescence
EMT	epithelial-mesenchymal transition
EDTA	Ethylenediamine tetraacetic acid
ERK1/2	extracellular signal-regulated kinase 1and 2
FDR	false discovery rate
FADD	Fas-associated protein with death domain
FAS	fatty acid synthase
FIMO	Find Individual Motif Occurrences
FKBP38	FK506-binding protein 38
FAK	focal adhesion kinase
FCS	foetal calf serum
FOXO3a	forkhead box O3
FOXK2	forkhead box protein K2
FA	formic acid
GEO	Gene Expression Omnibus
GO	Gene ontology
GSEA	gene set enrichment analysis
GADPH	Glyceraldehyde-3-phosphate dehydrogenase
g	gram
HDAC	histone deacetylase
HRP	horse radish peroxidase
h	hour
HCl	hydrochloric acid
HIF-1α	hypoxia-inducible factor 1
IgG	immunoglobulin G
ID1	inhibitor of DNA binding 1
IAP	inhibitors of apoptosis proteins
IC	inhibitory concentration
iTRAQ	isobaric tag for relative and absolute quantitation
IDH1	isocitrate dehydrogenase 1
IKK	IκB kinase
kg	kilogram
KSEA	kinase set enrichment analysis
L	litre
Lys	lysine
MRJP	major royal jelly proteins
m/z	mass per charge ratio
MMP	matrix metalloproteinase
MGO	methylglyoxal

MTT	3-[4,5-dimethylthiazole-2-yl]-2,5-diphenyltetrazolium bromide
µg	microgram
µL	microlitre
µM	micromolar
mA	milliampere
mg	milligram
mL	millilitre
mM	millimolar
min	minute
min	minute
MOMP	mitochondria outer membrane permeabilization
MAPK	mitogen-activated protein kinase
MLKL	mixed lineage kinase domain-like pseudokinase
ng	nanogram
nm	nanometre
NEDD9	Neural precursor cell-expressed developmentally down-regulated 9
NES	normalised enriched term
NF-κB	nuclear factor kappa B
ERα	oestrogen receptor alpha
p	p value
PSM	peptide-spectrum matching
%	percentage
PMA	phorbol 12-myristate 13-acetate
PBS	phosphate buffered saline
PI3K	phosphatidylinositol 3-kinase
p	phosphorylated
phospho-	phosphorylated
PARP	poly adenosine diphosphate-ribose polymerase
PVDF	polyvinylidene fluoride
PCA	principal component analysis
PCNA	proliferating cell nuclear antigen
PI	propidium iodide
PKCδ	protein kinase C-delta
PDK	pyruvate dehydrogenase kinase
PDHK1	pyruvate dehydrogenase kinase isoform1
qrt-RT-PCR	quantitative real-time reverse transcription polymerase reaction
ROS	reactive oxygen species
RT-PCR	real-time reverse transcription polymerase reaction
RTK	receptor tyrosine kinase
RIPK1	receptor-interacting protein kinase 1
rEGF	recombinant epidermal growth factor
Rb	retinoblastoma protein
RNA	ribonucleotide
RPMI-1640	Roswell Park Memorial Institute 1640 medium

RJ	royal jelly
Ser	serine
S	serine
STAT1	signal transducer and activator of transcription 1
STAT3	signal transducer and activator of transcription 3
NaCl	sodium chloride
SDS	sodium dodecyl sulphate
SHP1	Src homology region 2 domain-containing phosphatase-1
SILAC	stable isotope labelling using amino acids in cell culture
SD	standard deviation
STMN1	stathmin1
MS/MS	tandem mass spectrometry
TMT	tandem mass tag
TOR	target of rapamycin
TBST	TBS with 0.1% Tween 20
TPA	12-O-tetradecanoylphorbol-13-acetate
Thr	threonine
T	threonine
x g	times gravity of relative centrifugal force
TIMP1	tissue inhibitor of metalloproteinase 1
TiO2	titanium dioxide
TRADD	TNF receptor-associated Fas-associated protein with death domain
TRAF	TNFR-associated factor
TRAIL	TNF-related apoptosis-inducing ligand
TF	transcription factor
TEAB	triethylammonium bicarbonate
TFA	trifluoroacetic acid
TBS	tris buffered saline
TSC1/2	tuberous sclerosis complex
TNF	tumour necrosis factor
Tyr	tyrosine
Y	tyrosine
ULK1/2	Unc-51 like autophagy activating kinase 1 and 2
USD	United States dollars
u-PA	urokinase-plasminogen activator
Vps34	vacuolar protein sorting 34
VSN	variance stabilizing normalisation
VEGF	vascular endothelial growth factor
V	volt
v/v	volume by volume
H2O	water
w/v	weight by volume
α-MG	α-mangostin

CHAPTER 1
INTRODUCTION

1.1 A brief review on traditional medicine

The usage of natural resources as an herbal medicine has started a long time ago almost at the start of mankind. The evidence and documentation of herbal usage for treating illness has been estimated to occur in Sumerian civilization around 5000 BCE (1). Since then, the record of medicinal plants and other natural resources usage emerged across the globe from Egypt, Greek, Roman, the Arabs, India, China, and Africa (2-4). At first, the treatment of the ailments by utilising herbal plants and native sources appeared to be intuitive, like animals, and this confined knowledge generated through experiences was passed on to the next generation. A famous script of observation of medicinal plants is "*De Materia Medica*" written during Nero's Empire by Dioscorides, who has been recognised as one of the fathers of pharmacognosy along with Theophrastus (2). He described 944 drugs from 657 origin plants that were used to treat a broad spectrum of diseases for example relieve pain, fever, headache, and stomach ache, and cure wounds, burns, and stings. This document offered a foundation for "*Materia Medica*" or the history of pharmacy for the medieval and renaissance age that led to the establishment of pharmaceutical sciences during the early industrial revolution. During the Dioscorides period, in China, "*Shen Nong Ben Cao Jing*", a Chinese historic document in agriculture and medicinal plants, has been established and described three lists of herbs that can be divided into three groups, upper herbs that have stimulating properties with lower toxicity, middle herbs that have potential treatment activity but with toxicity, and lower herbs that contained most likely only poison (5). Not only herbs were described in these documents but also other natural resources for example minerals, animal parts, and extracts including bee products. The trend of herbal and traditional medicine as alternative and complementary treatments has become more attractive, especially for elders with health concerns or mild symptom illnesses, because several reasons for example anxiety

of using conventional medicine in long-term, good aspects on herbal medicine, and experience in the family (6). This is reflected through an increase in demand for medicinal plants and their derivatives, i.e., dried parts, crude and purified extracts, essential oils, and even gums that are used in nutraceuticals and dietary supplements, and for manufacturing in pharmaceuticals and cosmetics (7). The average growth is around 2.4% in volume and 9.2% in value with an estimated global trade of approximately USD 33 billion. In Thailand, a trade report from the Thai Ministry of Commerce from 2017-2020 (Fig. 1.1) showed an average value of Spices and medicinal plants exports at about USD 200 million with a sharp growth rate during 2016-2017 (8). The different geographical areas, biodiversity, and ecosystem of each civilisation have caused high diversity of plants and natural resources used in folk medicine. One of the traditional medicinal substances that have been reported of usage for treatment in different parts of the world is bee products. Bee products have been recorded both as sole substance or as mixtures with other herbs for wound healing, relief of fever and inflammation, and oral healthcare (9, 10). Apitherapy is a term describing the treatment or cure of illness using bee products. Humans started collecting honey from wild bees for consumption and ritualistic activity since 7,000 BCE in North Africa and cultivation of honeybees was observed in Egypt, Greek, China, and Mayan civilisation (11). Apiculture has started in Thailand since 1940s when the European honey bee (*Apis mellifera*) was introduced for cultivation and research in Chulalongkorn and Kasetsart University (12). In 2020, Thailand ranked 36th globally and 2nd in Southeast Asia with around 0.29% share of the honey market worldwide, representing approximately USD 19 million according to a report from the Department of Agricultural Extension, Ministry of Agriculture Cooperatives, Thailand. Moreover, besides honey, there are plenty of high-value by-products from honeybees for example royal jelly (approximately USD 75-200/kg), beeswax, propolis (bee glue), bee pollen, and even bee venom. The monetary worth and health benefits of these products have gained more attention and enhanced research activities in bee products properties, impact on

well-being, and illness prevention that will probably increase the value in favour of products from a certain area. Apart from its products, honeybees help the fruit farmers and horticulturist by acting as the main pollinators in several fruit gardens and farms. Taken together, apiculture in Thailand is growing and will be important in Thai agriculture and economy.

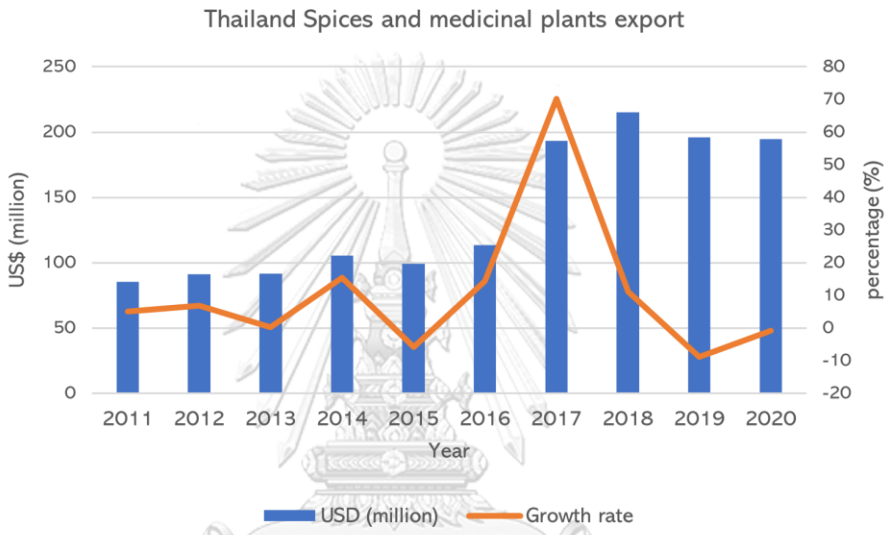

Figure 1.1 Value and growth rate of spices and medicinal plants export of Thailand during 2011-2020

1.1.1 Bee products properties and usage

Bee products, as described earlier, have been found to exhibit various activities and characteristics that are influenced by four main reasons: species of bees, geographical area, diversity of botanical sources, and collecting season, which will affect the constituents and their proportion in the products (13). The activities of these products have been studied in the form of crude extracts, purified partition, or even isolated compounds using various approaches (14). In this circumstance, we will describe only the isolated purified compounds to avoid the complexity that might arise from purity, absolute concentration, synergistic and antagonist effect, and unknown factors.

1.1.1.1 Honey

The first and most famous bee product is honey, which is produced from the digestion of floral nectar and is kept in honeycombs in the beehive primarily as a food supply. The sweetness of honey is related to the major composition by approximately 70-80 % of sugars, mainly glucose and fructose, with a lesser fraction of maltose and sucrose, and other complex sugars (15). Honey also contains amino acids with low amounts of protein, which serve as nitrogen sources, antibiotics mechanisms, and enzymes from bee salivary secretions (16). Other small amounts of constituents include organic acids, resulting in the pH of honey being in the range of 3.4 – 4.2, vitamins, and minerals (17). These components possibly originate from bees themselves, flowers, or even the soils of that area, creating a unique molecular fingerprint as well as characteristics and properties. As previously mentioned, a strong activity that could be observed from honey is antimicrobial activity owing to the supersaturated sugar content, low pH, H_2O_2 that is a by-product of glucose oxidation by a bee's enzyme glucosidase to generate gluconic acid, and non-peroxide compounds in specific types of honey. These contents are methylglyoxal (MGO) in manuka honey and defensin-1 in Revamil source (RS) honey (18). MGO is a breakdown product from 1,2-dicarbonyl, which forms from a non-enzymatic reaction between glucose and amino acids from heat treatment or prolonged storage (19). The antimicrobial activity is involved with disrupting the bacterial fimbriae and flagella structure and also damaging bacterial cell membrane (20). Another antimicrobial agent is defensin-I, which is an antimicrobial peptide (AMP) produced in hypopharyngeal glands and could be found in haemolymph where it acts as an innate immune response molecule against bacteria, fungi, and protozoa (21). The amount of defensin-I is varied in each of the bees and among their species that reflect the concentration of this AMP in honey. The mode of action of this AMP is likely to be involved with permeabilization of both gram-positive and negative bacterial cell membrane and antibiofilm formation but has less effect against multi-drug resistance strains of bacteria. Phenolic compounds are also

expressed and involved in this activity. Honey also expresses wound healing ability by preventing infection. Moreover, it has been reported that honey has immunomodulatory effects by major royal jelly proteins (MRJP) isoform 1 inducing tumour necrosis factor-alpha (TNFα) and matrix metalloproteinase (MMP) 9 expression in human keratinocytes that possibly stimulate the healing process (22). Anticancer activity in honey has also been discovered in isolated compounds that are various flavonoids and polyphenols for example chrysin, luteolin, apigenin, quercetin, and kaempferol. A report from thyme honey had found that a trihydroxyketone, which is a monoterpene, could induce apoptosis in human prostate cancer cell line PC-3 by inhibiting nuclear factor kappa B (NF-κB) activation via phosphorylation and IL-6 secretion (23).

1.1.1.2 Royal Jelly

Next, Royal jelly (RJ) is a nutrient-rich white to yellow acidic gelatinous product that contained a high amount of sugar (~10-16%), proteins and amino acids (~12-15%), and fat (~3-6%) with minor components of enzymes, vitamins, minerals, flavonoids, and phenolics (24). Due to the high density of nutrients, it serves as the main food during the development of larvae for worker bees and through the whole life of the queen (25). The proteins and amino acids are the major content of dry matter of RJ with approximately 80% of glycoproteins called MRJPs and minor fractions of apolipoprotein, enzymes, and defensin-1 (26). Jellein-I and -II, a product of MRJP-1 cleavage, has been shown to exhibit antibacterial activity on both grams of bacteria while royalisin, a homolog of defensin-1, appears to be effective against gram-positive bacteria only (27). Interestingly from lipid contents, 10-hydroxy-2decanoic acid, a unique fatty acid only found in RJ, has been reported to express anti-inflammatory and immunomodulator activities by inhibiting the histone deacetylase (HDAC) resulting in enhancing of expression of superoxide dismutase and reduction of LPS-stimulating inflammation in human monocytic leukaemia THP-1 cell line (28). Furthermore,

RJ protein and lipid constituents have been reported to benefit hyperlipidaemic and anti-ageing properties (29-31). However, there is no relevant report of anticancer activity in RJ.

1.1.1.3 Bee venom

Bee venom is a complex mixture containing peptides, proteins, enzymes, amines, volatile agents, phospholipids, and pheromones and has been used in apitherapy to treat chronic pain and inflammation, arthritis, and Parkinson's disease (32). The major components in the dry matter of bee venom are melittin, apamin, and phospholipid A2 (33). Melittin is an amphipathic peptide composed of 26-amino acids (AAs) with hydrophobic side chain AAs at N-terminal while positive side chain AAs at C-terminal. It is thought to interact with the anion lipid layer of the cell membrane and through accumulation creating pores, which cause the release of cell contents. However, anti-inflammatory effects have been observed with melittin (34). Its anticancer activity is involved with cell cycle arrest and induction of apoptosis via both the intrinsic and extrinsic pathways (35). Apamin is an α-helical peptide formed by 18 AAs cross-linked with two disulphide bonds. It penetrates the blood-brain barrier and appears to cause blocking of Ca^{2+}-dependent K^{+} channel and has been used for the treatment of central nervous system diseases (36). Phospholipase A2 is a Ca^{2+}-dependent bee enzyme that hydrolyses complex lipids on the cell surface, which causes inflammation and immune stimulation. While phospholipase A2 has allergic induction activity, its been shown to be effective for immunomodulation and ameliorate neurodegenerative and allergic disease (37, 38).

1.1.1.4 Propolis

Propolis or bee glue is a resinous yellow to black compound that was collected from plant resins by worker bees and mixed with wax and enzymes. It serves many roles in the beehive such as filler to seal cracks and holes of the hive, smoothing inner wall, preventing invasion, covering the corpse of an intruder inside the hive, and protecting the colony from diseases. The constituents of propolis in Thailand majorly consists of terpenes, flavonoids,

and phenolic esters, which possibly originated from the gum of the styrax tree (39). Caffeic acid phenethyl ester (CAPE) has been discovered as a main active compound. It exhibits antiviral, antibacterial, antifungal, anti-inflammatory, and anticancer activities. For antiviral activity, CAPE was found to inhibit viral integrase of HIV-1 (40), to repress hepatitis C virus replication (41), and recently been predicted *in silico* to inhibit SARS-CoV-2 main protease activity through binding into substrate pocket of the enzymes (42). It also increases in permeability of bacterial membranes and suppresses RNA polymerase activity (43). CAPE expresses anti-inflammation property via regulating NF-κB, a transcription factor that plays roles in various cell activity for example immune response, inflammation, and cell proliferation (44). Anticancer activity of CAPE was reported in breast carcinoma cell lines by induction of cell cycle arrest and apoptosis, and inhibiting angiogenesis through suppression of vascular endothelial growth factor (VEGF) (45). One of the phenolic esters, artepillin C, which originated from Baccharis (Asteraceae) (46) is found in high concentrations in Brazilian green propolis. Its effects include antibacterial, anti-inflammatory, and antitumour activity. The anticancer activity of artepillin C is mediated through the induction of cell cycle arrest at G_1 phase by repressing cyclin D/cyclin-dependent kinase (CDK) 4 activity in human colon cancer cell lines (47) and apoptosis through suppressing survivin, an anti-apoptotic protein, in oral squamous cell carcinoma cell line HSC-3 (48).

1.1.1.5 Bee pollen

Bee pollen, also known as ambrosia and when fermented is called bee bread, is a mixture of granules of plant pollen that are collected by worker bees and combined with nectar and bee secretions, which are stored in a specific place of the hive. It serves as a reserve food source for the hive colony. Its composition is highly varied based on geographic origin and the plants in the foraging area of worker bees so it could appear as a mono-floral or multifloral bee pollen. Compositions of bee pollen cover carbohydrates (~50%), AA and

proteins (~21%), lipids and fatty acids (5%), fibre (~8%), ash (~3%), vitamins, minerals, and other phenolic contents (49).

1.1.2 Programmed cell death and cell cycle arrest mechanisms

1.1.2.1 Cell cycle progression and regulation

Resistance to apoptosis or other programmed cell deaths has been a hallmark of cancer cells. Natural compounds exhibit various anticancer properties through cell cycle arrest and programmed cell death mechanisms including apoptosis, necroptosis, and autophagic cell death. Programmed cell death consists of several mechanisms and to simplify the order of these, cell cycle arrest will be described first.

Cell cycle progression (Fig. 1.2) is characterised by the growth and increase of its components including duplication of the genomic DNA during interphase. Subsequently mitosis, which consists of prophase, metaphase, anaphase, and telophase, takes place by segregation of replicated chromosomes into two separate cells during cell division. The interphase consumes most of the time in the cell cycle where cell growth and DNA replication occur with stringent regulation by multiple checkpoints. Interphase can be identified through the DNA content of the cells and classified into three phases including G_1, S, and G_2 phases. The transition of cell cycle is regulated by various groups of proteins, but the key regulators are the cyclin family proteins and CDKs. While CDKs protein levels appear to be stable throughout the cell cycle, cyclin proteins are in turn expressed and degraded during each phase. Only cyclin D, which contains three members cyclin D1, D2, and D3, are expressed all through the progression from G_1 to M phase, whereas the expressions of other cyclins are in order as follows: cyclin E from late G_1 during S and entry of G_2, cyclin A from S to G2 before entry of M, and cyclin B from early G_2 to M. CDKs are also organised into phase-related functions: with CDK4, CDK6 and CDK2 involved in G_1, CDK2 solely involved in S, and CDK1 in G_2. This shows the association between cyclins and CDKs in each phase. Starting from G_1, cyclin D interacts with CDK4 or CDK6 and forms a CDK-cyclin complex after

being stimulated by growth factors. These complexes then phosphorylate retinoblastoma protein (Rb), which inactivates Rb and causes the release of E2F transcription factors to activate the expression of downstream target genes required for G_1 transition to S for example cyclin E, Cdc25A, CDK2, cyclin A, CDK1, etc. Then, cyclin E binds to CDK2 causing activation by CDK7-cyclin H complex (CDK-activating kinase, CAK) of CDK2 and transition from G_1 to S phase. During S phase, cyclin A associates with CDK2, which is activated by CAK, and this complex helps facilitate DNA replication by activation of DNA polymerase and primase. After the DNA is duplicated, cyclin A binds to CDK1 and initiates entry to G_2 phase. Finally, cyclin B interacts with Cdc25-activated CDK1 and triggers M phase transition by activating cytoskeleton remodelling and organisation. If DNA damage has occurred in these transitions, ATM/ATR signalling cascade is activated and results in the activation of p53 tumour suppressor protein to upregulate the cyclin-dependent kinase inhibitors p21, which binds to CDK4/6-cyclin D and CDK1-cyclin B complexes and inhibits their activities together with other cell cycle arrest mechanisms (50). CDK1 is also regulated via phosphorylation at Thr14/Tyr15 by the Wee1 protein and to a lesser extent at Thr14 by the Myt1 protein (51). These phosphosites are removed by Cdc25A and Cdc25C phosphatases. However, the phosphatases are inactivated through phosphorylation of Cdc25A at Ser123 and Cdc25C at Ser216 by CHEK1 and CHEK2, downstream targets of DNA damage response by ATM/ATR signalling. The hyperphosphorylated Cdc25A and C are sequestered in the cytoplasm by 14-3-3 proteins (52). Prevention of CDK-cyclin complexes activation along the cell cycle progression arrests the cells at the stage where inhibition occurred. Cell cycle arrest is required for DNA repair and if the damage is irreparable the cell will be led to cell death. A longer period of cell cycle arrest has been linked to induction of apoptosis via dysregulation of the balance of proapoptotic and anti-apoptotic proteins which lead to mitochondrial membrane disruption then chromatin condensation, DNA fragmentation, and finally apoptosis (53). One explanation for this cell death is modulation of

JNK signalling cascade, deactivation of Rb, and activation of p53 involved with the apoptosis activation via regulation of apoptotic associated genes, upregulating of Bax while downregulating Bcl2, thereby triggering mitochondrial apoptosis (54).

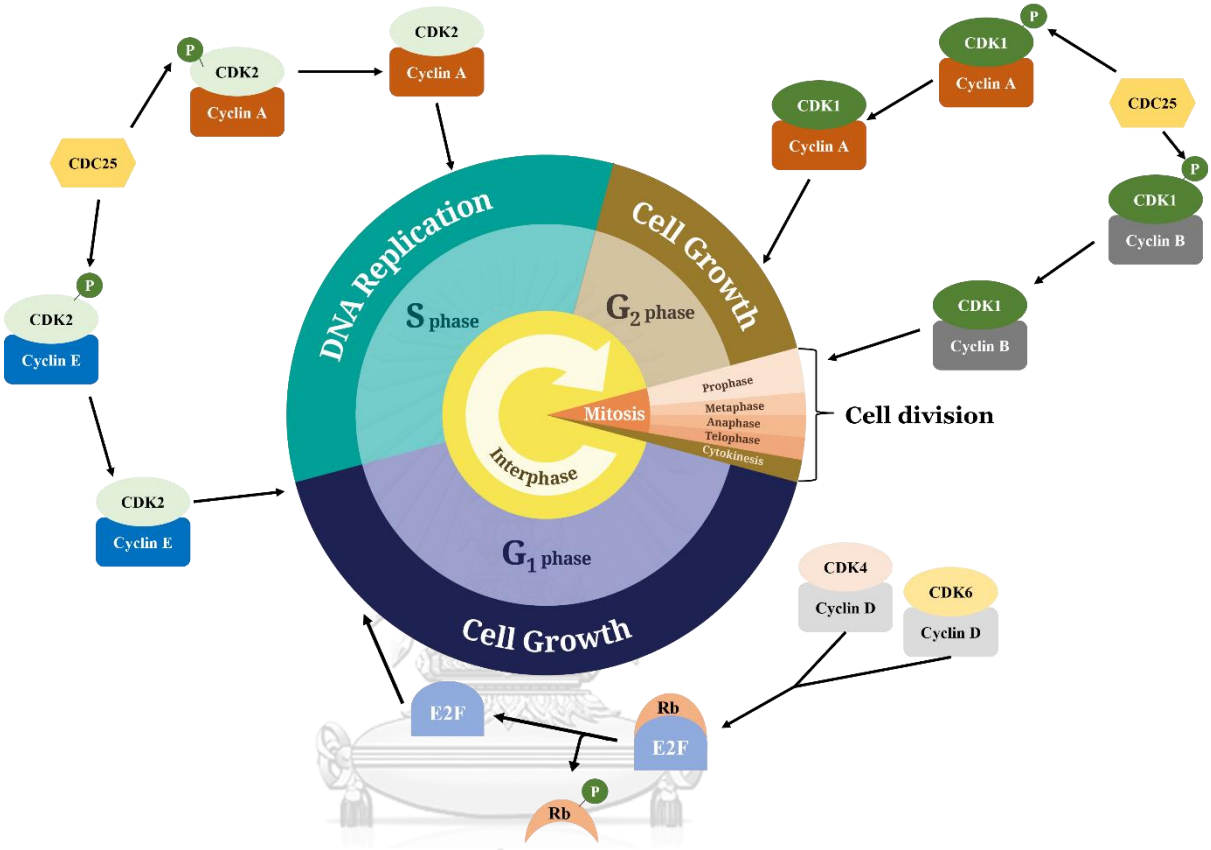

Figure 1.2 The stages of the cell cycle including associated cyclin-CDK complexes at each stage

1.1.2.2 Apoptosis

Apoptosis is a programmed cell death occurred through a series of cell structure changes at fine details that resulted in small pieces of the cells, called apoptotic bodies, which are later removed by macrophages without inflammation activation (55). In brief, the sequel of apoptotic cell death starts from the activation of apoptotic regulators through extrinsic or intrinsic signalling. Next, the effector machinery is stimulated by activated regulators and executed apoptosis mechanism. Then, the effector molecules were exported into the nucleus and cleaved their nuclear substrate resulting in changes in nuclei, like chromatin condensation

and DNA fragmentation (56). In the meantime, reorganisation of actin, loss of adhesiveness, and cell rounding can be observed. The convoluted cells appear to start contracting and blebbing resulting in shrinkage of the nuclear membrane, cell membrane, and organelles into apoptotic bodies. These apoptotic bodies are quickly phagocytosed by surrounding cells such as macrophages and parenchymal cells. The activation of apoptosis can be categorised into caspase-dependent and caspase-independent pathways.

Caspases are a group of cysteine proteases that recognised different substrate motifs and cleaved a protein where cysteine resides after an aspartic acid residue (57). They are involved in cell fate, differentiation, development. Regarding the caspase-dependent pathway, there are two mechanisms, extrinsic and intrinsic pathways, to activate the signalling cascade. First, the extrinsic pathway starts when death ligands trigger and activate death receptors (DRs), a group of plasma membrane receptors in the tumour necrosis factor (TNF) superfamily. DR contains a death domain (DD), which is a cytoplasmic tail with an approximate size of 80 AAs that is required for internalisation and activation (58). Interaction between DRs and death ligands for example Fas/FasL, TRAIL-R1/TRAIL, DR1/TNF, DR3/Apo3L, caused recruitment of protein complexes called death-inducing signalling complex (DISC). DISC consists of adaptor proteins (Fas-associated protein with death domain, FADD, and TNF receptor-associated Fas-associated protein with death domain, TRADD), initiator caspases (caspase-8/-10), and MAPK in some cases. After recruitment to DISC, initiator caspases were activated by dimerization and autocleavage. The activated initiators were responsible for the activation of effector caspase (caspase-3/-7) through cleavage of procaspase-3/-7. Then, these effector caspases cleave several important cellular structures and molecules led to formation of apoptotic bodies. An alternative pathway of this mechanism occurred through the cleavage of Bid that causes truncated Bid fragment involved in dysregulating of the mitochondria membrane. According to the latter event, mitochondria membrane was permeabilised and contributed to the leakage of cytochrome C and AIF that

also induce cell death. Moreover, recruitment of activated JNK to DISC has shown to be involved with facilitating caspase-8 activity by activation of E3 ubiquitin ligase Itch to ubiquitinate $cFLIP_L$, a caspase-8 inhibitor, led to degradation of $cFLIP_L$ (59). Second, the intrinsic pathway or mitochondrial pathway is activated by numerous molecules and events for example ER stress, hypoxia, DNA damage, and dysregulation of survival factors and apoptotic proteins balance. These events caused mitochondria outer membrane permeabilization (MOMP) (60). A famous signalling pathway of this mechanism is the p53-mediated intrinsic apoptosis pathway (61). Under cell stress events, p53 is stabilised and prevented from proteasomal degradation through inhibition of E3 ubiquitin ligase MDM2 that regulates p53 expression by ubiquitination. The increase in p53 protein level or activation of p53 by ATM/ATR pathway resulted in upregulation of p53-targeted genes, mainly pro-apoptotic BH3-only members of Bcl-2 protein family e.g., Bim, Bid, PUMA, Bad, Bik, Noxa, and Hararikiproteins. These proteins interacted with Bcl-2 causing dissociation of Bax and Bak proteins from Bcl2 while they also activated Bax and Bak proteins (62). Activated Bax and Bak facilitate the MOMP events by permeabilization of the mitochondrial outer membrane. The permeabilised mitochondria membrane releases two groups of proteins. The first group is the caspase activation group including cytochrome C that interacts with Apaf-1 and procaspase-9 to assemble apoptosome, Smac/DIABLO, and HrfA2/Omi serine protease. The last two proteins are associated with cell death by interrupting the function of inhibitors of apoptosis proteins (IAP), which normally prevents the activation of the apoptosome. Then, the activated caspase-9 in the apoptosome cleaved procaspase-3 to fully function caspase-3. Apart from caspase-associated apoptosis, the caspase-independent cell death mechanisms are associated with releasing of AIF and endonuclease G from mitochondria membrane through other mechanisms causing permeabilization for example high influx of calcium or neurotransmitter glutamate (63). Then, these proteins are localised into the nucleus causing DNA fragmentation and nuclear condensation that is named stage I condensation. This

process continues until chromatin condensation, which is the stage II condensation leading to nuclear collapse/disassembly (64).

1.1.2.3 Necroptosis

As mentioned above, besides apoptosis by caspase-dependent and caspase-independent pathways, several cell death mechanisms have been observed including necroptosis, autophagic cell death, and necrosis. Necrosis is an unorganised cell death resulting in cell membrane distortion and burst of intracellular components into the surrounding area, which will induce an inflammatory response. Necrosis occurs via several factors, including infection, toxic substance exposure, oxygen deprivation, and extreme environmental conditions. A recent study found that necrosis-like morphology can be regulated and has been termed necroptosis (65). Among all the necroptotic signalling pathways, TNF-induced necroptosis is extensively reported and investigated. Initiation of necroptosis by the TNF receptor family appears to be similar to the extrinsic apoptosis pathway but there are different groups of molecule complexes involved to guide the cells to necrotic death (66). In brief, trimerization of the cytoplasmic domain of TNFR occurred through the binding of TNF to TNFR. This structure involves in recruitment and assembly of protein complexes containing TRADD, cellular inhibitor of apoptosis protein 1 (cIAP1), cIAP2, receptor-interacting protein kinase 1 (RIPK1), TNFR-associated factor 2 (TRAF2), and TRAF5. In normal circumstances, RIPK1 is ubiquitinated with the E3 ubiquitin ligase cIAP1 and cIAP2 that lead to RIPK1 degradation and later activates NF-κB for cell proliferation (67). In necroptosis, cylindromatosis (CYLD), a deubiquitinate protein, prevents RIPK1 from degradation and allows the assembling of complex II by recruitment of caspase-8 and FADD (68). Under this circumstance, if caspase-8 inhibitors are presented, the cell will be directed to necroptosis. Then, RIPK1 is activated by autophosphorylation at serine 161. The activated RIPK1 assembles a complex named necrosome through recruitment of RIPK3 that is activated by autophosphorylation. Finally, the necrosome activates its substrate, mixed

lineage kinase domain-like pseudokinase (MLKL), causing oligomerisation and embedding into the cell membrane causing intracellular leakage and loss of cell stability.

1.1.2.4 Autophagic cell death

Autophagy is a eukaryote-specific cell survival and homeostasis process that catalyse undesired proteins in a double membrane organelle named autophagosome (69). It serves various roles in cells, including balancing energy sources, removal of misfolded or aggregated proteins, eliminating impaired organelles, exterminating pathogens, and introducing to cell death. Autophagy has been found in triggering cell death associated with necrosis, apoptosis, and autophagic cell death (70). Autophagic cell death occurs through the accumulation of autophagosomes and autolysosomes that continuously lyses the intracellular compartments and organelles resulting in cell blebbing with large vacuoles inside. Basically, autophagy is stimulated extracellularly or intracellularly in absence of growth factor/insulin signalling, hypoxia, and nutrient deprivation (69). Upon lack of growth factor or insulin stimuli, phosphatidylinositol 3-kinase (PI3K), a plasma membrane-associated lipid kinase, cannot activate Akt that prevents tuberous sclerosis complex (TSC1/2) complex from inhibition of Rheb GTPase activity. Then, deactivated Rheb cannot inhibit FK506-binding protein 38 (FKBP38) binding to mTORC. The mTORC protein inhibits autophagy by phosphorylating autophagy-related protein 13 (Atg13) when a nutrient is available, and a growth factor or insulin is presented. In addition to external stimuli, an energy-sensing kinase, target of rapamycin (TOR), is deactivated by nutrient deprivation, discharge of ATP, and hypoxic stress. This event allows Atg13 to interact with Unc-51 like autophagy activating kinase 1 and 2 (ULK1/2). Later, ULK1/2 activate autophagy-specific PI3KC3 complex 1, a complex of p150 protein, Beclin-1, vacuolar protein sorting 34 (Vps34), Autophagy and Beclin-1 regulator 1 (AMBRA1), and other organelle membranes (71). The activated PI3KC3 complex 1 phosphorylates phosphatidylinositol into phosphatidylinositol 3-phosphate to recruit DCFP1 and WIP1 proteins for phagophore formation. Then, conjugation of Atg5-Atg12 occurs in

parallel with LC3-II formation by conjugation of phosphatidylethanolamine with LC3-I protein. Both proteins/complexes are recruited to the phagophore and involved in the curvature of phagophores due to asymmetric recruitment. The curving of the phagophore allows it to engulf protein aggregates or damaged organelles and start to close the structure into autophagosomes and autolysosomes that is maturated by fusion with endosomes and lysosomes for proteolytic event.

1.1.3 α-mangostin and apigenin from bee products in Thailand and its anticancer activity

Recently, cancers have been reported for acquiring drug resistance that increases the complexity in treatment, recurrence, and relapse of the disease (72). Precision medicine and drug screening for novel multi-target anticancer compounds from natural resources and newly synthesized compounds for chemoprevention, treatment, and sensitizing in combination have been progressed vastly in the past few years (73-75). For decades, over 100 chemical compounds belonging to flavonoids, terpenes, leukotrienes, catechins, and phenolic substances have been extracted and isolated from bee products. Key compounds include α-mangostin (α-MG) and apigenin (APG). These two compounds have been reported for extraction and isolation from Thai bee products. α-MG was extracted from cerumen of Thai stingless bee (*Tetragonula laeviceps*) from mangosteen (*Garcinia mangostana* L.) and rambutan (*Nephelium lappaceum*) orchard in Chantaburi province (76). Cerumen is a propolis-like mixture of plant resins and stingless bee secretions that serves quite similar purposes to honeybee propolis. Whereas APG was isolated from bee pollen harvested from Pua district, Nan province, where corn (*Zea mays* L.) was the dominant plant species in the area.

1.1.3.1 α-Mangostin

Mangosteen, which is recognised as the queen of tropical fruit due to its unique taste, has been mass cultivated in South and Southeast Asia, which Thailand being the leader of

mangosteen export globally. It has been used in Thai traditional medicine for wound healing and to treat skin inflammation, diarrhoea, abdominal pain, and a chronic ulcer (77). The active compounds found highly in the mangosteen hull are majorly xanthones (α-, β-, and γ-mangostin, mangostanol, mangostenol, mangostanin. gartanine, garnicone derivatives, etc.), tannin, flavonoids, and other phenolic contents (78). α-MG, a bright yellow xanthone derivative found highly in the pericarps of mangosteen, has been firstly extracted and reported in 1855 by Schmid from mangosteen hull as reported by Yates and Stout in 1958 (79). Additionally, α-MG could be extracted from the root bark and stems of mangosteen and the *Allanblakia* family (80, 81). It has been shown to contain wound healing, antimicrobial, anti-malaria, anti-oxidation, anti-inflammation, and anticancer activities (82). According to its structure (Fig. 1.3), it expresses a high hydrophobic profile that reflects low solubility in water and high cell permeability, which results in less drug bioavailability from rapid absorption and metabolism at early time-point of administration but lower availability in body fluids and might be unreachable at the target site (83). Thus, multiple drug delivery strategies have been evolved to reduce these limitations (84).

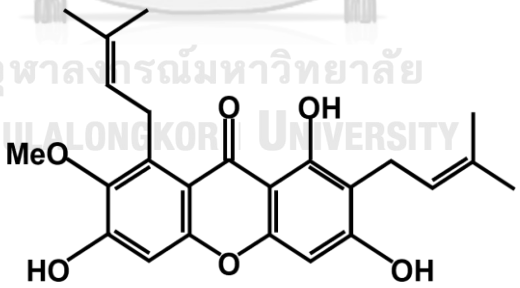

Figure 1.3 α-mangostin chemical structure

The antitumor effect of α-MG was first reported in human leukaemia cell lines HL-60, K562, NB4, and U937, by apoptosis induction in 2003 (85). The results showed that cleaved-caspase-3 expression and DNA fragmentation increases especially at 12 hours. They further observed in HL-60 cells that α-MG activated intrinsic apoptosis pathway as observed by reduction of caspase-9 and -3 and loss of mitochondria membrane potential causing

leakage of cytochrome C and apoptosis-inducing factor (AIF) into the cytosol (86). Moreover, in DLD-1, a human colon cancer cell line, α-MG repressed the expression of cyclin A, B1, D1, E1, CDK1, and phosphorylated-CDK1 (pCDK1) while promoting the expression of p27 that inhibits cyclin E/CDK2 activation, which resulted in cell cycle arrest at G_1 phase and induction of apoptosis (87). α-MG was also reported to induce apoptosis via caspase-independent pathway and sensitizing the cells in co-treatment with 5-FU (88). In human head and neck squamous cell lines HN-22, HN-30, and HN-31, α-MG caused apoptosis by interfering with the balance of apoptosis regulators via downregulating anti-apoptotic protein, Bcl-2, and upregulating pro-apoptotic protein, Bax, and cell cycle checkpoint regulator, p53 (89). They further found anti-invasiveness by downregulation of MMP-2 and MMP-9 in these cells when treated with α-MG (90). Antiproliferative activity of α-MG in human chondrosarcoma cell line SW1353 was observed by induction of apoptosis via both intrinsic and extrinsic pathways from increasing the expression of Bax, cleaved-caspase-3, -8, -9, and cytochrome C in cytosol and reducing the expression of Bcl2 and Bid (91). Activation of extracellular signal-regulated kinase 1 and 2 (ERK1/2), while inhibition of c-Jun N-terminal kinase 1 and 2 (JNK1/2) phosphorylation, Akt, and PDK1 was observed and suggested that α-MG alters the cell proliferation signalling. Similar to the effect observed in human colon cancer cell lines COLO205, MIP-101, and SW620 (92). Mitogen-activated protein kinase (MAPK), and specifically p38 MAPK, appears to be inhibited by α-MG in human hepatocarcinoma cell line SK-Hep-1 (93). Further work showed that α-MG reduced Akt signalling and tumour growth, arrested the cell cycle at G_1 phase, and induced mitochondria-associated apoptosis in xenografts of p53 mutation human breast cancer cell BJMC3879luc2 (94). Cell free kinase assay has shown that α-MG significantly inhibited CDK4 activity, possibly through binding to ATP pocket from molecular modelling, which illustrated cell cycle arrest at G_1 phase in prostate cancer cell line 22Rv1 and PC3 (95). Further study reported that α-MG suppressed cell progression from G_1 to S phase by upregulating the

expression of CHEK2 and p21, whereas downregulating the expression of cyclin D and proliferating cell nuclear antigen (PCNA), a protein involved in DNA replication and DNA repair process (96). Enzyme activity assays showed that α-MG could inhibit AKR1B10 activity to a lesser extent in comparison to γ-MG (97). AKR1B10 is an NADPH-dependent reductase, was upregulated in various cancers and inhibition of this protein expression and activity ameliorated the cancer progression (98). α-MG also appears to selectively bind to human DNA polymerase, DNA topoisomerase I and II that resulted in cell cycle arrest at G_2/M phase in human colon cancer HCT-166 (99). In breast cancer cell line MCF7, the expression level of oestrogen receptor alpha (ERα) and pS2, an oestrogen-responsive gene, was reduced after α-MG treatment (100). ERα appeared to correlate with the antiproliferation effect of α-MG because the cells gain more resistance to α-MG when ERα expression was knockdown. Shan *et al* reported that α-MG could inhibit activation of the STAT3 signalling pathway, which altered the expression of anti-apoptotic protein, Bcl-xL, and Mcl-1, causing permeabilization of the mitochondrial membrane that resulted in leakage of AIF and cytochrome C into cytosol inducing apoptosis (101). The inhibition of STAT3 by α-MG was discovered to be involved with upregulation and stabilisation of Src homology region 2 domain-containing phosphatase-1 (SHP1), a regulator of STAT3 (102). Later, α-MG was shown to inhibit the expression and activity of Fatty acid synthase (FAS), which are generally upregulated in breast cancer cells (103). Additionally, α-MG was identified to inhibit other proteins and enzymes that are associated with carcinogenesis and drug resistance for example isocitrate dehydrogenase 1 (IDH1) and ATP-binding cassette drug transporter (ABCG2) (104, 105). Though studies are showing that α-MG at high concentrations dysregulates the mitochondrial membrane and leads to apoptosis activation, α-MG also exhibits protective and anti-oxidative effects at lower doses by preventing peroxidative stress (106). Apart from the cytotoxicity effect in cancer cell lines, a study in F344 rats found that pre-treatment injection of crude α-MG extract from mangosteen pericarps has potential as a chemoprevention agent

in 1,2-dimethylhydrazine-induced colon carcinogenesis (107). This chemoprotection effect is also observed in oral administration with α-MG in Balb/c nude mice subcutaneously xenografted with human colon cancer cell line HT-29 (108).

Apart from the antiproliferative activity α-MG also exhibits anti-invasiveness and metastasis inhibition. In 2009, Hung *et al* discovered the antimetastatic effect of α-MG in human prostate carcinoma cell line PC-3 (109). The results showed that α-MG downregulated the expression level of MMP-2, MMP-9, and urokinase plasminogen activator (u-PA) by preventing the activation of JNK1/2, c-Fos, c-Jun, and NF-κB, including DNA binding activity of NF-κB and AP-1. Further studies in xenograft nude mice found that α-MG inhibited phosphorylation and activation of NF-κB and STAT3 that caused a reduction of NF-κB and STAT3 DNA binding activity (110). This deactivation led to downregulation of MMP-9, cyclin D1, and gp130, a cytokine receptor, but upregulation of tissue inhibitor of metalloproteinase 1 (TIMP1) This scenario also appeared in migration induction by 12-O-tetradecanoylphorbol-13-acetate (TPA) in human breast carcinoma cell line MCF-7 except that the researchers observed inhibition of phosphorylation on ERK1/2, instead of JNK1/2 and upregulation of IκBα expression (111). They extended this study in human lung adenocarcinoma cell line A549 by observing the effect of α-MG treatment on phorbol 12-myristate 13-acetate (PMA) inducing cell transition (112). The results showed that α-MG suppresses the activation of αvβ3 integrins, focal adhesion kinase (FAK), and ERK1/2. Whereas preventing PMA downregulating IκBα expression resulted in downregulation of MMP-2 and MMP-9. In addition, α-MG upregulates E-cadherin expression and downregulates N-cadherin, Snail, and Slug expression in human pancreatic cancer cell lines BxPC-3 suggesting that α-MG has the potential of suppressing epithelial-mesenchymal transition (EMT) therefore reducing the aggressiveness of the cancers (113-115).

Lastly, α-MG has been found to induce autophagic cell death in human glioblastoma cell lines GBM8401 and DBTRG-05MG by activation of AMP-activated protein kinase

(AMPK) resulting in phosphorylation of regulatory-associated protein of mTOR (raptor). This interacts with 14-3-3γ in the cytosol and prevents the activation of mTORC1, which under stress conditions will activate autophagy through ULK1 recruiting of the autophagic machinery (116). Orally administered α-MG in transgenic GFP-LC3 mice showed that autophagy was activated by increasing the expression of LC3, an autophagosome marker, without causing ER stress (117). However, ER stress from α-MG treatment has been shown in human prostate cancer but not prostate epithelial cells (118).

1.1.3.2 Apigenin

Apigenin is a flavonoid found in the genus Apiaceae, commonly known as umbellifers, including celery, parsley, chamomile, or carrot. It has also been detected in a broad variety of other plants including herbs, vegetables, citrus fruits, onion, wheat sprouts, and tea (119). Because of ubiquitously synthesis in most plants, APG became one of the most common active ingredients found in many traditional medicines. It presented various health benefits for example anti-inflammation, anti-oxidant, anti-ageing, anti-bacterial, and anti-tumour activities (120). In addition, it demonstrated low toxicity against non-cancerous cells in comparison to cancerous ones. The common structure of APG is 4',5,7-trihydroxyflavone as shown in Fig. 1.4. Water solubility is another concern of a compound in consideration for *in vivo* applications and potential drugs and can be observed through a log*P* value. The log*P* value expresses $\log_{10}$ of partition coefficient that is a solubility ratio of organic to aqueous phases of a compound, in general practice is the partitioning of the compound in octanol and water. The higher log*P* value is the higher affinity of a compound in organic solvents, which represented the hydrophobicity of the compound. The log*P* value of APG is 3.02 representing a hydrophobicity at the ratio of approximately 1000:1 of octanol to water. Therefore, APG appeared to have low solubility in water and bioavailability, which led to studies to enhance these properties in APG by encapsulation techniques (121, 122).

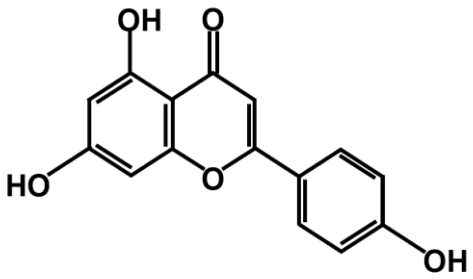

Figure 1.4 Apigenin chemical structure

Apigenin was found to trigger diverse mechanisms in several cancer cell lines. It has been shown to exhibit anticancer activity through for example induction of apoptosis, cell cycle arrest, metastasis inhibition, and anti-angiogenesis (123). APG anticancer activity had been firstly described in 1986 by Birt *et al* (124) where they observed anti-mutagenic effects in *Salmonella typhimurium* and anti-promotion of carcinogenesis by protecting the mouse skin epidermis from TPA-induced mutagenesis. The first report of APG-related cell death was published by Hirano *et al* (125) where APG caused cell death in human breast carcinoma cell line ZR-75-1. This led to the discovery of cell cycle arrest at G_2/M phase in APG-treated rat neuronal cell line B104 in 1994 by Sato *et al* (126). This arrest has then been linked to apparent DNA damage and upregulation of p53 in mouse embryo cell line C3H/10T1/2CL8 (127). APG also inhibits DNA topoisomerase I and II (Topo-I and -II) by interfering with TopoI/II-DNA binding (128, 129). This suggested that APG can perturb DNA damage mechanisms. Lepley *et al* reported cell cycle arrest at G_2/M phase in APG-treated mouse keratinocyte cell lines C50 and 308 by inhibiting CDK1 activity but not the expression level and downregulation of cyclin B1 (130). Moreover, they also found that the treatment of APG in human diploid foreskin fibroblast cell line CRL-2097 caused cell arrest at G_1 phase by upregulation of p21 expression, downregulation of cyclin D1 and A expression, inhibition of CDK2 activity, and prevention of Rb activation (131). Interestingly, Gupta *et al* found that APG treatment of unsynchronised human prostate cancer cell line CA-HPV-10 arrested the main population at G_2/M phase whereas synchronised cells by serum starvation were arrested

at G_1 phase (132). This result displayed that APG could suppress cell progression at different phases possibly by broad inhibition of various cyclins and CDKs. Further inspection in PC-3, LNCaP, 22Rv1, and DU145 suggested that APG caused cell suppression at G_1 phase by downregulating expression level of cyclin D1, D2, and E, and CDK2, 4, and 6, and upregulating expression level of cyclin-CDK complexes inhibitors, including p16, p18, p21, p27, and p53 including activation of p53 via DNA damage response pathway (132-134). Studies of associated signalling cascade revealed that APG dephosphorylated Rb at Ser780, 807, and 811 and inhibited several MAPK signalling pathways involved with cell proliferation except for ERK1/2 that was hyperphosphorylated (134, 135). However, activation of ERK1/2 does not activate ELK1, a downstream target for cell growth signalling (136). Moreover, the expression of p21 proved to be upregulated by the p53-independent mechanism through inhibition of histone deacetylase 1 and 3 (HDAC1 and HDAC3) that allows the transcriptional machinery to access p21 promoter for facilitating the expression and caused cell cycle arrest at G_1 phase (137). As described earlier, APG expressed antiproliferative activity by arresting cell progression not only at G_1, but also G_2/M phase. Regarding the cell transition from S to M phase, cyclin A, cyclin B, and CDK1 are necessary. They appeared to be suppressed both expression and activation by APG on several cell lines (138-141). γH2AX, a hallmark of DNA damage response, was expressed in APG-treated cells through activating of p53 by ATM/ATR pathway that consequently inhibited the activation of cdc25c, a phosphatase involved in activating cyclin B/CDK1 complex (142). Furthermore, activated p53 induced the transcription of various CDK inhibitors. In general, the signalling pathway related to cell growth, survival, and proliferation, for example, PI3K p85, Akt, JAK/STAT, p38, and GSK3β are inhibited (140). This series of actions that mainly targeted G_2 machinery in particular cell lines caused cell cycle arrest at G_2/M phase after APG exposure.

For induction of cell death mechanisms, APG also exhibits apoptotic activity by disrupting the balance of pro-apoptotic (Bax and truncated Bid) and anti-apoptotic (Bcl2 and survivin) proteins and reducing mitochondrial membrane potential thereby causing an efflux of cytochrome C and AIF into the cytosol resulting in activation of intrinsic apoptosis pathway (135, 143, 144). APG also stimulated the extrinsic apoptosis pathway by increasing death receptor protein 5 (DR5), TNFα TRAIL-R2, TNFR1/2, and cleaved-caspase-8 expression (145, 146). On autophagic cell death, in thyroid carcinoma cell line BCPAP, colorectal cancer cell line HCT116, and multiple myeloma cell line NCI-H929, autophagy markers were observed that are induction of Beclin-1 accumulation, suppression of p62, conversion of LC3-I to LC3-II, and accumulation of reactive oxygen species together with DNA damage (147, 148). In addition, APG also exhibits anti-invasiveness and anti-angiogenesis activities. Inhibition of metastasis by APG is associated with downregulation of uPA, MMP-2, and MMP-9, including secretion to extracellular matrix (149, 150) while anti-angiogenic activity has been described through downregulation of VEGF and HIF-1α expression resulting in inhibition of microvascular formation (151).

1.1.4 Phosphoproteins detection

The cell cycle is a highly dynamic and precise process. Each activation of a protein is due to a specific required function at the time and thus is heavily influenced by the phosphorylation of proteins to control their activity. The alteration of protein phosphorylation in each step of cell progression is governed by kinases and phosphatases. These kinases and phosphatases are strictly controlled and can be influenced by physical and chemical stimulants, which activated both intercellular and extracellular signalling pathways. Understanding phosphorylation changes during each process of the cycle offers an insight into the cellular framework of cell division. Studies of phosphoproteins after exposure to a compound were performed to elucidate how the compound interrupts cell progression. In past, the methods to observe a change in signalling pathway required large protein amounts of

the interest phosphorylation sites and a specific set of antibodies that are quite limited to detect several phosphorylation sites. Moreover, due to the dynamic nature of phosphorylation, a specific time for each phosphorylation site is needed to optimise for observation. Also, the experiment can be a tedious task due to the low-throughput technique. Recent mass spectrometry technology combined with the expansion of protein databases and development in phosphorylation prediction and detection allows the application of high-throughput techniques to study multiple phosphorylation sites in an experiment to occur, which is named phosphoproteomics.

The term phosphoproteome had been first mentioned in a 2D-gel electrophoresis study of the yeast proteome by Alms *et al* in 1999 (152). The limitations of previous techniques were difficulty in detection and quantification of transient, weak, or reversible phosphorylation, amounts of proteins/phosphoproteins needed for observation, time per course of an experiment, and complication of protein identification. The introduction of isotope-labelling tandem mass spectrometry in proteomics has addressed many of these limitations (153). Especially, the invention of electron transfer dissociation (ETD) for fragmentation step in tandem mass spectrometry has improved the confidence in the identification and quantification of labile phosphoryl groups on peptides (154). In parallel, label-free techniques have been improved through more advanced bioinformatics and statistics knowledge but technological challenges surrounding the amount of variation and detection limits remained. Isotope labelling, for example stable isotope labelling using amino acids in cell culture (SILAC), tandem mass tag (TMT), and isobaric tag for relative and absolute quantitation (iTRAQ), have been developed to cope with the quantitation issue by observing labelled isotope at MS^2 level thus improving detection sensitivity. Recently, a benchmarking study of quantification strategy for phosphoproteomics had reported that quantification of multiplex TMT-labelled at MS^2 level offers the most precise quantification method for complex biological samples, however, its accuracy for stoichiometry analysis is

still lower than the MS^3-based level (155). Moreover, a comparison study of pipelines for identification and posttranslational modification (PTM) site localisation from several famous peptide search engines had shown that PTM-score approach in MaxQuant-integrated engine Andromeda exhibited a high-reliability phosphosite identification and localisation, and allowed the users to easily adjust for specificity and sensitivity (156).

Furthermore, the technological improvements also brought about an increased number of potential phosphosites and highlights the lack of knowledge surrounding their functional meaning. Several phosphosite databases have been established using datasets of known sites from manually curated and/or computational predicted data, and generally contained information of sites and upstream regulators (157, 158). The two famous phosphosite databases that have been used by various kinase substrate prediction tools are PhosphoSitePlus (159) and Phospho.ELM (160) as a result of the validity of sites that were gathered only from literature and phosphoproteomics data. Downstream processing approaches for phosphoproteomics were performed to elucidate different aspects involving biological function and kinase activity. To determine a kinase activity on interesting sites, protein kinase substrate prediction tools for example NetworKIN (161), Musite (162), iGPS (163), were applied and can be extended for analysis of kinase activity. Next, Kinase set enrichment analysis (KSEA) (164) and Kinase Enrichment Analysis 2 (KEA2) (165) were tools for the prediction of kinase activity and were performed by over-representation analysis of known substrates set of kinases. The output of this prediction provided information on the activation and deactivation of kinases that can be further applied to infer the signalling pathway influenced by the treatment or condition of interest. Moreover, gene set enrichment analysis (GSEA) can be applied in discovering biological explanations of phosphorylation changes. However, GSEA was designed to determine the changes at transcription and translation level so phosphorylation might not suit well for this analysis because different phosphosites could have a contrasting impact on the function of the proteins.

In summary, phosphoproteins carried valuable biological information and it would be important to investigate how the treatment would affect the cellular function by regulating the signalling pathways through alteration of kinase and phosphatase activities. Thus, utilisation of GSEA and KSEA along with mapping phosphosites to kinase network by bioinformatics tools would provide insight into details of biological events that allow us to understand the mechanisms underlying the effect of treatment.

CHAPTER 2
EFFECT OF APIGENIN AND α-MANGOSTIN ON BT-474 BREAST AND SKOV-3 OVARIAN CANCER CELL LINES

2.1 Introduction

Breast and ovarian cancers have long been a severe illness and a major cause of death in females globally. Breast cancer is on the top of the female cancer list in both incident rate and mortality rate whereas ovarian cancer is ranked 8th in the list on both incident rate and mortality rate (166). However, considering the death ratio of gynaecology-associated female cancer, ovarian cancer is in the 2nd place after cervical cancer. While breast cancer has been raised in attention and various methods for diagnosis this cancer has been invented, ovarian cancer remains high in fatality due to its undefined signs and symptoms, making it essentially asymptomatic until at an advanced stage preventing its early diagnosis and treatment. For decades, surgery and chemotherapy, especially platinum- or taxol-based chemotherapy, plus more recently cancer immunotherapy for example trastuzumab or bevacizumab have been introduced and developed for cancer treatment, but they are not fully effective because of their adverse effects and the advent of resistance (167, 168). Hence, novel, or alternative treatments are necessary for the treatment of breast and ovarian cancer patients.

Natural products, especially herbs, have increased attention for use in cancer therapy in order to inhibit cell proliferation and induce apoptosis, with the hope of reducing adverse events as well as avoiding specific resistance that occurred in some cancers. Thus, many natural compounds or phytochemicals had been isolated, mainly from plants, such as lignans were shown to have potential application against breast cancer due to their phytoestrogen activity (169) and cryptotanshinone found in the traditional Chinese herbal medicine *Salvia miltiorrhiza* Bge. (170) The molecular mechanisms of action of some of these compounds have been reported. In breast cancer, ent-11α-hydroxy-15-oxo-kaur-16-en-19-oic-acid can

induce apoptosis of MCF-7 and MDA-MB-231 cancer cells differently (171). Sayeed *et al.* also reported that allyl isothiocyanate, found in many cruciferous vegetables, inhibited the proliferation of MCF7 depending on time and concentration (172). Also, it was highly cytotoxic to MCF-10A, which is a non-tumorigenic breast epithelial cell line. However, allyl isothiocyanate did not have an inhibitory effect against MDA MB-231 cells at all. Next, in ovarian cancer, proanthocyanidins from the leaves of Chinese bayberry (*Myrica rubra* Sieb. Et Zucc.) showed strong inhibition of cell growth (with cell cycle arrest at the G_1 phase), angiogenesis, cell migration, and invasion of A2780/CP70 cisplatin-resistant ovarian cancer cells (173). In addition to natural compounds, synthetic compounds had been reported to be challenging sources. For example, synthesized (1*E*,4*E*)-6-(1-(isopentyloxy)nonyl)-5-methoxynaphthalene-1,4-dione dioxime, which is a derivative from 1,4-naphthoquinone oxime, was reported to be strongly cytotoxic to the A2780 ovarian cancer cell line with half-maximal inhibitory concentration (IC_{50}) value of 8.26 ± 0.22 μM (174). Furthermore, O^2-(acetoxymethyl)-1-(*iso*-butylamino)diazen-1-ium-1,2-diolate and O^2-(acetoxymethyl)-1-(isopropyl amino) diazen-1-ium-1,2-diolate, synthesized from primary amine-based diazeniumdiolates, reduced the proliferation of SKOV-3 and ES2 ovarian cancer cells at 0.033–1.0 mg/mL after 24 h exposure (175).

The aim of this work was to evaluate the *in vitro* cytotoxicity of α-MG and APG on breast and ovarian cancers. α-MG is mainly isolated from *Garcinia mangostana* pericarp (176) and the cerumen of the stingless bee *Tetragonula laeviceps* (76), while APG is the main compound extracted from Roman chamomile *Chamaemelum nobile* (L.) (177) and *Apis mellifera* bee pollen (178). Both compounds have been reported to have various bioactivities, including anti-biofilm (179), anti-aging (180), anti-inflammation (181), and anti-gout (182) activities. Furthermore, only a few works have reported that both compounds can contribute to cancer prevention. Especially when considering only gynaecological cancer, α-MG can inhibit the growth of HeLa human cervical cancer cells [19] but there are no reports on the

SKOV-3 ovarian cancer cell line, while only a few studies showed antiproliferative activity of APG on this cancer cell line (183, 184). Thus, more data regarding antiproliferation mechanisms is necessary. Human breast cancer BT-474 cell line, which was derived from a ductal carcinoma, and human ovarian adenocarcinoma SKOV-3 cell lines were used as a model breast cancer cell line [10]. Normal mammary epithelial fibroblast MCF-10A cell line was used as a non-transformed control. Whereas, due to limitations of normal ovary cells availability, CCD-986Sk skin fibroblast, and WI-38 lung fibroblast cell lines were used as model normal human cells instead of a normal ovarian epithelial cell line. Next, doxorubicin (Dox), a currently used chemotherapeutic drug, was used as a positive control. The cytotoxicity was observed by using the 3-[4,5-dimethylthiazole-2-yl]-2,5-diphenyltetrazolium bromide (MTT) assay. Change in morphology of the treated cells was observed under light microscopy. Programmed cell death was investigated through flow cytometry following annexin V-Alexa flour 488 and propidium iodide (PI) staining, while cell cycle arrest was performed likewise except after PI staining only. The activity of caspase-3, -8, and -9 were also evaluated for apoptosis activity validation. Furthermore, changes in transcript expression levels of selected representative inflammation-associated genes, proto-oncogenes, autophagy-associated genes, and apoptosis-associated genes were investigated by quantitative real-time reverse transcription polymerase chain reaction (qrt-RT-PCR). Overall, the obtained data give a broader insight into how α-MG and APG inhibit the growth of BT-474 breast and SKOV-3 ovarian cancer cell lines.

2.2 Materials and methods

2.2.1 Cell culture

The human BT-474 ductal carcinoma cell line (BT-474, ATCC no. HTB20) was cultured in Roswell Park Memorial Institute (RPMI) 1640 medium containing 10 % (v/v) foetal calf serum (FCS) while human ovarian adenocarcinoma derived cell line SKOV-3 (ATCC no. HTB77 were cultured in McCoy's 5A (modified) medium supplemented with

10% (v/v) foetal calf serum (FCS). As for comparison in breast cancer experiment, normal mammary epithelial fibroblast (MCF-10A, ATCC no. CRL-10317) was used and cultured in Dulbecco's modified Eagle medium and Ham's F-12 medium (DMEM/F12) supplemented with 5% horse serum, 20 ng/mL recombinant epidermal growth factor (rEGF), 0.5 mg/mL hydrocortisone, 10 μg/mL insulin and 100 ng/mL cholera toxin. The untransformed (normal) human skin fibroblast CCD-986Sk (ATCC no. CRL-1947) and lung fibroblast WI-38 (ATCC no. CCL-75) cell lines were used in comparing to SKOV-3 cells. Both CCD-986Sk and WI-38 cells were cultured in MEM (Eagle's Minimum Essential Medium) supplemented with 10% (v/v) FCS and all cell lines were cultured and tested at 37 °C with 5% (v/v) CO_2 in a humidified environment.

2.2.2 Cell viability and proliferation by the surrogate MTT assay

BT-474, MCF-10A, CCD-986Sk, and WI-38 cells were cultured in 96-well plates seeded at 1×10^4 cells/well containing 200 μL of media overnight, while SKOV-3 cells were cultured in the same manner but seeded at 5×10^3 cells/well. Then, the cells were treated with various concentrations of APG, α-MG, Dox or the dimethyl sulfoxide (DMSO) solvent only (control). BT-474, MCF-10A, and SKOV-3 cells were treated for 24, 48, and 72 h while CCD-986Sk and WI-38 cells were treated for 72 h only. After the indicated incubation (exposure) time was reached, 10 μL of 5 mg/mL of MTT solution was added into each well and cultured as before for 3 h to allow the formazan formation. The culture medium was then removed, and the formazan was solubilized by the addition of 150 μL of DMSO and the absorbance was measured by microplate reader at 560 nm (A_{560}). The cell viability (%) was calculated as equation below

$$\% \text{ cell viability} = \frac{(A_{560} \text{ treated cells} - A_{560} \text{ blank})}{(A_{560} \text{ untreated cells} - A_{560} \text{ blank})} \times 100$$

The IC_{50} value of each compound was calculated from the graphical plot of the relative number of viable cells (%) *vs*. the test compound concentration.

2.2.3 Cell imaging

BT-474 cells at 1×10^6 and SKOV-3 cells at 5×10^5 cells in 5 mL of medium in a 25-cm2 flask were cultured overnight and treated the next day with 0.1% (v/v) DMSO alone (control) or DMSO containing α-MG (9.75 (BT-474) and 7.309 (SKOV-3) μM), apigenin (37.01 (BT-474) and 18.502 (SKOV-3) μM) or doxorubicin (0.46 (BT-474) and 0.431 (SKOV-3) μM) for 24, 48, and 72 hr. Live-cell images were captured using a Nikon Eclipse TS100 microscope coupled with a DS-L3 imaging system at 40×, 100×, and 200× magnifications

2.2.4 Apoptosis and cell cycle analysis

Test cells were cultured as in cell images above and harvested at the indicated time by trypsinization with 0.05% (w/v) trypsin in 0.5 mM EDTA buffer, washed twice with cold phosphate-buffered saline (PBS) using centrifugation at 3,000 x *g* for 5 min at 4 °C to harvest the cells each time. For apoptosis detection, the cell pellets were resuspended in 50 μL of binding buffer (10 mM HEPES pH 7.4, 140 mM NaCl, and 2.5 mM $CaCl_2$) and stained by 5 μL of annexin V-Alexa flour 488 and 5 μL of PI for 30 min at room temperature in the dark. For the cell cycle study, the cell pellets were fixed in 200 μL of cold 70% (v/v) ethanol at -20 ^oC overnight, harvested and washed as above. The washed cell pellet was then suspended in 250 μL PBS with 0.1 mg/mL RNase A and incubated at 37 ^oC for 30 min, washed as above and resuspended in staining buffer (12.5 μL of 1 mg/mL PI in PBS) and incubated at room temperature in dark for 30 min. The samples were then analysed by flow cytometry on a FC 500 MPL cytometer (Beckman Coulter, Brea, CA) recording 10,000 events per sample. The experiment was performed in triplicate.

2.2.5 Caspase activity assay

Test cells were plated and treated as stated above under apoptosis and cell cycle studies. The treated cells were harvested by trypsinization at 12 and 24 h and then subjected to the caspase-3, -8 and -9 colorimetric assay kits (catalog no. ab39401, ab39700, and ab65608,

Abcam, UK) as per the manufacturer's instructions. Briefly, after harvesting, the cells were washed with cold PBS and centrifuged at 800 x *g*. The cell pellets were then lysed with 50 µL of chilled cell lysis buffer, incubated on ice for 10 min, clarified by centrifugation at 10,000 x*g* for 1 min and the supernatants were harvested into a new microcentrifuge tube. The protein concentration of each sample was measured by the Bradford assay and then adjusted to 100 µg of protein/ 50 µL of cell lysis buffer and applied to each well of a 96-well plate. Next, 50 µL of 2x reaction buffer was added with a final concentration of 10 mM dithiothreitol into each sample well. After mixing, the respective substrate of each caspase was added to each well and incubated at 37 ºC for 1–2 h. Finally, the absorbance of each reaction was measured at 400–405 nm on a microplate reader. Each experiment was performed in triplicate.

2.2.6 Analysis of transcript expression levels by RT-qPCR

Cell lines were treated and processed as previously described in the apoptosis detection assay until the cell pellet was collected. After cell harvesting, total RNA from each sample was extracted using a RNeasy mini kit (catalog no. 74104, Qiagen, CA, USA). The RNA concentration and purity were evaluated by spectrophotometer at an absorbance of 260 and 280 nm. The qrtRT-PCR was performed using the One-Step SYBR® PrimeScript™ RT-PCR kit II (Perfect Real-time; catalog no. R086A, Takara, Japan). The PCR mixture contained 20 ng of total RNA, 0.4 µM of both forward and reverse primers, 1 µL of PrimeScript™ Enzyme Mix II, and 1x one step SYBR® RT-PCR buffer IV. The nucleotide sequences of the primers used in this study are listed in Table 2.1.

Amplification and quantification of each gene of interest were carried out using the Minicon® system (Bio-rad, CA). The thermocycling was performed as follows. First, the total RNA was reverse transcribed into cDNA at 42 ºC for 5 min. Then, real-time qPCR was performed by an initial 95 ºC for 10 s followed by 40 cycles of 95 ºC for 10 s and 60 ºC for 30 s. Dissociation analysis was performed to validate the specific product for each primer pair. All

target genes were normalized to that for *GADPH* expression in each sample and compared as the relative expression level between the control and treated samples. The normalized relative expression level was calculated due to a quantification cycle (C_q) value as formula below.

A normalized relative gene expression level = $2^{-\Delta\Delta C_q}$

Table 2.1 Targeted genes and oligonucleotides for amplification in RT-qPCR assay.

Gene	Forward primer (5'→3')	Reverse primer (5'→3')
Reference gene		
GAPDH	GGGCATCCTGGGCTACTCTG	GAGGTCCACCACCCTGTTGC
Inflammation-associated genes		
Cox2	TCTGCAGAGTTGGAAGCACTCTA	GCCGAGGCTTTTCTACCAGAA
NFκB	ATGGCTTCTATGAGGCTGAG	GTTGTTGTTGGTCTGGATGC
Proto-oncogene		
CTNNB1	CTTGTGCGTACTGTCCTTCG	AGTGGGATGGTGGGTGTAAG
Autophagy-associated gene		
CathepsinB	CAGCGTCTCCAATAGCGA	AGCCCAGGATGCGGAT
Apoptosis-associated genes		
BCL2	ATGTGTGTGGAGACCGTCAA	GCCGTACAGTTCCACAAAGG
Caspase3	TGTTTGTGTGCTTCTGAGCC	CACGCCATGTCATCATCAAC
Caspase7	CCAATAAAGGATTTGACAGCC	GCATCTGTGTCATTGATGGG
Caspase8	GATCAAGCCCCACGATGAC	CCTGTCCATCAGTGCCATAG
Caspase9	CATTTCATGGTGGAGGTGAAG	GGGAACTGCAGGTGGCTG

2.2.7 Statistical analysis.

Data are presented as the mean ± one standard deviation (1SD), derived from three independent repeats in each experiment. The data were analysed by one-way analysis of variance (ANOVA) followed by Tukey's multiple-comparisons test for the significance of differences between the means. Significance was accepted at the $p < 0.01$ and $p < 0.05$ levels. All analyses were performed using the SPSS version 19.0 program (IBM corporation, Chicago, IL, USA)

2.3 Results

2.3.1 Cytotoxicity effect of α-MG and APG on BT-474 and MCF-10A cell lines

BT-474 cells treated with α-MG inhibited their proliferation depending on concentration. All three incubation times revealed the marked antiproliferation activity of α-MG, although α-MG at 48 h was slightly most effective for the same level of inhibition (Fig. 2.1A). APG was inhibitory after 48 and 72 h, but not at 24 h (Fig. 2.1B), while Dox was cytotoxic at all three time points but only weakly at 24 h (Fig. 2.1C). Therefore, all three compounds were cytotoxic to cells depending on time and concentration. Derived IC_{50} of α-MG, APG and Dox were summarized in Table 2.2. At all assayed time points, α-MG was more cytotoxic to BT-474 cells than APG. At 24 h, BT-474 cells were only sensitive to α-MG, whereas proliferation of BT-474 cells inhibited by APG and Dox occurred after longer exposures.

Since all three compounds were cytotoxic to BT-474 cells, it was necessary to find out if these compounds were also cytotoxic to normal cells. In this study, the MCF-10A normal breast cells were used as a representative control. From Figure 2.1D-F, it was of note that the inhibition manner of these three compounds on MCF-10A and BT-474 cells was similar. In addition, APG was the least cytotoxic compound against MCF-10A cells, especially at the early time point (24 h exposure). The derived IC_{50} of these three compounds against MCF-10A cells was summarized in Table 2.2. Comparing the IC_{50} between BT-474 and MCF-10A cells at each time point, both α-MG and APG were slightly more cytotoxic to BT-474 than MCF-10A cells. Of note was that Dox was more cytotoxic to MCF-10A cells, especially at the early (24 h) exposure. At a concentration as low as 1.72 μM, Dox-induced 100% MCF-10A cell mortality at 48 and 72 h (Fig. 2.1F).

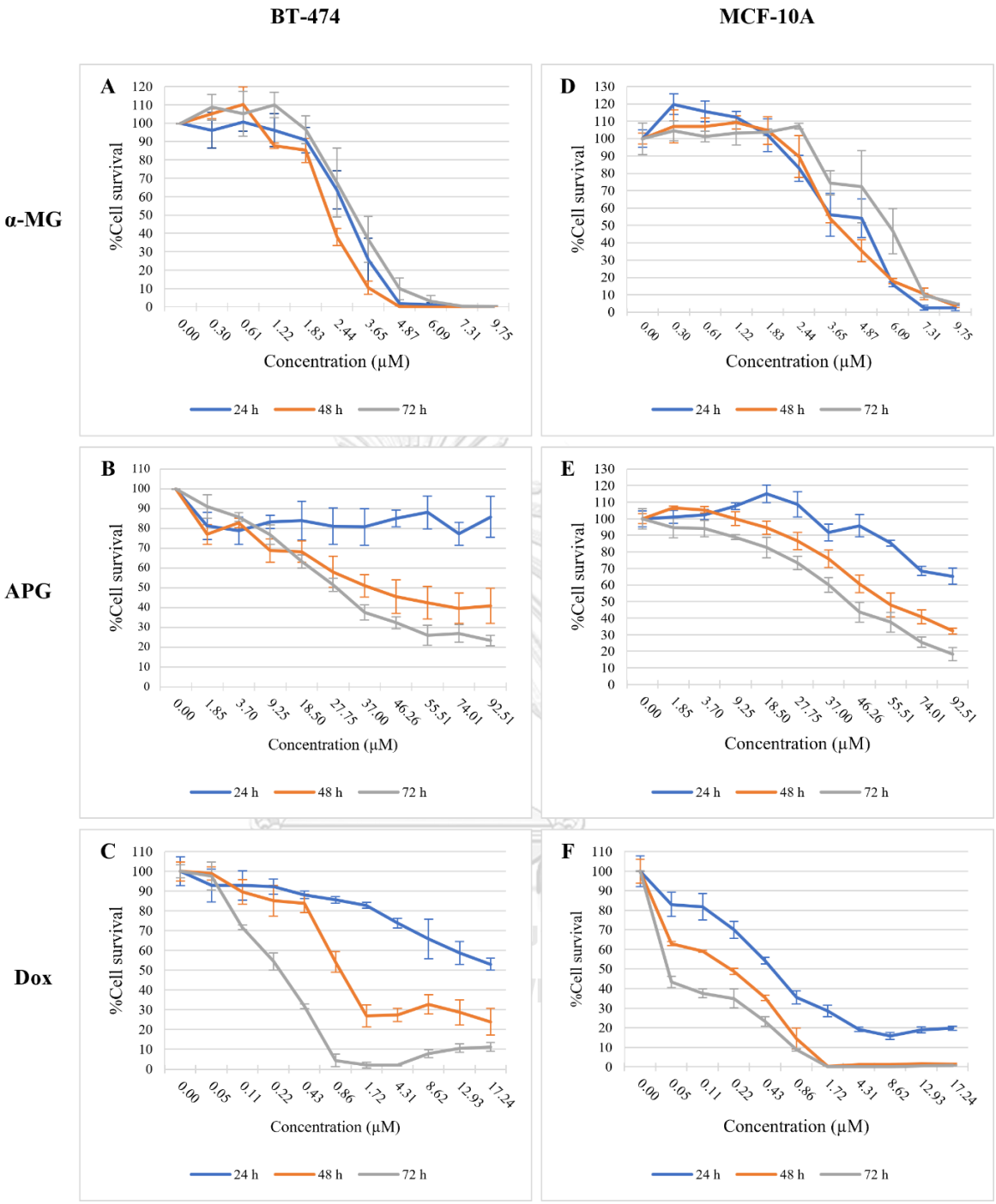

Figure 2.1 Cytotoxicity effect of the compounds on BT474 and MCF-10A cell lines.

(A, D) α-MG, (B, E) APG, and (C, F) Dox on BT-474 cells and MCF-10A. The cell survival (%) was estimated by the MTT assay after 24, 48 and 72 h exposure (blue, orange and grey line, respectively). Data are shown as the mean ±SD, derived from three independent repeats.

Table 2.2 IC_{50} of α-MG, APG and Dox against BT-474 and MCF-10A cells

Compound	BT-474			MCF-10A		
	24 h	48 h	72 h	24 h	48 h	72 h
α–MG	2.91 ± 0.64	2.28 ± 0.11	3.15 ± 0.80	4.17 ± 1.17	3.97 ± 0.10	5.09 ± 0.73
APG	ND	47.24 ± 8.84	28.15 ± 3.36	ND	60.91 ± 9.81	44.37 ± 2.41
Dox	ND	1.05 ± 0.18	0.28 ± 0.04	0.57 ± 0.06	0.20 ± 0.02	0.06 ± 0.004

ND = not determined

2.3.2 Cell morphology of BT-474 and MCF-10A cell lines after α-MG and APG treatment

In order to observe the morphological changes in BT-474 cells, α-MG, APG, and Dox at 9.75 µM, 37.01 µM, and 0.46 µM, respectively, were chosen along with 0.1% DMSO. At 100× magnification, at all three time points (24, 48, and 72 h), strange morphologies of the cells treated by each compound were evident, but not in the DMSO control. The longer the treatment (exposure) time was, the more floating cells and lower density of attached cells were noted (Fig. 2.2A). At 200× magnification and 48 h time point, clear colony formation was evident in the control (DMSO-treated) cells, whereas the smallest colonies were observed in the Dox-treated cells. Thus, Dox may inhibit the proliferation of BT-474 cells by inhibiting their migration/invasion (Fig. 2.2B). Although colonies were formed in the α-MG and APG-treated BT-474 cells, more vacuoles were evident within the cells. Overall, some indicators of potential apoptosis-like cell blebbing and shrinkage were also observed in treated cells by the three compounds, but not the control cells.

Considering Table 2.2, although α-MG was cytotoxic to MCF-10A normal cells, the shape and density of the α-MG treated MCF-10A cells were similar to the control (DMSO only treated) cells at all three assayed time points (Figure 2.3A and B). After 72 h, α-MG-treated MCF-10A cells were still attached to the substratum. After 24 h, at any time no IC_{50} value was determined (> 92.51 (APG) and 17.24 (Dox) µM) for APG- and Dox-treated cells (Table 2.2), similar shaped cells to the control were seen, and were still noticed in samples with longer exposure times, except that a lower cell density was prevalent in the Dox-treated

cells. Thus, BT-474 breast cancer cells may have a greater sensitivity to these compounds than MCF-10A normal breast cells, potentially indicating that these three compounds may be practical chemotherapeutic agents**.**

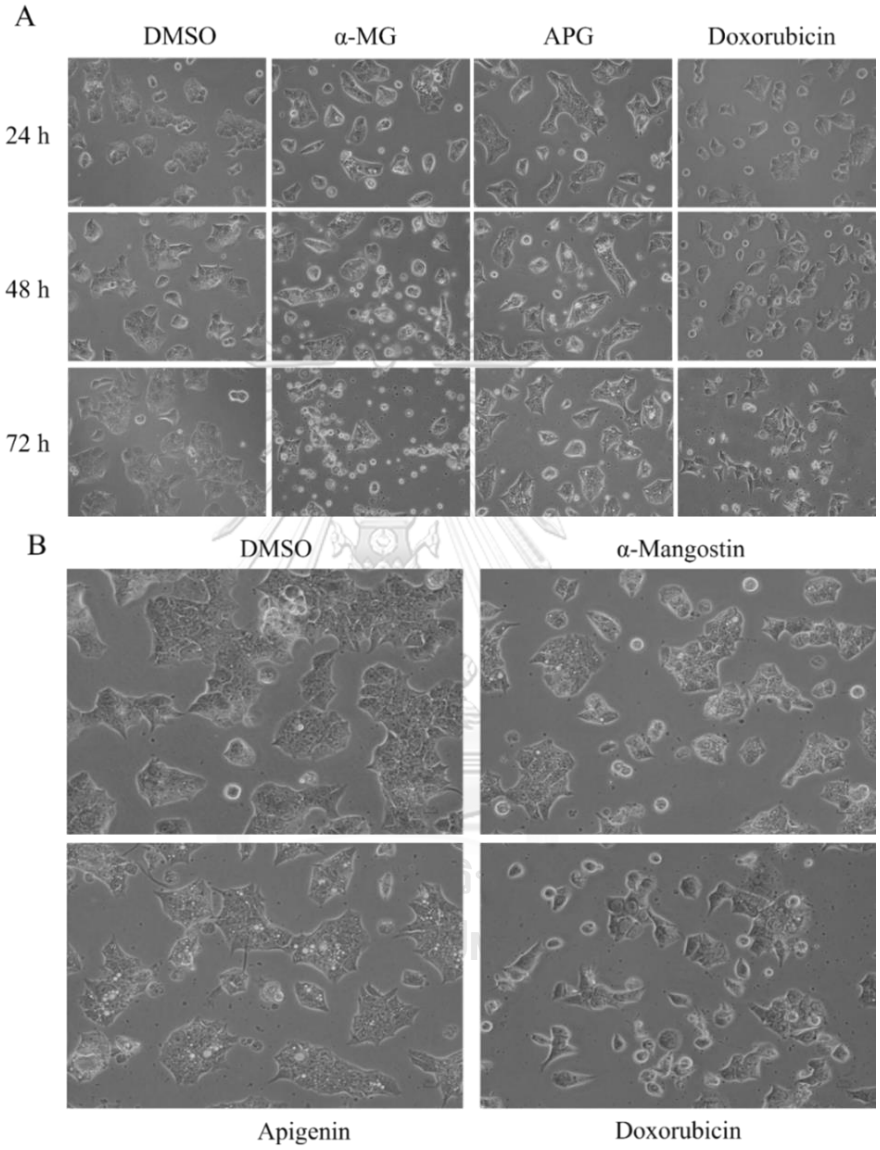

Figure 2.2 Morphology of BT-474 cells after α-MG and APG treatment.

The cells were treated with 0.1% (v/v) DMSO only (control), α-MG (9.75 μM), APG (37.01 μM) and Dox (0.46 μM) after 24, 48, and 72 h at (A) 100× magnification and (B) the same treatment after 48 h at 200× magnification. Images are representatives of those seen from at least three such fields of view per sample from three independent repeats.

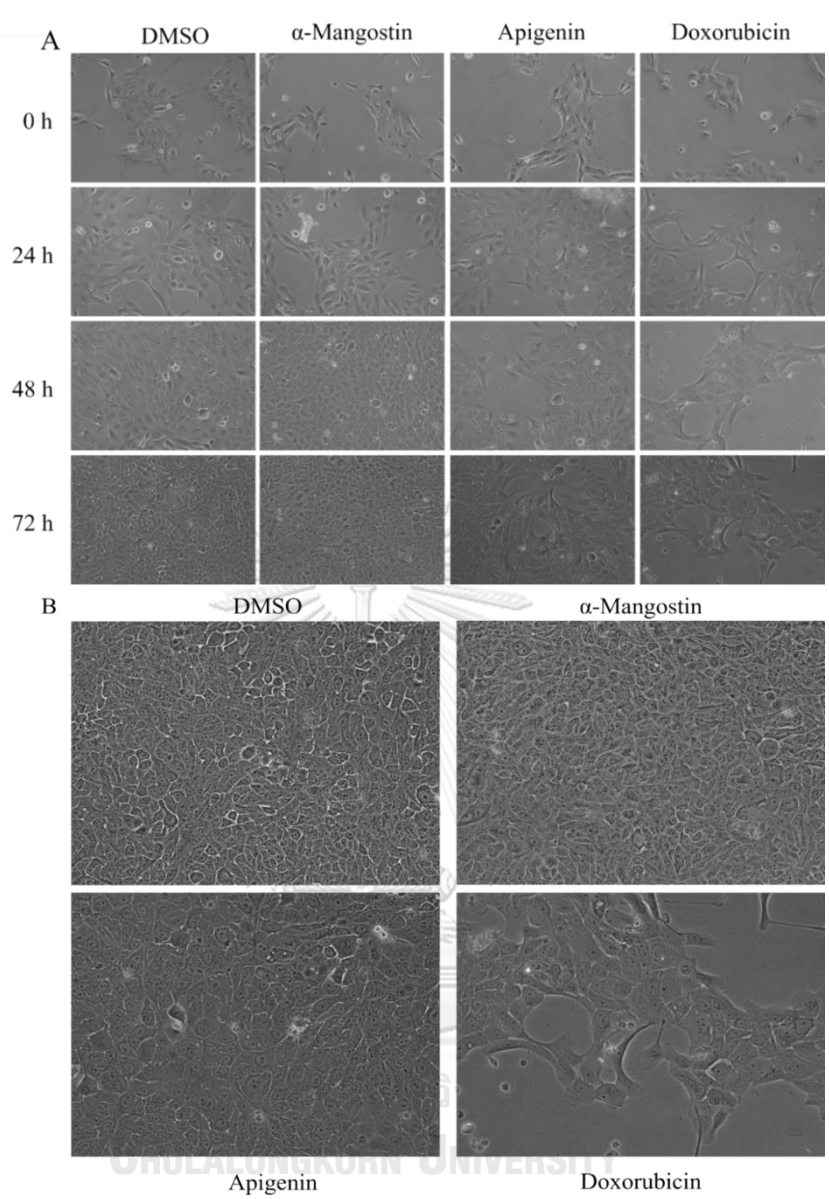

Figure 2.3 Morphology of MCF-10A after α-MG and APG treatment.

The cells were treated with 0.1% (v/v) DMSO only (control), α-MG (9.75 μM), APG (37.01 μM) and Dox (0.46 μM) after 24, 48 and 72 h at (A) 100× magnification and (B) the same treatment after 48 h at 200× magnification. Images are representatives of those seen from at least three such fields of view per sample from three independent repeats.

2.3.3 Not apoptosis but necrosis was observed in BT-474 cell line after α-MG and APG treatment

From the observed changes in the BT-474 cell morphology (Fig. 2.2), especially the increasing number of vacuoles in the treated cells, programmed cell death was possibly presented. Treated BT-474 cells were stained using annexin V and PI, and flow cytometric analysis revealed that both α-MG (9.75 µM) and APG (37.01 µM) induced a significant level of necrosis to BT-474 cells since early exposure time (24 h; p <0.01) onwards. However, APG induced a significant level of early (p <0.05) and late (p <0.01) apoptosis at 24 h exposure, while Dox (0.46 µM) caused early apoptosis of BT-474 cells at an early exposure time (24 h). Longer exposure times caused an increased number of necrotic cells, although early apoptotic cells were still detected in the 48 and 72 h time points (Fig. 2.4C and E).

From this flow cytometric analysis (Fig. 2.4), APG and α-MG appeared to mainly induce necrosis in BT-474 cells at 24 h, although some apoptotic cells could still be observed. To further evaluate the possibility of apoptosis, caspase-3, -8, and -9 activities were assayed from BT-474 cells after exposure to these compounds for 12, 24, and 48 h. However, the significant increase in the relative caspase activity, compared to that in the control cells, was only detected at 48 h (p <0.01). The activity of caspase-3 was clearly increased by all three compounds, while the activity of caspase-8 and -9 was upregulated by Dox (Fig. 2.5)**.**

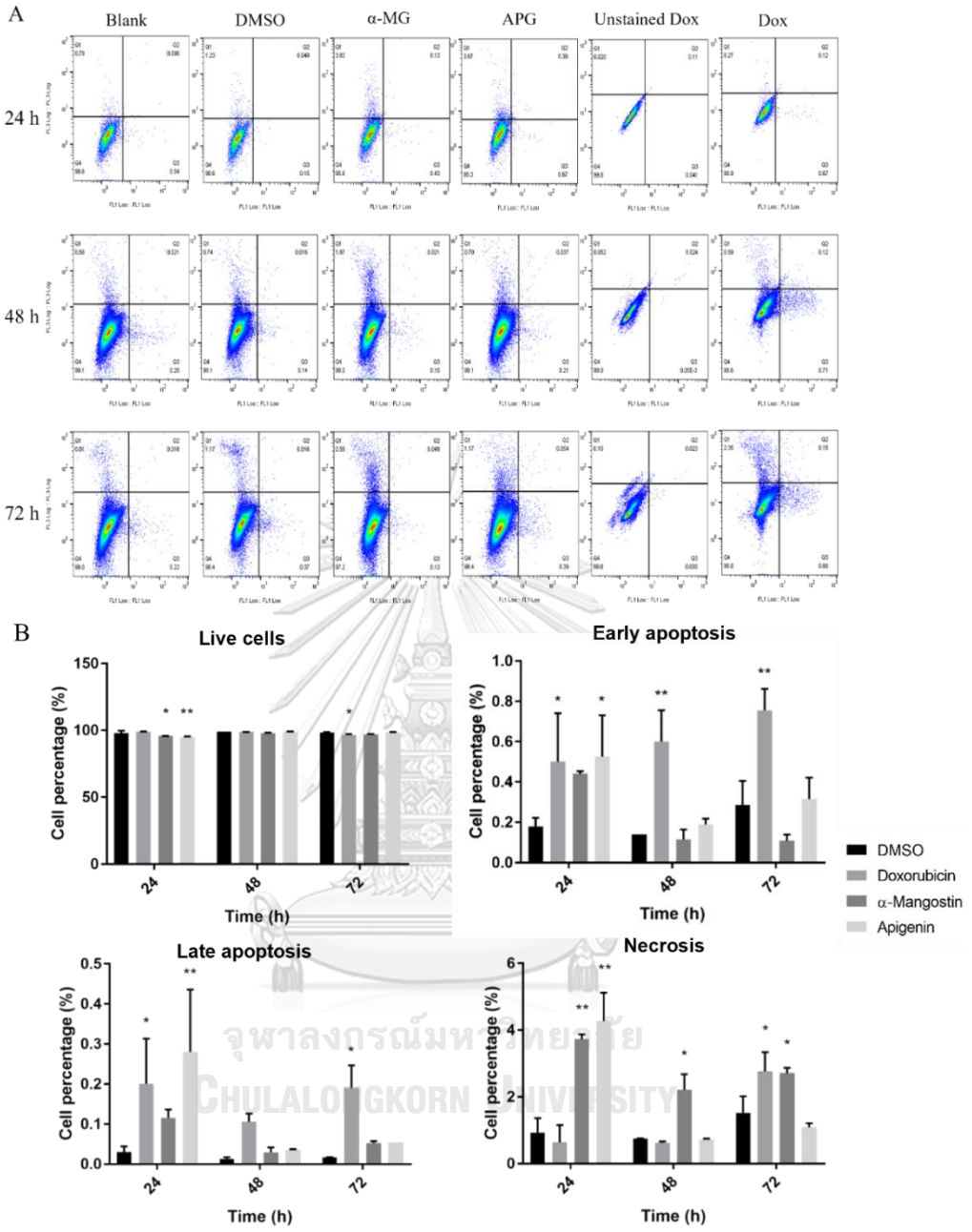

Figure 2.4 Flow cytometric analysis of BT-474 cells.

The cells were stained with annexin-V and PI after treatment in 0.1% (v/v) DMSO only (control), α-MG (9.75 µM), APG (37.01 µM) or Dox (0.46 µM) for 24, 48 and 72 h. (A) FACS profiles described the intensities of annexin-V at X-axis and PI at Y-axis. The results are representative of those seen from three replications. The derived % positive cells in each status were shown in bar chart (B). * and ** represent a significant difference between the control and treatment cells in each group at *p*-value < 0.05 and <0.01, respectively.

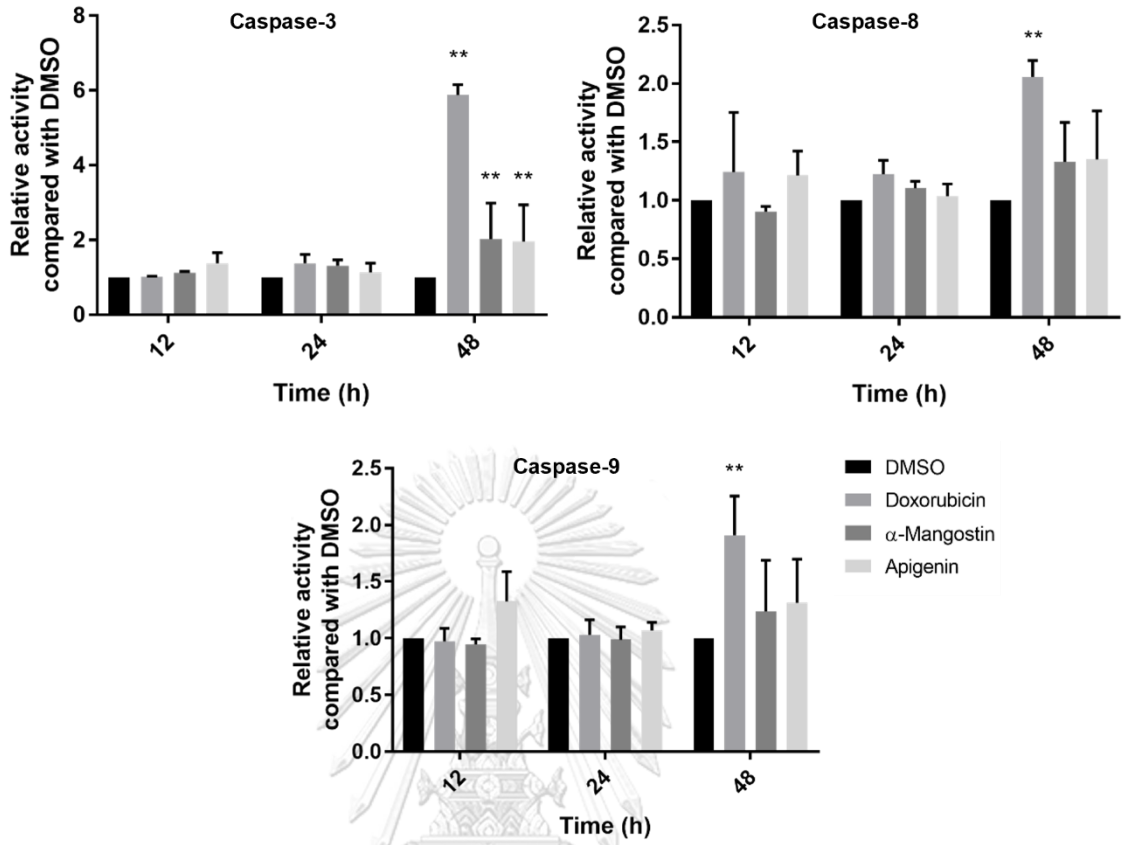

Figure 2.5 Relative caspase activity in Dox-, α-MG- and APG-treated BT-474 cells.

Cells were treated with 0.1% (v/v) DMSO alone (control) or containing α-MG (9.75 µM), APG (37.01 µM) or Dox (0.46 µM) for 12, 24 and 48 h and then assayed for caspase-3, caspase-8, and caspase-9 activities. Data are shown as the mean ±SD, derived from three replications, where ** represents a significant difference between the control and treated cells at *p*-value <0.01.

2.3.4 Cell cycle arrest of BT-474 after α-MG and APG treatment

The possibility of cell-cycle arrest was analysed using flow cytometry of PI-stained BT-474 cells after each treatment. Both α-MG (9.75 µM) and APG (37.01 µM) induced detectable levels of cell cycle arrest at the G_1-phase from 24 h exposure onwards, whilst Dox (0.46 µM) arrested the cell-cycle at the S-phase in an early exposure (24 h), but at the G_2/M-phase at 72 h (Fig. 2.6).

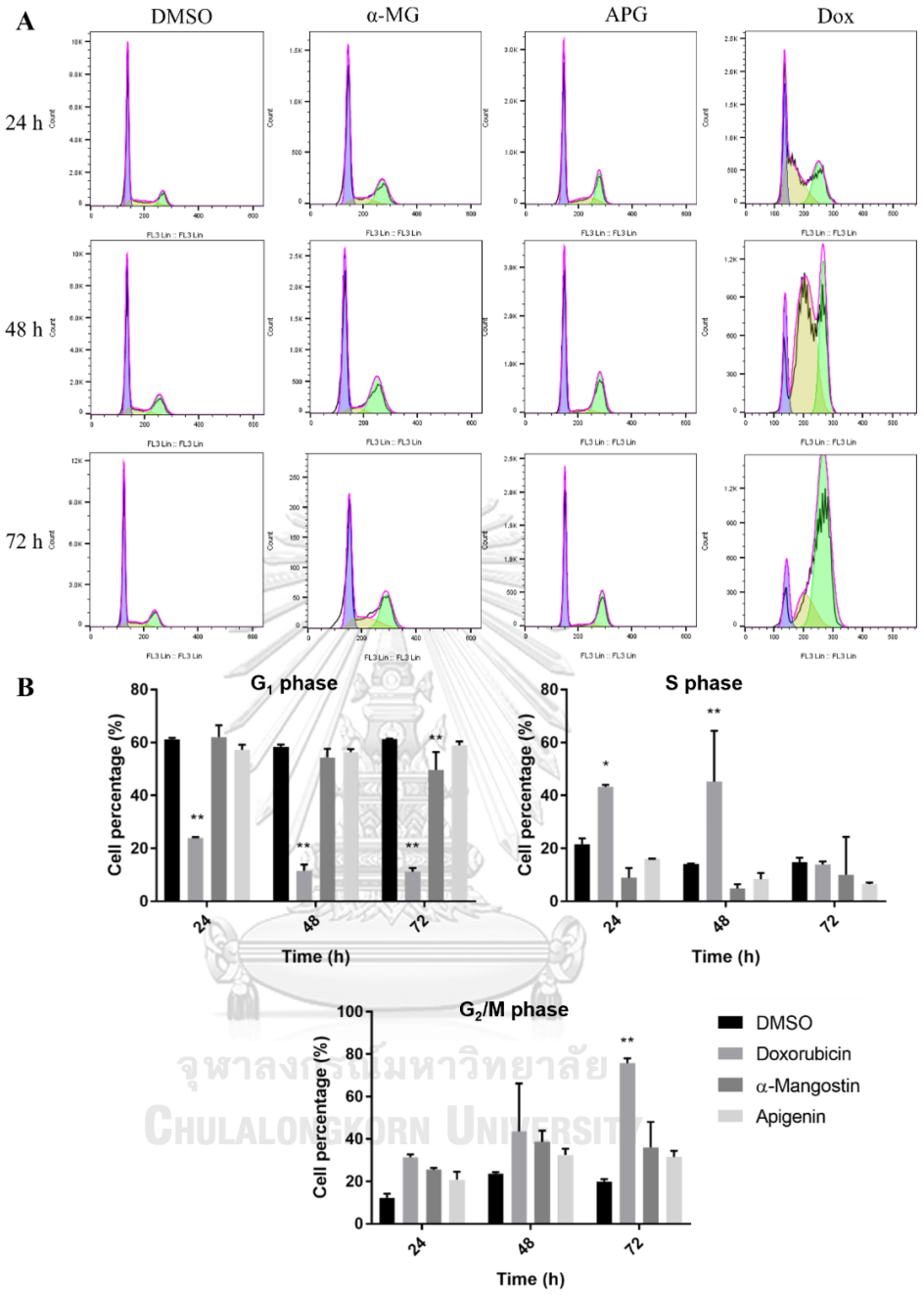

Figure 2.6 Cell cycle arrest of BT-474 cells after the treatment.

The cells were treated with 0.1% (v/v) DMSO only (control), α-MG (9.75 µM), APG (37.01 µM) or Dox (0.46 µM) for 24, 48 and 72 h. (A) Flow cytometric histograms (5 000 events), representative of those seen from three replications, and (B) the derived mean % (± SD) of cells in the G_1, S, and G_2/M phase of the cell cycle. * and ** represent a significant difference between the control and treated cells at *p*-value <0.05 and <0.01, respectively.

2.3.5 Gene expression alteration by α-MG and APG treatment in BT-474 cell line

α-MG and APG might affect the proliferation or death of BT-474 cells were summarized in Figure 2.7, where Cox2 was significantly up-regulated by both α-MG and APG (p <0.01), but not by Dox, while CathepsinB was significantly up-regulated by α-MG only, and BCL2 was not significantly altered by all three compounds. Here, α-MG and APG significantly up-regulated only CASP8 transcript levels (P<0.01), and not CASP3, CASP7 or CASP9. Overall, it seems that in addition to necrosis, α-MG induced cell death by apoptosis with potential association with inflammation and autophagy, while APG likewise had the same role except without autophagy

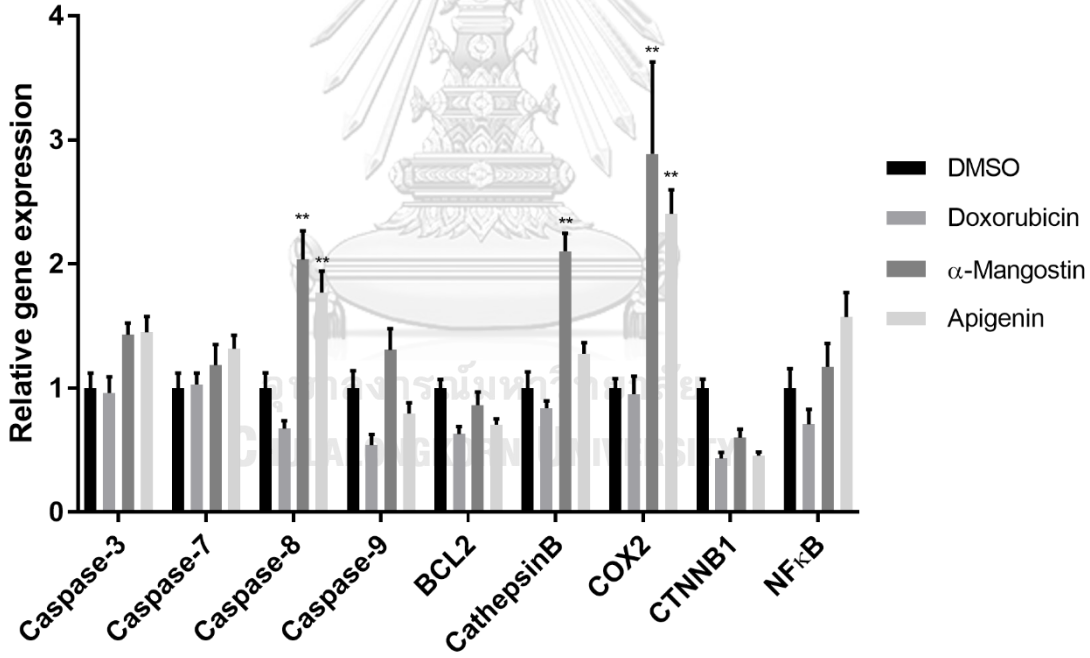

Figure 2.7 Real-time quantitative PCR analysis of selected genes in BT-474 cells.
BT-474 cells were cultured with 0.1% (v/v) DMSO alone (control) or containing α-MG (9.75 μM), APG (37.01 μM) or Dox (0.46 μM) for 24 h. Data are shown as the mean ± SD, derived from three independent repeats. Significant differences between the control and treated cells in each group are shown at the "**", which represents p-value <0.01 level.

2.3.6 Cytotoxicity effect of α-MG and APG on SKOV-3 cell line

In order to determine the cytotoxic IC_{50} values of α-MG, apigenin, and doxorubicin for direct comparison (Table 2.3, 2.4, Fig. 2.8, and 2.9), SKOV-3 ovarian cancer cells were cultured on a small scale (5 × 103 cells in 200 μL of the medium in each well of a 96-well plate). Regarding the viability of the treated SKOV-3 cells, α-MG, APG, and Dox all clearly inhibited cell growth in a dose-dependent manner (Fig. 2.8). Both APG and Dox also showed a time-dependent inhibition, but not α-MG. However, at any given time point, α-MG was more toxic to the SKOV-3 cells than APG was, with the cytotoxicity being 10.8-fold at 24 h to 5.9-fold higher at 24 and 72 h, respectively (Table 2.3). All three compounds affected the number of viable cells and growth of SKOV-3 cells from an early exposure time (24 h). The longer the exposure to APG, the significantly lower was the IC_{50} value, but the compound remained less inhibitory than α-MG and, especially, doxorubicin.

After 24 h of exposure, apigenin was nontoxic to CCD-986Sk and WI-38 cells, in contrast to α-MG. The IC50 value of apigenin for CCD-986Sk cells was not obtained since it resulted in 70% cell survival even at a high concentration of the compound (92.510 μM) (Fig. 2.9, Table 2.4); furthermore, the relative cell survival of 100% detected at 1.156-55.506 μM indicated that apigenin did not affect cell proliferation/survival (Fig. 2.9B). Likewise for WI-38 cells, apigenin at 1.156-2.313 μM did not affect the cell growth, and a concentration of up to 27.753 μM was nontoxic to the cells. Although α-MG was toxic to CCD-986Sk cells, the cytotoxicity was about 4-fold less than that in SKOV-3 cells. As with apigenin, the IC_{50} value of Dox for CCD-986Sk cells was not obtained since the compound did not affect the growth of this cell line. However, for WI-38 cells, Dox was more cytotoxic than α-MG (Table 2.3).

Table 2.3 IC_{50} value of α-MG, APG and Dox on SKOV-3 cells.

Compound	IC_{50} value (µg/mL) at an incubation time of:		
	24 h	48 h	72 h
α-MG	2.466 ± 0.338	2.977 ± 0.054	3.062 ± 0.349
APG	26.538 ± 6.204	21.175 ± 5.249**	18.197 ± 3.095**
Dox	0.534 ± 0.084	0.343 ± 0.023	0.117 ± 0.008

** indicates a significant difference to the IC_{50} value of 24 h when treated with the same compound.

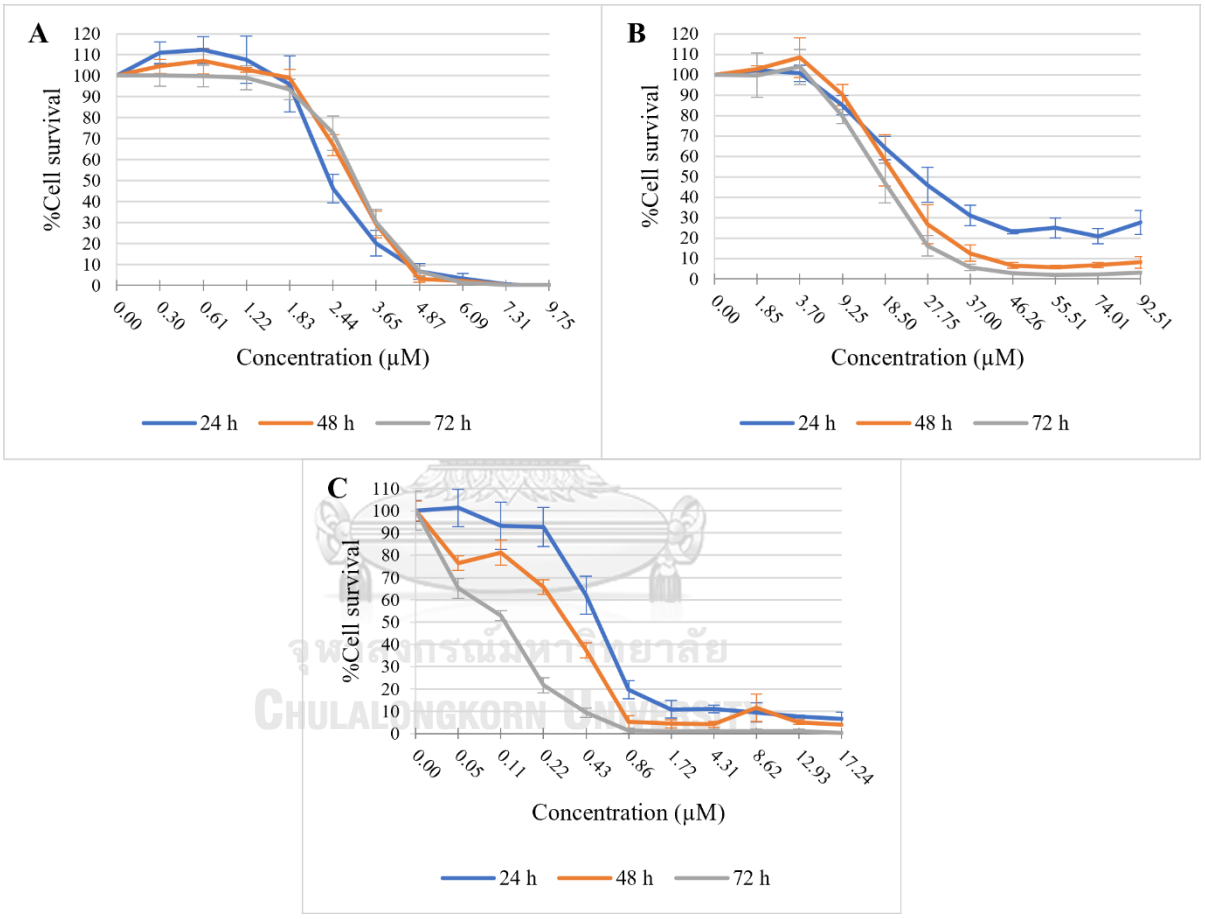

Figure 2.8 Cytotoxicity effect of the compounds on SKOV-3 cell line.

(A) α-MG, (B) APG, and (C) Dox in SKOV-3 cells. Cell survival (%) was estimated after treatment for 24, 48, and 72 h (blue, orange, and grey lines, respectively). Data are shown as the mean ± 1SD, derived from three independent repeats.

Table 2.4 IC_{50} value of α-MG and APG on CCD-968Sk and WI-28 cells after 72 h treatment.

Compound	IC_{50} value (µg/mL)	
	CCD-986Sk cells	WI-28 cells
α-MG	9.805 ± 3.169	1.502 ± 0.464
APG	ND	36.873 ± 0.971
Dox	ND	0.604 ± 0.156

ND = not determined

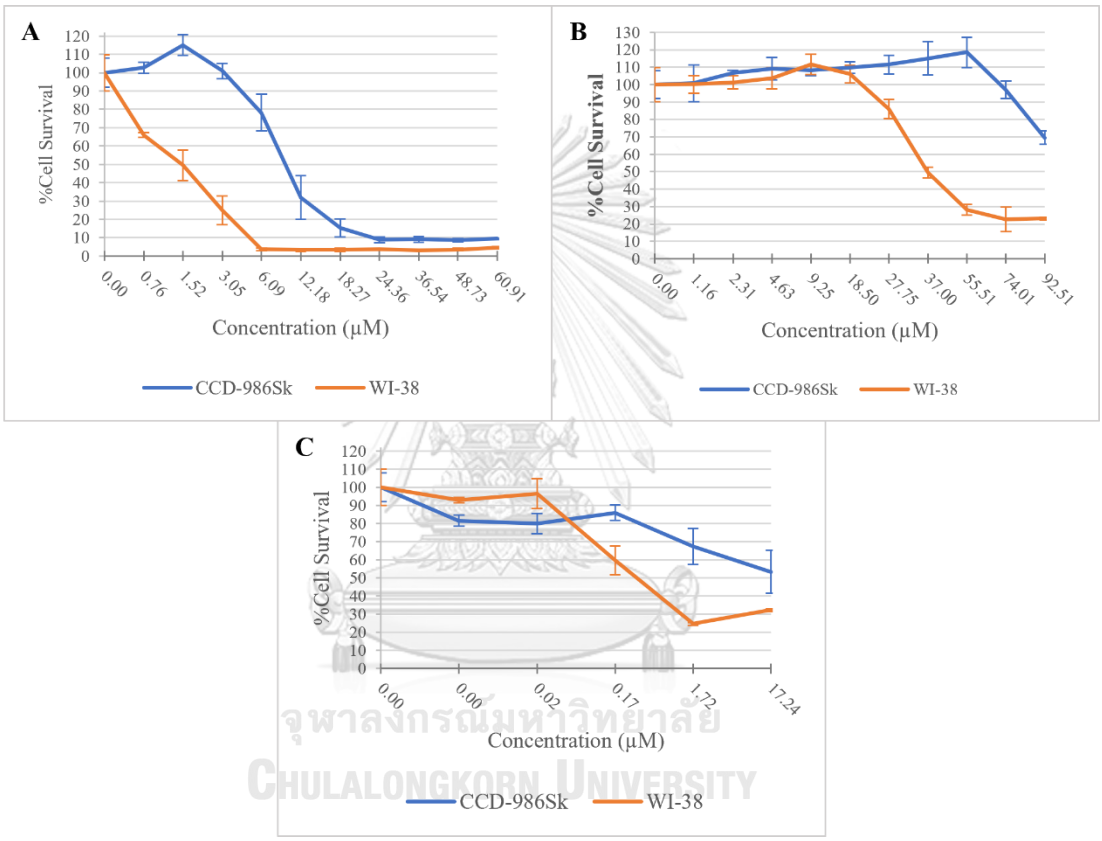

Figure 2.9 Cytotoxicity effect of the compounds on CCD-986Sk and WI-38 cell lines.

(A) α-MG, (B) APG, and (C) Dox in CCD-986Sk skin fibroblasts (blue line) and WI-38 lung fibroblasts (orange line). Cell survival (%) was estimated after 72 h of treatment. Data are shown as the mean ± 1SD, derived from three independent repeats.

2.3.7 Cell morphology of SKOV-3 cell line after α-MG and APG treatment

For all the other experiments, the SKOV-3 cells were cultured on a larger scale at 5 × 10^5 cells in 5 mL of medium in T25 flasks. Since α-MG treatment of the SKOV-3 cells at the IC_{50} value obtained from the small scale (200 μL) culture (Table 2.3) was not effective at all in the larger-scale cultures, the concentration of α-MG was increased to 3× the IC_{50} value. The most obvious changes observed are summarized in Fig. 2.10. Hence, the potency of α-MG at any given concentration depended directly on the density and number of cells as well as its dose. This phenomenon has been reported before in other studies (185-187). Morphological changes in the treated SKOV-3 cells were evident at the later exposure times compared with the control (DMSO-treated cells). After 24 h of exposure, the SKOV-3 cells treated with each test compound looked somewhat similar to the control cells; however, after 48 and 72 h, the treated cells had a lower cell density and a higher proportion of unadhered and round cells (Fig. 2.10A). At the higher magnification of 200×, it was evident that after 48 h of exposure, the α-MG-treated SKOV-3 cells were mostly damaged, with very few spindle-shaped cells present. Cell shrinkage was observed in the α-MG- and apigenin-treated SKOV-3 cells, whereas some cell blebbing was seen in the doxorubicin-treated cells. In addition, the apigenin- and doxorubicin-treated SKOV-3 cells had more vacuoles (Fig. 2.10B)

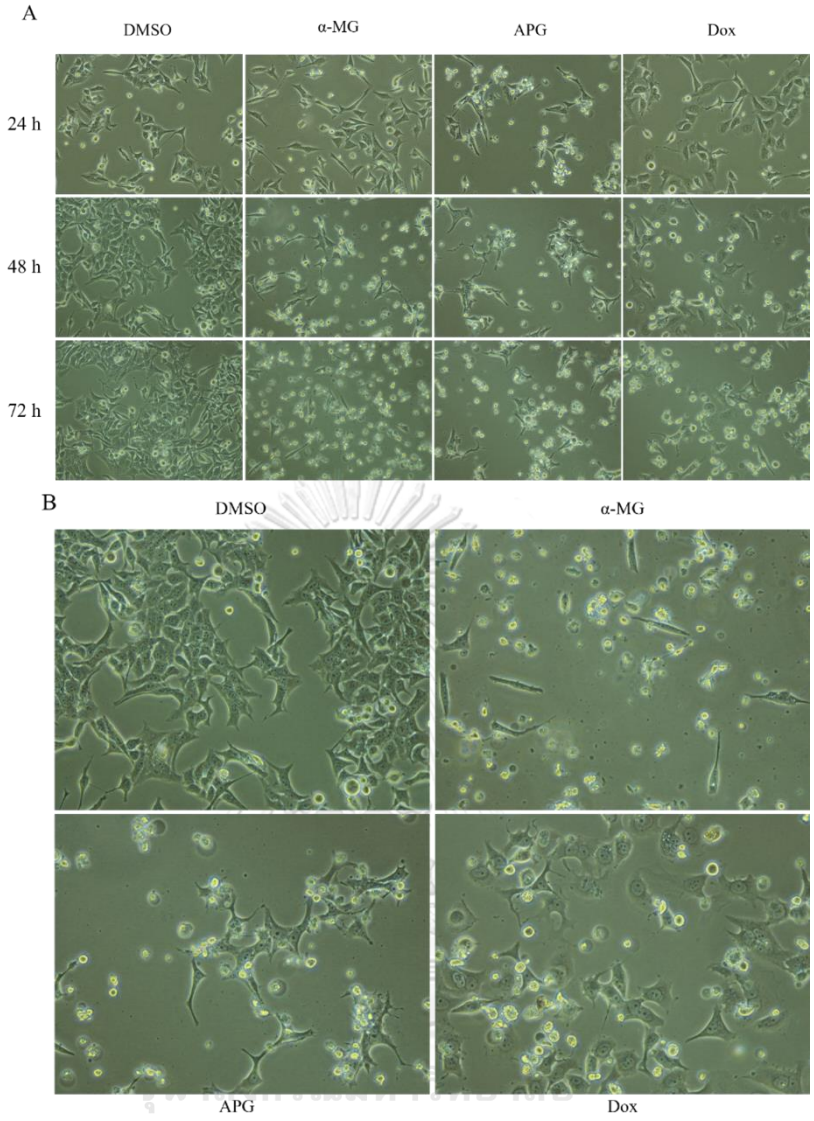

Figure 2.10 Morphology of treated SKOV-3 cells.

The cells were treated with 0.1% (v/v) DMSO alone or DMSO containing α-MG (7.309 μM), APG (18.502 μM), or Dox (0.431 μM) for (A) 24, 48, and 72 hh (100× magnification) and (B) after 48 h (200× magnification). Images shown are representative of those seen from at least three such fields of view per sample and three independent repeats.

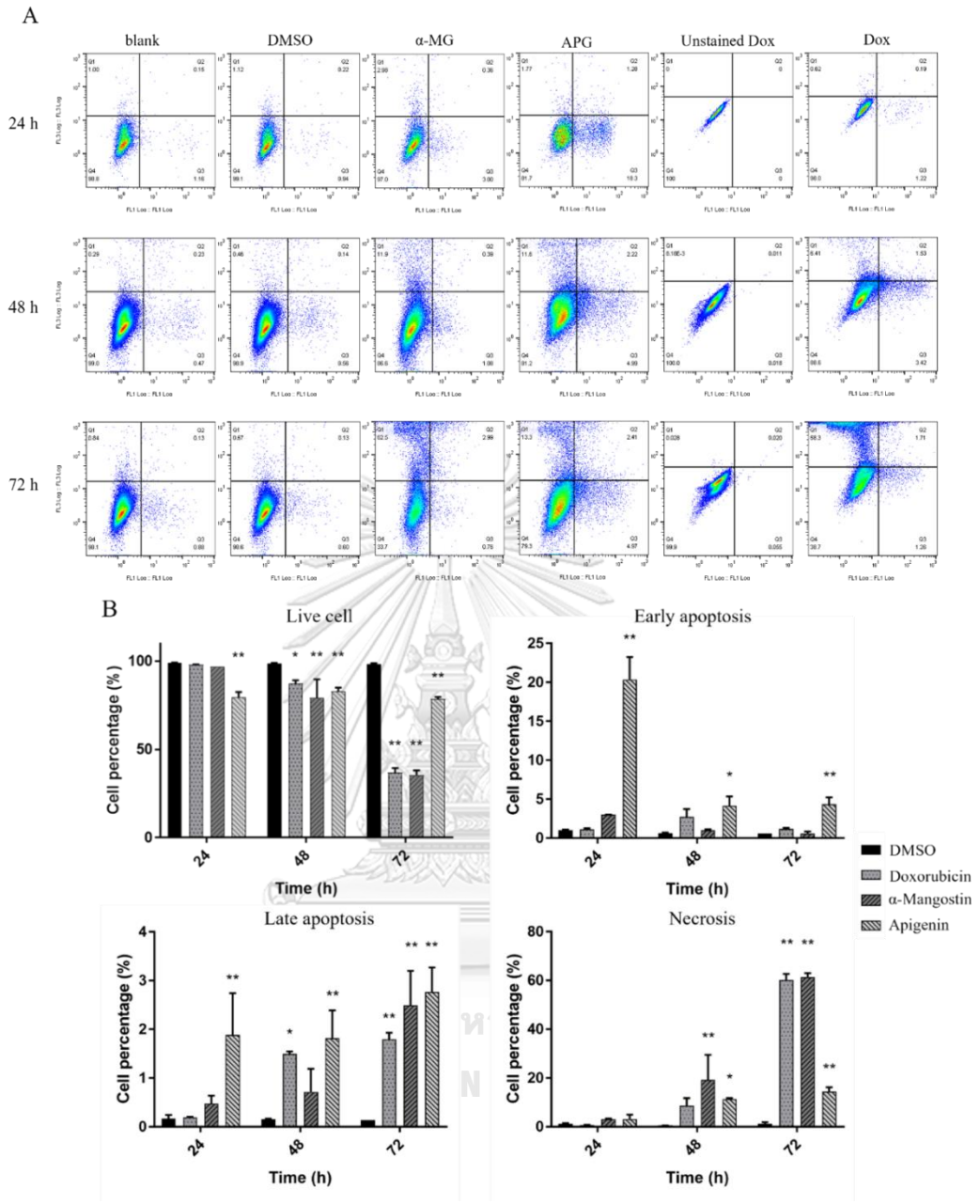

Figure 2.11 Flow cytometric analysis of SKOV-3 cells.

The cells were stained for annexin-V and propidium iodide (PI) after incubation of cells in 0.1% (v/v) DMSO alone or DMSO containing α-MG (7.309 μM), APG (18.502 μM), or Dox (0.431 μM) for 24, 48, and 72 hr. (A) FACS profiles represented intensities of annexin V on X-axis and PI on Y-axis, and (B) derived histogram analyses are shown for 10,000 events and are representative of those seen from three replications. * and ** represent a significant difference between the control and treated cells at $p < 0.05$ and $p < 0.01$, respectively.

2.3.8 Apoptosis was observed in SKOV-3 cell line after APG treatment

Since a lower density of cells was observed after a longer exposure to α-MG, APG, and Dox, suggesting cell death, as well as inhibition of proliferation, the possibility of the induction of programmed cell death, was further investigated. The SKOV-3 cells were treated with the same concentration of each reagent as used for evaluating the change in morphology. Programmed cell death can be analysed by staining target cells with annexin V and PI, whereas cell cycle arrest can be investigated by staining target cells with PI alone. In both cases, the staining level for each cell can be quantitatively determined using flow cytometry.

Due to apoptosis causes a loss of membrane phospholipid asymmetry (188), the phosphatidylserine that is normally located in the cytosol is flipped outside, allowing annexin V (conjugated with Alexa fluor 488) to bind to it. Thus, the annexin V-Alexa fluor 488 conjugate can bind to apoptotic but not to viable cells. At a longer time beyond death, necrotic cells have an even more damaged and leaky membrane that allows PI to pass into the nucleus and bind to the DNA. Thus, viable cells are negative for both annexin V-Alexa fluor 488 and PI staining, showing only autofluorescence. Apoptotic cells will be positive for annexin V-Alexa fluor 488 (green fluorescence) but negative for PI staining, whereas necrotic cells will be positive for both annexin V-Alexa fluor 488 and PI staining (red and green fluorescence, respectively) (26). Flow cytometry can also be used to quantitatively analyse cell cycle arrest, where the amount of bound PI (and thus red fluorescence) equates to the amount of DNA; thus, the cell cycle position (subphases G_1, S, and G_2/M) is identified by the DNA content through PI staining.

After staining with annexin V-Alexa fluor 488 and PI, it was evident that APG had caused a significant level of early and late apoptosis from 24 h onwards, but with less early apoptosis at the later time points, and subsequently caused significant necrosis, especially at 72 h (Fig. 2.11A and B). On the other hand, Dox caused a significant level of both late apoptosis and necrosis, but only after a longer exposure of 72 hr. Although α-MG gave a

similar result to doxorubicin, the level of necrosis was significantly increased and detected slightly earlier (from 48 h) than the 72 h time span for the other compounds (Fig.2.11).

From Fig. 2.11, it was evident that the programmed cell death of the SKOV-3 cells was induced by each of the three compounds and that it involved apoptosis (early and/ or late). Hence, apoptosis was further investigated by evaluating the cellular caspase activity. As is known, both caspase-8 and caspase-9 are involved respectively in the initiation of extrinsic and intrinsic pathway, whereas the apoptosis-mediating caspase-3 is executioner of apoptosis and triggered through both extrinsic and intrinsic pathways. Herein, the very early exposure time (12 and 24 h) to each compound was evaluated. The activity of caspase-3 was significantly ($p < 0.05$) increased in the α-MG-treated SKOV-3 cells after 12 h of exposure, while its activity was also significantly ($p < 0.01$) increased in both the α-MG- and APG-treated cells after 24 h of exposure, but the numerical increase observed in the Dox-treated cells was not significant (Fig.2.12). Caspase-8 activity was not significantly changed by all three treatments at both time points. Although the caspase-9 level was numerically increased in all treatments at 24 h, it was only statistically significant ($p < 0.01$) for the apigenin-treated SKOV-3 cells. Thus, it may be possible that the early apoptosis induced by apigenin in SKOV-3 cells at 24 h was influenced by the intrinsic pathway.

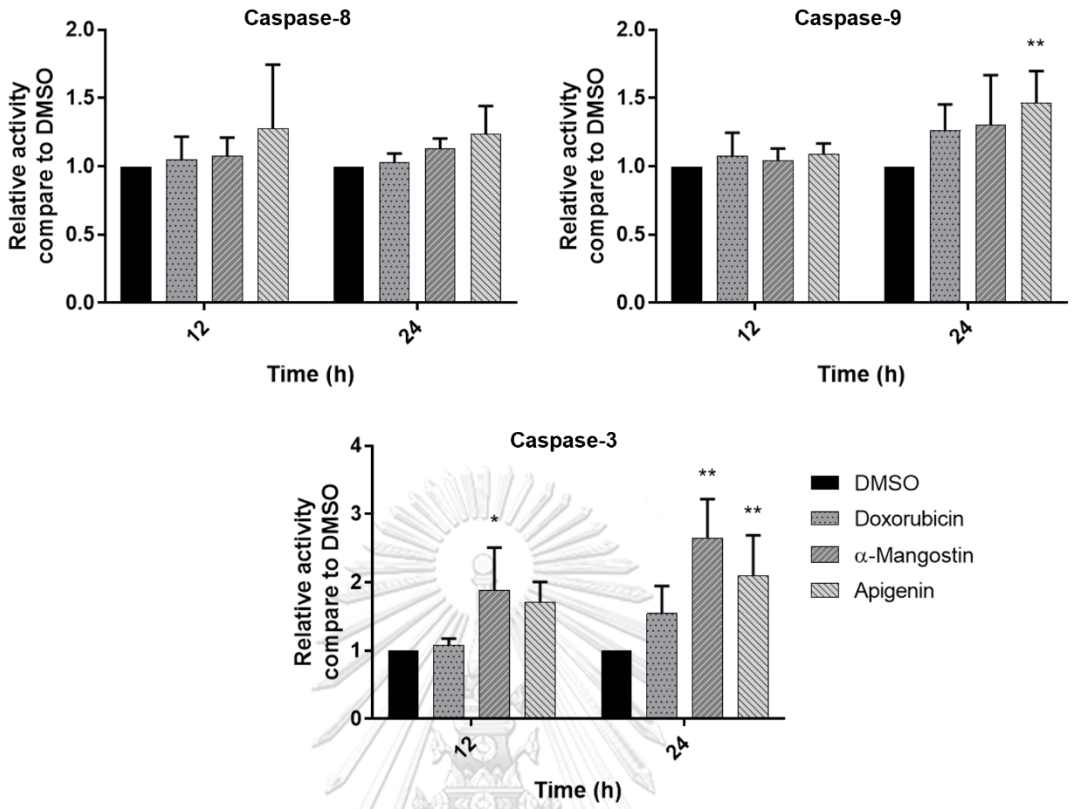

Figure 2.12 Relative caspase activity in Dox-, α-MG-, and APG-treated SKOV-3 cells. Cells were treated with 0.1% (v/v) dimethyl sulfoxide (DMSO) alone (control) or DMSO containing α-MG (7.309 μM), APG (18.502 μM), or Dox (0.431 μM) for 12 and 24 h and then assayed for caspase-8, caspase-9, and caspase-3 activity. Data are shown as the mean ± 1SD, derived from three replications, where * and ** represent a significant difference between the control and treated cells at $p < 0.05$ and $p < 0.01$, respectively.

2.3.9 SKOV-3 cell was arrested at G_2/M phase after α-MG and APG treatment

Next, we evaluated if cell cycle arrest was induced in the SKOV-3 cells by these compounds. After 24 h exposure, α-MG had induced arrest at the G_2/M phase ($p < 0.01$), whereas APG likewise arrested the cells only after 48 h exposure (Fig. 2.13). Thus, α-MG caused the cell cycle arrest faster than APG, which concurs with α-MG being more cytotoxic to SKOV-3 cells (Table 2.3).

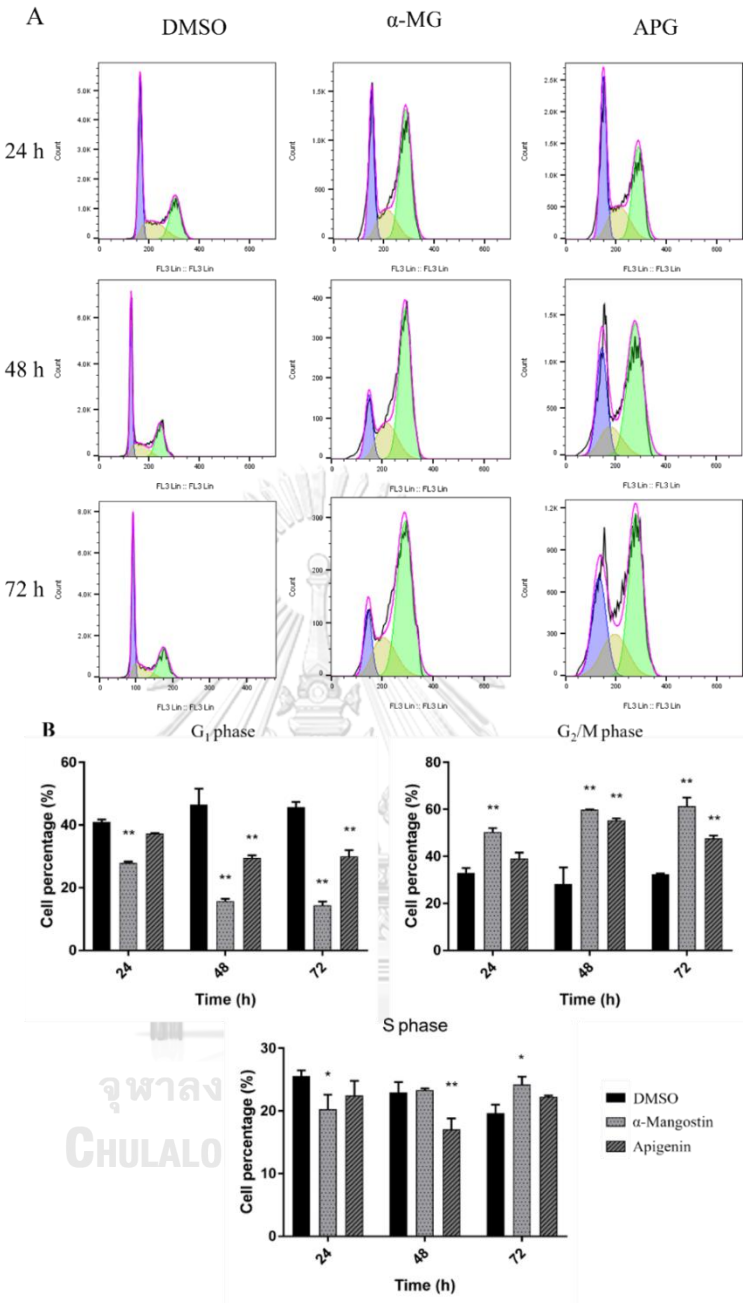

Figure 2.13 Cell cycle arrest of SKOV-3 cells after the treatment.

The cells were treated with 0.1% (v/v) dimethyl sulfoxide (DMSO) alone (control) or DMSO containing α-MG (7.309 μM) or APG (18.502 μM) for 24, 48, and 72 hr. (A) Flow cytometric histograms (5,000 events) representative of those seen from three replications, and (B) the derived mean % (± 1SD) of cells in each phase of the cell cycle after 24, 48, and 72 h treatment. * and ** represent a significant difference between the control and treated cells at $p < 0.05$ and $p < 0.01$, respectively.

2.3.10 Gene expression alteration by α-MG and APG treatment in SKOV-3 cell line

To determine in deeper detail how α-MG and APG affect the proliferation or death of SKOV-3 cells, changes in the transcript expression levels of selected genes from four groups were investigated. The first group was inflammation-associated genes, of which cyclooxygenase 2 (COX2) and nuclear factor kappa B (NFκB) were representatives. The second group was proto-oncogenes, from which catenin beta 1 (CTNNB1) was selected. The third group was autophagy-associated genes, with cathepsin B (CTSB) being a representative. The last group was apoptosis-associated genes, from which B-cell lymphoma 2 (BCL2), and the caspase genes CASP3, CASP7, CASP8, and CASP9 were selected. The data are summarized in Fig. 2.14. Although a trend of mostly an increase in the gene expression level relative to that in the control cells was numerically observed for all tested genes (except for NFκB) among the different treatments, the upregulation was significant only for BCL2 ($p < 0.01$) and COX2 ($p < 0.05$) in the APG- and α-MG-treated SKOV-3 cells, respectively.

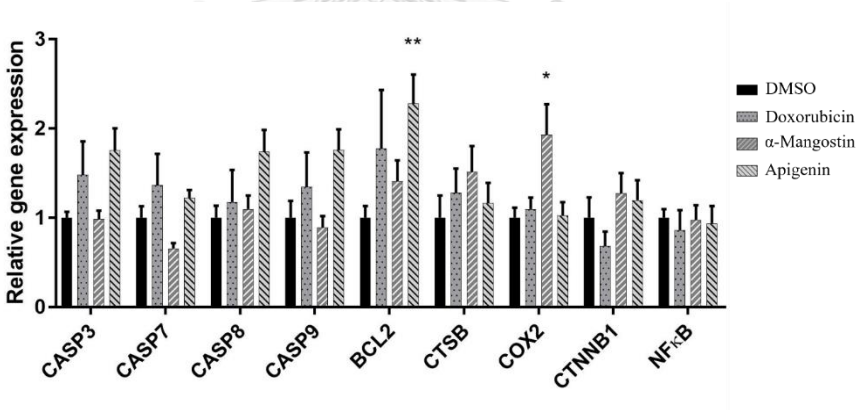

Figure 2.14 Real-time quantitative PCR analysis of selected genes in SKOV-3 cells.
SKOV-3 cells were cultured with 0.1% (v/v) dimethyl sulfoxide (DMSO) alone (control) or DMSO containing α-MG (7.309 μM), APG (18.502 μM), or Dox (0.431 μM) for 24 hr. Data are shown as the mean ± 1SD, derived from three independent repeats. * and ** represent a significant difference between the control and treated cells in each group at $p < 0.05$ or $p < 0.01$, respectively.

2.4 Discussion

Here, we report the *in vitro* potential of α-MG and APG on the growth inhibition in BT-474 and SKOV-3 cell lines in direct comparison with the effect of Dox, a currently used chemotherapeutic agent. These two compounds (α-MG and APG) were selected since flavonoid phenolic compounds have increasingly been reported to have potential beneficial roles against cancers (189). With some congruence, breast and gynaecological cancers, especially ovarian cancer, have been reported to be related to each other owing to their similar genetic basis (190), while a patient with breast cancer was later found to have primary ovarian small cell carcinoma and endometrioid adenocarcinoma of the uterus (191). Indeed, an increased risk of breast and ovarian cancers has been reported to be associated with germline mutations in BRCA1 and BRCA2 (192). This led us to investigate the role of both compounds in breast cancer BT-474 and ovarian adenocarcinoma SKOV-3 cells.

There have been diverse reports that oxidative stress, chronic inflammation, and cancer are closely linked (193-195). Not only do reactive oxygen species (which cause oxidative stress in cells) damage biological molecules, but they can also lead to chronic inflammation and eventually mediate chronic diseases such as cancer. In addition, the oxidative stress caused by the abnormal activation of nuclear factor E2-related factor 2 due to epigenetic alterations can increase chemo-resistance in cancer cells (196). Thus, compounds with antioxidant or free-radical-scavenging activities are likely to be beneficial for preventing cancer. Both compounds in this study have been reported to express these protective activities (178, 197).

Apoptosis is a caspase-dependent process that is important in preventing metastasis and cancer progression (198). CASP3, CASP8, and CASP9 are typically assayed in apoptosis studies since they are situated at pivotal junctions in the apoptosis pathways. As initiator caspases, caspase-8 and 9 subsequently activate caspase-3, which goes on to induce apoptosis in the cell. Furthermore, caspase-7 and -8 can cause inflammation in the host (199-201).

Although necrosis was the main cause of BT-474 cell death after treatment with α-MG or APG, the expression of *CASP8* transcripts was significantly upregulated by both compounds in these cells, which implies that apoptosis was still directly involved with caspase expression via the extrinsic pathway. The expression of *BCL2* tended to be numerically decreased by both α-MG and APG, but this was not significant. Nevertheless, the numerical reduction in the *BCL2* expression level is consistent with cell death by apoptosis (202, 203). Sano *et al.* reported a correlation between COX2 transcript levels as an inflammatory marker and the survival of locally advanced oral squamous cell carcinoma (204). Furthermore, butyrate induced the expression of *RUNX2* and *COLIAI* genes, which play important roles in the differentiation and anti-inflammatory mediators in SaOS-2 osteosarcoma cells (205). Increased expressions of COX2 and NF-κB, which can lead the cells to apoptosis by downregulating the anti-apoptotic genes, were screened as representatives, where NF-κB is linked between cancer and inflammation. Increased COX2 and NF-κB transcript levels induced by Dox were not found in BT-474 cells, and so Dox induced an antiproliferative activity without any anti-inflammation activity, and the cytotoxicity was likely mediated by apoptosis from caspase activity observation. In contrast to Dox, both α-MG and APG increased the transcriptional level of COX2 significantly, which indicates their potential for inflammation in α-MG-treated and APG-treated BT-474 cells. The data was supported by programmed cell death analysis, where the treated cells mainly died by necrosis, which is typically linked with inflammation (206). The morphology of Dox-treated BT-474 cells was not changed much compared to the control cells, which also coincided with the numerically decreased expression level of *BCL2* (albeit not significant), an apoptosis-associated gene. Though the transcript expression levels of *CASP3, CASP7, CASP8,* and *CASP9* were all not significantly changed, the apoptosis induced by Dox in BT-474 cells was possibly involved with the activation of these caspases. Hence, the cell stress or the condition of mitochondria should be further investigated. The proto-oncogene (*CTNNB1*) tended to be

downregulated by all three compounds in BT-474 cells, which may lead to the cell growth inhibition and apoptosis induction, although this decrease was not significant.

Considering the morphology of treated BT-474 cells, a lot of vacuoles were observed following α-MG and APG treatment, which may show that the cell death occurred through alternative ways in addition to necrosis and apoptosis. Autophagic cell death is associated with multiple large vacuoles observation and could be one of the possible explanations regarding the morphology of the treated cells. This type of cell death occurs through the mechanism that disassembles dysfunctional components to recover nutrients from aged or damaged cytoplasm and organelles for survival, however, the prolonged period of this event led to cell death by other means. This recycling method results in the formation of phagocytosis vacuoles (207) similar to what has been observed in this study. Moreover α-MG significantly upregulated *CathepsinB* transcript levels in BT-474 cells, and so α-MG-induced cytotoxicity may involve autophagy as well. However, a more specific experiment on autophagy is needed to take place for this conclusion.

In the context of SKOV-3, APG was toxic to the cells but not to normal cells. α-MG showed almost similar toxicity as that of Dox to SKOV-3 cells, but it was unfortunately also toxic to the WI-38 normal lung fibroblasts even though, at less than 6.091 μM, it was deemed safe for CCD-986Sk skin fibroblasts. Cell-type specificity with α-MG is of concern and has been reported before (208-210). Moreover, after exposure to α-MG for 24 hr, the transcript expression level of *COX2* (inflammation-associated gene) was significantly upregulated, whereas that of NF-κB remained the same as in the control cells. Thus, by 24 hr, the promotion of apoptosis in α-MG-treated SKOV-3 cancer cells had not reduced the inflammatory response. However, the changes in gene expression should be observed after longer exposures to α-MG, since NF-κB plays a role in activating many inflammatory factors, such as TNF-α, interleukin (IL)-6, IL-8, matrix metalloproteinase, COX2, and nitric oxide synthase (211). It remains plausible that α-MG may affect the expression of *NF-κB* earlier

(faster) than *COX2*. Therefore, the application of α-MG in a broad systemic application for cancer prevention and treatment is not suitable.

For APG-treated SKOV-3 cancer cells, significantly increased caspase-9 activity was detected after 24 h of exposure, which is the same timing as the onset of early apoptosis. Hence, the death of APG-treated SKOV-3 cells was likely to have been induced by the intrinsic pathway. The intrinsic apoptosis induction by APG is related to DNA damage, ROS accumulation, and dysfunction of mitochondria membrane potential in other cell lines (142, 212). In gene expression analysis, the expression of *BCL2* (an anti-apoptotic gene) transcripts, but not those of *CTNNB1* (a proto-oncogene), was significantly upregulated by APG, implying that other biomolecules or pathways are involved in this apoptotic process. This notion is potentially supported by Otake *et al.* (213), who reported that the overexpression of *BCL2* in lymphocytes alone did not cause cancer, whereas the simultaneous overexpression of *BCL2* and *MYC* (a proto-oncogene) could induce aggressive B-cell malignancies, including lymphoma.

In the future, in order to enhance the efficacy of α-MG and APG as chemotherapeutic agents for ovarian cancer, other application approaches could be applied, such as with fatty acid-conjugated compounds (214), or the synergistic inhibition induced by co-administration with other promising compounds (215). Moreover, the toxicity of these compounds in an *in vivo* model system, such as the rat, should be determined (216, 217).

CHAPTER 3
PHOSPHOPROTEINS ALTERATION AFTER APIGENIN TREATMENT IN SKOV-3 OVARIAN CANCER CELL LINE

3.1 Introduction

Ovarian cancers are particularly important, as it is one the cancers that are generally caught too late due to their symptoms often attributed to other conditions affecting women. This led to the disease being called the "silent killer" amongst the population. It has been ranked in the global cancer report for the 8th common causes and mortality rate with 3.4% and 4.7% of all cancers in females in 2020 (166). Further observation on gynaecological cancer statistics has found that ovarian cancer has the highest fatality ratio at approximately 66.01% (207,252 death from 313,959 cases) when compared to other cancers in this group as ordered by incidences, cervix uteri (56.58%), corpus uteri (23.33%), vulva (38.52%), and vagina (44.64%). So far only a little information is known on the origin and underlying mechanisms in this cancer subtype (218, 219). Moreover, ovarian cancer has been reported to gain chemoresistance, especially when relapsing and recurrence occurred, preventing it from treatment with the previous drugs and deterioration the progress of the diseases, which have brought challenges in chemo-therapy notably taxol- and platinum-based drugs (220, 221). Not only ineffective in the treatment of recurrence malignancies, but chemotherapy also caused adverse events that led to reduced quality of life (222, 223). Hence, novel or alternative medications are necessary for ovarian cancer treatment.

Natural compounds from folk medicine have been immensely in focus for the past decades for their beneficial health functions, such as anti-ageing, anti-diabetes, antioxidation, anti-inflammation, and anticancer activities (224-226). Apigenin (APG), a flavone found highly in various plants, especially chamomile, parsley, celery, citrus fruits, parsley, basil, and

onions, has been reported for exhibiting ameliorative effects, including anti-oxidation, anti-inflammation, and anticancer activities (120, 227, 228). APG anticancer activity had been firstly described by Birt *et al* (124) where they observed anti-mutagenic and anti-promotion of carcinogenesis activity on mutagenesis inducing in *Salmonella typhimurium* and mouse skin epidermis. This had led to APG being tested on several cancer cell lines including colorectal, breast, lung, prostate, cervical, ovarian, glioblastoma, leukaemia, melanoma, pancreatic, and osteosarcoma cancer cell lines establishing its potency surrounding anti-cancer and cancer-preventing functions (123, 229, 230). APG was found to trigger diverse mechanisms in different cancer cell lines to exhibit anticancer activity including induction of apoptosis, cell cycle arrest, metastasis inhibition, and anti-angiogenesis (123, 231, 232). In addition, it demonstrated low cytotoxicity against non-cancerous cells in comparison with cancerous alternatives, which is one of the requirements for becoming a clinical candidate (233). Despite these advances, only limited information is known about the mechanisms underlying APG exposure on ovarian cancer. In the A2780 ovarian cancer cell line, APG was reported to inhibit cell progression at G_2/M phase and reduce metastasis through inhibition of focal adhesion kinase (FAK) expression (234, 235). It also suppressed self-renewal capacity in SKOV-3-derived sphere-forming cells, a subpopulation group of SKOV-3 ovarian adenocarcinoma cell lines (183). In addition, our recent study has found that APG appeared to induce apoptosis via intrinsic pathway and cell cycle arrest at G_2/M phase in ovarian adenocarcinoma cell line SKOV-3 (236).

Central to establishing adequate treatment regimens is the underlying knowledge of the mechanism of action of a compound. As described earlier, much is known about the phenotypic impact of APG on several cancers, but mechanistic information is lacking. In this study, we want to address this lack by identifying pathways and mechanisms likely impacted by APG resulting in antiproliferative activity in cancer cell lines. The cell cycle is largely driven by phosphorylation activity through several kinases (237). Notably, the prominent

cyclin-dependent kinases (CDK) family plays an important role in this progression. For CDKs to function properly, a regulatory subunit called cyclin binds to its CDKs counterpart and formed a complex of heterodimer proteins that will later be activated or deactivated upon phosphorylation on different phosphosites of CDKs (238). These processes are strictly regulated in signal level, time, and space to achieve the goal of each step in the cell cycle. Moreover, other cellular mechanisms for example MAPK, PI3K/Akt, JAK/STAT, and Wnt signalling pathways are actively controlled through multiple phosphorylation steps and have been reported to be involved with cell cycle regulation (239, 240). Before the advanced technology in mass spectrometry was introduced, the study of these signalling pathways appeared to be laborious and time consuming due to a low-throughput technique and limitations in detection availabilities. In order to study the changes of these phosphosites, advancing in tag labelling systems for proteomics allows researchers to perform a relative quantitative experiment in observing alterations of protein expression and phosphorylation in a high-throughput manner (241). We therefore opted to use phosphoproteomics to study the impact of APG on phosphorylated proteins and identify several key functions likely involved in the demonstrated cell cycle arrest.

3.2 Materials and methods

3.2.1 Chemicals and cell line

SKOV-3 cell line, McCoy's 5A (modified) medium, trypsin-EDTA (0.25%), Apigenin, and DMSO were purchased from Sigma-Aldrich® (Merck, UK). Foetal calf serum and PBS (pH 7.4) were purchased from Gibco (Thermo Fischer Scientific, UK). APG was dissolved in 185 µL DMSO to make approximately 100 µM APG in DMSO stock and stored in -20 °C refrigerator. Antibodies were purchased as follows, anti-GAPDH (ab181602), anti-mouse IgG-HRP (ab6789) and anti-rabbit IgG-HRP (ab6721) from Abcam, and anti-phospho-stathmin 1 Ser25 (PA5-37628), anti-phospho-Rb Thr373 (PA5-64767), anti-stathmin 1 (MA5-33064), anti-Rb (MA5-11387) from Thermo Scientific.

3.2.2 Cell culture and treatment

The human cancer-derived cell line used in this study was ovarian adenocarcinoma (SKOV-3, ATCC no. HTB77). The cell line was cultured in McCoy's 5A (modified) medium supplemented with 10 % (v/v) foetal calf serum at 37 °C with 5 % (v/v) CO2 in a humidified environment. The cell was passaged at 90% cell confluency in T-75 flask or approximately twice a week.

3.2.3 Survival curve recreation and effective doses calculation

The cell viability percentage from the previous study MTT assay was used as input for generating cell survival curve by a log-logistic model with 4 parameters using drm() function in 'drc' package (version 3.0-1) in R. The effective doses were generated by ED()function from the same package.

3.2.4 Early antiproliferative activity of APG

Cells were seeded and the experiment was performed as described in the cell viability observation section above. On the next day, the cells were treated with concentrations represented $IC_{10,}$ $IC_{20,}$ $IC_{30,}$ IC_{40}, $IC_{50,}$ and IC_{60} with the medium as baseline control and DMSO as solvent control. MTT was added at 0.5, 1, 1.5, 3, 6, 12, 18, and 24 h for observing the cell activity representing viable cells and incubated in culture condition for 3h. The experiment was done from three biological replicates and summarised to generate this plot. The antiproliferation activity of APG was assessed by observation of formazan solution dissolved in DMSO using plate reader machine at an absorbance of 560 nm and further processed for cell viability percentage by calculating:

$$Cell\ viability\ (\%) = 100 \times \left(\frac{A_{560}\ treated\ cells - A_{560}\ blank}{A_{560}\ control\ cells - A_{560}\ blank}\right)$$

3.2.5 Sample collection and preparation for MS/MS analysis

For phosphoproteomics the cells were plated at 2×10^6 cells/10-cm dish the day and incubated for 16h before the experiment. Then, the cells were treated with APG at IC_{10}, $IC_{20,}$ and IC_{30} for 30, 60, and 90 minutes with no treatment at 0 minute and DMSO treatment for 90 minutes as controls. The treated cells were collected by washing with ice cold 1X PBS pH 7.4 for three times, adding 400 µL of lysis buffer (100 mM TEAB, 0.05% (W/V) Rapigest, 1X protease inhibitor (cOmplete Mini EDTA-free, Roche), 1X phosphatase inhibitors (phoStop, Roche) and 25 U of benzonase per 1/mL lysis buffer) and scraping thoroughly. The lysates were left to sit for 45 minutes on ice for complete lysis and heated to 80 °C for 10 minutes with 800 rpm rotation to eliminate cellular activity. The lysates underwent protein quantification by Coomassie Plus (Bradford) assay. 100 µg of each sample was taken for in-solution digestion by trypsin. In-solution digestion started from reducing disulphide bond and alkylating to prevent rebinding of thiol group by 4 mM DTT at 60 °C for 10 minutes followed by 14 mM iodoacetamide at room temperature for 30 minutes in dark. Then, 2 µg of trypsin was added to make 50:1 (protein:trypsin) ratio and incubated at 37 °C with agitation at 500 rpm overnight. Each of the digested samples was randomly labelled with TMT by mixing 800 µg of TMT in LC-MS grade ACN (acetonitrile) and incubating at room temperature for an hour with a gentle vortex every 10 minutes. Next, hydroxylamine in 100 mM TEAB buffer (0.3% (v/v) final) was added to quench excess TMT and incubated at room temperature for 15 minutes. The samples were pooled together into a 2 mL low bind tube then dried to completion in a vacuum centrifuge at 4 °C by removing ACN. The dried sample was re-suspended in 500 µL 1% TFA (trifluoroacetic acid) in 100 µM TEAB buffer, sonicated for 10 minutes and incubated at 37 °C for 50 minutes with 500 rpm for hydrolysis using Rapidgest. The sample was centrifuged at 13,000*x*g at 4 °C for 15 minutes. Next, the sample was desalted in a C-18 column by following the manufacturing instructions. The column was calibrated with 100% (v/v) methanol and washed with 1% (v/v) TFA in H_2O. The maximum

loading volume of C-18 column is 300 µL, so samples were repeat loaded in the same column twice or more. The desalted peptide sample was eluted from the column by 300 µL 0.1% TFA in 50% ACN then centrifuged at 3000*x*g for 1 minute and repeated for complete elution. The eluted sample was dried by vacuum centrifugation at 4 °C until completely dried. The sample was further fractionated into 5 fractions by high pH reverse phase system with a gradually increasing hydrophobicity ratio at pH 10. Each fraction was dried with vacuum centrifugation until completion.

3.2.6 Enrichment of phosphopeptides with TiO_2 beads

For phosphopeptide enrichment, each sample fraction was resuspended with loading buffer (5% TFA, 1M glycolic acid in 80% (v/v) ACN) and sonicated for 10 minutes or until completely dissolved. The TiO_2 beads were weighed and around 10 mg resuspended in 200 µL loading buffer. Then, 20 µL TiO_2 beads were added into each fraction and the mixture solution was kept agitated at 1600 rpm for 20 minutes at room temperature. The mixture was centrifuged at 2000*x*g for 1 minute to pellet the bead and remove the supernatant into a new low-bind tube. This supernatant part contained an unbound mixture that can be used for further experiments if required. The beads were washed with 150 µL loading buffer with agitation at room temperature for 10 minutes. Then, the beads were centrifuged at 2000*x*g for 1 minute and the supernatant discarded. The beads were washed for a second time with 150 µL 1%TFA in 80% (v/v) ACN with the same agitation and centrifugation steps as the first wash. For the last washing step, the beads were washed with 150 µL 0.2% TFA in 10% (v/v) ACN repeating the agitation and centrifugation steps. The beads were dried in a vacuum centrifuge for 30 minutes. For elution, 100 µL of the first elution buffer (1% ammonium hydroxide in H_2O) was added into the beads and the mixture was agitated at 1600 rpm for 10 minutes at room temperature. The beads were centrifuged at 2000*x*g for 1 minute and the supernatant was collected into a new low bind tube. Then, 100 µL of the second elution buffer (5% ammonium hydroxide in H_2O) was added into the beads and performed the same steps as

the first elution. The supernatants from the first and second elution were pooled together and dried by vacuum centrifugation until completion.

3.2.7 MS/MS analysis

The phospho-enriched fractionated samples were injected and analysed using an Ultimate 3000 RSLC™ nanosystem (Thermo Scientific, Hemel Hempstead) coupled to QExactive™ mass spectrometry (Thermo Scientific). The sample was loaded onto the trapping column (Thermo Scientific, PepMap100, C18, 300 µm X 5 mm), using partial loop injection, for 7 minutes at a flow rate of 4 µL/min with 0.1% (v/v) Formic acid (FA). The sample was resolved on the analytical column (Easy-Spray C18 75 µm x 500 mm 2 µm column) using a gradient of 97% A (0.1% FA) 3% B (99.9% ACN 0.1% FA) to 60% A 40% B over 120 minutes at a flow rate of 300 nL/min. The data-dependent program used for data acquisition consisted of a 120,000 resolution full-scan MS scan (AGC set to 3E6 ions with a maximum fill time of 100 ms) the 12 most abundant peaks were selected for MS/MS using a 60,000 resolution scan (AGC set to 1E5 ions with a maximum fill time of 110 ms) with an ion selection window of 1.2 m/z and a normalised collision energy of 32 and a first mass set to a fixed value of 100.0 m/z. a 90-second dynamic exclusion window was used to avoid repeated selection of peptides for MS/MS.

3.2.8 Data handling and analysis

The raw data from QEx-Hfx mass spectrometer were analysed by MaxQuant software (version 1.6.5). Most of the settings of MaxQuant were left as default except for: set fractions from 1 to 5, set PTM to true, in Group-specific parameters: Type to reporter ion on MS2 and select 11-plex TMT, cysteine carbamidomethylating in fix modifications, for variable modifications, are N-terminal acetylation, methionine oxidation and phosphorylation at serine/threonine/tyrosine (S/T/Y), digestion is set to Trypsin/P which allows searching for cleavage of carboxyl side of the Lys and Arg even if a Pro follows and allowed up to 2 missed cleavages. The mass spectra were searched against *Homo sapiens* UniProtKB one protein per

gene database (UP000005640_9606.fasta, https://www.uniprot.org/proteomes/_UP000005640), decoy and reverse database with 1% false discovery rate (FDR) filtration at three levels, which are site decoy fraction, peptide-spectrum matching (PSM) and protein. Both unmodified and modified (oxidation of Met, N-terminal acetylation, and phosphorylation of Ser/Thr/Tyr (STY)) of unique and razor (peptides which match to multiple proteins) peptides were used for protein quantification.

3.2.9 Identification of differentially phosphorylated proteins

To determine the effect of APG on SKOV-3 phosphorylation, the phosphosites output from MaxQuant were used to observe the difference of phosphorylation in proteins among various treatments and times. Before pre-processing of reporter intensities, the phosphosites were filtered by using strict criteria for confident phosphosites, which is phosphorylation occurred on STY with a localization probability of ≥ 0.75 and PEP (Posterior error probability) ≤ 0.01. The intensities from each reporter of all replicates were log-transformed and plotted into a figure of boxplots to observe the data distribution. The data were grouped into multiple categories by UniProt accession number, phosphorylated amino acid, phosphorylated position within proteins, and phosphorylation level using group_by() and summarize() function in 'dplyr' package. Then, Loess normalisation was applied against DMSO at 90 minutes (IC_0 90min) within each biological replicate. The batch effect was removed by using 'ComBat' package with the following setting, batches as biological replicates and covariates as treatments. The data in each step of data processing, original, Loess-transformed, and batch correction, were analysed by principal component analysis using the prcomp() function in base R. The visualization of normalization data and PCA were executed by 'ggplot2' and 'ggbiplot' package. ANOVA was used to analyse the phosphosites related to time, concentration, and covariation between these factors. Later, p-values were corrected using the standard Benjamini-Hochberg correction methodology. The significant phosphosites were identified with a restriction of adjusted p-value < 0.10.

3.2.10 Gene set enrichment analysis (GSEA) on a Pre-ranked gene list test

The coefficient values of each factor from the ANOVA test were extracted and their associated Uniprot accession was converted to Gene symbol. In the case of proteins with multiple phosphosites, the mean values were calculated. This ranked file was used as input to a GSEA (version 4.0.3) and analysed using the Pre-ranked gene list analysis (242). The tests were performed on KEGG and Gene Ontology database with the numbers of permutations allowed at 10000. The terms with p-value < 0.05 and FDR < 0.25 were considered statistically significant.

Next, given that the data for analysis had been transformed by Loess normalisation against solvent control at 90 minutes and batch correction we also performed the equivalent of a one-sample t-test using the 'limma' package. This analysis tests for deviations from 0, which would indicate a significant effect of APG on the cells as compared to DMSO. Similar to the ANOVA results above, the t statistics were extracted and used as an input to a GSEA Pre-ranked list analysis. The enriched terms were filtered at FDR ≤ 0.25 and plotted into a scatter plot with lines to show the direction of changes in each function.

3.2.11 NetworKIN analysis

The significant phosphosites were collected by factors in the ANOVA tests, concentration, time, and interaction between concentration and time. The UniProt accession numbers from each significance list were inputted into NetworKIN (http://www.NetworKIN.info/) workflow block (243). Then, phosphosites, phosphorylated positions within protein, were manually selected and the kinase predictions were performed as pre-setting preference. The results were filtered with a minimum score of 2.0 with a maximal distance to the best prediction of each site (max. difference) of 4.0. The negative and positive effects of each factor from each site were grouped by sorting the AVOVA coefficient of each factor and given to NetworKIN for analysis as described above.

3.2.12 SDS-PAGE and Western blot

The assay was performed to observe the expression level of interesting phosphosites captured from the statistical analysis. SKOV-3 cells were seeded at approximately 1×10^6 cells per 60 mm dish in McCoy's 5A medium and cultured overnight (16-18 h) before treatment and harvest. The cells were treated with APG at IC_{30} and DMSO. The cells were harvested at 15-minute, 30-minute, 1, 1.5, 3, 6, and 9-h timepoints. At each timepoint, the cell culture dish was placed on ice and washed twice with cold 1x PBS, carefully removing the PBS residue. Next, 300 µL of RIPA buffer (25 mM Tris pH7.5, 150 mM NaCl, 1% (v/v) Triton X-100, 0.5% (w/v) sodium deoxycholate and 0.1% (w/v) SDS) containing phosphatase (1x PhosSTOP Easy pack, Roche) and protease inhibitor cocktails (1x Protease Inhibitor cocktail, Himedia) was added and incubated on ice until completely lysed, approximately 10-15 min. The lysate was then moved into a clean microcentrifuge tube. The lysates were centrifuged at 14000 x*g* at 4°C for 10 min and the supernatant was collected into a new tube. Then the lysates were flash-frozen by liquid N_2 and stored at -80°C until use. The lysates were measured for protein concentration by BCA assay before electrophoresis. For SDS-PAGE, the samples were mixed with 5x reducing sample buffer (250 mM Tris-HCI (pH 6.8), 10% (w/v) Sodium dodecyl sulphate (SDS), 40% (v/v) glycerol and 5% (v/v) 2-mercaptoethanol) and heated to 95 ˚C for 5 minutes. The treated sample was loaded at 10 µg per well and separated by SDS-PAGE. The gel electrophoresis was performed at 100V, 400mA for 120 minutes. For Western-blot, the proteins in the gel were transferred to PVDF membrane (Immuno-Blot® PVDF membrane for protein blotting, Bio-rad USA) in transfer buffer (25 mM Tris, 192 mM glycine, 20% (v/v) methanol, and 0.2% (w/v) SDS) with Trans-Blot® SD semi-dry transfer cell (Bio-rad, USA) at 220mA, 15V for 42 minutes. The membrane was blocked with 5% (w/v) BSA in 1x TBS (20 mM Tris pH 7.5, 150 mM NaCl) containing 0.1% Tween® 20 (TBST) on a rocker at room temperature for an hour. The blot was washed three times in TBST at RT for 5min and probed with rabbit anti-phospho-STMN1-S25 or rabbit anti-

phospho-Rb-T373 polyclonal antibody in 5% (w/v) BSA in TBST at 4 ˚C overnight. The membrane was washed as in the previous step and incubated with goat anti-rabbit IgG conjugated with HRP (diluted 1:10000) in 5% BSA in TBST at room temperature for an hour. Then, the membrane was washed again. For detection, Amersham® ECL western blotting detection reagents (GE Healthcare, UK) were mixed at manufacturer suggestion ratio and overlayed on the membrane then incubated for 1 minute to generate signals. The signals on blots were captured by Amersham® imager 600 (GE Healthcare, UK). After signal detection, the membrane was subjected to removal of antibodies for reprobing by incubating the membrane at RT with mild stripping buffer (200mM glycine pH 2.2, 0.1% (w/v) SDS, 1% (v/v) Tween20) for 10 min, twice. The membrane was washed with TBST for 4 times followed by blocking with 5% (w/v) BSA in TBST and probed with total protein antibody followed by anti-GAPDH antibody. The phosphosite signals were normalised against GAPDH and total protein expression level and visualised by a bar chart.

3.3 Results

3.3.1 Early effect of APG on SKOV-3 cell line

The data at 24h from the MTT assays in chapter 2 were used to create a general four-parameter log-logistic model analysis by the "drc" package in R. The model was described by the equation below,

$$y = C + \frac{D - C}{1 + exp\{b(log(x) - log(E))\}}$$

where C is response at the lower limit, D is response at the upper limit, b is the slope and E is the dose giving 50% of the upper response (IC_{50}). The plot of this model was illustrated in figure 3.1. The output of log-logistics model from 'drc' package was displayed as a curve with parameters described in Table 3.1. Based on the model, several ICs were calculated and are shown in Table 3.2. These concentrations were used in the further experiment of APG effect in SKOV-3 cell line in this study.

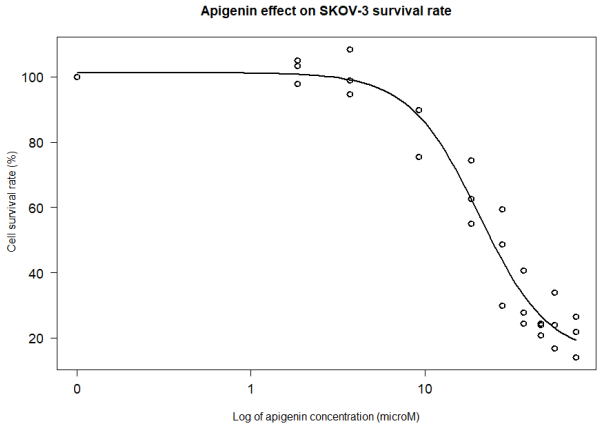

Figure 3.1 Cell survival plot generated from the "drc" package with all data points presented.

Table 3.1 The summary output of four parameters log-logistic model

Model fitted: Log-logistic (IC_{50} as parameter) (4 parameters)				
	Parameter estimates:			
	Estimate	Std. Error	t-value	p-value
Slope:(Intercept)	2.16270	0.44053	4.9093	4.269e-05 ***
Lower Limit:(Intercept)	14.15984	6.12952	2.3101	0.02908 *
Upper Limit:(Intercept)	101.26482	2.80752	36.0691	< 2.2e-16 ***
IC_{50}:(Intercept)	20.45820	2.06195	9.9218	2.496e-10 ***
Significant codes: 0 '*' 0.001 '**' 0.01 '*' 0.05 '.' 0.1 ' ' 1**				
Residual standard error: 7.394571 (26 degrees of freedom)				

Table 3.2 Estimation of various ICs level of APG effect against SKOV-3

Estimated effective doses		
	Estimate (μM)	Std. Error
IC_{10}	7.407	1.488
IC_{20}	10.777	1.495
IC_{30}	13.827	1.493
IC_{40}	16.961	1.635
IC_{50}	20.458	2.062
IC_{60}	24.677	2.914

To better understand how quickly APG acts on the SKOV-3 cell line we looked at the MTT derived cell numbers over time in the context of exposure. While the MTT assay might not be the best method to represent cell proliferation, it offered an approach to detect viable cells through detection of NAD(P)H-dependent oxidoreductase activity, a mitochondria

enzyme, that plays a vital role in the central metabolic pathways of the cells (244). The results show that APG impacts the cells in a two-stage process: 1) within the first 2h a concentration-dependent effect on SKOV-3 can be observed 2) which is then propagated onwards from 5h up to 24h resulting in the significantly reduced either cell proliferation rate or numbers of the viable cells (Fig. 3.2).

The immediate early effect on cell proliferation suggests that APG disrupts early cellular processes restricting cell numbers. The impact of this restriction defines how significant the final proliferation rate is. For example, while IC_{10} and IC_{20} are affected within the first 2h the suppression of cell proliferation is relatively similar when compared to the medium control. IC_{30} and onwards show a clear drop in cell survival.

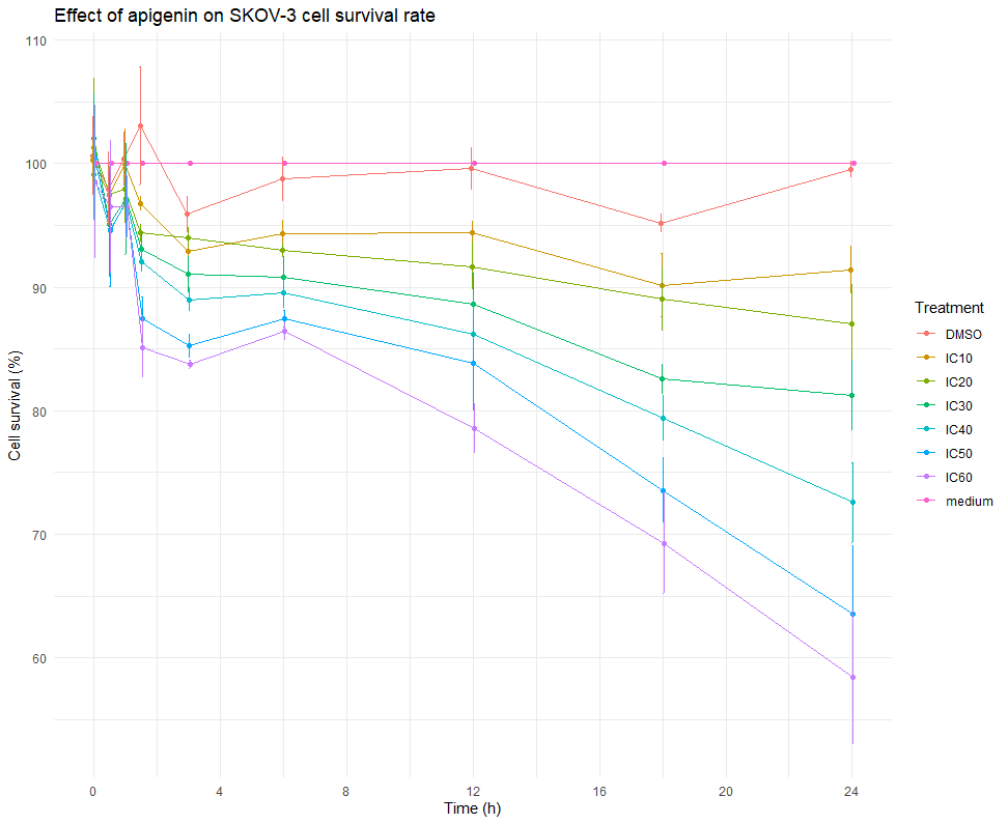

Figure 3.2 Cell survival plot from early timepoint experiment.

The cells were seeded at 5×10^3 cells/well and treated with the inhibition concentration of APG shown in the plot on the next day.

3.3.2 Establishing molecular responses to APG exposure

To study the alteration of cellular signalling by APG we performed an 11-plex TMT-labelling phosphoproteomics for quantification and traceability of these changes in a dose and time-dependent manner. The consideration of time points in our experimental design is related to early antiproliferative activity of APG and previous studies in prostate cancer cell lines, which showed that APG could reduce the phosphorylation of ERK1/2, Akt in retinoblastoma at 1, 3, and 4 hours, respectively (135, 245).

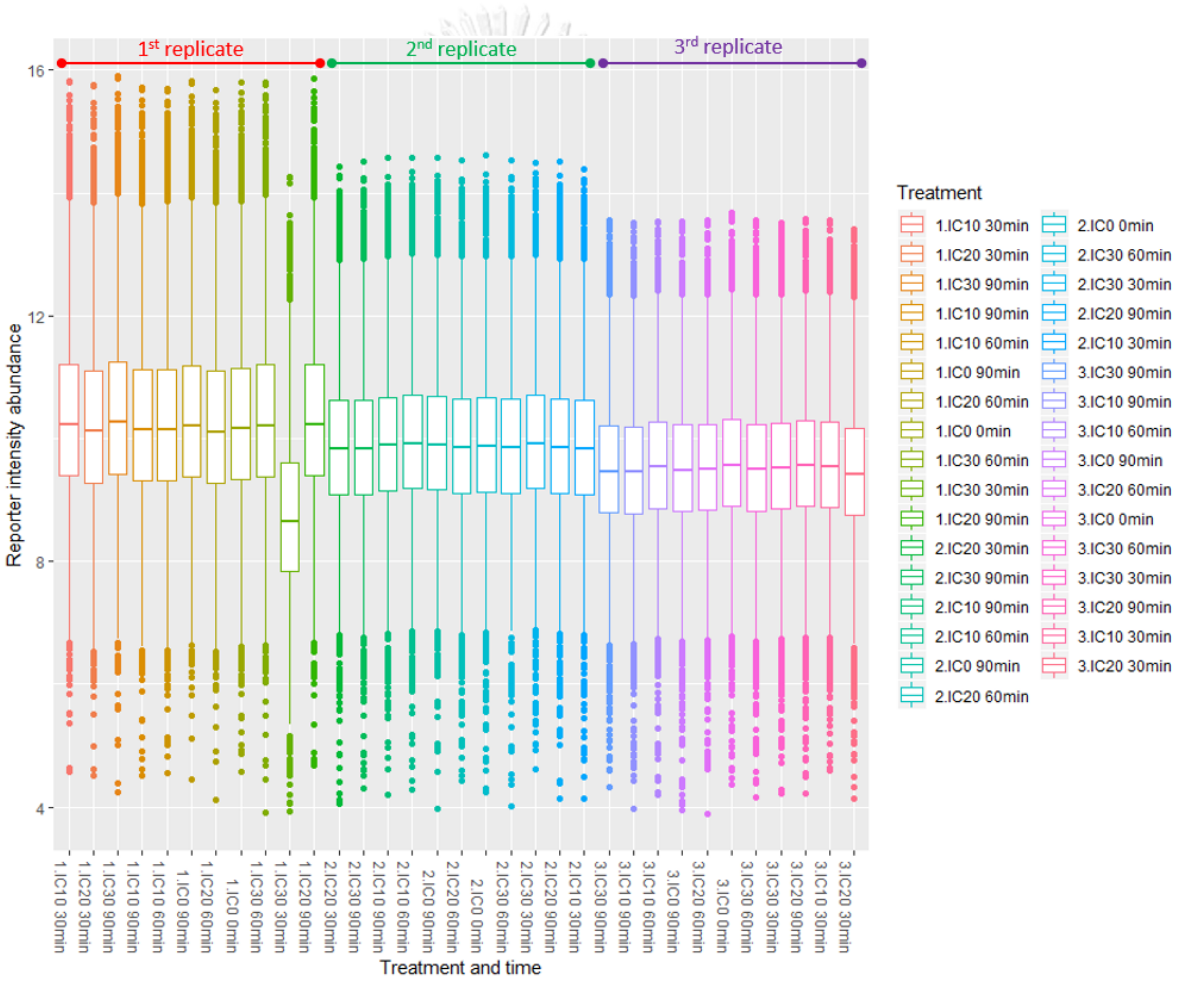

Figure 3.3 Boxplot of log-transformed reporter ion intensity from phosphosites in all replicates.

The number in the front of the treatment indicated biological replicate.

Boxplots of the log-transformed reporter ion intensities (Fig. 3.3) show that the 10th reporter (IC_{30} at 30 minutes of the first replicate) had a much lower intensity compared to others in the same replicate. Within each replicate, distributions looked similar suggesting that at least within a replicate data was comparable (Fig. 3.4). A principal component analysis of the data showed that a batch effect related to replicate was present (Fig. 3.5A). Specifically, the plot shows that the lower intensity channel from the boxplot (the 10th reporter, in yellow circle) was highly dispersed from other reporter ions. Three normalisation methods, median sweeping, quantile normalisation, and variance stabilizing normalisation (VSN), had been performed in an attempt to handle this channel. The results showed that though the boxplots of normalisation data (Fig. Appx.A1) could bring this channel back to a similar level as compared to others from the PCA plots (Fig. Appx.A2), it remained to be scattered away from other channels. This evidence suggests that none of the normalization approaches could rescue the difference in signal intensity. Further checking of the raw data confirmed that this event is unlikely a biological phenomenon and following tests are required to identify the technical source of this issue. Thus, the 10th reporter intensity from the first biological replicate was removed from the analysis. After loess normalisation and batch correction, the PCA plot appeared that batch effect has been reduced and the association of treatment and time across different replicates could be observed (Fig. 3.4B). Initially, the early 30-minute timepoint (green oval) shifts significantly to the right, followed by another shift back at 60 minutes (blue oval). There is no additional shifting observed at the 90-minute timepoint (purple oval). This suggested that there was a high alteration of phosphorylated proteins within 30 minutes of APG treatment.

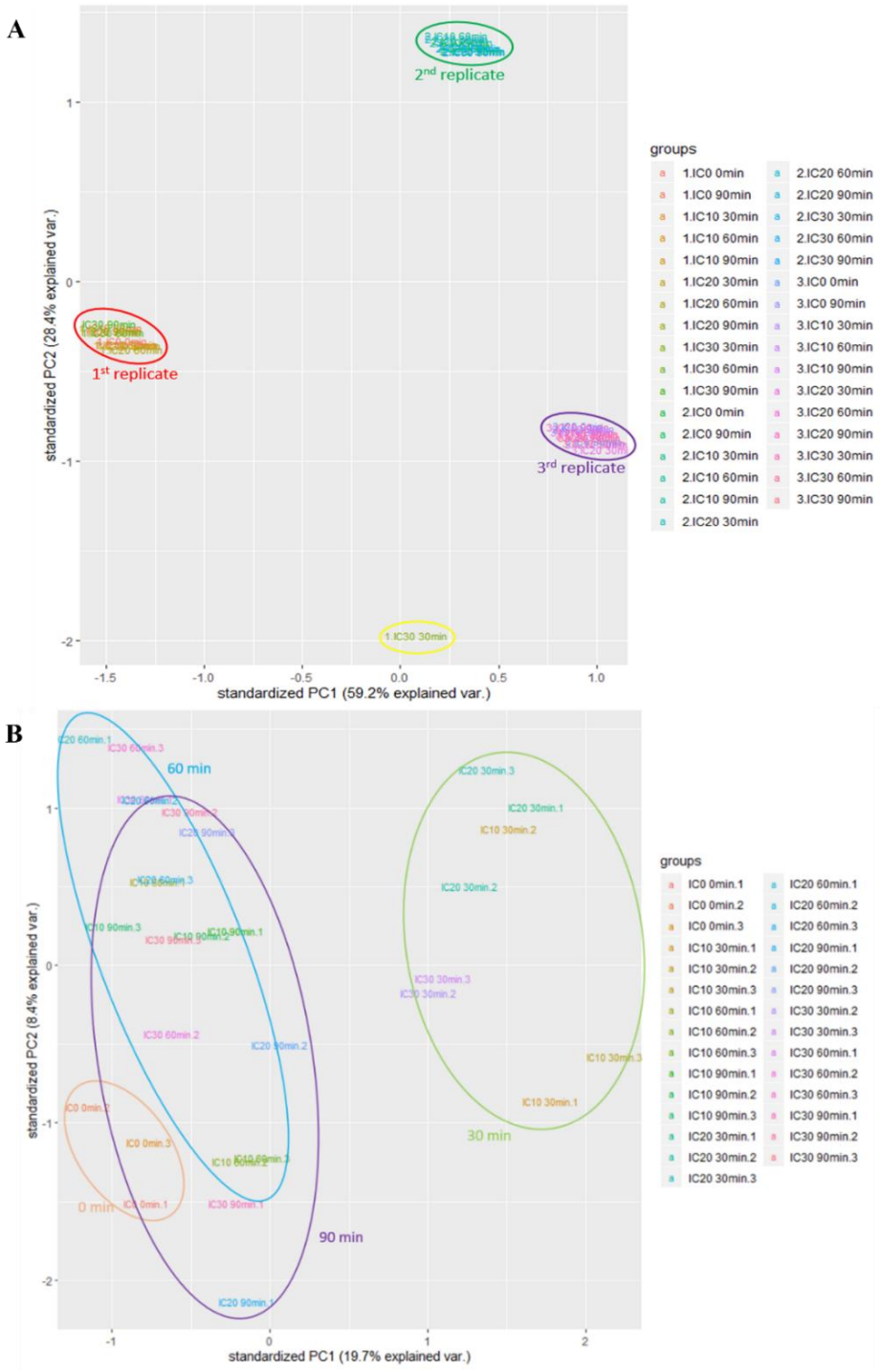

Figure 3.4 PCA plot of data grouped by all levels in each phosphosite.

(A) Log intensities of all reporters. (B) Data after Loess normalisation and batch correction. Number indicated biological replicate of that channel. Ellipse shape indicated the group of samples by time, orange for 0 min, green for 30 min, blue for 60 min, and purple for 90 min.

3.3.3 Identification of differentially phosphorylated proteins

To identify proteins whose phosphosites were altered as a result of APG exposure an ANOVA model was applied to the data. Here 3 parameters were evaluated, change over time, change over concentration, and the interaction between these two. The latter parameter identifies proteins whose phosphorylation patterns are changing together over concentration and time. This allows us to identify even small steady changes over concentration and time which may be insufficient for each single parameter separately to return a significant result. Significant phosphosites from the ANOVA were captured at FDR < 10% and the unique proteins were extracted. We found 27 unique proteins associated with concentration, 48 with time, and 73 with the interaction component. To better understand what might be happening functionally we further performed functional enrichment analysis on these lists using DAVID. This showed that only two terms from annotation term lists in the interaction component, acetylation, and citrullination, were significantly enriched (Fig. Appx.B1). Functional clustering within DAVID then revealed that chromatin and nucleosome-related terms were aggregated in the highest rank with an enrichment score of 1.828 (Table Appx.B1).

To develop a better understanding of the functional changes occurring within this experiment and to address the lacking functional enrichment observed using DAVID, a gene-set enrichment analysis (GSEA) was performed. The coefficient values from ANOVA test of each phosphosite were extracted with its phosphosites. For proteins with multiple phosphosites, we calculated the mean change and used this as input to the approach.

The GSEA results were filtered at FDR ≤ 0.25. This identified 18 terms associated with the concentration of which only 1 was associated with a positive enrichment, no significantly associated terms for time, and 41 terms associated with the interaction component (Fig. 3.5). A closer inspection of the pathways associated with concentration showed that the only positive normalised enriched term (NES) was ‘negative regulation of transmembrane transport’ while the other 14 significant enriched terms showed negative

correlation, 8 of which are involved with epigenetics and chromatin regulation of gene expression whereas the others correlated to cellular transport and cytoskeleton activity. Interestingly, 4 out of 8 epigenetics significant terms specifically related to chromatin organisation. Terms such as chromatin assembly and chromatin organisation are involved in the regulation of transcription, chromatin assembly or disassembly, and nucleosome organisation. In addition, other terms related to epigenetics such as regulation of posttranscriptional gene silencing, negative regulation of gene expression epigenetic, regulation of gene silencing, and gene silencing by RNA were identified. Within the interaction list (Fig. 3.5C) all terms were shown to have positive NES scores including the most significant terms including negative regulation of gene expression epigenetic, chromatin organisation involved in regulation of transcription, chromatin assembly, chromatin assembly or disassembly, nucleosome organization, DNA packaging complex, nucleosomal-DNA binding, regulation of gene expression epigenetic, regulation of gene silencing and nucleosome binding. Moreover, the dot plot (Fig. Appx.C) showed that terms related to epigenetics and chromatin/nucleosome regulation acquired a high hits ratio on both concentration (~30% on 3 terms) and interaction (>30% on 9 terms). Venn diagram (Fig. 3.5A) illustrated 9 terms that were found in both sets and they were mostly related to regulation of gene expression and chromatin organisation including terms such as regulation of gene silencing, negative regulation of gene expression epigenetic, regulation of posttranscriptional gene silencing, nucleosome organization, chromatin organization involved in regulation of transcription, chromatin assembly or disassembly and cell differentiation.

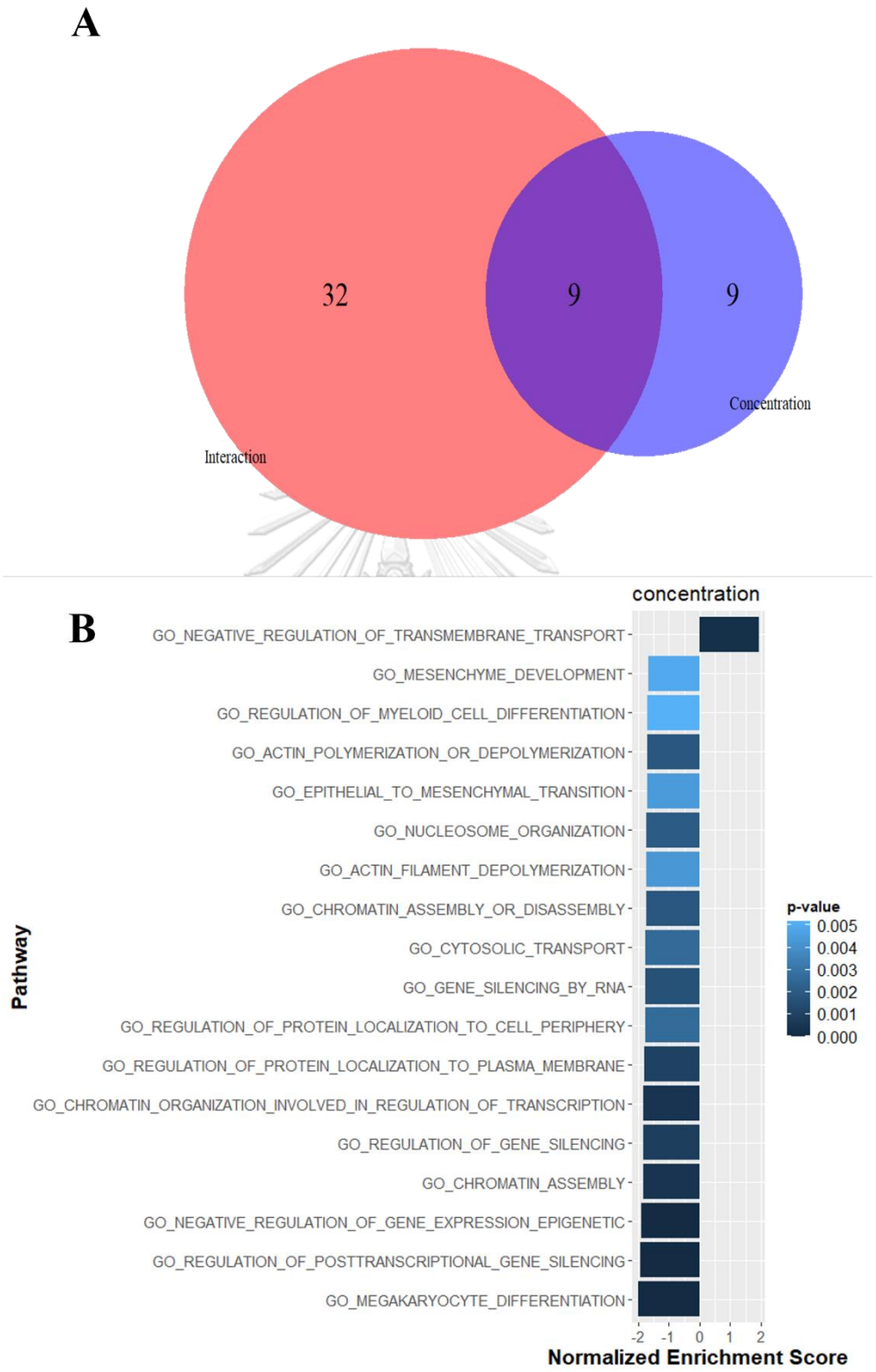
A
32
9
9
Interaction
Concentration
B
concentration
GO_NEGATIVE_REGULATION_OF_TRANSMEMBRANE_TRANSPORT
GO_MESENCHYME_DEVELOPMENT
GO_REGULATION_OF_MYELOID_CELL_DIFFERENTIATION
GO_ACTIN_POLYMERIZATION_OR_DEPOLYMERIZATION
GO_EPITHELIAL_TO_MESENCHYMAL_TRANSITION
GO_NUCLEOSOME_ORGANIZATION
GO_ACTIN_FILAMENT_DEPOLYMERIZATION
GO_CHROMATIN_ASSEMBLY_OR_DISASSEMBLY
GO_CYTOSOLIC_TRANSPORT
GO_GENE_SILENCING_BY_RNA
GO_REGULATION_OF_PROTEIN_LOCALIZATION_TO_CELL_PERIPHERY
GO_REGULATION_OF_PROTEIN_LOCALIZATION_TO_PLASMA_MEMBRANE
GO_CHROMATIN_ORGANIZATION_INVOLVED_IN_REGULATION_OF_TRANSCRIPTION
GO_REGULATION_OF_GENE_SILENCING
GO_CHROMATIN_ASSEMBLY
GO_NEGATIVE_REGULATION_OF_GENE_EXPRESSION_EPIGENETIC
GO_REGULATION_OF_POSTTRANSCRIPTIONAL_GENE_SILENCING
GO_MEGAKARYOCYTE_DIFFERENTIATION
Pathway
-2
-1
0
1
2
Normalized Enrichment Score
p-value
0.005
0.004
0.003
0.002
0.001
0.000

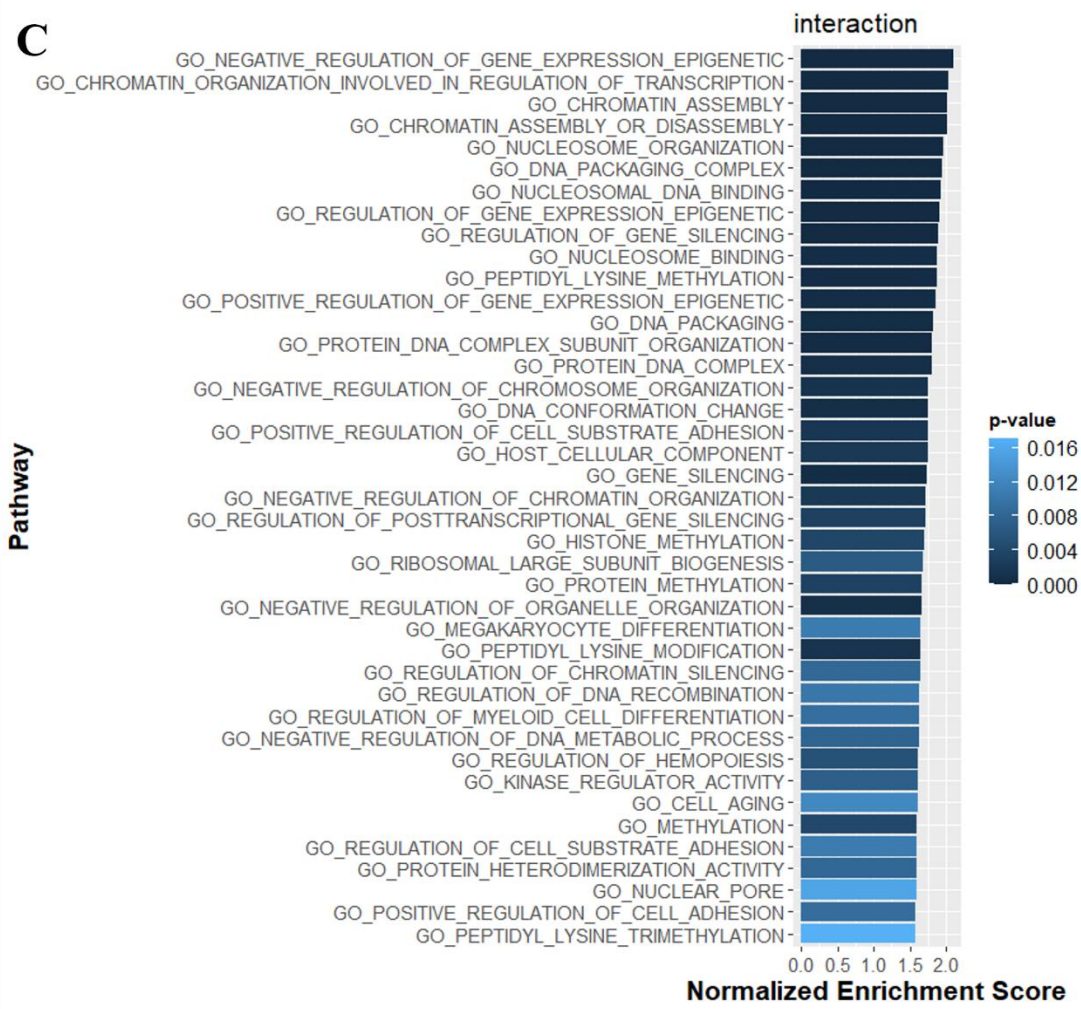

Figure 3.5 Bar chart of enriched term from significant phosphosites.

(A) Venn diagram of significant terms from interaction (Red) and concentration (Blue) list. Number indicated terms in each set. (B) Concentration factor list and (C) interaction between concentration and time list were computed in Broad's GSEA Pre-ranked list test.

Due to the significant differences observed in the PCA plot at 30 minutes we then also performed an in-depth analysis of the early effect of APG exposure. First, we performed an ANOVA comparing each concentration at the 30-minute timepoint against the 0-minute control. After p-value adjustment, significant phosphosites were captured using a 5% FDR cut-off. This approach identified 140 and 177 phosphosites from concentration and time factors respectively that resulted in 118 and 136 unique proteins from both lists. Unique proteins from both lists underwent DAVID functional annotation enrichment. The resulting terms were filtered at FDR ≤ 0.25 and visualised using bar charts (Fig. 3.6) and dot plots (Fig. 3.7). 10 terms were found to be associated with concentration, 4 of which related to DNA and chromatin activity. The clustering chart (Table 3.3) has shown that two clusters of enriched terms were found to obtain quite a high enrichment score that were chromatin-related and cell-cell adhesion terms with approximately enrichment score (ES) 2.2 on both clusters. In parallel, 12 terms were associated with time (Fig. 3.6B and 3.7B) representing the same functional chromatin-related and cell-cell adhesion-related clusters. The clustering results appeared to be the same clusters (Table 3.4) found associated with concentration, cell-cell adhesion (ES 2.42), and chromatin-related (ES 1.72) terms. Venn diagram of protein and phosphosites for DAVID input (Fig. 3.8A and B) showed 84 proteins with 93 phosphosites that are in common between the time and concentration lists. From these results, we could imply that the core phosphosites, which are affected by dose and time factors, influenced the regulation of gene expression by chromatin remodelling and cell-cell adhesion activity. This further raises an interesting effect of APG on SKOV-3 epigenetic arrangement and adhesion.

To further explore the functional changes within our exposure we made use of the loess normalisation applied within our pre-processing pipeline. As the data we are analysing already represents a ratio between treatment and 90 min control (including the 0-minute control) we asked the question whether there are super-pathway based trajectories governed by the phosphoproteomics data. To address this challenge, we performed a limma analysis

that compares the derived ratio to the null distribution. The t-statistics were extracted and used as an input to the GSEA analysis used earlier. The results (Fig. 3.9) illustrated 102 terms with two major patterns: 1) an A-shaped pattern group that indicates increasing activity at 30 minutes and 2) a V-shaped pattern group that associated-terms were repressed early. Within the A-shaped group terms related to various signalling pathways, including MAPK, ERBB, and a few immune response signalling, and other several biological processes such as amide and peptide biosynthetic and metabolic process, transport vesicle, demethylation, and stress response were identified. On the other hand, within the V-shaped group terms related to transcription control by epigenetics and histone-nucleosome-chromatin modifications and organisation were highlighted. Interestingly, the demethylation term was found to increase in activity at 30 minutes, which appeared to behave conversely to histone and peptidyl lysine methylation and trimethylation. Venn diagram of GSEA result comparing t-test results (Fig. 3.8C in red circle) and the ANOVA results (Fig. 3.8C in green and blue circles) found similar 29 terms that were associated with gene expression regulation, which are epigenetics regulation and histone-chromatin activities, organisation, modifications, and assembly or disassembly. Taken together, these results reflect an interesting consequence of actions after treatment with APG, which increases in activity of signalling cascades while decreasing activity on epigenetics and chromatin organisation at 30 minutes.

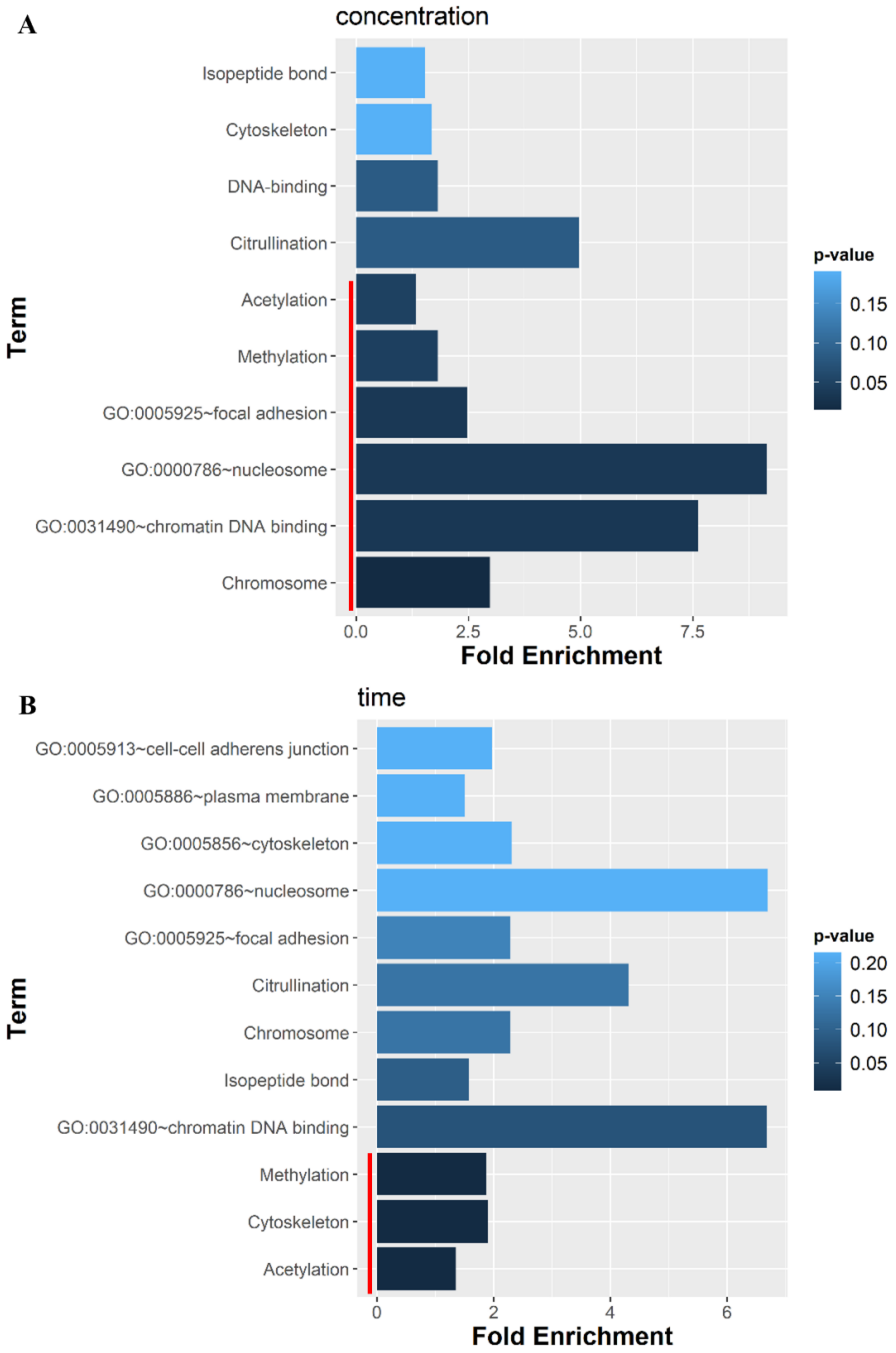

Figure 3.6 Bar charts of DAVID annotation terms of 30 minutes significant phosphosites. Using (A) concentration or (B) time lists at 5% cut-off. The plots showed significant terms filtered by FDR <0.25. The red line indicated Term with Benjamini-Hochberg adjusted p-value < 0.05.

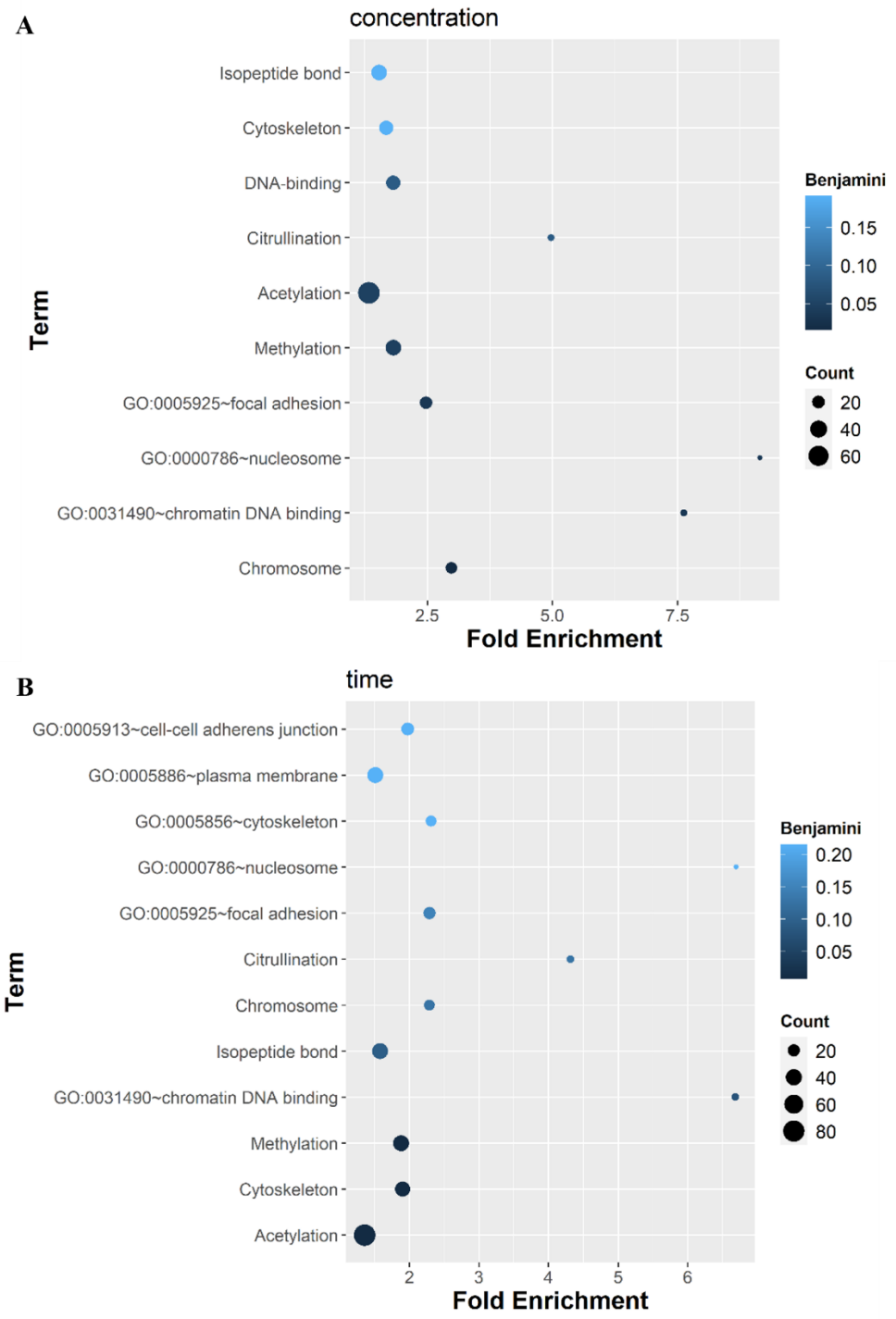

Figure 3.7 Dot plots of DAVID enriched term from 30 minutes significant phosphosites. (A) Concentration factor list and (B) time list

Table 3.3 Significance clustering group from DAVID clustering chart of 30 minutes significant phosphosites from concentration list

ANNOTATION CLUSTER 1		ENRICHMENT SCORE: 2.2712275002037656									
CATEGORY	Term	Count	%	PValue	Genes	List Total	Pop Hits	Pop Total	Fold Enrichment	Benjamini	FDR
GOTERM_MF_DIRECT	GO:0031490~chromatin DNA binding	7	5.932203	1.30E-04	O75367, P10412, Q7LBC6, P16403, P16402, P16401, P40763	114	14	1738	7.622807	0.034062	0.034062
GOTERM_CC_DIRECT	GO:0000786~nucleosome	6	5.084746	2.07E-04	Q71DI3, O75367, P10412, P16403, P16402, P16401	116	10	1768	9.144828	0.035226	0.035226
GOTERM_BP_DIRECT	GO:0006334~nucleosome assembly	8	6.779661	5.48E-04	Q9NVP2, P06748, Q71DI3, O75367, P10412, P16403, P16402, P16401	111	24	1697	5.096096	0.445525	0.445525
UP_KEYWORDS	Citrullination	7	5.932203	0.00185	P42166, Q71DI3, P10412, Q9BQG0, P16403, P16402, P16401	118	22	1844	4.972265	0.083361	0.082439
GOTERM_BP_DIRECT	GO:0098532~histone H3-K27 trimethylation	3	2.542373	0.011967	P10412, P16403, P16402	111	3	1697	15.28829	1	1
GOTERM_BP_DIRECT	GO:0080182~histone H3-K4 trimethylation	3	2.542373	0.036598	P10412, P16403, P16402	111	5	1697	9.172973	1	1
GOTERM_BP_DIRECT	GO:0016584~nucleosome positioning	3	2.542373	0.036598	P10412, P16403, P16402	111	5	1697	9.172973	1	1
GOTERM_CC_DIRECT	GO:0000790~nuclear chromatin	7	5.932203	0.080149	Q9H1E3, Q9NVP2, O75367, Q9Y618, P16402, P16401, P40763	116	47	1768	2.269993	1	1
GOTERM_BP_DIRECT	GO:0000122~negative regulation of transcription from RNA polymerase II promoter	13	11.01695	0.103754	Q9NRY4, Q9Y618, O75367, P10412, Q6KC79, P16403, P16402, P16401, P17844, Q71DI3, Q9NPF5, P40763, P26358	111	125	1697	1.589982	1	1
ANNOTATION CLUSTER 2		ENRICHMENT SCORE: 2.210982234697643									
CATEGORY	Term	Count	%	PValue	Genes	List Total	Pop Hits	Pop Total	Fold Enrichment	Benjamini	FDR
GOTERM_MF_DIRECT	GO:0098641~cadherin binding involved in cell-cell adhesion	19	16.10169	0.003197	Q9H2G2, Q14247, Q15149, Q15599, Q96TA1, Q13813, Q14847, Q86W92, Q09666, O60716, P35611, P42166, Q9Y570, P55196, P46940, P00533, Q9C0C2, Q96HC4, P21333	114	141	1738	2.054374	0.420376	0.420376
GOTERM_CC_DIRECT	GO:0005913~cell-cell adherens junction	19	16.10169	0.005945	Q9H2G2, Q14247, Q15149, Q15599, Q96TA1, Q13813, Q14847, Q86W92, Q09666, O60716, P35611, P42166, Q9Y570, P55196, P46940, P00533, Q9C0C2, Q96HC4, P21333	116	149	1768	1.943532	0.414191	0.414191
GOTERM_BP_DIRECT	GO:0098609~cell-cell adhesion	16	13.55932	0.012251	Q9H2G2, Q14247, Q15149, Q15599, Q96TA1, Q13813, Q14847, Q86W92, Q09666, P35611, P42166, Q9Y570, P55196, P46940, Q9C0C2, Q96HC4	111	125	1697	1.956901	1	1

Table 3.4 Significance clustering group from DAVID clustering chart of 30 minutes significant phosphosites from time list

ANNOTATION CLUSTER 1		ENRICHMENT SCORE: 2.4252015808050453									
CATEGORY	Term	Count	%	PValue	Genes	List Total	Pop Hits	Pop Total	Fold Enrichment	Benjamini	FDR
GOTERM_CC_DIRECT	GO:0005913~cell-cell adherens junction	22	16.17647	0.002175	Q9H4G0, Q15942, Q14247, Q15149, Q15599, Q96TA1, Q13813, Q14847, Q9NQW6, Q96PY5, Q09666, O60716, P35611, Q04637, Q16181, P42224, Q9Y570, P46940, P00533, Q9C0C2, Q96HC4, P21333	132	149	1768	1.977629	0.215404	0.215404
GOTERM_MF_DIRECT	GO:0098641~cadherin binding involved in cell-cell adhesion	21	15.44118	0.002622	Q9H4G0, Q14247, Q15149, Q15599, Q96TA1, Q13813, Q14847, Q9NQW6, Q96PY5, Q09666, O60716, P35611, Q04637, Q16181, P42224, Q9Y570, P46940, P00533, Q9C0C2, Q96HC4, P21333	130	141	1738	1.991162	0.364442	0.364442
GOTERM_BP_DIRECT	GO:0098609~cell-cell adhesion	18	13.23529	0.009298	Q9H4G0, Q14247, Q15149, Q15599, Q96TA1, Q13813, Q14847, Q9NQW6, Q96PY5, Q09666, P35611, Q04637, Q16181, P42224, Q9Y570, P46940, Q9C0C2, Q96HC4	128	125	1697	1.909125	1	1
ANNOTATION CLUSTER 2		**ENRICHMENT SCORE: 1.7290223141718402**									
CATEGORY	Term	Count	%	PValue	Genes	List Total	Pop Hits	Pop Total	Fold Enrichment	Benjamini	FDR
GOTERM_MF_DIRECT	GO:0031490~chromatin DNA binding	7	5.147059	2.73E-04	O75367, P10412, Q7LBC6, P16403, P16402, P16401, P40763	130	14	1738	6.684615	0.075834	0.075834
UP_KEYWORDS	Citrullination	7	5.147059	0.003863	Q8IYB3, P10412, Q9BQG0, Q14684, P16403, P16402, P16401	136	22	1844	4.314171	0.12695	0.124869
GOTERM_BP_DIRECT	GO:0098532~histone H3-K27 trimethylation	3	2.205882	0.004256	P10412, P16403, P16402	128	10	1768	6.69697	0.215404	0.215404
GOTERM_BP_DIRECT	GO:0016584~nucleosome positioning	3	2.205882	0.01586	P10412, P16403, P16402	128	3	1697	13.25781	1	1
GOTERM_BP_DIRECT	GO:0006334~nucleosome assembly	6	4.411765	0.029022	P06748, O75367, P10412, P16403, P16402, P16401	128	24	1697	3.314453	1	1
GOTERM_CC_DIRECT	GO:0000786~nucleosome	5	3.676471	0.04784	O75367, P10412, P16403, P16402, P16401	132	5	1697	7.954687	1	1
GOTERM_BP_DIRECT	GO:0080182~histone H3-K4 trimethylation	3	2.205882	0.04784	P10412, P16403, P16402	128	5	1697	7.954687	1	1
GOTERM_BP_DIRECT	GO:0000122~negative regulation of transcription from RNA polymerase II promoter	13	9.558824	0.218743	Q9NRY4, Q14938, O75367, P10412, Q6KC79, P15822, P16403, P16402, P16401, P42224, Q9NPF5, P40763, P26358	128	125	1697	1.378813	1	1
GOTERM_CC_DIRECT	GO:0000790~nuclear chromatin	6	4.411765	0.265752	P42224, Q9H1E3, O75367, P16402, P16401, P40763	132	47	1768	1.709865	1	1

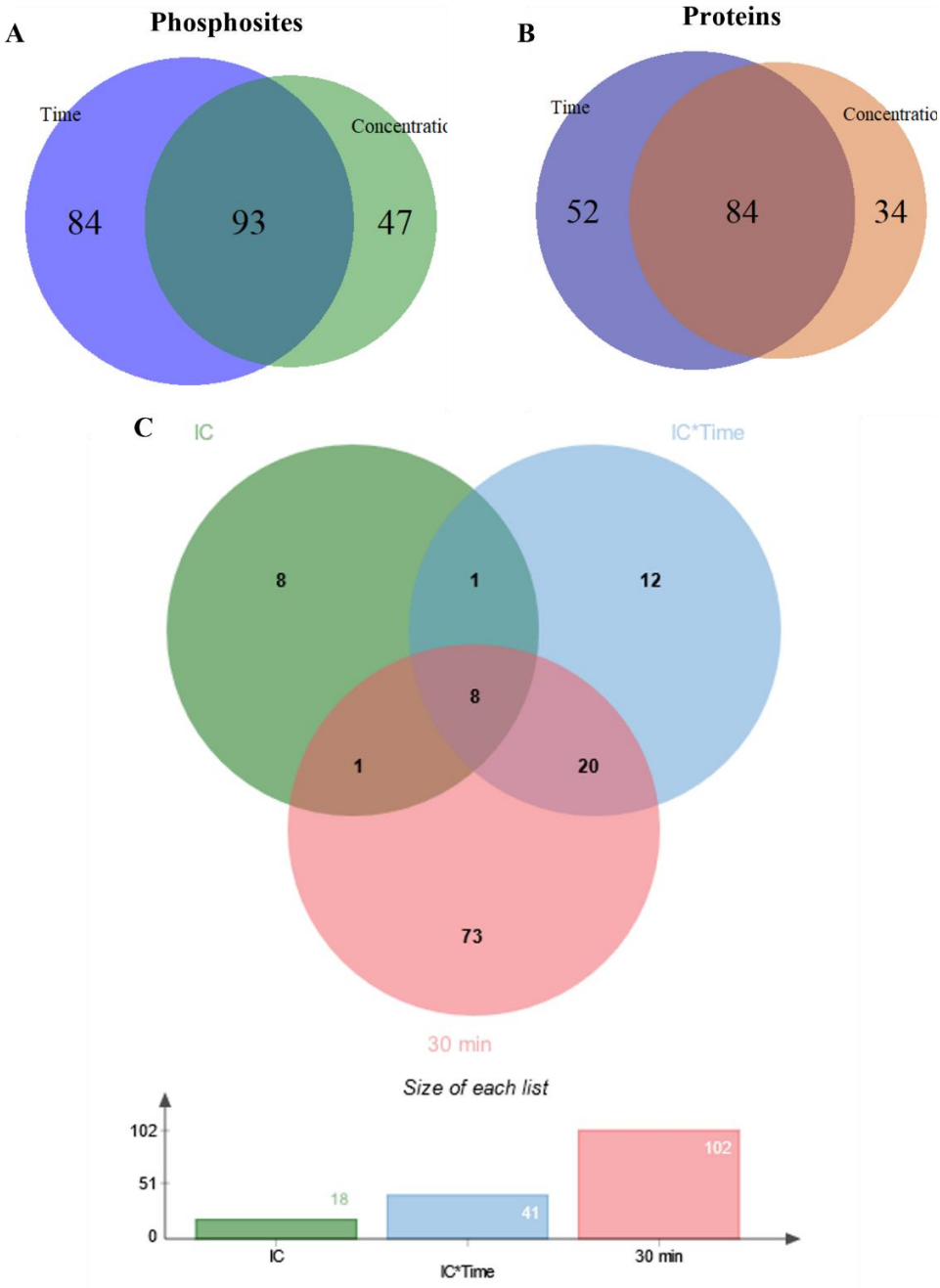

Figure 3.8 Venn diagram of output from ANOVA test on 30-minute data.

(A) The significant phosphosites were captured at BH adjusted p-value < 0.05 and grabbed (B) only UniProt accession for DAVID analysis. (C) Venn diagram of GSEA output illustrated data input from results of ANOVA of full dataset separated by concentration (Green) and interaction (Blue) list and data input from one-sample t-test at 30-minute (Red) of each treatment.

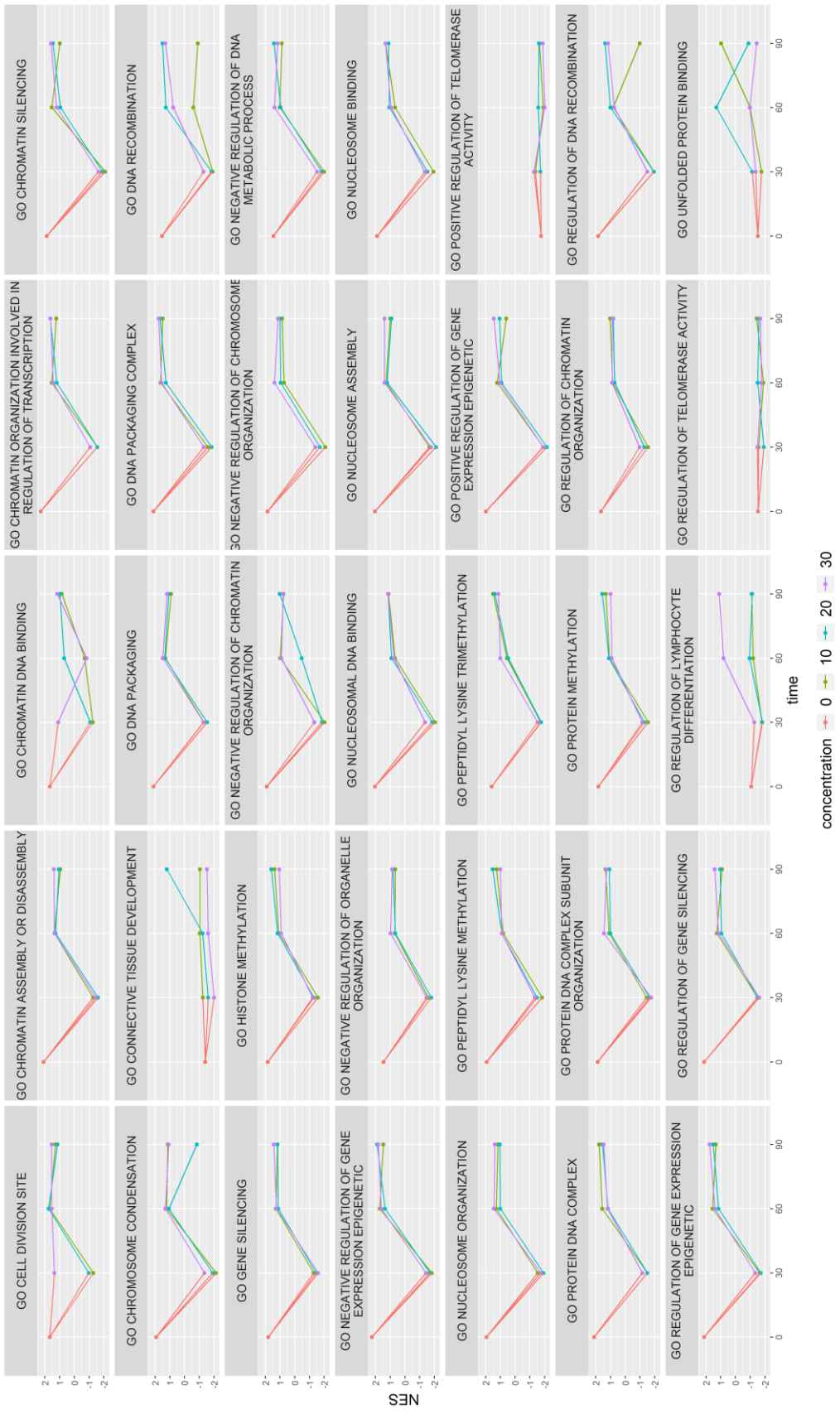
GO CELL DIVISION SITE
GO CHROMATIN ASSEMBLY OR DISASSEMBLY
GO CHROMATIN DNA BINDING
GO CHROMATIN ORGANIZATION INVOLVED IN REGULATION OF TRANSCRIPTION
GO CHROMATIN SILENCING
GO CHROMOSOME CONDENSATION
GO CONNECTIVE TISSUE DEVELOPMENT
GO DNA PACKAGING
GO DNA PACKAGING COMPLEX
GO DNA RECOMBINATION
GO GENE SILENCING
GO HISTONE METHYLATION
GO NEGATIVE REGULATION OF CHROMATIN ORGANIZATION
3O NEGATIVE REGULATION OF CHROMOSOME ORGANIZATION
GO NEGATIVE REGULATION OF DNA METABOLIC PROCESS
GO NEGATIVE REGULATION OF GENE EXPRESSION EPIGENETIC
GO NEGATIVE REGULATION OF ORGANELLE ORGANIZATION
GO NUCLEOSOMAL DNA BINDING
GO NUCLEOSOME ASSEMBLY
GO NUCLEOSOME BINDING
GO NUCLEOSOME ORGANIZATION
GO PEPTIDYL LYSINE METHYLATION
GO PEPTIDYL LYSINE TRIMETHYLATION
GO POSITIVE REGULATION OF GENE EXPRESSION EPIGENETIC
GO POSITIVE REGULATION OF TELOMERASE ACTIVITY
GO PROTEIN DNA COMPLEX
GO PROTEIN DNA COMPLEX SUBUNIT ORGANIZATION
GO PROTEIN METHYLATION
GO REGULATION OF CHROMATIN ORGANIZATION
GO REGULATION OF DNA RECOMBINATION
GO REGULATION OF GENE EXPRESSION EPIGENETIC
GO REGULATION OF GENE SILENCING
GO REGULATION OF LYMPHOCYTE DIFFERENTIATION
GO REGULATION OF TELOMERASE ACTIVITY
GO UNFOLDED PROTEIN BINDING
NES
time
concentration
0
10
20
30

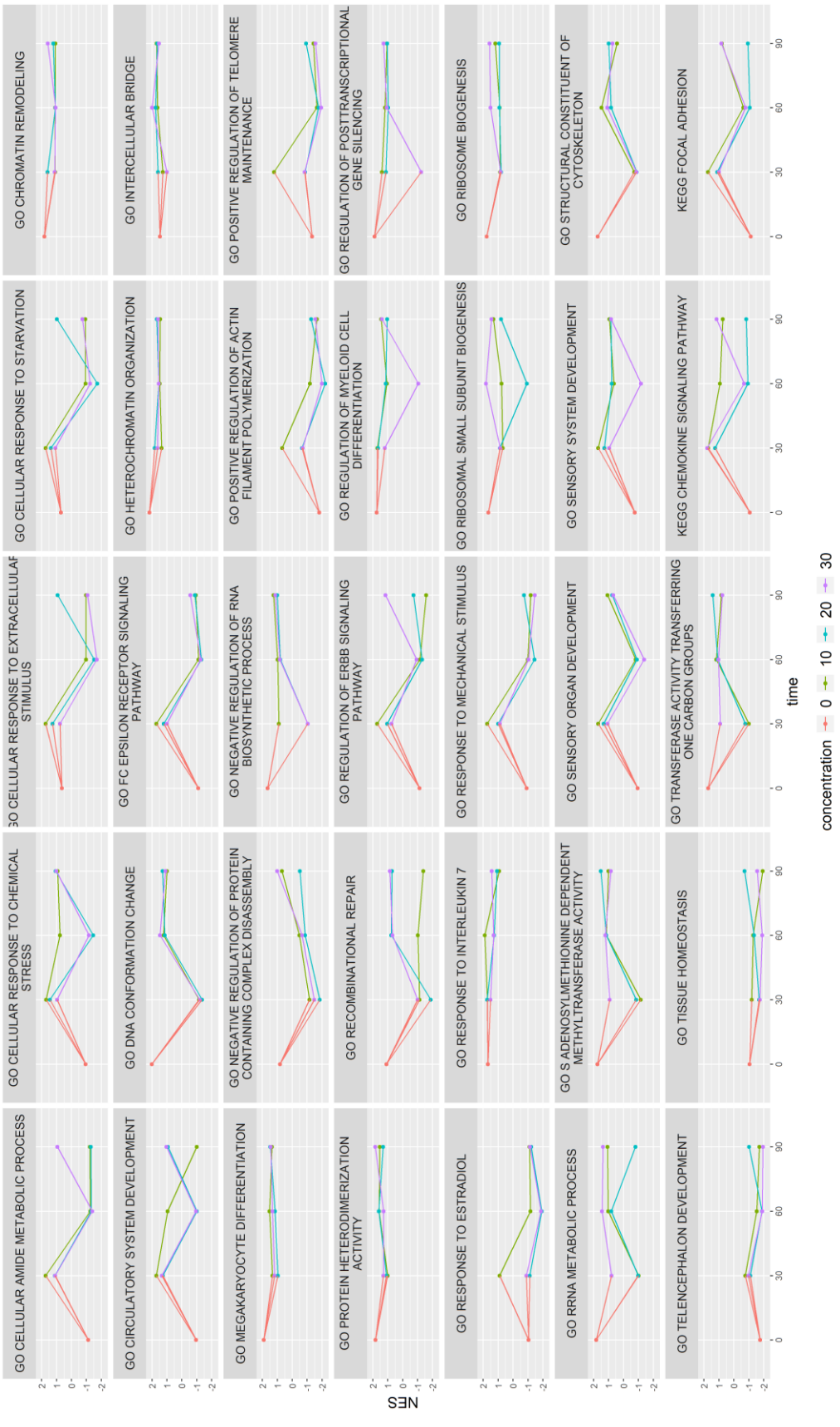
GO CELLULAR AMIDE METABOLIC PROCESS
GO CELLULAR RESPONSE TO CHEMICAL STRESS
GO CELLULAR RESPONSE TO EXTRACELLULAR STIMULUS
GO CELLULAR RESPONSE TO STARVATION
GO CHROMATIN REMODELING
GO CIRCULATORY SYSTEM DEVELOPMENT
GO DNA CONFORMATION CHANGE
GO FC EPSILON RECEPTOR SIGNALING PATHWAY
GO HETEROCHROMATIN ORGANIZATION
GO INTERCELLULAR BRIDGE
GO MEGAKARYOCYTE DIFFERENTIATION
GO NEGATIVE REGULATION OF PROTEIN CONTAINING COMPLEX DISASSEMBLY
GO NEGATIVE REGULATION OF RNA BIOSYNTHETIC PROCESS
GO POSITIVE REGULATION OF ACTIN FILAMENT POLYMERIZATION
GO POSITIVE REGULATION OF TELOMERE MAINTENANCE
GO PROTEIN HETERODIMERIZATION ACTIVITY
GO RECOMBINATIONAL REPAIR
GO REGULATION OF ERBB SIGNALING PATHWAY
GO REGULATION OF MYELOID CELL DIFFERENTIATION
GO REGULATION OF POSTTRANSCRIPTIONAL GENE SILENCING
GO RESPONSE TO ESTRADIOL
GO RESPONSE TO INTERLEUKIN 7
GO RESPONSE TO MECHANICAL STIMULUS
GO RIBOSOMAL SMALL SUBUNIT BIOGENESIS
GO RIBOSOME BIOGENESIS
GO RRNA METABOLIC PROCESS
GO S ADENOSYLMETHIONINE DEPENDENT METHYLTRANSFERASE ACTIVITY
GO SENSORY ORGAN DEVELOPMENT
GO SENSORY SYSTEM DEVELOPMENT
GO STRUCTURAL CONSTITUENT OF CYTOSKELETON
GO TELENCEPHALON DEVELOPMENT
GO TISSUE HOMEOSTASIS
GO TRANSFERASE ACTIVITY TRANSFERRING ONE CARBON GROUPS
KEGG CHEMOKINE SIGNALING PATHWAY
KEGG FOCAL ADHESION
NES
time
concentration 0 10 20 30

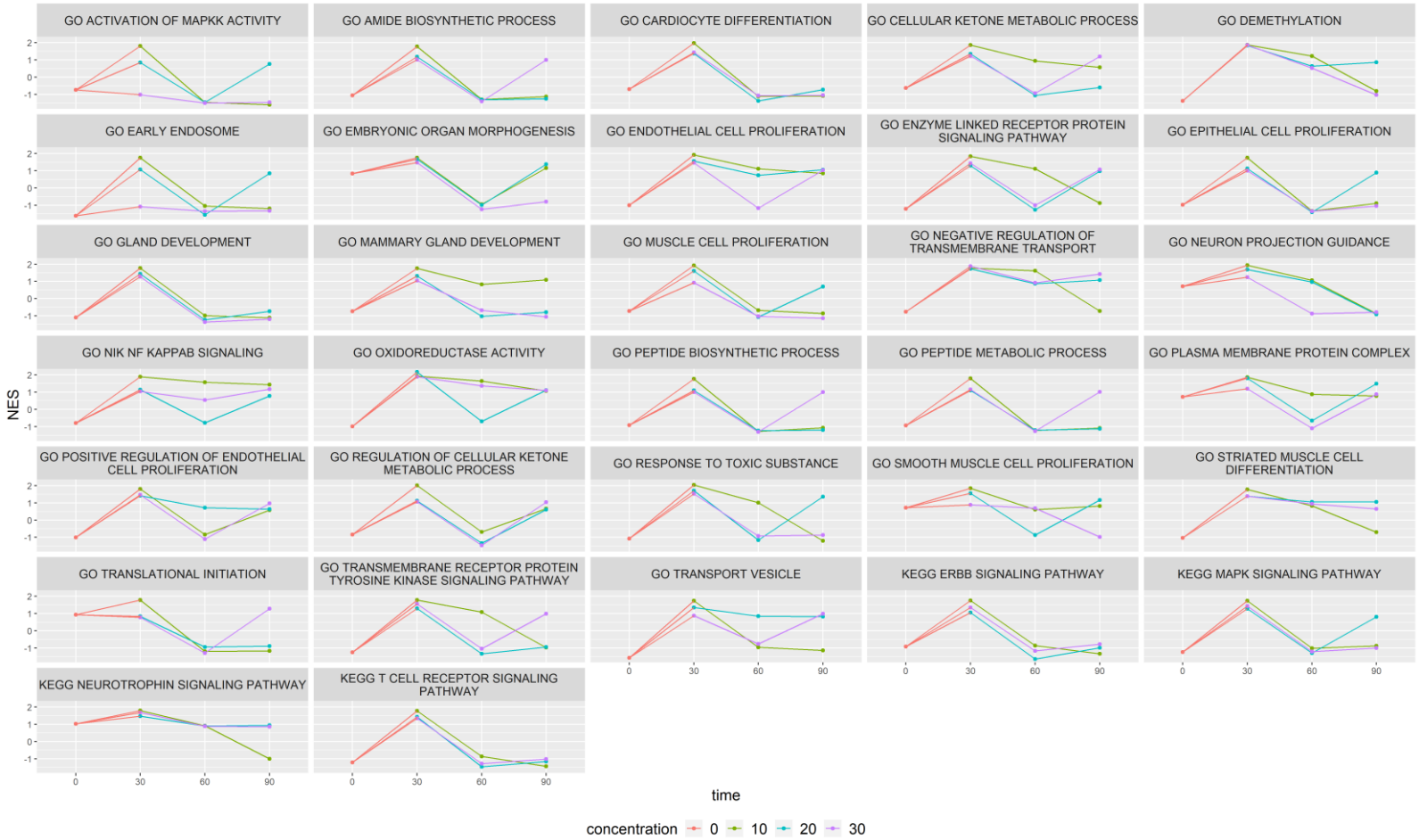

Figure 3.9 Summary plot of GSEA output from one-sample t-test.

The enriched terms were filtered at FDR ≤ 0.25 and generated into scatterplots with line. X-axis indicated time in minutes while Y-axis indicated normalised enrichment score. Each line in plots represented each concentration in this study, IC0(red), IC10 (green), IC20 (blue) and IC30 (purple).

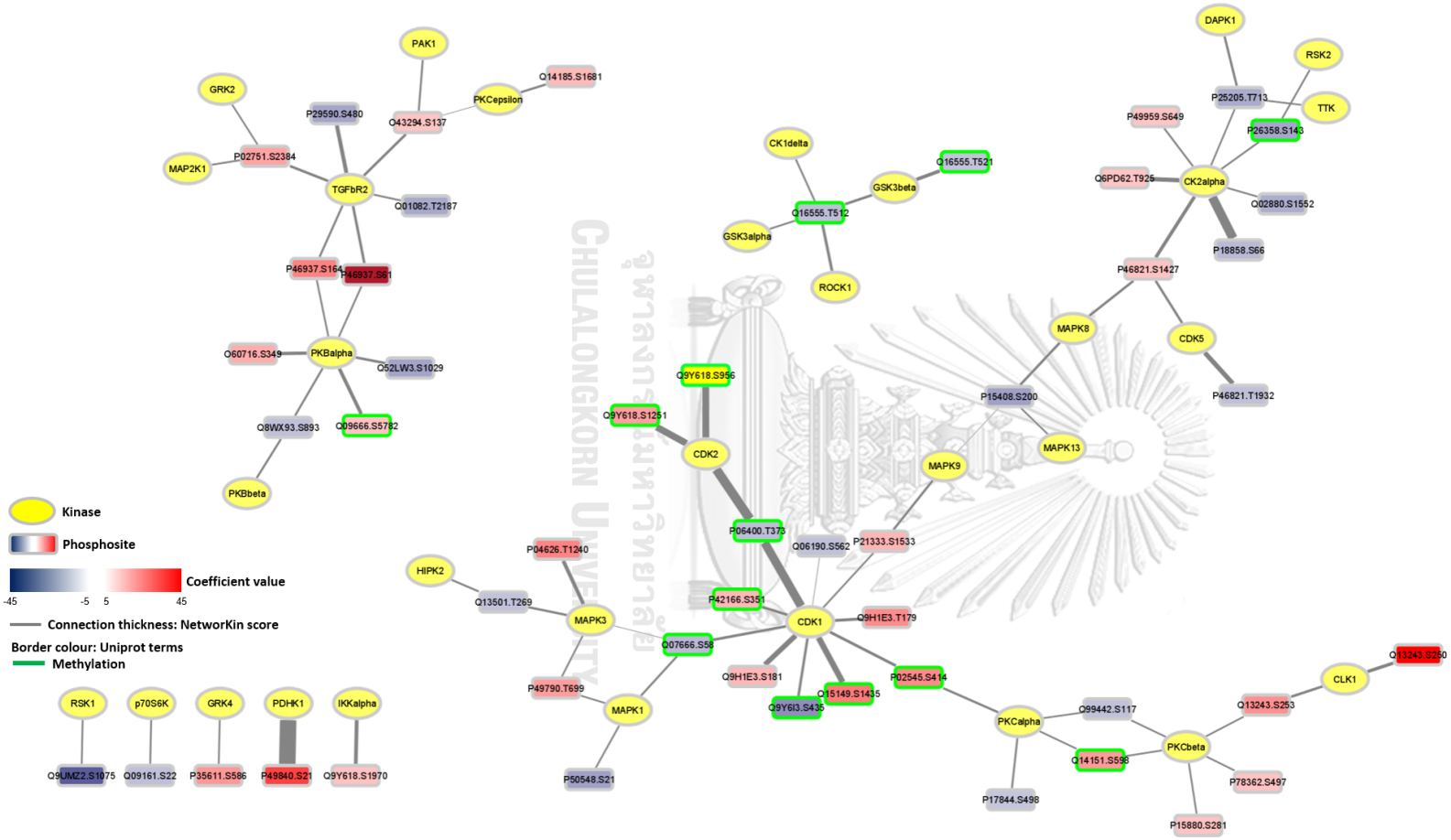

Figure 3.10 Phosphosites and kinases network from NetworKIN analysis.

Kinases were labelled in oval shapes with yellow fill whereas phosphosites were round rectangles, which fill by gradient colour related to its coefficient value. The thickness of each connection string correlated with NetworKIN score, the higher the score is the thicker the string would be.

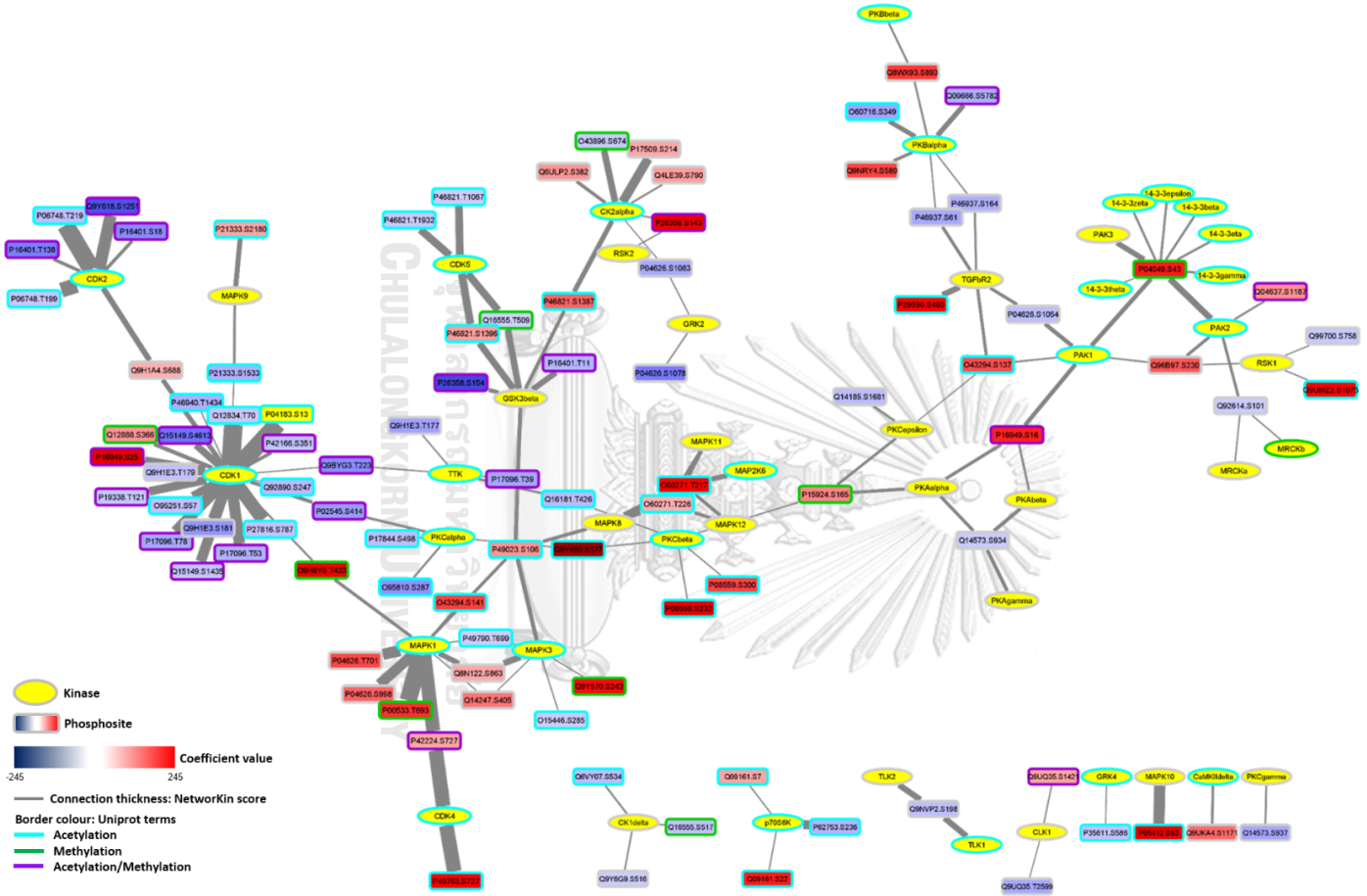

Figure 3.11 Phosphosites and kinases network from NetworKIN analysis using significances from 30 min ANOVA analysis.

Kinases were labelled in oval shapes with yellow fill whereas phosphosites were round rectangles, which fill by gradient colour related to its coefficient value. The thickness of each connection string correlated with NetworKIN score.

3.3.4 Identification of upstream kinase activity affecting identified phosphosites

To understand the possible underlying mechanisms that lead to the observed changes in phosphosites we analysed the sites using NetworKIN. This analysis identifies upstream kinase interactions by calculating a score combining likelihood ratios between the likelihood ratio of a network proximity score calculated from the STRING network and the likelihood ratio of the NetPhorest probability that is computed by associating given sequence sites to phosphorylation-binding domain preferential motif sequences on kinases (243). The score displays the possibility that a kinase would have an influence on that site, both through direct and indirect interactions. In this study, we set a cut-off score at 2.0, which is considered to be a significant interaction (246).

The significant phosphosites from concentration, time, and interaction lists were inputted to NetworKIN for analysis. In general, kinases can be organized into several groups by domain similarity, catalytic site and outer area, and known functions (247). The results from whole phosphosite analysis reported several kinases, involved with cell cycle progression, proliferation, survival, and apoptosis. Especially the AGC (PKB/AKT, PKC, GRK, and RSK families), CMGC (CDK, MAPK, GSK3, and CLK families), and CAMK (DAPK) kinase groups were identified. To get a better overview of the results we used a network representation of kinase and phosphosite interactions using Cytoscape (Fig. 3.10). Three networks with five individual interactions could be observed. The largest network included CDK1 kinase, a highlight important cell cycle progression kinase especially in G_2/M phase (238), with a set of high interaction score phosphosites. From this network, CK2α was connected to CDK1 via several MAPK kinases and had been shown to interact with a group of genes involved with DNA catalytic activity, particularly P49959 (Double-strand break repair protein MRE11, MRE11A), P25205 (DNA replication licensing factor, MCM3), P26358 (DNA methyltransferase 1, DNMT1), Q02880 (DNA topoisomerase-2 beta, TOP2B) and P18858 (DNA ligase 1, LIG1). In the second network, TGFbR2 interacted with O43294

(transforming growth factor beta 1-induced transcript 1 protein, TGFB1I1), P29590 (promyelocytic leukaemia protein, PML) and Q01082 (spectrin beta chain, non-erythrocytic 1, SPTBN1). Noticeably, S21 of P49840 (glycogen synthase kinase-3 alpha, GSK3A) acquired a high score at 60.254 in association with PDHK1 (pyruvate dehydrogenase kinase isoform1, PDK1). Phosphorylation of this site inhibits primary substrate binding with GSK3A thus effect its activity (248). We further mapped proteins associated with methylation (green bordered sites in Fig. 3.14) and found that they were enriched around CDK1 that highlights a regulatory component to control methylation and acetylation by the kinase after APG exposure.

We further wanted to compare the full dataset with the focused 30 min analysis performed earlier. This resulted in a larger network with 95 unique phosphosites and 46 possible upstream kinases reported in this map (Fig. 3.11). The map portrayed a larger single network that contained multiple kinases shown in the previous analysis, especially CDK1 and MAPK1 nodes that were connected with a large number of phosphosites. Both networks highlighted that CDK1 is a likely key kinase in mediation of APG exposure. Mapping of the coefficients associated to CDK1-associated phosphosites (Table Appx.D1 and D2) suggested that APG might decrease the catalytic activity of CDK1 and resulting in the observed cell cycle arrest. Interestingly, many of the CKD1 associated phosphosites are known to be involved with acetylation or methylation highlighting the importance of epigenetic alteration associated with APG exposure. In contrast, MAPK1 associated phosphosites appeared to have positive coefficient values and were mostly involved with various signalling pathway such as EGFR, ERBB2 (Her2), raptor, STAT1 and TGFB1I. Notably, while phosphosites from CK2α node in the whole data analysis were found to be involved with DNA catalytic activity, the results from 30 minutes analysis did not show a similar effect of APG at this timepoint suggesting a more dynamical interaction with APG.

3.3.5 Significant phosphosites in phosphoproteomics analysis observed by western blotting

To verify the phosphoproteomics study, phosphorylation changes on two significant phosphosites were observed through western blotting. As reported in NetworKIN network map, CDK1-associated methylation-related phosphosites were our first group of targets (Table Appx.D1 and D2). Among the phosphosites from both whole data and 30 minutes network, only phospho-STMN1-Ser25 (pSTMN1-S25) and phospho-Rb1-Thr373 (pRb1-T373) were available for purchase. Heatmaps of pSTMN1-S25 and pRb1-T373 from phosphoproteomics study illustrated the increase of phosphorylation at 30 minutes and subsequently decreasing along the time course (Fig. 3.12). Western blots were performed with three biological replicates and detection of the protein, the specific phosphosite, and GAPDH were performed on the same membrane. The expression level of the pSTMN1 (Fig. 3.13B) shows that phosphorylation on this site was increased within the first 30 minutes and decreased afterwards similar to what has been observed in the phosphoproteomics. The expression level of pRb1-T373 (Fig. 3.14B) also indicated an early upregulation after treatment, decreasing at 60 and 90 minutes and then returning close to the level of control.

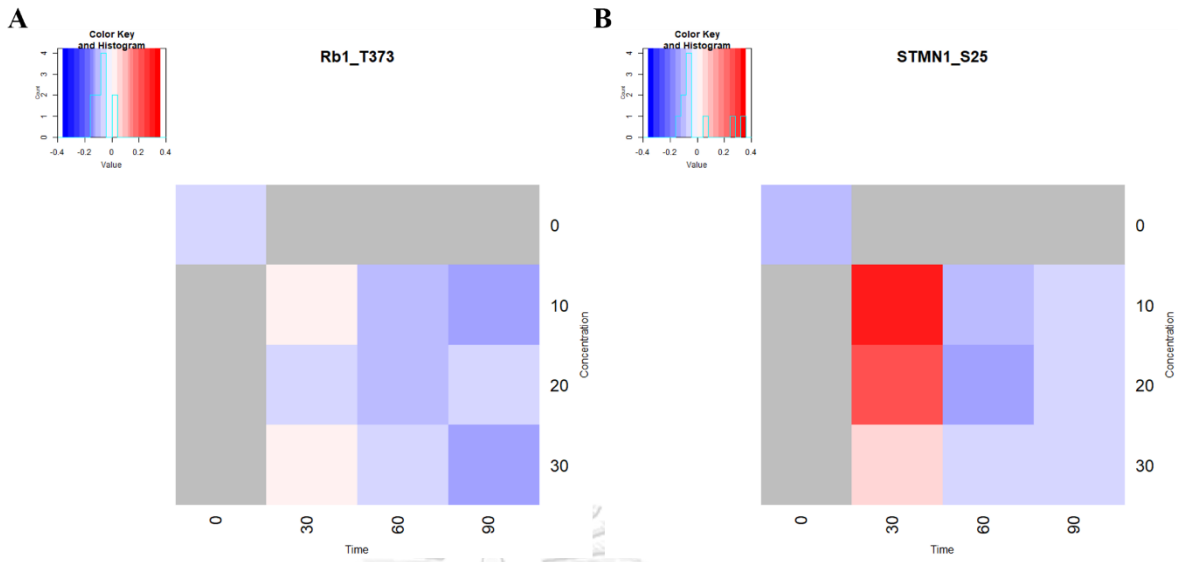

Figure 3.12 Heatmap of phospho-Rb1-T373 and phospho-STMN1-S25 from phosphoproteomics analysis.

X-axis indicated time while Y-axis indicated inhibition concentration used in the experiment. The phosphorylation changes were indicated in spectrum from hypophosphorylation in blue to hyperphosphorylation in red.

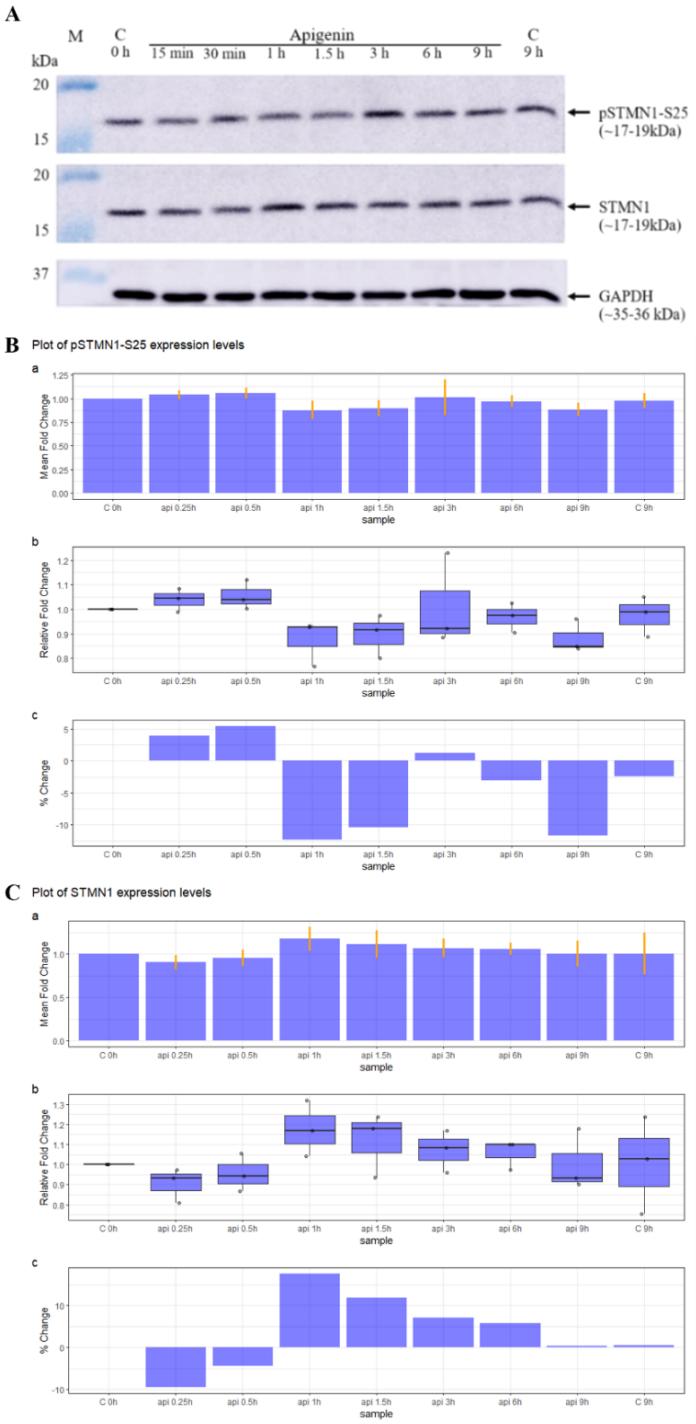

Figure 3.13 APG effect on phosphorylation of serine 25 on STMN1 protein.

(A) The membrane was probed with primary antibodies in this order, anti-pSTMN1-S25 antibody (upper) then, after stripping, anti-STMN1 (middle) and anti-GAPDH (lower) antibodies. The signals were detected by chemiluminescence assay. Expression level of (B) pSTMN1-S25 and (C) STMN1 were shown in relative fold change by bar chart (upper) and boxplots (middle) and percentage change in bar chart (lower)

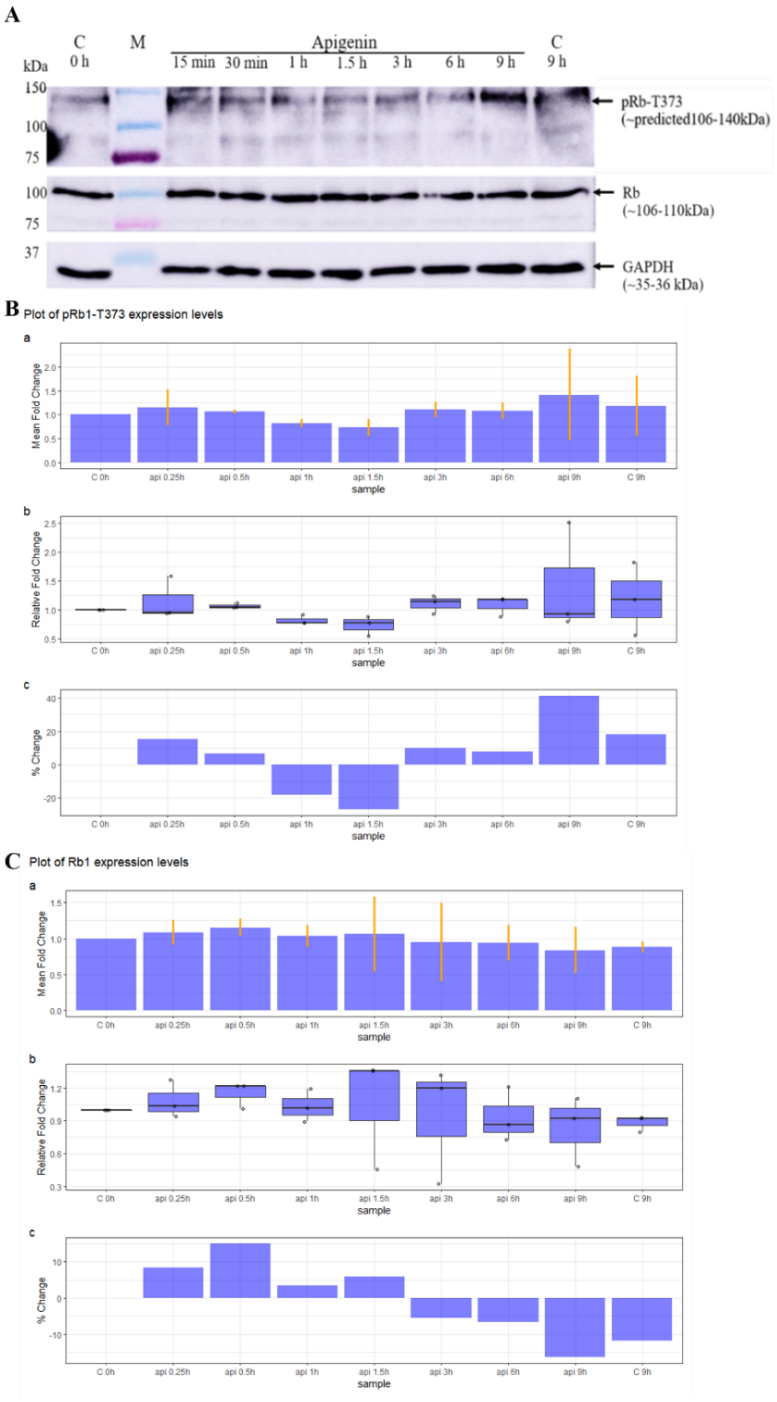

Figure 3.14 APG effect on phosphorylation of threonine 373 on Rb1 protein.

(A) The membrane was probed with primary antibodies in this order, anti-pRb11-T373 (upper) antibody then, after stripping, anti-Rb1 (middle) and anti-GAPDH (lower) antibodies. The signals were detected by chemiluminescence assay. Expression level of (B) pRb1-T373 and (C) Rb1 were shown in relative fold change by bar chart (upper) and boxplots (middle) and percentage change in bar chart (lower)

3.4 Discussion

Apigenin had been previously found to exhibit antiproliferative activity against ovarian cancer cell lines but the information regarding the mechanisms is limited. It had been reported that APG affects cell cycle arrest at G_2/M phase in the A2780 ovarian cancer cell line via reduction of gene expression of inhibitor of DNA binding 1 (ID1) which leads to an increase of gene expression of activating transcription factor 3 (ATF-3) (235). ATF-3 is a transcription factor involved in cell growth, apoptosis, and carcinogenesis. However, its function in cancer progression is highly debated in the public domain (249-251). ID1 functions in a broad range of cellular processes and is involved as an oncogene in carcinogenesis. Additionally, overexpression of ID1 is correlated with a poor cancer prognosis in patients (252). APG also reduced invasiveness and metastasis of this cell line via decreasing focal adhesion kinase (FAK) protein stability through ubiquitinating FAK resulting in proteolysis (234). For SKOV-3 ovarian adenocarcinoma, which is the cell line used in this study, APG had been shown to reduce self-renewal capacity in SKOV-3-derived sphere-forming cell and antiproliferative activity against taxol-resistant SKOV-3 by reduction of Axl and Tyro2 receptor tyrosine kinase expression on both mRNA and protein level (183, 184).

APG had been reported that its antiproliferative activity was associated with epigenetic manipulation by inhibition of DNMT, HDAC, and EZH2, which control the epigenetics on both DNA and histone modifications level (137, 253, 254). The compound was reported to interact directly with ribosomal protein S9 that resulted in the suppression of CDK1 expression by an unknown mechanism (255). Furthermore, the expression of $p21^{waf1}$ was upregulated through increasing nucleosome accessibility of the $p21^{waf}$ promoter region through inhibition of HDAC1 and HDAC3 expression and activity by APG. Overexpression of p21 could result in inhibition of CDK1-cyclin B1 complex formation and activation by binding to this complex (256). Moreover, p21 interacts with PCNA that results in blockage of

PCNA from facilitating DNA replication (141, 257). According to the analysis of the 30-min dataset, differential phosphorylated DNMT sites were found on Ser143 and Ser154. Hyperphosphorylation of DNMT1 on Ser143 and Ser154 is associated with the stability of DMNT1 and its activity, a decrease in phosphorylation especially at Ser154 resulted in a loss of catalytic activity and protein level (258, 259). In addition, phosphorylation of Ser143 was found to increase while Ser154 was decreased. This evidence suggests that APG disrupts DNMT1 stability and activity in SKOV-3 cells. Furthermore, significant histone H1b phosphosites appeared at Thr11, Ser18, and Thr138 and they were hypophosphorylated. Since histone H1b is directly involved with the maintenance of chromatin structure and hyperphosphorylated H1b markedly at the N-terminal facilitates the chromatin decondensation (260), missing phosphorylation on these sites suggests that APG condenses the chromatin structure. Altogether, our results are in line with many associated functions of APG exposure and highlight the importance of epigenetic perturbation as a result of APG exposure.

Furthermore, cell-cell adhesion-associated functions likely represent the APG-associated anti-invasiveness. APG had been reported to inhibit metastasis and invasiveness of multiple cancer cell lines by regulating the expression of adhesion molecules. In A2780 cells, APG reduces FAK stability and its signalling pathway. Moreover, Franzen *et al* reported that APG inhibited phosphorylation of FAK and Src and attenuated the motility of PC3-M human prostate cancer cells by disrupting the formation of invasion mechanism (261). Activation of FAK/Src signalling involves actin cytoskeleton remodelling and regulation of invadopodium, an extracellular matrix invasion process driven by actin polymerization, associated with tumour invasion (262). A component of invadopodium structure is cortactin (CTTN), which stabilizes the actin filament branch in lamellipodia, a part of cell-matrix protrusion structures, through recruitment of Arp2/3 complexes (263). According to the PC3-M cell study, cortactin appears to be suppressed on the protein level but the downregulation mechanism had not been

characterised further. In our study, significant hyperphosphorylation was found on CTTN, possibly, regulated by MAPK1 (ERK2) and 3 (ERK1) at Ser405 (Fig. 3.11). Phosphorylation on this site facilitates the binding of E3 ubiquitin ligase and thus resulting in degradation of CTTN via the proteasome (264). Additionally, APG was reported to downregulate the expression of NEDD9, a scaffold protein involved in the formation and recruitment of components in invadopodia complexes (265). These results highlight that APG not only expresses antiproliferative activity, but also anti-tumour invasion and metastasis ability confirmed by the results obtained in this study.

NetworKIN analysis on full and 30 minutes dataset had identified a set of kinases, which likely interacted with the significant phosphosites. Interestingly, both network maps illustrated that CDK1 was a main kinase that was influenced by APG in SKOV-3 cells. CDK1 had been reported to be upregulated in ovarian cancer cells compared to normal cells (266). The disruption of CDK1 activity and expression resulted in apoptosis and cell cycle arrest at G_2/M phase. APG inhibits the activation and expression of cyclin B and Cdc25c, both working consequently as a regulator of CDK1 (147, 267). This could explain how APG exhibits more antiproliferative activity against CDK1-overexpressing cancer cells than normal cells. Moreover, CDK1 associates with multiple proteins involved with methylation, acetylation, and demethylation, and these CDK1-phosphorylated proteins were found to be increased after APG treatment. MAPK1 also showed an enhanced interaction with phosphosites observed in our study, which reflected the rapidness of phosphoproteins alteration occurred by APG treatment. This was further confirmed through the GSEA results that at 30 minutes where various signalling pathways governed by receptor tyrosine kinase (RTKs) pathway were increased in their activity.

A broader analysis of APG treatment within the literature highlighted the association with DNA damage responses in cooperation with alteration of genes involved with cell cycle progression thereby halting cell progression followed by apoptosis in various cell lines. The

different outcomes of arrest phases are possibly related to cell lineage, genotype and phenotype including mutations of each cell line, and environmental cues. APG can activate the DNA damage response pathway, which acts as a checkpoint in cell progression throughout interphase, resulting in either cell cycle arrest at G_1 or G_2/M phase. In G_1/S checkpoint, APG has been reported to activate Ataxia-telangiectasia mutated (ATM) through phosphorylation by protein kinase C-delta (PKCδ) (268). Activation of ATM signalling cascade then causes activation of CHK2 by phosphorylation of Thr68 and results in degradation of Cdc25A by phosphorylation at Ser123 (269) and activation of p53 by phosphorylation at Ser15. This activates the expression of p21, a cyclin-dependent kinase inhibitor (270). Both events halt cell progression through the S phase by inhibiting the assembly, nuclear import, and activity of CDK4-cyclin D and CDK2-cyclin E complexes allowing the DNA repair process to take place. DNA damage irreparable cells are led to apoptosis (271). An increase in phospho-p53-Ser15 was found in G_1 arrest prostate cancer cell lines after treatment with APG (134). DNA damage checkpoint in G_2 phase also occurs by ATR/ATM signalling cascade. After CHK1 and CHK2 are activated by ATR/ATM, they deactivate Cdc25A and Cdc25C phosphatase via phosphorylation at Ser216 preventing them to activate CDK1 by dephosphorylation of Thr14/Tyr15 usually regulated by Wee1 and Myt1 (272, 273). The cells are stalled to enter the mitotic phase by CDK1-cyclin B complex for DNA repair mechanisms. Moreover, APG was found to downregulate DNA repair genes and inhibit topoisomerase activity (274, 275). According to our findings, phospho-CDK1-T14/Y15 (Fig. Appx.E1 and 2) are hyperphosphorylated at different timepoints and phosphorylation at T14 sites are associated with the hyperphosphorylated status of Cdc25C at S216 (Fig. Appx.E7). Our dataset did not contain the remaining phosphosites associated with this pathway such as CHK1-Ser317/345, CHK2-T68, Cdc25A-Ser123/T506 and Wee1-S549. However we can show that ERK1/2 is activated through hyperphosphorylation of Thr202/Tyr204 on ERK1 and Thr185/Tyr187 on ERK2 at 30 minutes (Fig. Appx.E3-6)

which is an important DNA damage response activation (276). ERK1/2 is not only involved in regulating the cell cycle but also regulates cell proliferation, survival, and death (277). Therefore, more evidence and proteins related to this pathway are needed for clarification. Furthermore, p21 is upregulated by a p53-independent mechanism after APG treatment (137). Zhang *et al* reported that in KYSE-510 cells, which is an inactivated p53 mutant, APG triggers an increase in expression of p63 and p73 that contain a similar DNA binding region (>60% amino acid identity). These could possibly activate the p21 promoter (278). Pandey *et al* found that APG inhibits HDAC1 and HDAC3 expression and activity resulting in an increase of acetylated-histone H3 that appeared to interact with the p21 promoter (137). There are also other regulators of p53-independent p21 expression, which are associated with antiproliferative activity, cell cycle arrest, and apoptosis induction of p21, for example, TGF-β, EGF, c-Myc, and others (279). From the findings above, due to APG treatment causing alteration in the regulation of gene expression through changes in epigenetics and histone modifications, it is interesting how this affects the modulation of transcription in cells. There are accessible public domain gene expression datasets related to APG treatment that can be explored and analysed for upstream regulation and biological functions. This analysis would possibly extend the knowledge from the cellular signalling network to biological activity after APG exposure. Furthermore, analysis of changes in kinase activity describes the activation and inhibition of target kinases and signalling cascades that influence by the treatment. This analysis can be done through the calculation of phosphoproteomics data using available tools like KSEA, KEA2, and IKAP. The kinase activity and gene expression analysis results will be valuable information for interpreting the link between the upstream regulator of signalling pathways through possible biological effects from these changes after APG treatment.

CHAPTER 4
KINASE ACTIVITY AND LITERATURE ANALYSES

4.1 Introduction

From previous analyses, the predominant activities of APG associated with phosphorylation alteration observed at an early stage of exposure were related to enhancing the activation of MAPK signalling while suppressing the regulation of epigenetics, histone modifications, and chromatin organisation. There are a few experiments that need to be done to validate the analyses and findings following the western blot studies however the lab access restriction due to the pandemic situation has prevented this to happen. Therefore, we opted to perform further computational analyses to clarify further detail of the effect of apigenin on cancer cell lines. In this part, Kinase Set Enrichment Analysis (KSEA) and analyses of public domain transcriptomics data of apigenin treatment in cancer cell lines will be further used to extend the knowledge.

Understanding of signalling cascades has been a central establishment of treatment in several diseases, especially anti-cancer mechanisms. Phosphoproteomics allows for high-throughput quantification of differentially expressed phosphoproteins in a single experiment (280). The changes of phosphorylation on sites are governed by kinases or phosphatases whose effects can be traced to establish the downstream pathway of each kinase using the obtained phosphoproteomics data (281). However, several kinases can regulate a single phosphorylation site, which makes the interpretation of its effect challenging. Several computational tools have been developed to better understand this complexity (165, 282, 283). One such tool, KSEA, is used to study the activation and inhibition of the global kinase pathway through the quantification of kinase-substrate activities (164). KSEA utilises kinase-substrate databases, like PhosphositePlus (284), Phospho.ELM (160), PhosphoPOINT (285), and NetworKIN (161), to calculate relative kinase scores from the phosphoproteomics dataset based on kinase's substrate sets. The method itself is closely related to GSEA but employs a

different statistical computation. The scores represent the activation or inhibition of the given kinase, which could further be used for pathway annotation inference to describe biological events after treatment with APG in this cell line.

APG alters the regulation of epigenetics and histone modifications that should result in changes in gene expression patterns. Because the effect from our experiment was observed at an early timepoint, the consequences of phosphoproteins alteration might become visible in later hours. Exploring the transcriptomics data related to APG treatment in cancer cells might help to link the influence of APG on phosphorylation regulation and gene expression shift. So far only breast cancer cell line based transcriptomics datasets are available in the public domain. These studied cell lines MCF-7, MDA-MB-231, and MDA-MB-468 breast adenocarcinoma cell lines, where the two latter cell lines are triple-negative breast cancer cells associated with high mortality rate and poor prognosis due to lack in response of oestrogen, progesterone, and ERBB2/Her2 targeting treatment (286). Interestingly, treatment with APG in all of the cell lines had been reported to cause cell cycle arrest at G_2/M phase similar to the SKOV-3 cell line (139, 141, 287) thus there might be similarity in the regulation of gene expression pattern and central signalling pathway regarding cell growth, proliferation, and division that led to this outcome. From the differential analysis of phosphoproteomics data, phosphorylation sites on transcription factors (TFs) appeared either significantly phosphorylated or dephosphorylated especially at 30 minutes, which could result in activation or inactivation of these TFs causing alteration on the target gene expressions.

We therefore aim to investigate the effect of APG on kinase activities and their biological function and to validate the phosphoproteomics analysis by linking the activation or inactivation of TFs via phosphosites alteration to gene expression profiles of associated TFs in public domain datasets.

4.2 Materials and methods

4.2.1 KSEA

To perform KSEA, the dataset is reorganised for matching the analysis requirements. The batch-corrected and loess-transformed phosphoproteomics data from the previous analysis were extracted and calculated for inverse logarithmic value. These values together with protein ID, the amino acid of the phosphosite, and position within proteins were used for analysis with the 'KSEAapp' package (version 0.99.0) in R. The KSEA was performed by KSEA.Scores() that predicts kinase-substrate associations through analysis of each input dataset with the publicly available database (KSData) including PhosphoSitePlus (284) and NetworKIN database (243) with the cut-off setting at the score equal to or higher than 2. The results were summarised into a table by filtering any row containing Benjamini-Hochberg adjusted p-value ≤ 0.05. A heatmap containing only significant kinases with a minimum substrate of 3 using KSEA.Heatmap() function is then generated. In order to understand how these significant kinases are associated with biological function, they were used as input to STRING for enrichment analysis. The significant terms were captured at strength ≥ 2 with FDR ≤ 0.05.

4.2.2 Literature review summarising

A total of 76 publications reported the effects of apigenin on cancer cells illustrating cell cycle arrest. These publications were categorised based on the arrest phase of the cell cycle in the G_1 and G_2/M checkpoints. From these, changes of proteins, phosphoproteins, and enzymatic activity together with the cell line name and organ origin were recorded and used to generate tables of cell and associated changes of expression and activity. To simplify the analysis, these changes were reduced to increase, decrease, and no meaningful change though not considering the degree of changes and other involved factors for example concentration, time, and detection methods. The tables were used as input to the heatmap.2() function from 'gplots' package to generate a clustered representation of the results. Rows and columns with more than 90% missing data were removed.

4.2.3 Analysis of public domain transcriptomics data

Transcriptomics datasets related to APG treatment were obtained from Gene Expression Omnibus (GEO). Three APG exposure datasets were obtained representing breast adenocarcinoma cell lines MCF-7 – GSE119552 (288), MDA-MB-231 – GSE120550 (289), and MDA-MB-468 – GSE133968 (290). The datasets were obtained using R through the GEOquery. The data were $\log_2$-transformed and quantile-normalised then assessed by boxplots and PCA. Next, differential expression analyses were executed through comparison of apigenin treatment versus control using fit linear model followed by empirical Bayes statistics for differential expression within the 'limma' package. P-values were adjusted with Benjamini-Hochberg. Functional enrichment analyses were performed using two approaches DAVID and GSEA. For DAVID, the significances were filtered by $\log_2$ fold change less than -1 or more than 1 and FDR at cut-off 0.05 and separated into upregulated and downregulated sets. DAVID annotation clusters that contained enrichment scores > 1.8 were considered to be significant. For GSEA, t-statistics were extracted and used as input to GSEA for the Pre-ranked gene list analysis. In the case of redundant genes in the differential expression results, mean values of t-statistics were computed and used as an input value for GSEA. The tests were performed on the KEGG and Gene Ontology databases with the numbers of permutations set to 10000. The terms with FDR < 0.05 were considered statistically significant. The results were visualised by 'ggplot2' package.

4.2.4 Transcription factors and public domain gene expression analysis

Possible transcription regulators were identified from the significant phosphosite list using the list of human transcription factors from Lambert *et al* (291). Then, available DNA binding domain motifs of the identified TFs were captured as .meme files from JASPAR^{2020} database (292) that were computed in Find Individual Motif Occurrences (FIMO) (293) of the MEME suite (294) for possible motif-matched locations on human genome. The locations were used for identifying the downstream genes of given location by mapping to TxDb

objects from UCSC build hg19 genome database of 'Homo.sapiens' package. The heatmaps displaying the expression profile of plausible target genes of the TFs were generated according to the given sets of the previously identified targets. Overlapping analysis was performed by upset() function from 'UpSetR' package. Finally, the target genes were classified into upregulated and downregulated sets and were computed for over-representing analysis by DAVID functional annotation analysis in similar approach to previous analysis. Furthermore, the significant TF targets from CHIP-Seq or curated datasets from literature (295-299) or ENCODE Portal database (300) have been analysed.

4.3 Results

4.3.1 APG inhibits CDKs activities and enhances kinases in MAPK signalling pathway and pyruvate dehydrogenase kinase (PDK) activities

KSEA analysis on our phosphoproteomics data identified 22 kinases that can be categorised into three groups of kinase activity changes (Fig. 4.1). The first group are kinases that were enhanced at 30 minutes and reduced in activity afterwards including MAPK8, MAPK9, PRKD1, VRK1, CDK3, and RPS6KB1. The second group of kinases were increased at 30 minutes and then returned to the time 0 activity including PDK1, PDK2, PDPK1, ERBB2, PRKCA, PRKCB, MAPK14, MAP2K1, MAP2K2, and RET. The last group of kinases was inhibited at 30 minutes then either activated or continued to have less activity later comprising CDK1, CDK2, CDK4, PLK1, STK38, and LATS1.

This suggested that APG had a significant effect on kinase activity at 30 minutes. Except for CDK3, it is obvious that CDK1, CDK2, and CDK4, which are the main cell cycle regulators across the interphase, were associated with the suppression of cell progression by APG. Enrichment analysis found 20 GO Biological process terms including regulation of Golgi inheritance, mitotic nuclear envelope disassembly, Golgi disassembly, negative regulation of pyruvate dehydrogenase activity, regulation of biosynthetic process from pyruvate, positive regulation of deacetylase activity, positive regulation of production of

miRNAs involved in gene silencing by mRNA, histone phosphorylation, and positive regulation of cell size as well as 10 terms from Molecular Function, i.e., histone kinase activity, cyclin-dependent protein serine/threonine kinase activity, histone threonine kinase activity, calcium-dependent protein kinase C activity, MAPK kinase activity, MAP kinase activity, histone kinase activity (H3-T6 specific), JUN kinase activity, pyruvate dehydrogenase (acetyl-transferring) kinase activity, MAP-kinase scaffold activity; and only one from Cellular Component, i.e., mitochondrial pyruvate dehydrogenase complex (Fig. 4.2). The regulation of epigenetics and histone modifications is also highlighted here. CDK1 and CDK2, which were suppressed, were governed by two terms (histone phosphorylation and kinase activity) from the total of six terms associated with the modifications. Interestingly, four energy metabolism-related terms were identified mainly targeting pyruvate dehydrogenase activity in this analysis through PDK1 and PDK2.

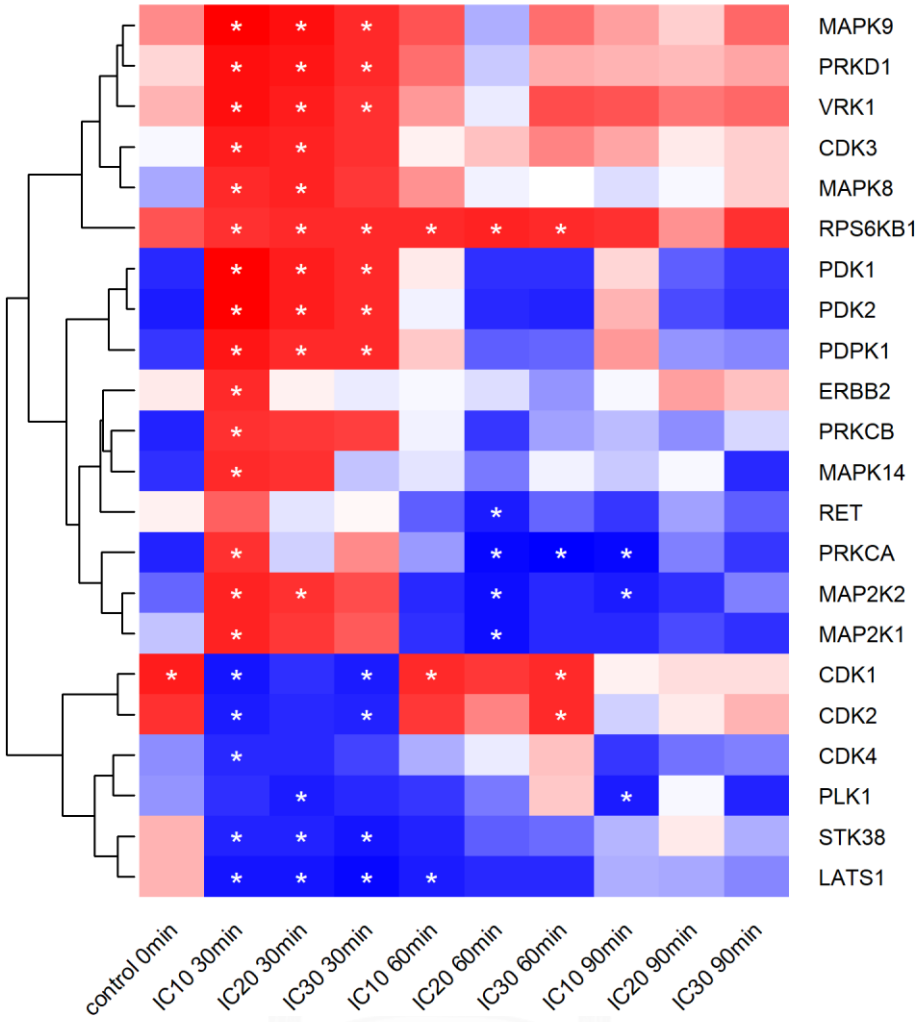

Figure 4.1 Heatmap of Kinase set enrichment analysis.

Red and blue represented increasing and decreasing in kinase activity, respectively. * indicated the significant change (FDR < 0.05) in kinase activity.

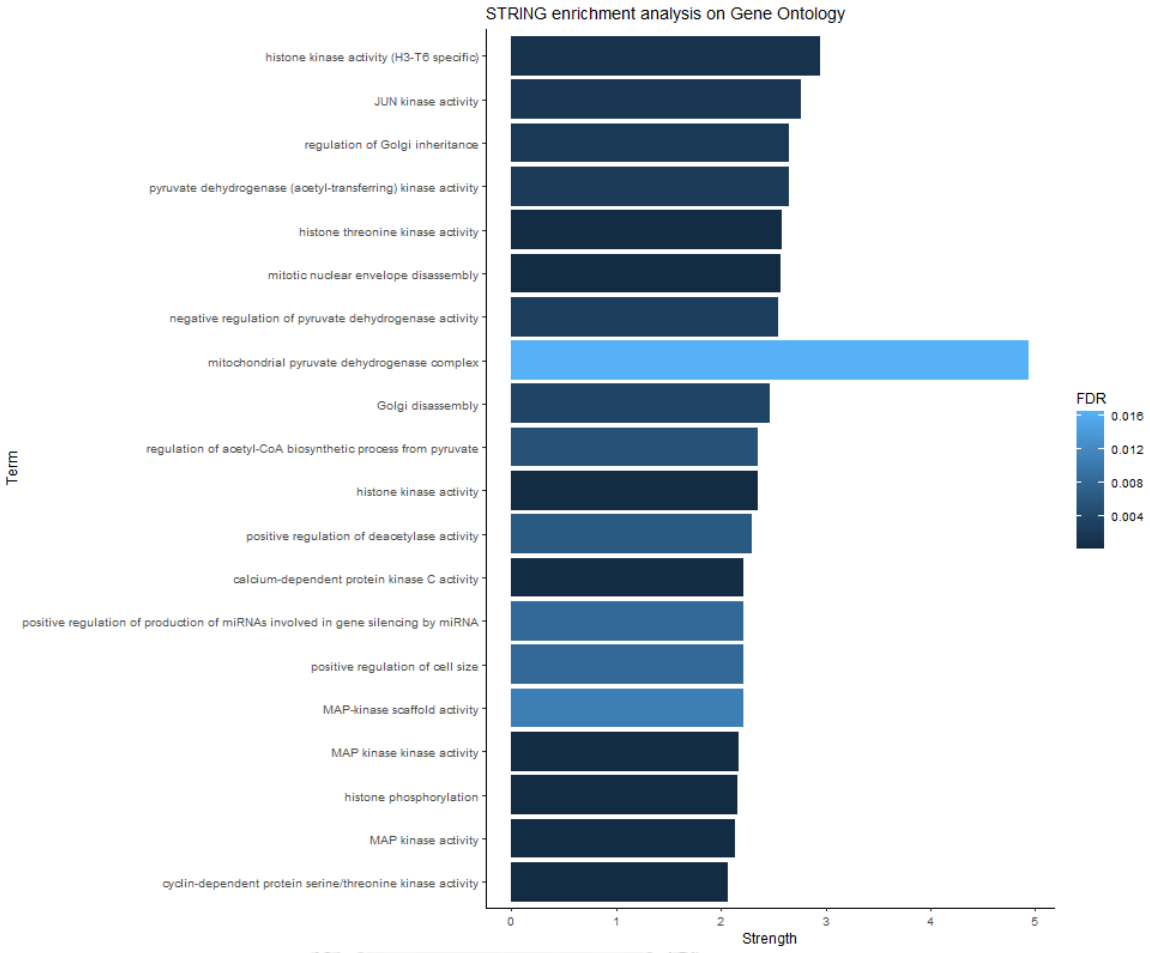

Figure 4.2 Barplot of significant terms from Gene ontology database with STRING analysis. The significant terms are filtered at FDR ≤ 0.05 and strength ≥ 2.0

4.3.2 Literature analysis

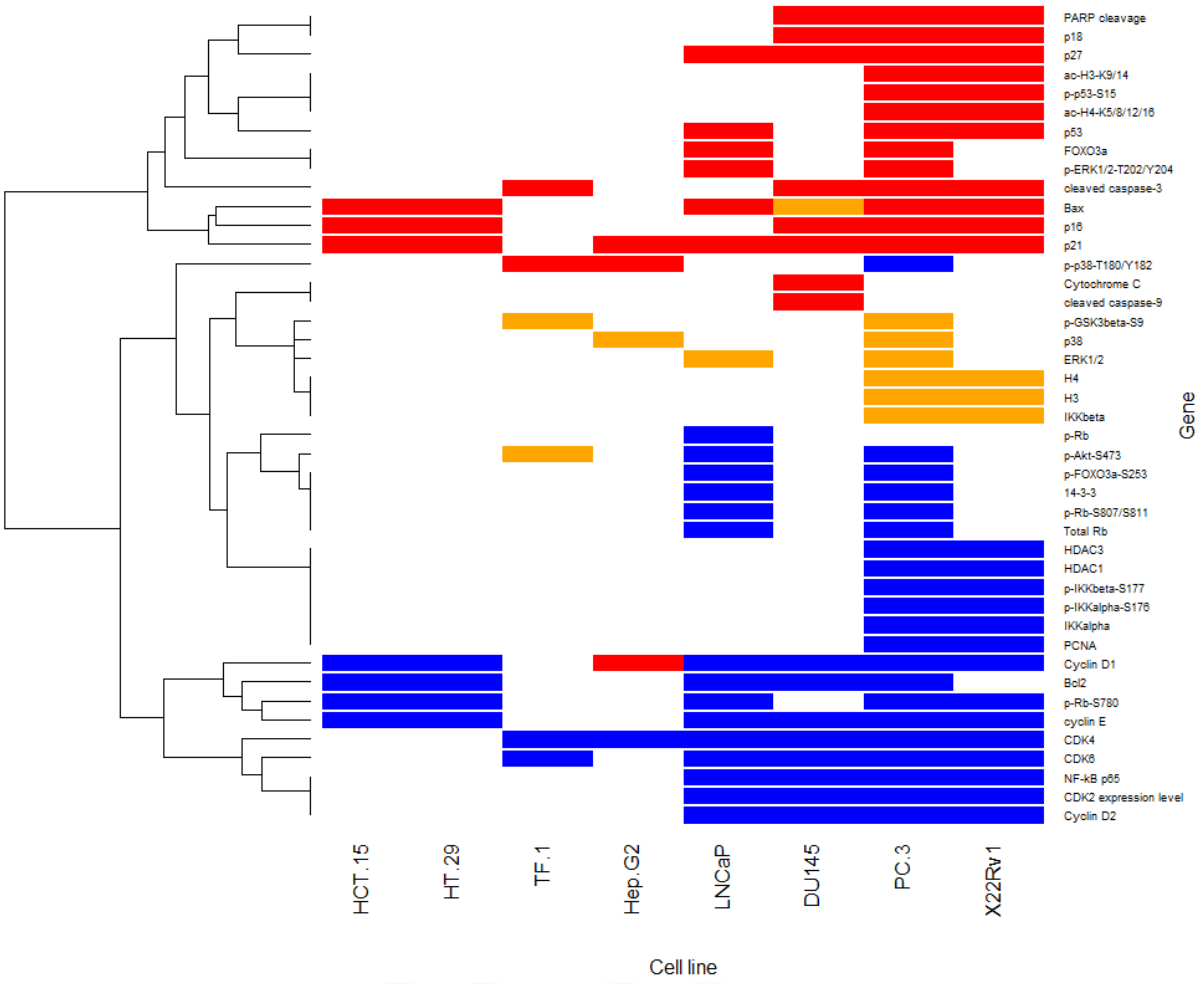

Figure 4.3 Heatmap of cluster result of protein and activities associated with cell lines that are arrested at G_1 phase when treated with APG.

X-axis indicated cell lines while Y-axis indicated proteins or activities. Colour illustrated status as follows, increase in red, decrease in blue, and unchanged in orange.

To better understand the known interactions between APG and its antiproliferative effects, including the various genes and protein complexes that have been studied, a compilation of 76 publications mentioning APG exposure was performed. From the 76 publications, the results showed 16 articles that describe APG to arrest cell cycle at G_1 phase, and 60 articles suggesting a G_2/M phase arrest. Within the reported G_1 arrests, data from 13 cell lines representing 8 origins including skin (CCD-1079Sk), prostate (LNCaP, DU145,

22Rv1, and PC-3), colon (HCT-15, HCT-116, and HT-29), liver (HepG2), tongue (SCC-25), cervix (HeLa), myeloid cell (TF1) and monocyte (THP-1) were extracted. Hierarchical clustering of the most studied genes in these publications showed that there are 43 consensus terms from a total of 88 terms (Fig. 4.3). Terms that appeared to be increased (red) were associated with cyclin-dependent kinase inhibitors (CDKi - p16, p18, p21, and p27), apoptosis indicators (Bax, PARP cleavage, cytochrome C, cleaved caspase-3 and -9), chromatin modifications (acetylated-histone H3-Lys3/14 and acetylated-histone H4-Lys5/8/12/16), DNA damage response (p53 and phospho-53-Ser15) and other components in signalling pathway (phospho-ERK1-Thr202/Tyr204 and FoxO3a). The increase in modifications of ERK1/2, histone H3, and H4 (as observed in row 9, phosphorylation in ERK1/2, and row 4&6, acetylation in histone H3 and H4, respectively) was not caused by changes in the expression level as observed in the orange cluster of the heatmap (Fig. 4.3, row 3 (ERK1/2), 4 (histone H4), and 5 (histone H3)) (135, 137). Activation of p38 MAPK that is associated with stress response was observed to increasing phospho-p38-Thr180/Tyr182 of TF1 human erythroid leukaemia and HepG2 hepatocarcinoma cell lines whilst deactivation of these sites was observed in the PC3 cell line. Importantly, APG did not alter the expression level of p38 on these cell lines (135, 140, 301). On the contrary, within the decreasing group of cell cycle components (blue) major components of cell cycle kinases during G_1 progression and transition towards S phase (CDK4/6, cyclin D1/D2, CDK2, and cyclin E), expression level and phosphorylation of Rb a key regulator of cell progression from G_1 to S phase (phospho-Rb, phospho-Rb-Ser780, and phospho-Rb-Ser807/811), DNA synthesis (PCNA), anti-apoptotic protein (Bcl2), histone deacetylase (HDAC1 and HDAC3), and signalling cascade involved with cell survival, proliferation, and tumour invasion (phospho-Akt-Ser473, phospho-FoxO3a-Ser253, 14-3-3, NF-κB p65, IKKα, phospho-IKKα-Ser176, and phospho-IKKβ-Ser177) were found. From this set of G_1 arrest-related literature, APG exhibits anti-proliferative activity by increasing chromatin accessibility by inhibiting HDAC expression

and activity, upregulating CDK inhibitors expression while downregulating cell cycle regulators and components associated with G_1 phase, triggering DNA damage response via p53-dependent pathway and induction of apoptosis. Additionally, upregulation of p27 via FoxO3a activation through deactivating Akt and suppressing of IKKα/β activation that is critical for NF-κB activation results in cell cycle arrest and reduction of tumour migration in, at least, the prostate cancer cell lines (302, 303).

Within the literature associated with G_2 arrest, 48 cell lines from 19 tissues containing breast (SK-BR-3, BT-474, MCF7, MDA-MB-231, MDA-MB-468, and Hs578T), colon (SW480, HCT-116, HT-29, and Caco-2), skin (OCM-1, 518A2, A375, and C8161), liver (HepG2 and Huh7), pancreas (AsPC-1, HPAF-II, MIA PaCa2, and S2-013), oesophagus (JROECL33 and KYSE-510), myeloid cell (HL-60, K562, and KG-1a), monocyte (U937 and THP-1), T cell (Jurkat and CCRF-CEM), B cell (NCI-H929, U2932, and OCI-LY10), brain (A172, U1242-MG, and U87-MG), tongue (SCC-25), nasopharynx (HONE1 and CNE2), bladder (T24), kidney (ACHN), thyroid gland (BCPAP), salivary gland (ACC2), embryo (NT2-D1), and lung (A549, NCI-H460, and NCI-H1299) were identified. The clustering of terms in G_2/M phase arrest group (Fig. 4.4) displayed two groups, a set of increased and decreased components (red and blue respectively). The terms associated with an increase in G_2/M arrest contained apoptotic markers (Bax, cytochrome C, PARP cleavage, cleaved caspase-3, -8, and -9) and DNA damage response pathway (γH2AX, p53, phospho-53-Ser15, and p21). Interestingly, phospho-CDK1-Tyr15, an inactivation site of CDK1, expression was decreased in the human pancreatic cancer cell line and in only this publication while other cell lines including human myeloid leukaemia and renal cancer cell lines occur to be hyperphosphorylated (140, 142, 267). Dephosphorylation of this phosphosite is linked to the activation of CDK1 activity in pancreatic cancer cell lines.

On the other hand, within the downregulated group (blue), cell cycle facilitators and components for progression from S to G_2 then to M phase (Cdc25A, Cdc25C, CDK2, CDK1,

cyclin A, and B1) together with two regulators from G_1 phase (CDK4 and cyclin D1), anti-apoptotic genes (Bcl2 and Bcl-xl), and activation of cell survival and growth signalling (p38, phospho-Akt-Ser473, phospho-STAT3-Tyr705, phospho-mTOR-Ser2448 and phospho-ERK2-Thr183/Tyr185) were characterised. Moreover, APG not only suppresses CDK1 expression level but also reduces CDK1 activity in human colon cancer cell line SW280 (304). It is therefore apparent that APG exhibits antiproliferative activity by downregulating cell progression machinery of transition from S entering to G_2 until M phase through triggering of DNA damage response, reducing cell survival and growth signalling, and increasing apoptotic activity within the G_2 group.

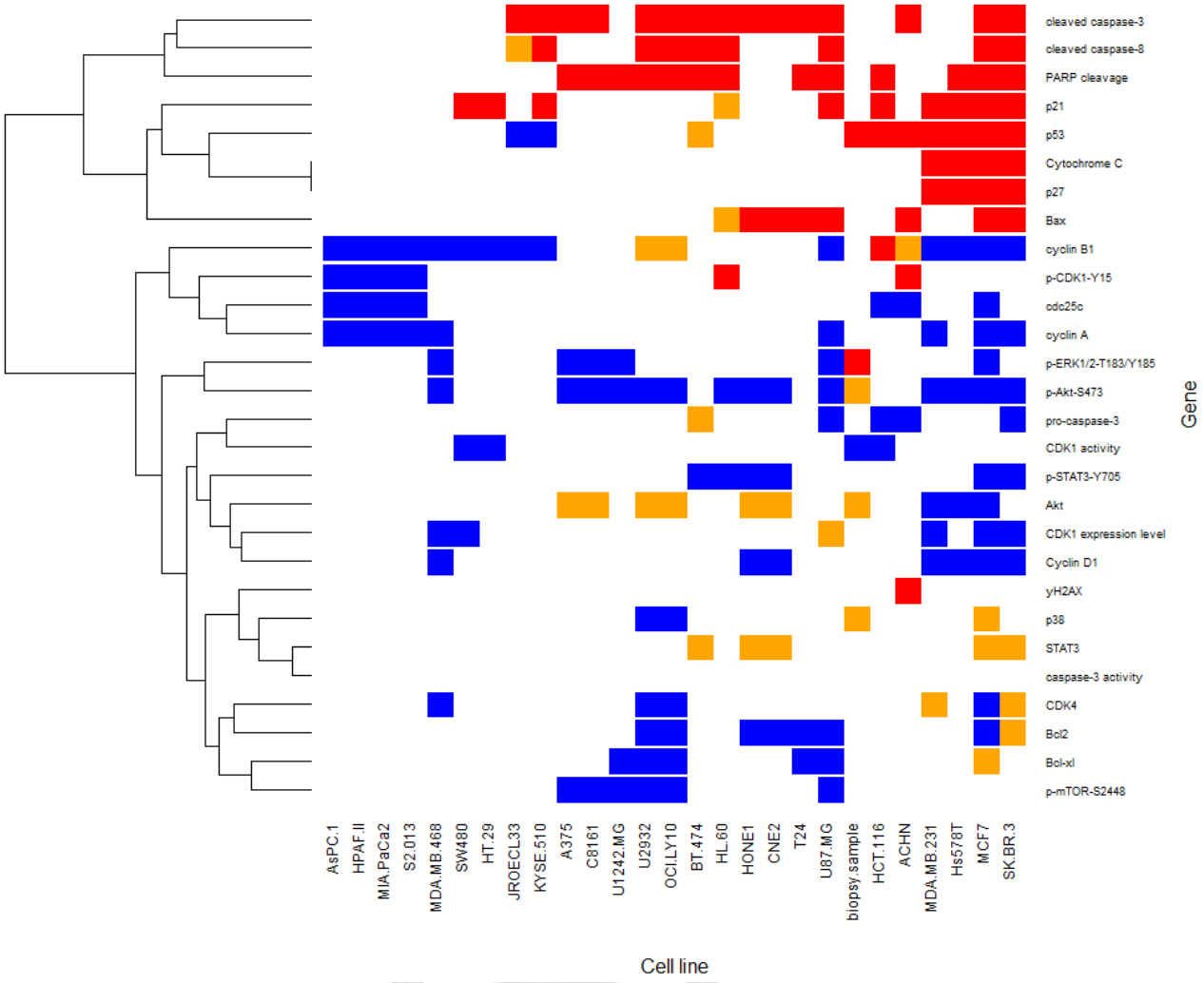

Figure 4.4 Heatmap of cluster result of protein and activities associated with cell lines that are arrested at G_2/M phase when treated with APG.

X-axis indicated cell lines while Y-axis indicated proteins or activities. Colour illustrated status as follows, increase in red, decrease in blue, and unchanged in orange.

Remarkably, p21, a member of CIP/KIP (CDK interacting protein/Kinase inhibitory protein) is reported to be upregulated consistently in both the G_1 group, 9 from 13 cell lines, and in G_2/M group, 16 from 48 cell lines. This evidence suggested p21 plays a vital role in the antiproliferative activity of APG. In addition, there are 5 cell lines that were reported for cell cycle arrest on both G_1 and G_2/M phases including HepG2, HT-29. HCT-116, SCC-25 and THP-1. It has been reported by Lepley and Pelling that, in CCD-1079Sk human skin

fibroblast cell line, treatment of unsynchronised cells results in cell arrest at G_2/M phase, while in synchronised cells by FBS starvation before treatment, cells were arrested at G_1 phase (131). This phenomenon was similarly observed in SCC-25 human oral squamous carcinoma cell line (305). Moreover, the effect from different culture medium components was reported for example, in THP-1 (myeloid leukaemia) culturing in RPMI-1640 medium supplemented with 5% FBS cells arrested at G1 phase after treatment (268) whereas supplementing the medium with 10% FBS resulted in an arrest at G_2/M phase (306), in HT-29 (colon) when cultured in RPMI-1640 medium, the cells arrested at G_1 phase (307), whilst the culture in DMEM medium led to arrest in G_2/M phase (255, 304), and in HCT-116 (colon) G_1 phase arrest was observed when cultured in McCoy's 5A medium (145), whereas culture in RPMI-1640 resulted in G_2/M cell cycle arrest (148). Moreover, APG concentration used for treatment appears to arrest HepG2 human hepatocarcinoma cell line at different phases. Although the authors claimed to use half-maximal inhibition concentration (IC_{50}) for both experiments, 20 µg/ml resulted in the arrest in G_1 phase (301), while at 8 µg/ml caused G_2/M cell arrest (308). This evidence therefore highlights the complex interactions that result from exposure to APG.

4.3.3 Public domain data analysis

To better understand the impact of APG on the underlying molecular responses we analysed cancer cell lines exposed to AGP gene expression datasets. The MDA-MB-468 dataset contained fewer APG exposed biological replicated and yielded no results. The remaining results presented here therefore focus on the MCF7 and MDA-MB-231 data. After differential analysis, a total of 1504 significant genes that consisted of 638 upregulated and 866 downregulated genes were obtained from MCF7 dataset while the MDA-MB-231 dataset yielded 420 significant genes of which 181 genes were upregulated and 239 genes were downregulated.

Enrichment analyses in the MCF7 dataset yielded one significant cluster representing upregulation of the intrinsic apoptotic pathway via p53 signalling through DNA damage (Table 4.1) and four significant clusters representing downregulated genes including carcinogenesis associated Wnt and Hippo signalling pathway, sialylation, extracellular matrix structural constituent, and cellular water homeostasis (Table 4.3). Similarly, enrichment analyses of the MDA-MB-231 dataset resulted in the identification of an upregulation of "transcription by zinc finger proteins" (Table 4.2) and downregulation of mitotic nuclear division and segregation of sister chromatids through the attachment of microtubules to the kinetochore (Table 4.4).

To use a more sensitive method, a GSEA based approach was applied. Here 131 terms were overlapping between the treatment of APG in MCF7 (total of 453 terms) and MDA-MB-231 (total of 1,112 terms) cell lines (Fig. 4.5A). The overlap terms were organised by trends into two groups, same direction and opposite direction between both cell lines focusing on only GO Biological process terms. Within the first groups (Fig. 4.5B and C), the positive terms were majorly involved with RNA processing both mRNA and non-coding RNA, regulation of translation machinery, and ribosome metabolism. Examples of these terms were DNA-templated transcription elongation and termination, 3'-mRNA processing, RNA splicing, spliceosome, the establishment of RNA localisation, mRNA export from the nucleus, ribonucleoprotein complex biogenesis, ribosome biogenesis, maturation of small-subunit rRNA, ncRNA processing, and protein folding. Whereas the negative terms were involved with protein localisation, actin polymerisation, and cell migration activity such as negative regulation of actin filament depolymerisation, protein localisation to periphery and plasma membrane, filopodium assembly, and regulation of notch signalling pathway.

Within the opposite direction group, upregulated in MCF7 but downregulated in MDA-MB-231 (Fig. 4.6A and B respectively) terms related to cell cycle activity,

chromosome organisation, and cell division were identified. This highlights how different cell lines with similar backgrounds respond with different dynamics to APG exposure.

314 upregulated terms that were not overlapping but part of the MCF7 line included terms similarly related to DNA replication, mRNA metabolism, tRNA metabolic process, telomere organisation, regulation of mitochondrial gene expression, regulation of cell cycle checkpoint, and chaperone-mediated protein folding (Fig. 4.7A). In addition, 40 downregulated terms were identified and represented autophagosome organisation, vacuole transportation, and regulation of macrophage-derived foam cell differentiation (Fig. 4.7B). Repeating this selection for the MDA-MB-231 dataset, 43 upregulated terms were found with similar terms surround mRNA catabolic process, protein translation and protein transportation (Fig. 4.8A) and terms corresponding to regulation of cell-matrix adhesion, chromosome segregation, acetyl-CoA biosynthetic process, phosphate catabolic process, vesicle transportation, and tissue remodelling were found generally from 970 downregulated terms (Fig. 4.8B).

Table 4.1 Significance clustering group from DAVID clustering chart of upregulated significant gene from MCF7 dataset

ANNOTATION CLUSTER 1					ENRICHMENT SCORE: 1.8919198194943427						
CATEGORY	Term	Count	%	PValue	Genes	List Total	Pop Hits	Pop Total	Fold Enrichment	Benjamini	FDR
GOTERM_BP_DIRECT	GO:0010332~response to gamma radiation	7	1.160862	4.17E-04	GPX1, CHEK2, MYC, XRCC2, BCL2, BRCA2, TP73	521	31	16032	6.948424	0.210997	0.210747
GOTERM_BP_DIRECT	GO:0006978~DNA damage response, signal transduction by p53 class mediator resulting in transcription of p21 class mediator	5	0.829187	0.001459	TFAP4, CHEK2, BRCA1, BRCA2, TP73	521	16	16032	9.616123	0.462191	0.461644
GOTERM_BP_DIRECT	GO:0042771~intrinsic apoptotic signaling pathway in response to DNA damage by p53 class mediator	5	0.829187	0.0172	CHEK2, PMAIP1, AEN, BRCA2, TP73	521	31	16032	4.96316	1	0.99921
GOTERM_BP_DIRECT	GO:0010165~response to X-ray	4	0.66335	0.033046	XRCC2, PMAIP1, BRCA2, TP73	521	22	16032	5.594835	1	0.99921
GOTERM_BP_DIRECT	GO:0008630~intrinsic apoptotic signaling pathway in response to DNA damage	5	0.829187	0.061263	CHEK2, BCL2, E2F1, BRCA1, TP73	521	46	16032	3.344738	1	0.99921
GOTERM_BP_DIRECT	GO:1901796~regulation of signal transduction by p53 class mediator	7	1.160862	0.209969	HDAC2, EXO1, CHEK2, CHEK1, TAF4B, BRCA1, TP73	521	123	16032	1.751229	1	0.99921

Table 4.2 Significance clustering group from DAVID clustering chart of upregulated significant gene from MDA-MB-231 dataset

ANNOTATION CLUSTER 1					ENRICHMENT SCORE: 1.9391671003403443						
CATEGORY	Term	Count	%	PValue	Genes	List Total	Pop Hits	Pop Total	Fold Enrichment	Benjamini	FDR
GOTERM_BP_DIRECT	GO:0006355~regulation of transcription, DNA-templated	18	10.97561	0.008626	ZNF121, SAP30BP, EAF1, ZBTB21, ZNF23, ZNF35, ZNF75A, TAF1D, NOCT, ZNF614, ZNF317, SNIP1, ZNF547, SRFBP1, ZNF468, ZNF432, ZNF311, ZNF596	106	1315	15177	1.959868	1	1
GOTERM_MF_DIRECT	GO:0003676~nucleic acid binding	13	7.926829	0.012989	N6AMT1, ZBED9, ZNF121, ZBTB21, ZNF23, ZNF75A, CHAMP1, ZNF614, ZNF317, ZNF547, ZNF468, ZNF432, ZNF596	105	851	15254	2.21926	0.400804	0.398539
GOTERM_MF_DIRECT	GO:0046872~metal ion binding	22	13.41463	0.013587	KLF10, EGR1, ZNF121, CDKN1A, ZBTB21, AMPD1, YOD1, ZNF23, ZNF35, ZNF75A, ZFP36, MTF1, ZC3H11A, NOCT, CHAMP1, ZNF614, ZNF317, ZNF547, ZNF468, ZNF432, ZNF311, ZNF596	105	1865	15254	1.713714	0.400804	0.398539

Table 4.3 Significance clustering group from DAVID clustering chart of downregulated significant gene from MCF7 dataset

ANNOTATION CLUSTER 1					ENRICHMENT SCORE: 2.1185317486606254						
CATEGORY	Term	Count	%	PValue	Genes	List Total	Pop Hits	Pop Total	Fold Enrichment	Benjamini	FDR
KEGG_PATHWAY	hsa05217:Basal cell carcinoma	11	1.361386	1.01E-04	TCF7L2, TCF7L1, FZD2, WNT11, WNT2B, APC, FZD4, WNT3A, PTCH1, FZD8, AXIN2	290	54	6559	4.607216	0.012289	0.011886
KEGG_PATHWAY	hsa04390:Hippo signaling pathway	17	2.10396	8.10E-04	TCF7L2, TCF7L1, FZD2, WNT2B, FZD4, TGFB3, WNT3A, ITGB2, FZD8, AXIN2, CTGF, WNT11, APC, ID2, ID1, CTNNA3, BMPR1B	290	149	6559	2.580491	0.06584	0.063681
KEGG_PATHWAY	hsa04550:Signaling pathways regulating pluripotency of stem cells	15	1.856436	0.002903	FZD2, WNT2B, FZD4, WNT3A, DLX5, FZD8, AXIN2, TBX3, WNT11, APC, ID2, ID1, ID4, ID3, BMPR1B	290	138	6559	2.458396	0.141655	0.137011
GOTERM_BP_DIRECT	GO:0030182~neuron differentiation	11	1.361386	0.006475	BRSK1, MEF2C, FZD2, WNT11, WNT2B, FZD4, WNT3A, ID1, FZD8, ID3, ITM2C	674	95	16032	2.754209	0.760083	0.758814
GOTERM_BP_DIRECT	GO:0060070~canonical Wnt signaling pathway	10	1.237624	0.007911	TCF7L2, TCF7L1, FZD2, WNT11, WNT2B, APC, FZD4, WNT3A, DIXDC1, FZD8	674	83	16032	2.865825	0.816776	0.815412
KEGG_PATHWAY	hsa04916:Melanogenesis	11	1.361386	0.012259	TCF7L2, TCF7L1, FZD2, WNT11, WNT2B, FZD4, WNT3A, ADCY4, GNAS, FZD8, ADCY5	290	100	6559	2.487897	0.243907	0.23591
KEGG_PATHWAY	hsa04310:Wnt signaling pathway	13	1.608911	0.017303	TCF7L2, TCF7L1, FZD2, WNT2B, FZD4, WNT3A, FZD8, PRICKLE1, AXIN2, CXXC4, MAPK10, WNT11, APC	290	137	6559	2.146162	0.278408	0.26928
KEGG_PATHWAY	hsa05166:HTLV-I infection	16	1.980198	0.148809	CDKN2B, FZD2, WNT2B, FZD4, IL1R1, TGFB3, WNT3A, ITGB2, ADCY4, FZD8, ADCY5, KAT2B, WNT11, APC, TP53INP1, HLA-DPB1	290	253	6559	1.430339	0.963391	0.931804
GOTERM_BP_DIRECT	GO:0007223~Wnt signaling pathway, calcium modulating pathway	4	0.49505	0.224059	TCF7L2, FZD2, WNT11, FZD4	674	39	16032	2.439626	1	0.998664
ANNOTATION CLUSTER 2					ENRICHMENT SCORE: 2.0425019472548724						
CATEGORY	Term	Count	%	PValue	Genes	List Total	Pop Hits	Pop Total	Fold Enrichment	Benjamini	FDR
GOTERM_BP_DIRECT	GO:0097503~sialylation	7	0.866337	1.25E-04	ST6GAL1, ST6GALNAC1, ST3GAL4, ST8SIA4, ST3GAL5, ST3GAL1, ST6GALNAC5	674	20	16032	8.325223	0.124908	0.1247
GOTERM_BP_DIRECT	GO:0009311~oligosaccharide metabolic process	7	0.866337	4.78E-04	ST6GAL1, ST6GALNAC1, ST3GAL4, ST8SIA4, ST3GAL5, ST3GAL1, ST6GALNAC5	674	25	16032	6.660178	0.238501	0.238103
GOTERM_BP_DIRECT	GO:0001574~ganglioside biosynthetic process	6	0.742574	6.97E-04	ST6GALNAC1, ST3GAL4, ST8SIA4, ST3GAL5, ST3GAL1, ST6GALNAC5	674	18	16032	7.928783	0.255687	0.25526
GOTERM_MF_DIRECT	GO:0008373~sialyltransferase activity	6	0.742574	9.20E-04	ST6GAL1, ST6GALNAC1, ST3GAL4, ST3GAL5, ST3GAL1, ST6GALNAC5	678	19	16104	7.500699	0.79121	0.79121
GOTERM_BP_DIRECT	GO:0006486~protein glycosylation	11	1.361386	0.017249	ST6GAL1, ST6GALNAC1, FUT9, OAS2, B3GNT5, B3GALT4, ST3GAL4, ST8SIA4, ST3GAL5, ST3GAL1, ST6GALNAC5	674	110	16032	2.378635	1	0.998664
GOTERM_BP_DIRECT	GO:0018279~protein N-linked glycosylation via asparagine	6	0.742574	0.025102	ST6GAL1, ST6GALNAC1, ST3GAL4, ST3GAL5, ST3GAL1, ST6GALNAC5	674	40	16032	3.567953	1	0.998664
KEGG_PATHWAY	hsa00604:Glycosphingolipid biosynthesis - ganglio series	4	0.49505	0.02598	B3GALT4, ST3GAL5, ST3GAL1, ST6GALNAC5	290	15	6559	6.031264	0.352168	0.340622
GOTERM_CC_DIRECT	GO:0030173~integral component of Golgi membrane	7	0.866337	0.030331	CSGALNACT1, ST6GAL1, ST3GAL4, ST8SIA4, ST3GAL5, ST3GAL1, STEAP2	732	56	17280	2.95082	0.615728	0.605112
GOTERM_MF_DIRECT	GO:0003836~beta-galactoside (CMP) alpha-2,3-sialyltransferase activity	3	0.371287	0.032197	ST3GAL4, ST3GAL5, ST3GAL1	678	7	16104	10.17952	1	1
GOTERM_BP_DIRECT	GO:0016266~O-glycan processing	5	0.618812	0.21674	ST6GAL1, MUC1, B3GNT5, ST3GAL4, ST3GAL1	674	57	16032	2.086522	1	0.998664
GOTERM_CC_DIRECT	GO:0032580~Golgi cisterna membrane	5	0.618812	0.372925	CSGALNACT1, ST6GAL1, FUT9, ST3GAL4, ST3GAL1	732	73	17280	1.616887	1	0.985185

Table 4.3 Significance clustering group from DAVID clustering chart of downregulated significant gene from MCF7 dataset (cont.)

ANNOTATION CLUSTER 3					ENRICHMENT SCORE: 1.8124573042547245						
CATEGORY	Term	Count	%	PValue	Genes	List Total	Pop Hits	Pop Total	Fold Enrichment	Benjamini	FDR
KEGG_PATHWAY	hsa04512:ECM-receptor interaction	12	1.485149	0.001416	COL2A1, SV2B, COL24A1, LAMB2, ITGB4, COL4A4, COL11A2, COL4A5, ITGB7, CD36, ITGB6, THBS3	290	87	6559	3.11962	0.086401	0.083569
KEGG_PATHWAY	hsa05146:Amoebiasis	11	1.361386	0.017925	COL2A1, NOS2, COL24A1, IL1R1, TGFB3, LAMB2, COL4A4, COL11A2, ITGB2, GNAS, COL4A5	290	106	6559	2.347072	0.278408	0.26928
GOTERM_MF_DIRECT	GO:0005201~extracellular matrix structural constituent	6	0.742574	0.143874	FBN2, COL2A1, COL24A1, COL4A4, COL11A2, COL4A5	678	66	16104	2.159292	1	1
ANNOTATION CLUSTER 4					ENRICHMENT SCORE: 1.8096803689649						
CATEGORY	Term	Count	%	PValue	Genes	List Total	Pop Hits	Pop Total	Fold Enrichment	Benjamini	FDR
GOTERM_BP_DIRECT	GO:0042476~odontogenesis	6	0.742574	0.004808	TGFB3, AQP6, ID3, AXIN2, AQP3, AQP1	674	27	16032	5.285856	0.719693	0.718491
GOTERM_MF_DIRECT	GO:0015254~glycerol channel activity	4	0.49505	0.012245	AQP6, AQP3, AQP1, AQP7P3	678	12	16104	7.917404	1	1
GOTERM_BP_DIRECT	GO:0009992~cellular water homeostasis	4	0.49505	0.015368	AQP6, AQP3, AQP1, AQP7P3	674	13	16032	7.318877	1	0.998664
GOTERM_BP_DIRECT	GO:0015793~glycerol transport	4	0.49505	0.015368	AQP6, AQP3, AQP1, AQP7P3	674	13	16032	7.318877	1	0.998664
GOTERM_MF_DIRECT	GO:0015250~water channel activity	4	0.49505	0.023062	AQP6, AQP3, AQP1, AQP7P3	678	15	16104	6.333923	1	1
GOTERM_BP_DIRECT	GO:0006833~water transport	4	0.49505	0.043242	AQP6, AQP3, AQP1, AQP7P3	674	19	16032	5.007653	1	0.998664

Table 4.4 Significance clustering group from DAVID clustering chart of downregulated significant gene from MDA-MB-231 dataset

ANNOTATION CLUSTER 1					ENRICHMENT SCORE: 4.756633090853542						
CATEGORY	Term	Count	%	PValue	Genes	List Total	Pop Hits	Pop Total	Fold Enrichment	Benjamini	FDR
GOTERM_BP_DIRECT	GO:0007062~sister chromatid cohesion	10	5.154639	1.91E-06	CENPE, KIF18A, CENPI, ZWILCH, KNTC1, KIF2C, BUB1, NDC80, SPC24, SPC25	176	98	15177	8.799281	0.002232	0.002232
GOTERM_CC_DIRECT	GO:0000777~condensed chromosome kinetochore	9	4.639175	3.79E-06	DCTN5, CENPE, ZWILCH, KNTC1, KIF2C, BUB1, NDC80, SPC24, SPC25	185	82	16400	9.72973	8.86E-04	8.74E-04
GOTERM_BP_DIRECT	GO:0051301~cell division	15	7.731959	3.12E-05	BORA, ZWILCH, KIF14, CABLES1, CDC25C, NDC80, CENPE, CCNB2, PARD6B, CNTRL, KNTC1, KIF2C, BUB1, SPC24, SPC25	176	332	15177	3.896067	0.018175	0.018175
GOTERM_BP_DIRECT	GO:0007067~mitotic nuclear division	11	5.670103	4.16E-04	ASPM, CCNB2, BORA, ZWILCH, KNTC1, KIF2C, CDC25C, BUB1, NDC80, SPC24, SPC25	176	236	15177	4.019333	0.161873	0.161873
ANNOTATION CLUSTER 2					ENRICHMENT SCORE: 2.509412377675893						
CATEGORY	Term	Count	%	PValue	Genes	List Total	Pop Hits	Pop Total	Fold Enrichment	Benjamini	FDR
GOTERM_CC_DIRECT	GO:0000776~kinetochore	8	4.123711	2.93E-05	KAT2B, CENPE, KIF18A, CENPI, ZWILCH, KIF2C, BUB1, NDC80	185	79	16400	8.977078	0.003427	0.003383
GOTERM_BP_DIRECT	GO:0051315~attachment of mitotic spindle microtubules to kinetochore	3	1.546392	0.003536	CENPE, KIF2C, NDC80	176	8	15177	32.33736	0.612357	0.612357
GOTERM_BP_DIRECT	GO:0051310~metaphase plate congression	3	1.546392	0.00679	CENPE, KIF2C, NDC80	176	11	15177	23.51808	0.686366	0.686366
GOTERM_CC_DIRECT	GO:0000775~chromosome, centromeric region	3	1.546392	0.130372	CENPE, KIF2C, NDC80	185	56	16400	4.749035	1	0.991416

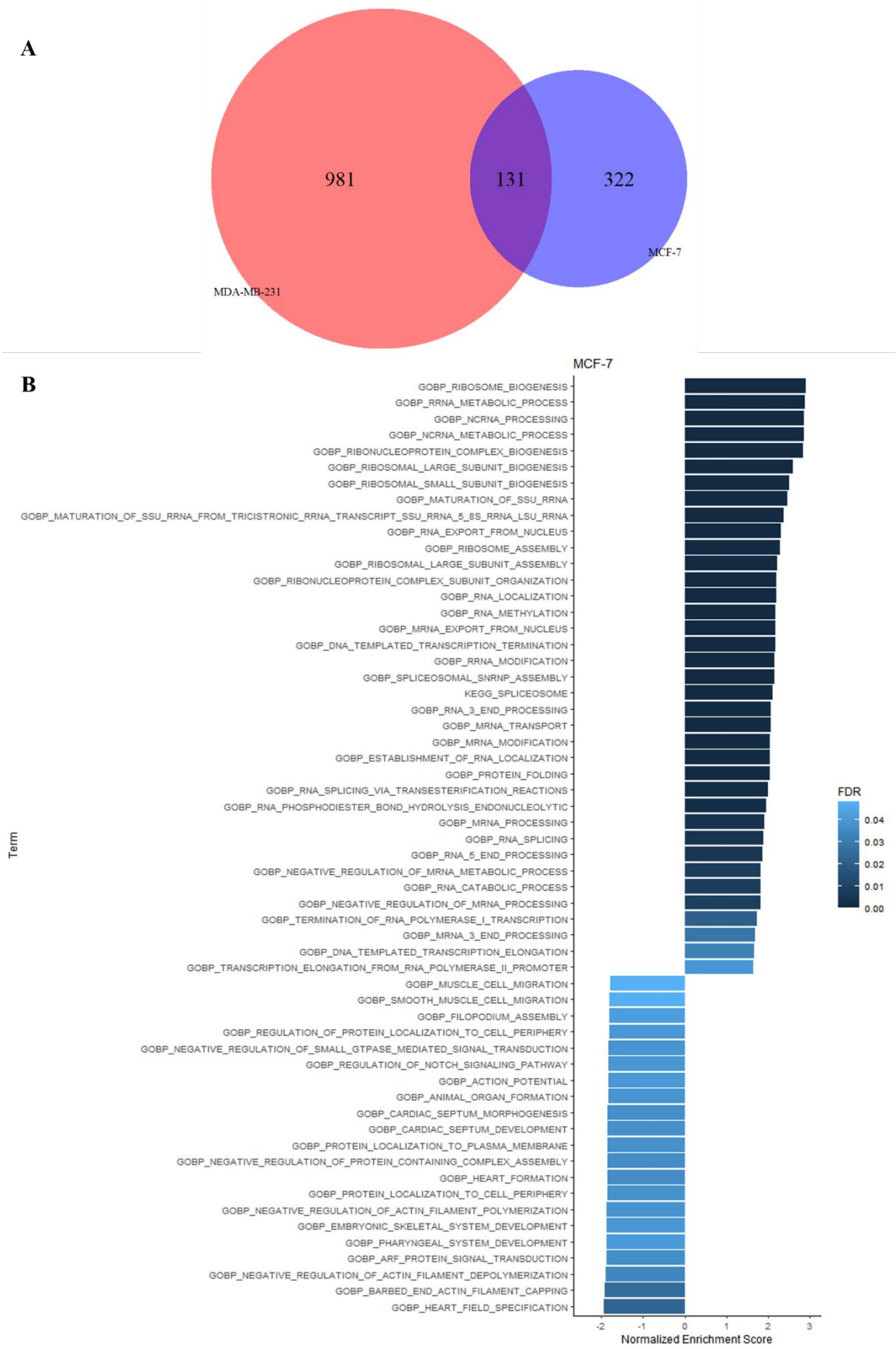
A
981
131
322
MDA-MB-231
MCF-7
B
MCF-7
GOBP_RIBOSOME_BIOGENESIS
GOBP_RRNA_METABOLIC_PROCESS
GOBP_NCRNA_PROCESSING
GOBP_NCRNA_METABOLIC_PROCESS
GOBP_RIBONUCLEOPROTEIN_COMPLEX_BIOGENESIS
GOBP_RIBOSOMAL_LARGE_SUBUNIT_BIOGENESIS
GOBP_RIBOSOMAL_SMALL_SUBUNIT_BIOGENESIS
GOBP_MATURATION_OF_SSU_RRNA
GOBP_MATURATION_OF_SSU_RRNA_FROM_TRICISTRONIC_RRNA_TRANSCRIPT_SSU_RRNA_5_8S_RRNA_LSU_RRNA
GOBP_RNA_EXPORT_FROM_NUCLEUS
GOBP_RIBOSOME_ASSEMBLY
GOBP_RIBOSOMAL_LARGE_SUBUNIT_ASSEMBLY
GOBP_RIBONUCLEOPROTEIN_COMPLEX_SUBUNIT_ORGANIZATION
GOBP_RNA_LOCALIZATION
GOBP_RNA_METHYLATION
GOBP_MRNA_EXPORT_FROM_NUCLEUS
GOBP_DNA_TEMPLATED_TRANSCRIPTION_TERMINATION
GOBP_RRNA_MODIFICATION
GOBP_SPLICEOSOMAL_SNRNP_ASSEMBLY
KEGG_SPLICEOSOME
GOBP_RNA_3_END_PROCESSING
GOBP_MRNA_TRANSPORT
GOBP_MRNA_MODIFICATION
GOBP_ESTABLISHMENT_OF_RNA_LOCALIZATION
GOBP_PROTEIN_FOLDING
GOBP_RNA_SPLICING_VIA_TRANSESTERIFICATION_REACTIONS
GOBP_RNA_PHOSPHODIESTER_BOND_HYDROLYSIS_ENDONUCLEOLYTIC
GOBP_MRNA_PROCESSING
GOBP_RNA_SPLICING
GOBP_RNA_5_END_PROCESSING
GOBP_NEGATIVE_REGULATION_OF_MRNA_METABOLIC_PROCESS
GOBP_RNA_CATABOLIC_PROCESS
GOBP_NEGATIVE_REGULATION_OF_MRNA_PROCESSING
GOBP_TERMINATION_OF_RNA_POLYMERASE_I_TRANSCRIPTION
GOBP_MRNA_3_END_PROCESSING
GOBP_DNA_TEMPLATED_TRANSCRIPTION_ELONGATION
GOBP_TRANSCRIPTION_ELONGATION_FROM_RNA_POLYMERASE_II_PROMOTER
GOBP_MUSCLE_CELL_MIGRATION
GOBP_SMOOTH_MUSCLE_CELL_MIGRATION
GOBP_FILOPODIUM_ASSEMBLY
GOBP_REGULATION_OF_PROTEIN_LOCALIZATION_TO_CELL_PERIPHERY
GOBP_NEGATIVE_REGULATION_OF_SMALL_GTPASE_MEDIATED_SIGNAL_TRANSDUCTION
GOBP_REGULATION_OF_NOTCH_SIGNALING_PATHWAY
GOBP_ACTION_POTENTIAL
GOBP_ANIMAL_ORGAN_FORMATION
GOBP_CARDIAC_SEPTUM_MORPHOGENESIS
GOBP_CARDIAC_SEPTUM_DEVELOPMENT
GOBP_PROTEIN_LOCALIZATION_TO_PLASMA_MEMBRANE
GOBP_NEGATIVE_REGULATION_OF_PROTEIN_CONTAINING_COMPLEX_ASSEMBLY
GOBP_HEART_FORMATION
GOBP_PROTEIN_LOCALIZATION_TO_CELL_PERIPHERY
GOBP_NEGATIVE_REGULATION_OF_ACTIN_FILAMENT_POLYMERIZATION
GOBP_EMBRYONIC_SKELETAL_SYSTEM_DEVELOPMENT
GOBP_PHARYNGEAL_SYSTEM_DEVELOPMENT
GOBP_ARF_PROTEIN_SIGNAL_TRANSDUCTION
GOBP_NEGATIVE_REGULATION_OF_ACTIN_FILAMENT_DEPOLYMERIZATION
GOBP_BARBED_END_ACTIN_FILAMENT_CAPPING
GOBP_HEART_FIELD_SPECIFICATION
Term
-2
-1
0
1
2
3
Normalized Enrichment Score
FDR
0.04
0.03
0.02
0.01
0.00

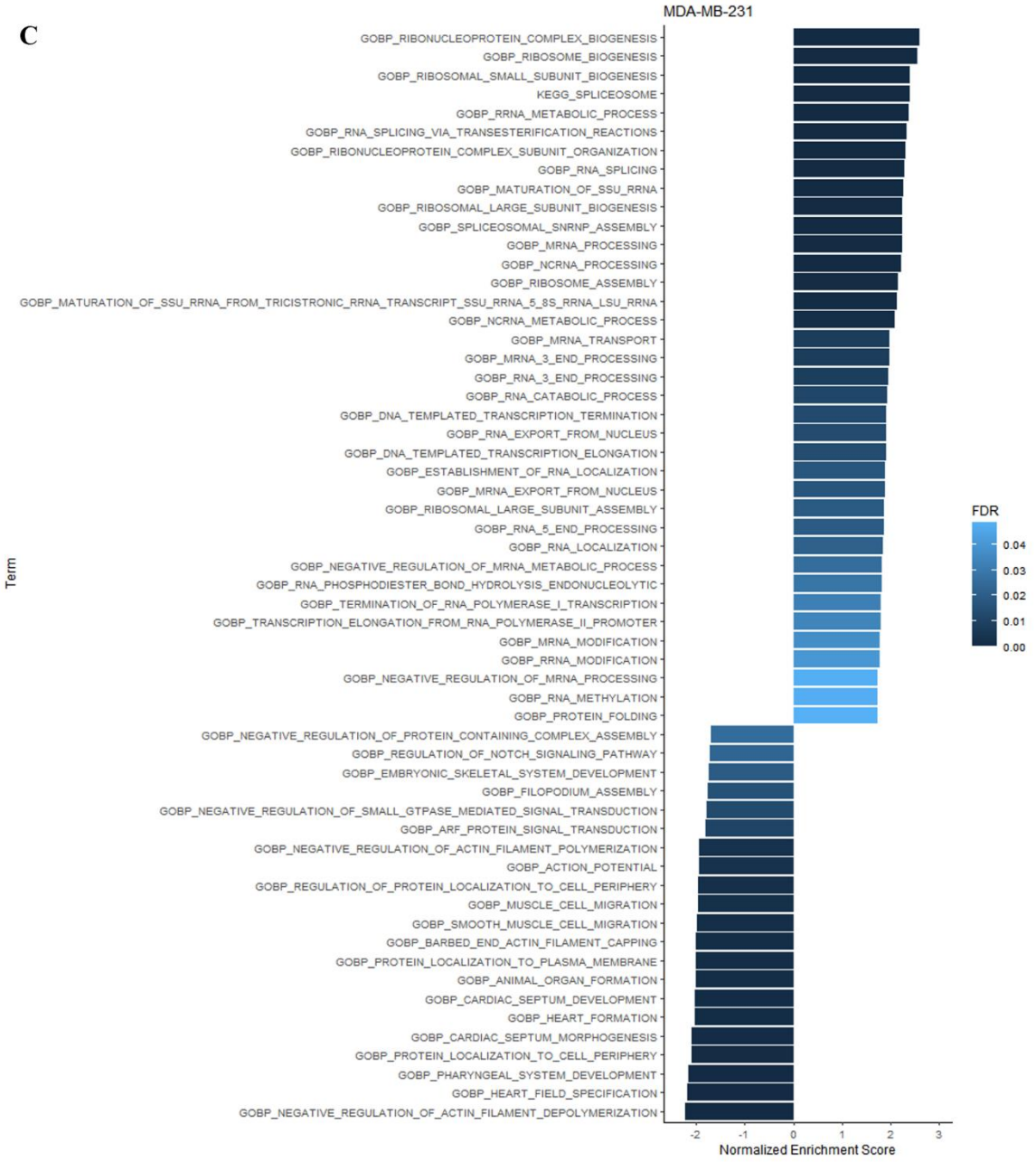

Figure 4.5 Overlap terms with the same direction in both cell lines from GSEA results.

(A) Venn diagram of GSEA results from MCF7 and MDA-MB-231 datasets. (B) Bar chart of significant terms of GSEA result from (A) MCF7 dataset and (B) MDA-MB-231 dataset. Significant terms were filtered at FDR $\leq$ 0.05. X-axis represented normalised enrichment score while Y-axis described terms, and colour shading indicated FDR score.

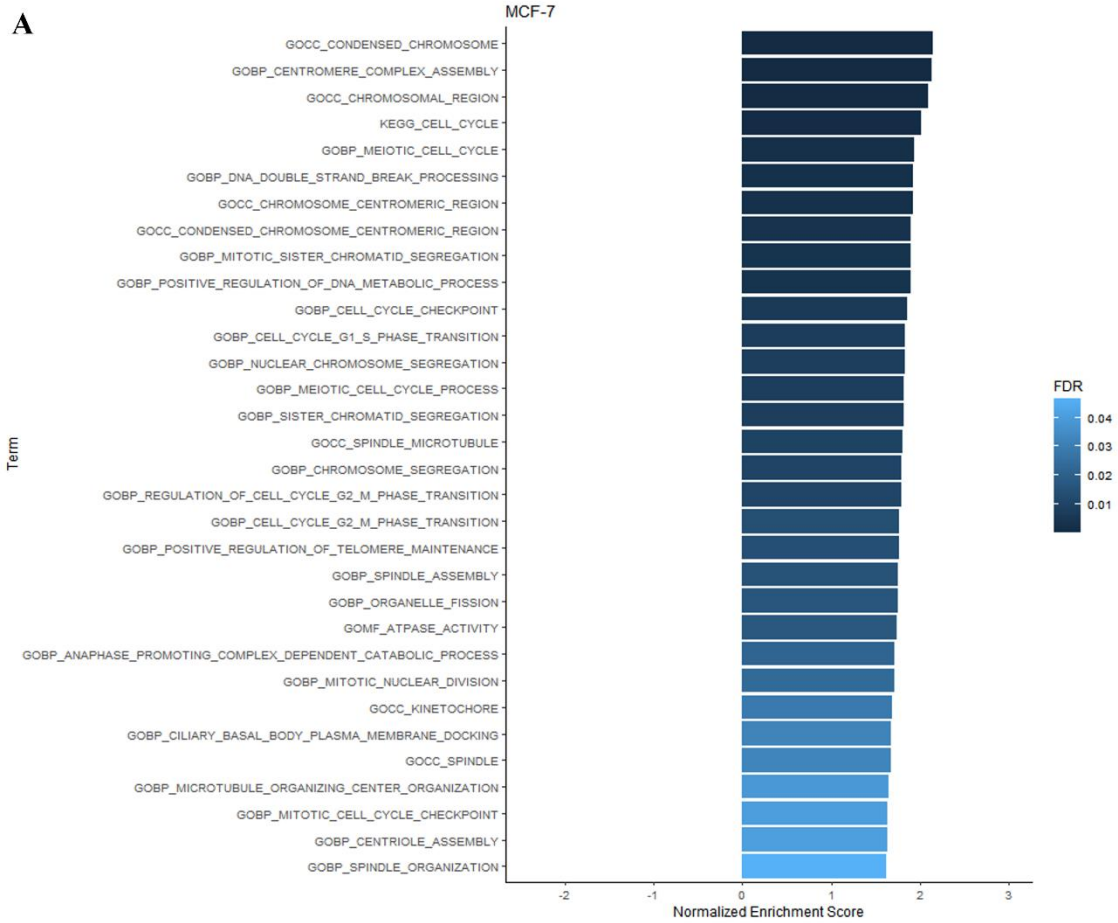

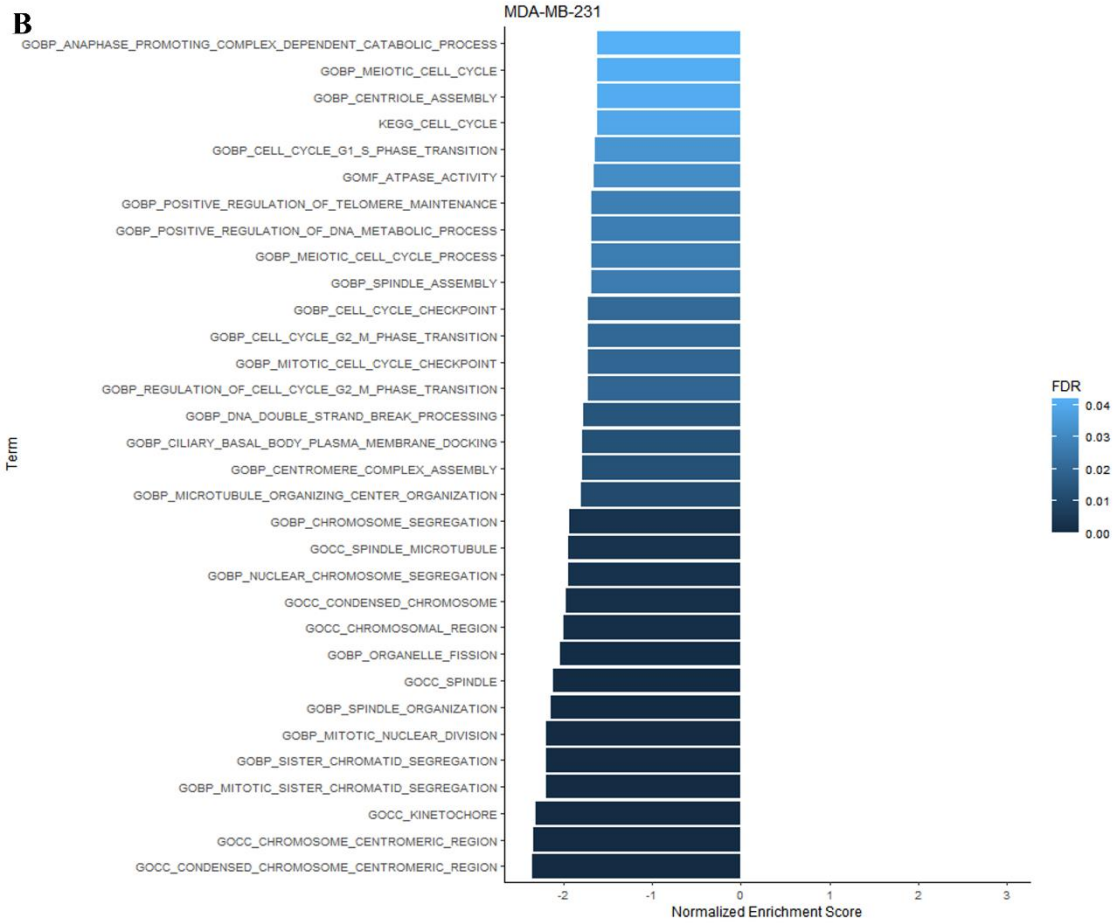

Figure 4.6 Bar chart of overlap terms with opposite direction between the cell lines from GSEA results.

Bar chart of significant terms of GSEA result from (A) MCF7 dataset and (B) MDA-MB-231 dataset. Significant terms were filtered at FDR ≤ 0.05. X-axis represented normalised enrichment score while Y-axis described terms, and colour shading indicated FDR score.

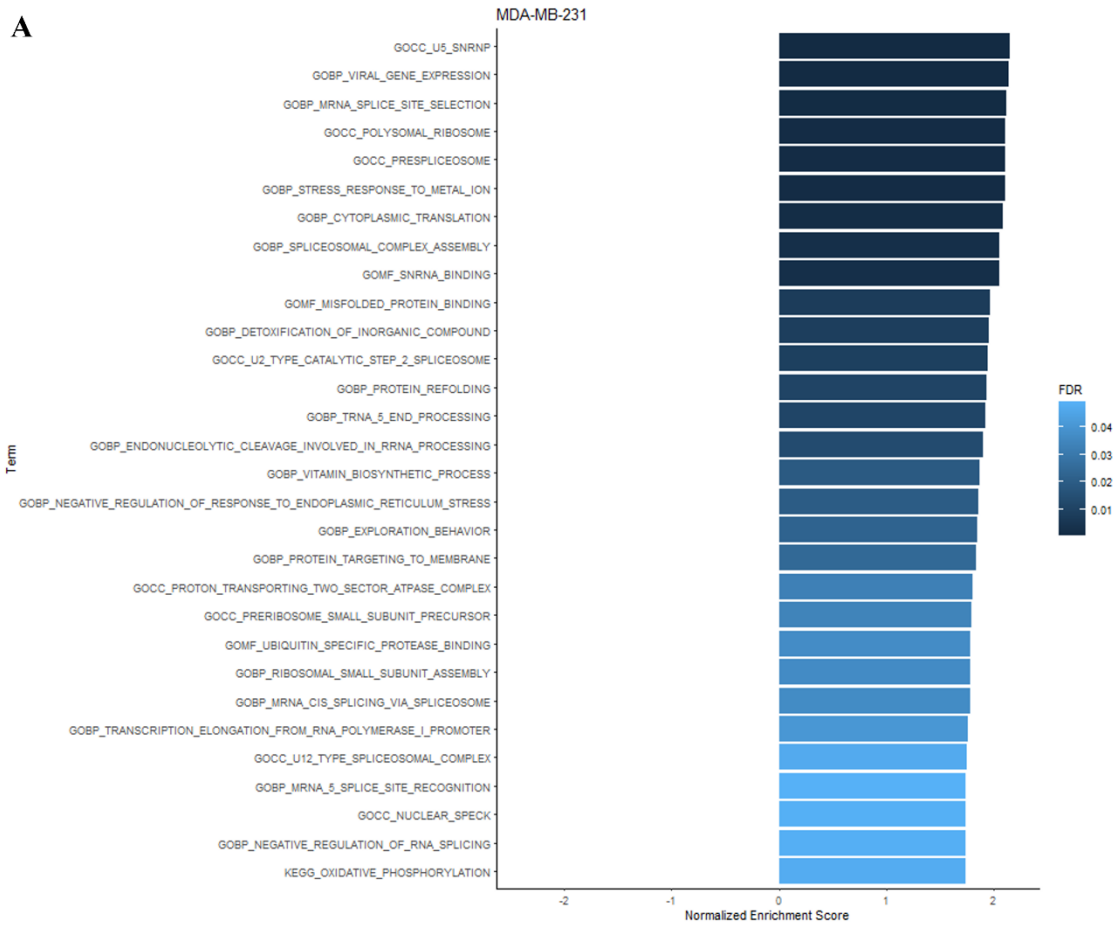

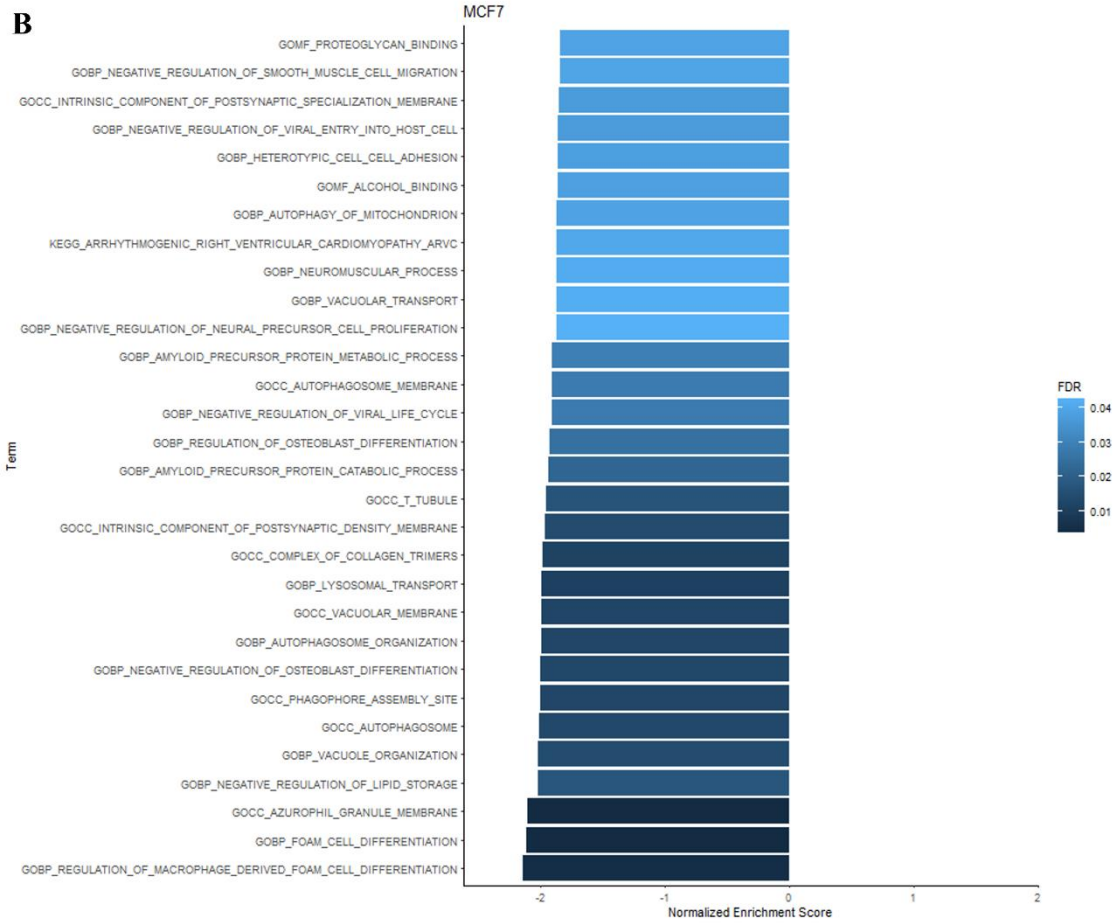

Figure 4.7 Bar chart of top 30 significant no overlapping terms of GSEA result from MCF7 dataset.

(A) Upregulated and (B) downregulated terms. Significant terms were filtered at FDR ≤ 0.05. X-axis represented normalised enrichment score while Y-axis described terms, and colour shading indicated FDR score.

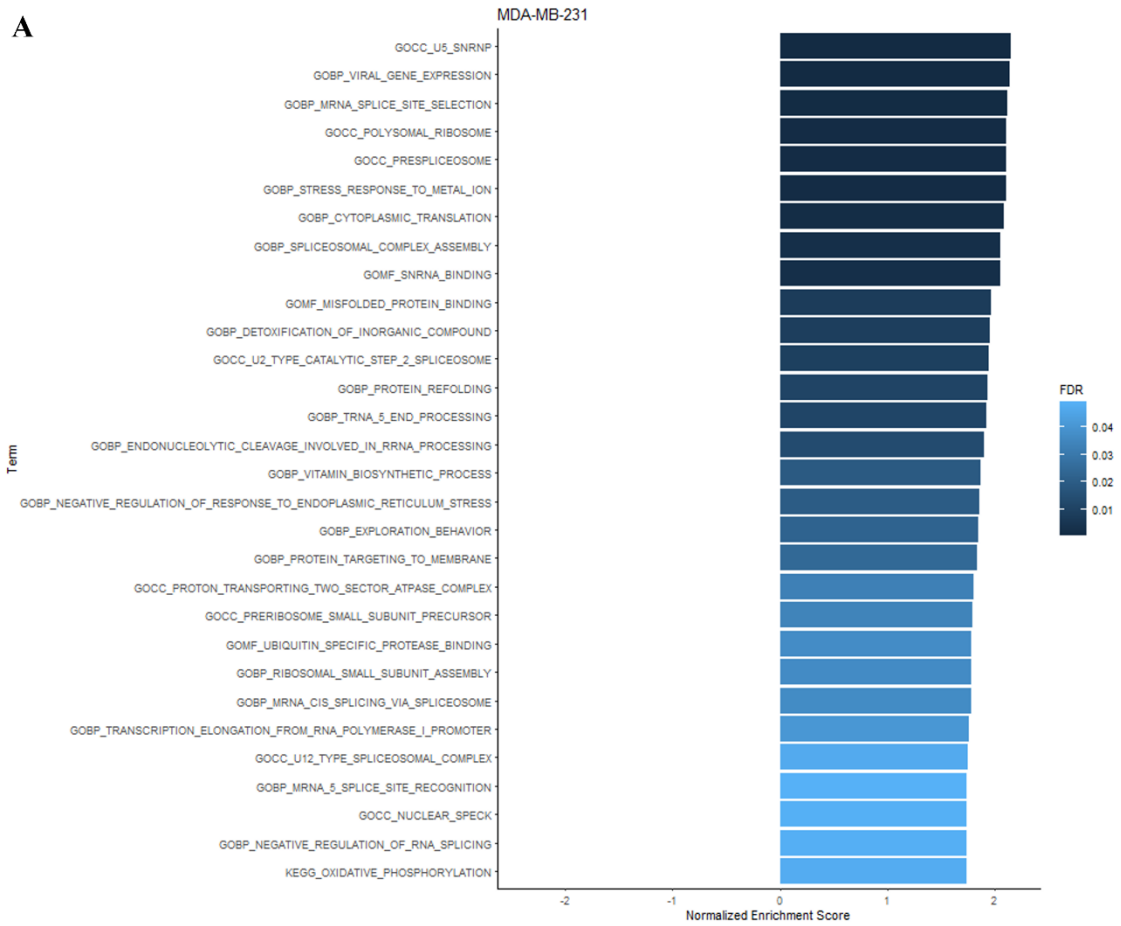

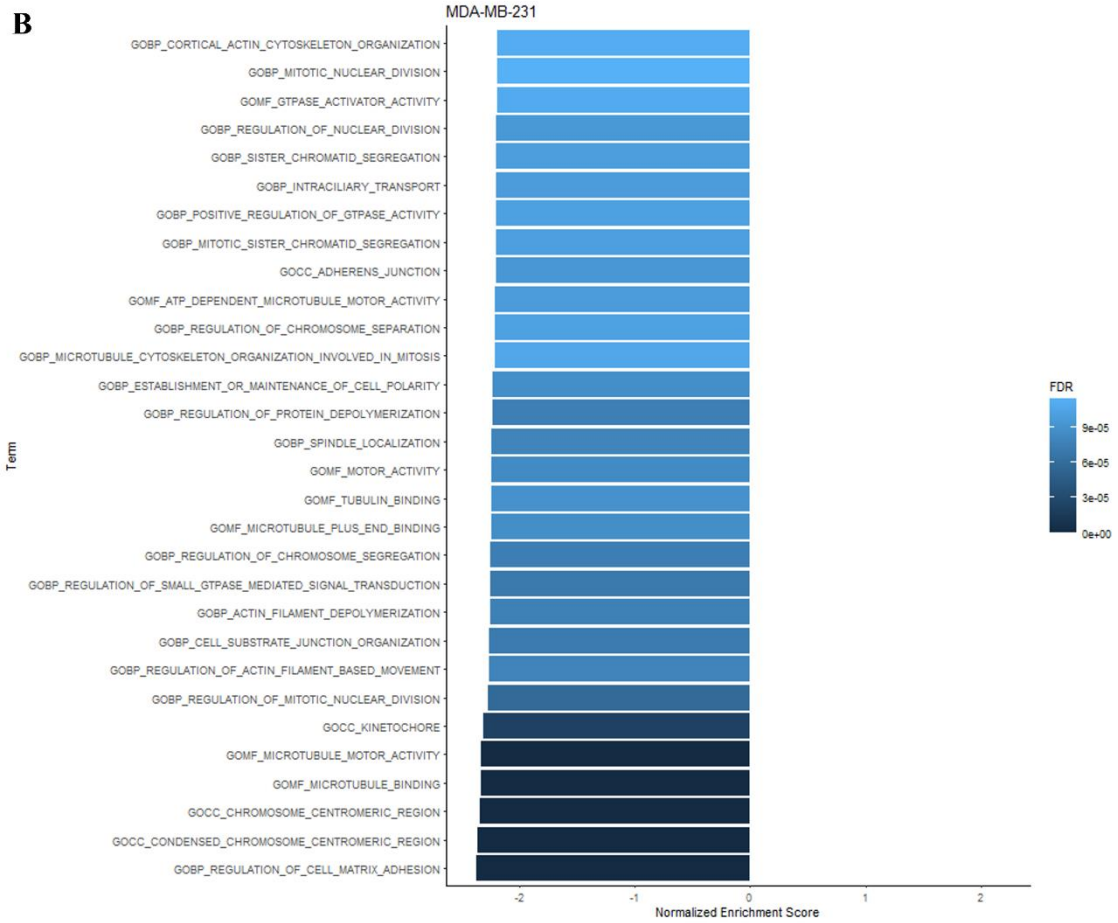

Figure 4.8 Bar chart of top 30 significant no overlapping terms of GSEA result from MDA-MB-231 dataset.

(A) Upregulated and (B) downregulated terms. Significant terms were filtered at FDR ≤ 0.05. X-axis represented normalised enrichment score while Y-axis described terms, and colour shading indicated FDR score.

4.3.4 Transcription factors determination on significant phosphosites and expression profiles of their target genes

Gene expression regulation is governed by several processes. So far we have identified likely epigenetic modification and the ability to modify the activity of transcription factors (TFs). To test which likely TFs could be involved in APG exposure we performed an upstream analysis based on the significant phosphosites identified. Within the whole dataset nine possible TF sites were found (Fig. 4.9A) representing a hyperphosphorylated group containing DNMT1 Ser143, ERF Ser21, YBX1 Ser165, and FOSL2 Ser200, and a hypophosphorylated group including ZNF609 Ser433, MECP2 Ser216, FOXK2 Ser398, SAFB2 Ser598, and CIC Thr1318. Within the 30 minutes list (Fig. 4.9B), the hyperphosphorylated group is composed of JUN Ser63, ARHGAP35 Ser589, NFIX Ser265, STAT3 Ser727, DNMT1 Ser143, HOXB6 Ser214, and STAT1 Ser727 while the hypophosphorylated group is comprised of ZNF609 Ser433, KAT7 Ser57, HIVEP1 Ser779, DNMT1 Ser154, GLYR1 Ser122, HMGA1 Thr53, HMGA1 Thr39, and HMGA1 Thr78. Noticeably, the hyperphosphorylated DNMT Ser143 and hypophosphorylated ZNF609 Ser433 appeared in both lists.

To link between these TFs and their effect on the regulation of gene expression, the TFs were queried in the Jaspar[2000] database for their motif sequences and were mapped to detect possible target genes in the human genome by FIMO. Genes with the motif in the sequence were then extracted and visualised using the gene expression data. Only seven out of the fifteen possible TF motifs were found in Jaspar[2000] comprising the motifs of ERF, FOSL2, FOXK2, JUN, NFIX, STAT1, and STAT3. Possible target genes were identified and used for generating heatmaps of gene expression profiles regulated by each TF. From the MCF7 dataset, the heatmaps were generated from a significant gene list filtered by possible target genes of ERF (540), FOSL2 (534), FOXK2 (503), JUN (512), NFIX (610), STAT1 (562), and STAT3 (559) where numbers in each bracket referred to the number of genes (Fig.

Appx.F1-7). Within the MDA-MB-231 dataset, the heatmaps were created similarly for ERF (153), FOSL2 (148), FOXK2 (147), JUN (137), NFIX (159), STAT1 (166), and STAT3 (165) (Fig. Appx.G1-7). Observing the heatmaps, the results revealed comparability among the expression profiles across all TFs, which had led us to investigate the overlapped genes from all TFs. Set intersections of all TFs were applied in significantly upregulated or downregulated gene sets and visualised by UpSet. From the MCF7 dataset, the plots showed that 41 of 436 genes appeared in all TFs in the upregulated set (Fig. 4.10A) and 131 of 598 genes presented in the downregulated set (Fig. 4.10B). While the MDA-MB-231 dataset was responsible for 52 overlapped genes from 198 genes in the downregulated set (Fig. 4.11B) and no overlapped genes across all TFs were found in the upregulated set (Fig. 4.11A). Likewise, this phenomenon occurred in public domain ChIP-Seq datasets from the ENCODE portal database. The Venn diagram of target genes of FOSL2, JUN, STAT1, and STAT3 from ENCODE datasets (Fig. 4.12) displayed a high number of overlapping genes across all TFs. Further inspection of these plots led us to a conclusion that the target genes were vastly shared across the TFs in this analysis thus over-representation analysis for every TF would lead to similar terms. Therefore, all possible target genes from all TFs were separated into upregulation and downregulation sets in both cell lines and were used as input to the DAVID functional annotation tool.

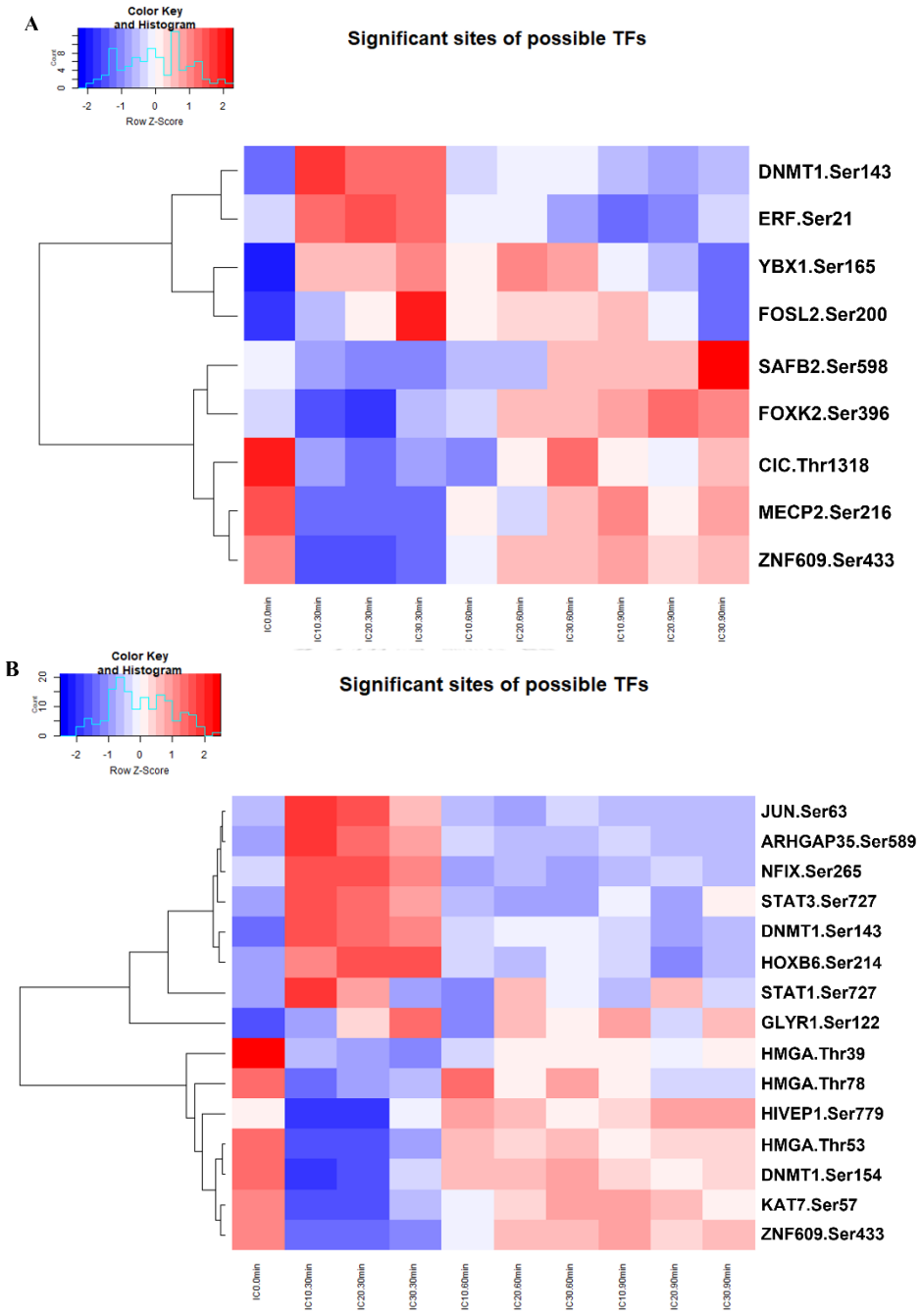

Figure 4.9 Heatmaps representing expression profiles of significant phosphosites that are possible transcription factors.

(A) whole data analysis and (B) 30-minute data analysis. X-axis indicated the treatment of that column. Y-axis represented phosphosites where HNGC gene symbol resided before first dot followed by phosphorylated amino acid and position within proteins. Colour indicated phosphorylation level where red is hyperphosphorylated and blue is hypophosphorylated.

Table 4.5 Possible transcription factors from significant phosphosites

Protein ID	Entry name	Protein names	Gene names	Length	significant phosphosites
Q96RK0	CIC_HUMAN	Protein capicua homolog	CIC KIAA0306	1608	T1318
P26358	DNMT1_HUMAN	DNA (cytosine-5)-methyltransferase 1 (Dnmt1) (EC 2.1.1.37) (CXXC-type zinc finger protein 9) (DNA methyltransferase HsaI) (DNA MTase HsaI) (M.HsaI) (MCMT)	DNMT1 AIM CXXC9 DNMT	1616	S143, S154
P50548	ERF_HUMAN	ETS domain-containing transcription factor ERF (Ets2 repressor factor) (PE-2)	ERF	548	S21
P15408	FOSL2_HUMAN	Fos-related antigen 2 (FRA-2)	FOSL2 FRA2	326	S200
Q01167	FOXK2_HUMAN	Forkhead box protein K2 (G/T-mismatch specific binding protein) (nGTBP) (Interleukin enhancer-binding factor 1)	FOXK2 ILF ILF1	660	S398
Q49A26	GLYR1_HUMAN	Putative oxidoreductase GLYR1 (EC 1.-.-.-) (3-hydroxyisobutyrate dehydrogenase-like protein) (Cytokine-like nuclear factor N-PAC) (Glyoxylate reductase 1 homolog) (Nuclear protein NP60) (Nuclear protein of 60 kDa) (Nucleosome-destabilizing factor) (hNDF)	GLYR1 HIBDL NDF NP60	553	S122
P17096	HMGA1_HUMAN	High mobility group protein HMG-I/HMG-Y (HMG-I(Y)) (High mobility group AT-hook protein 1) (High mobility group protein A1) (High mobility group protein R)	HMGA1 HMGIY	107	T39, T53, T78
P17509	HXB6_HUMAN	Homeobox protein Hox-B6 (Homeobox protein Hox-2.2) (Homeobox protein Hox-2B) (Homeobox protein Hu-2)	HOXB6 HOX2B	224	S214
P05412	JUN_HUMAN	Transcription factor AP-1 (Activator protein 1) (AP1) (Proto-oncogene c-Jun) (V-jun avian sarcoma virus 17 oncogene homolog) (p39)	JUN	331	S63
O95251	KAT7_HUMAN	Histone acetyltransferase KAT7 (EC 2.3.1.48) (Histone acetyltransferase binding to ORC1) (Lysine acetyltransferase 7) (MOZ, YBF2/SAS3, SAS2 and TIP60 protein 2) (MYST-2)	KAT7 HBO1 HBOa MYST2	611	S57
P51608	MECP2_HUMAN	Methyl-CpG-binding protein 2 (MeCp-2 protein) (MeCp2)	MECP2	486	S216
Q14938	NFIX_HUMAN	Nuclear factor 1 X-type (NF1-X) (Nuclear factor 1/X) (CCAAT-box-binding transcription factor) (CTF) (Nuclear factor I/X) (NF-I/X) (NFI-X) (TGGCA-binding protein)	NFIX	502	S265
Q9NRY4	RHG35_HUMAN	Rho GTPase-activating protein 35 (Glucocorticoid receptor DNA-binding factor 1) (Glucocorticoid receptor repression factor 1) (GRF-1) (Rho GAP p190A) (p190-A)	ARHGAP35 GRF1 GRLF1 KIAA1722 P190A p190ARHOGAP	1499	S589
Q14151	SAFB2_HUMAN	Scaffold attachment factor B2 (SAF-B2)	SAFB2 KIAA0138	953	S598
P42224	STAT1_HUMAN	Signal transducer and activator of transcription 1-alpha/beta (Transcription factor ISGF-3 components p91/p84)	STAT1	750	S727
P40763	STAT3_HUMAN	Signal transducer and activator of transcription 3 (Acute-phase response factor)	STAT3 APRF	770	S727
P67809	YBOX1_HUMAN	Y-box-binding protein 1 (YB-1) (CCAAT-binding transcription factor I subunit A) (CBF-A) (DNA-binding protein B) (DBPB) (Enhancer factor I subunit A) (EFI-A) (Nuclease-sensitive element-binding protein 1) (Y-box transcription factor)	YBX1 NSEP1 YB1	324	S165
P15822	ZEP1_HUMAN	Zinc finger protein 40 (Cirhin interaction protein) (CIRIP) (Gate keeper of apoptosis-activating protein) (GAAP) (Human immunodeficiency virus type I enhancer-binding protein 1) (HIV-EP1) (Major histocompatibility complex-binding protein 1) (MBP-1) (Positive regulatory domain II-binding factor 1) (PRDII-BF1)	HIVEP1 ZNF40	2718	S779
O15014	ZN609_HUMAN	Zinc finger protein 609	ZNF609 KIAA0295	1411	S433

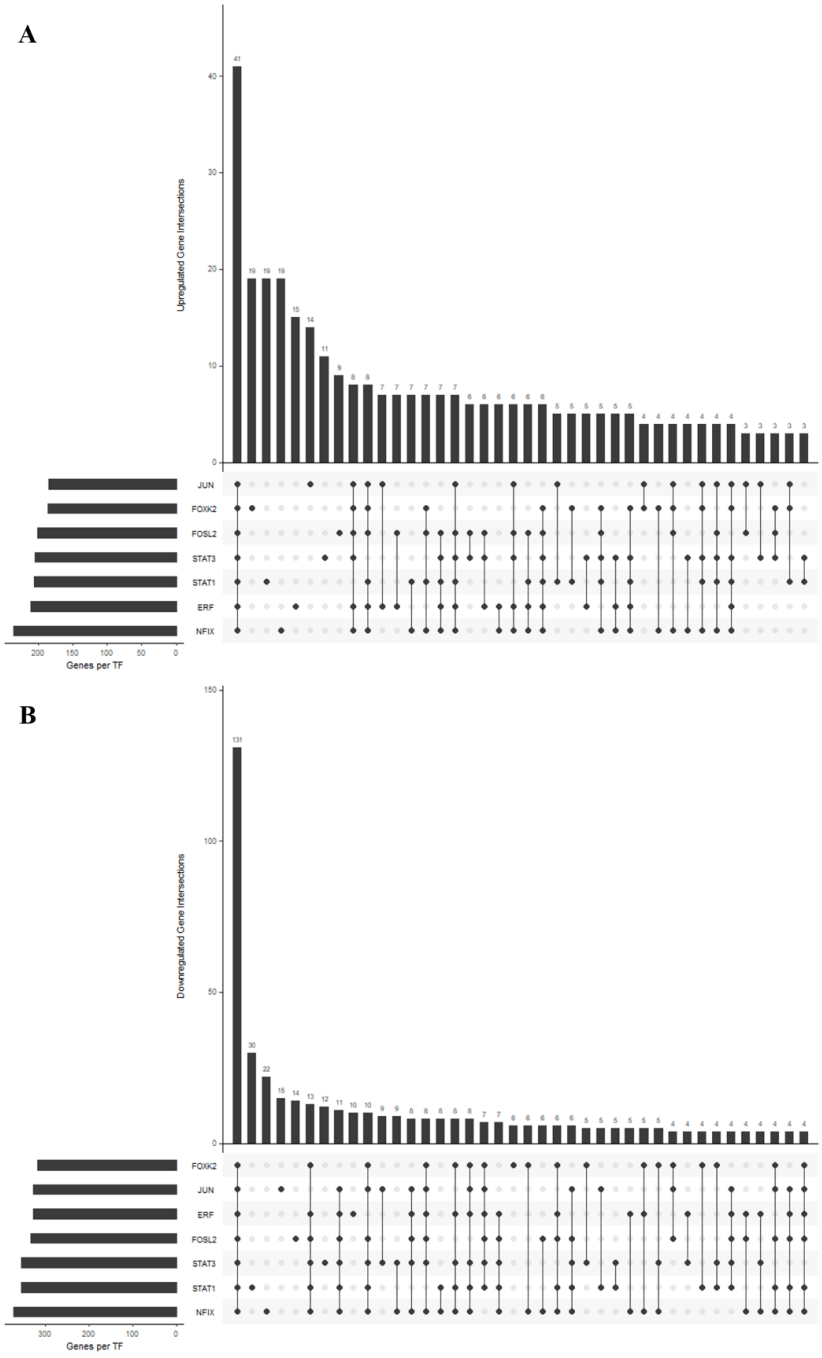

Figure 4.10 Bar chart of overlapping analysis of possible TF-target significant genes from MCF7 dataset.

(A) Upregulated genes and (B) Downregulated genes. Significant genes were filtered at FDR ≤ 0.05 and matched to all possible TF targets. X-axis represented associated TF, while Y-axis indicated overlapping gene number.

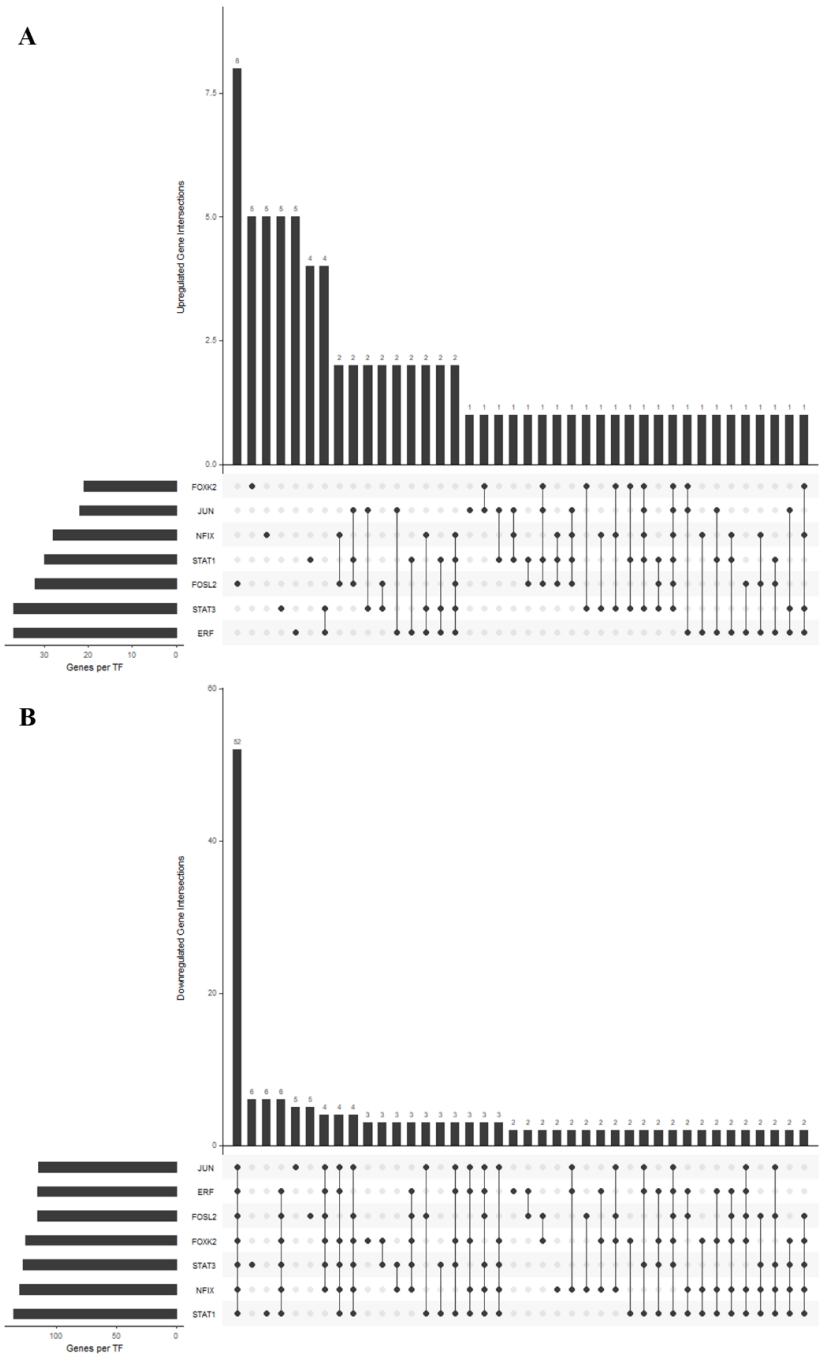

Figure 4.11 Bar chart of overlapping analysis of possible TF-target significant genes from MDA-MB-231 dataset.

(A) Upregulated genes and (B) Downregulated genes. Significant genes were filtered at FDR ≤ 0.05 and matched to all possible TF targets. X-axis represented associated TF, while Y-axis indicated overlapping gene number.

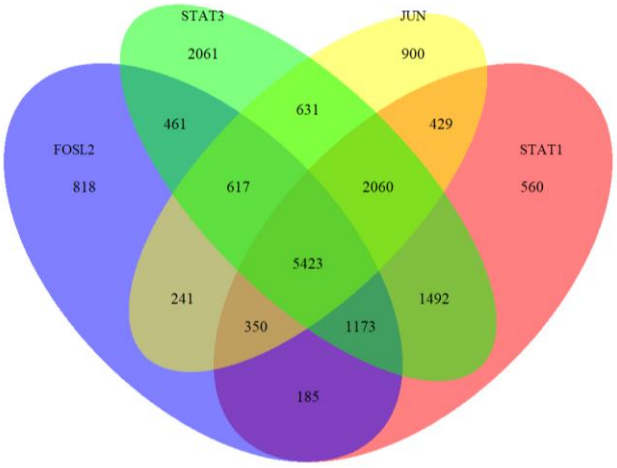

Figure 4.12 Venn diagram of target genes of FOSL2, JUN, STAT1, and STAT3 from ENCODE portal database.

The DAVID functional cluster analyses showed that, in MCF7 data, there was an increase in DNA damage response by p53 involved in with intrinsic apoptotic signalling pathway, folic acid metabolic process, and nitrogen metabolism (Table 4.6) while the decreases in sialylation, cardiomyopathy activity, and extracellular matrix-cell interaction can be observed (Table 4.7). In MDA-MB-231 results, there were two closely correlating clusters in the downregulation set that are mitotic nuclear division and attachment of mitotic spindle microtubules to kinetochore involved with sister chromatid segregation (Table 4.8), although there was no significant cluster in the upregulated set. This result is quite similar to the DAVID output of the significantly downregulated genes from the full MDA-MB-231 dataset.

Our analysis shows an increase in RNA metabolism and cell phase transition while a decrease in cell migration, posttranslational modifications, and protein localisation in both cell lines. Despite the different reports in cell cycle arrest both cell lines were affected by APG. DNA damage response via p53 signalling pathway was found in MCF7 cells while inhibition of sister chromatid segregation was observed in MDA-MB-231 cells. In summary, the treatment of APG exhibited antiproliferative activity at different cellular processes between the two cell lines.

Table 4.6 Significance clustering group from DAVID clustering chart of possible TF-targeted upregulated significant genes from MCF7 dataset

ANNOTATION CLUSTER 1					ENRICHMENT SCORE: 2.2762033753054						
CATEGORY	Term	Count	%	PValue	Genes	List Total	Pop Hits	Pop Total	Fold Enrichment	Benjamini	FDR
GOTERM_BP_DIRECT	GO:0006978~DNA damage response, signal transduction by p53 class mediator resulting in transcription of p21 class mediator	5	1.146789	5.32E-04	TFAP4, CHEK2, BRCA1, BRCA2, TP73	398	16	16032	12.58794	0.271422	0.271422
GOTERM_BP_DIRECT	GO:0010332~response to gamma radiation	5	1.146789	0.006868	CHEK2, XRCC2, BCL2, BRCA2, TP73	398	31	16032	6.497001	1	1
GOTERM_BP_DIRECT	GO:0042771~intrinsic apoptotic signaling pathway in response to DNA damage by p53 class mediator	4	0.917431	0.040599	CHEK2, AEN, BRCA2, TP73	398	31	16032	5.197601	1	1
ANNOTATION CLUSTER 2					**ENRICHMENT SCORE: 2.131253052740413**						
CATEGORY	Term	Count	%	PValue	Genes	List Total	Pop Hits	Pop Total	Fold Enrichment	Benjamini	FDR
GOTERM_BP_DIRECT	GO:0006730~one-carbon metabolic process	7	1.605505	6.51E-05	CA12, DHFR, MTHFD1L, CA2, MTHFD2L, MAT1A, CA13	398	29	16032	9.723098	0.066358	0.066358
GOTERM_BP_DIRECT	GO:0046655~folic acid metabolic process	3	0.688073	0.065125	DHFR, MTHFD1L, MTHFD2L	398	17	16032	7.108484	1	1
KEGG_PATHWAY	hsa00670:One carbon pool by folate	3	0.688073	0.095323	DHFR, MTHFD1L, MTHFD2L	182	19	6559	5.690283	1	1
ANNOTATION CLUSTER 3					**ENRICHMENT SCORE: 1.9236053805215176**						
CATEGORY	Term	Count	%	PValue	Genes	List Total	Pop Hits	Pop Total	Fold Enrichment	Benjamini	FDR
GOTERM_BP_DIRECT	GO:0006730~one-carbon metabolic process	7	1.605505	6.51E-05	CA12, DHFR, MTHFD1L, CA2, MTHFD2L, MAT1A, CA13	398	29	16032	9.723098	0.066358	0.066358
GOTERM_MF_DIRECT	GO:0004089~carbonate dehydratase activity	3	0.688073	0.04393	CA12, CA2, CA13	391	14	16104	8.825722	1	1
KEGG_PATHWAY	hsa00910:Nitrogen metabolism	3	0.688073	0.078547	CA12, CA2, CA13	182	17	6559	6.359729	1	1
GOTERM_BP_DIRECT	GO:0015701~bicarbonate transport	4	0.917431	0.090032	CA12, SLC26A2, CA2, CA13	398	43	16032	3.747108	1	1

Table 4.7 Significance clustering group from DAVID clustering chart of possible TF-targeted downregulated significant genes from MCF7 dataset

ANNOTATION CLUSTER 1					ENRICHMENT SCORE: 2.2823198501983217						
CATEGORY	Term	Count	%	PValue	Genes	List Total	Pop Hits	Pop Total	Fold Enrichment	Benjamini	FDR
GOTERM_BP_DIRECT	GO:0097503~sialylation	7	1.170569	2.88E-05	ST6GAL1, ST6GALNAC1, ST3GAL4, ST8SIA4, ST3GAL5, ST3GAL1, ST6GALNAC5	518	20	16032	10.83243	0.036048	0.035991
GOTERM_BP_DIRECT	GO:0009311~oligosaccharide metabolic process	7	1.170569	1.15E-04	ST6GAL1, ST6GALNAC1, ST3GAL4, ST8SIA4, ST3GAL5, ST3GAL1, ST6GALNAC5	518	25	16032	8.665946	0.095719	0.095566
GOTERM_BP_DIRECT	GO:0001574~ganglioside biosynthetic process	6	1.003344	2.07E-04	ST6GALNAC1, ST3GAL4, ST8SIA4, ST3GAL5, ST3GAL1, ST6GALNAC5	518	18	16032	10.3166	0.103575	0.10341
GOTERM_MF_DIRECT	GO:0008373~sialyltransferase activity	6	1.003344	2.75E-04	ST6GAL1, ST6GALNAC1, ST3GAL4, ST3GAL5, ST3GAL1, ST6GALNAC5	521	19	16104	9.760986	0.207046	0.207046
GOTERM_CC_DIRECT	GO:0030173~integral component of Golgi membrane	7	1.170569	0.008755	CSGALNACT1, ST6GAL1, ST3GAL4, ST8SIA4, ST3GAL5, ST3GAL1, STEAP2	554	56	17280	3.898917	0.237505	0.234188
GOTERM_BP_DIRECT	GO:0018279~protein N-linked glycosylation via asparagine	6	1.003344	0.008871	ST6GAL1, ST6GALNAC1, ST3GAL4, ST3GAL5, ST3GAL1, ST6GALNAC5	518	40	16032	4.642471	1	0.998801
GOTERM_MF_DIRECT	GO:0003836~beta-galactoside (CMP) alpha-2,3-sialyltransferase activity	3	0.501672	0.019621	ST3GAL4, ST3GAL5, ST3GAL1	521	7	16104	13.24705	1	1
GOTERM_BP_DIRECT	GO:0006486~protein glycosylation	9	1.505017	0.025895	ST6GAL1, ST6GALNAC1, FUT9, OAS2, ST3GAL4, ST8SIA4, ST3GAL5, ST3GAL1, ST6GALNAC5	518	110	16032	2.532257	1	0.998801
KEGG_PATHWAY	hsa00604:Glycosphingolipid biosynthesis - ganglio series	3	0.501672	0.093182	ST3GAL5, ST3GAL1, ST6GALNAC5	228	15	6559	5.753509	0.87591	0.864728
GOTERM_CC_DIRECT	GO:0032580~Golgi cisterna membrane	5	0.83612	0.205482	CSGALNACT1, ST6GAL1, FUT9, ST3GAL4, ST3GAL1	554	73	17280	2.136393	1	0.988796
GOTERM_BP_DIRECT	GO:0016266~O-glycan processing	3	0.501672	0.55286	ST6GAL1, ST3GAL4, ST3GAL1	518	57	16032	1.628937	1	0.998801
ANNOTATION CLUSTER 2					ENRICHMENT SCORE: 2.018433409205084						
CATEGORY	Term	Count	%	PValue	Genes	List Total	Pop Hits	Pop Total	Fold Enrichment	Benjamini	FDR
KEGG_PATHWAY	hsa05412:Arrhythmogenic right ventricular cardiomyopathy (ARVC)	9	1.505017	0.002038	CACNG6, TCF7L2, TCF7L1, ITGB4, CTNNA3, ITGB7, CACNA1C, ITGB6, SGCG	228	67	6559	3.864297	0.112801	0.111361
KEGG_PATHWAY	hsa05414:Dilated cardiomyopathy	9	1.505017	0.008251	CACNG6, TGFB3, ITGB4, GNAS, ITGB7, CACNA1C, ITGB6, SGCG, ADCY5	228	84	6559	3.082237	0.277639	0.274095
KEGG_PATHWAY	hsa05410:Hypertrophic cardiomyopathy (HCM)	7	1.170569	0.052358	CACNG6, TGFB3, ITGB4, ITGB7, CACNA1C, ITGB6, SGCG	228	78	6559	2.581703	0.683563	0.674836
ANNOTATION CLUSTER 3					ENRICHMENT SCORE: 1.9265065178016516						
CATEGORY	Term	Count	%	PValue	Genes	List Total	Pop Hits	Pop Total	Fold Enrichment	Benjamini	FDR
KEGG_PATHWAY	hsa04512:ECM-receptor interaction	11	1.839465	7.82E-04	COL2A1, SV2B, COL24A1, LAMB2, ITGB4, COL4A4, COL4A5, ITGB7, CD36, ITGB6, THBS3	228	87	6559	3.637276	0.09184	0.090667
KEGG_PATHWAY	hsa04510:Focal adhesion	14	2.341137	0.026034	SHC2, COL24A1, LAMB2, ITGB4, VEGFC, THBS3, MAPK10, COL2A1, COL4A4, PDGFC, ERBB2, COL4A5, ITGB7, ITGB6	228	206	6559	1.955076	0.509828	0.50332
KEGG_PATHWAY	hsa04151:PI3K-Akt signaling pathway	18	3.010033	0.081649	COL24A1, LAMB2, ITGB4, VEGFC, THBS3, GHR, CASP9, RBL2, EFNA1, COL2A1, CDK6, LPAR6, COL4A4, PDGFC, COL4A5, ITGB7, ITGB6, FGF13	228	340	6559	1.522988	0.815666	0.805253

Table 4.8 Significance clustering group from DAVID clustering chart of possible TF-targeted downregulated significant genes from MDA-MB-231 dataset

ANNOTATION CLUSTER 1					ENRICHMENT SCORE: 4.756633090853542						
CATEGORY	Term	Count	%	PValue	Genes	List Total	Pop Hits	Pop Total	Fold Enrichment	Benjamini	FDR
GOTERM_BP_DIRECT	GO:0007062~sister chromatid cohesion	10	5.154639	1.91E-06	CENPE, KIF18A, CENPI, ZWILCH, KNTC1, KIF2C, BUB1, NDC80, SPC24, SPC25	176	98	15177	8.799281	0.002232	0.002232
GOTERM_CC_DIRECT	GO:0000777~condensed chromosome kinetochore	9	4.639175	3.79E-06	DCTN5, CENPE, ZWILCH, KNTC1, KIF2C, BUB1, NDC80, SPC24, SPC25	185	82	16400	9.72973	8.86E-04	8.74E-04
GOTERM_BP_DIRECT	GO:0051301~cell division	15	7.731959	3.12E-05	BORA, ZWILCH, KIF14, CABLES1, CDC25C, NDC80, CENPE, CCNB2, PARD6B, CNTRL, KNTC1, KIF2C, BUB1, SPC24, SPC25	176	332	15177	3.896067	0.018175	0.018175
GOTERM_BP_DIRECT	GO:0007067~mitotic nuclear division	11	5.670103	4.16E-04	ASPM, CCNB2, BORA, ZWILCH, KNTC1, KIF2C, CDC25C, BUB1, NDC80, SPC24, SPC25	176	236	15177	4.019333	0.161873	0.161873
ANNOTATION CLUSTER 2					ENRICHMENT SCORE: 2.509412377675893						
CATEGORY	Term	Count	%	PValue	Genes	List Total	Pop Hits	Pop Total	Fold Enrichment	Benjamini	FDR
GOTERM_CC_DIRECT	GO:0000776~kinetochore	8	4.123711	2.93E-05	KAT2B, CENPE, KIF18A, CENPI, ZWILCH, KIF2C, BUB1, NDC80	185	79	16400	8.977078	0.003427	0.003383
GOTERM_BP_DIRECT	GO:0051315~attachment of mitotic spindle microtubules to kinetochore	3	1.546392	0.003536	CENPE, KIF2C, NDC80	176	8	15177	32.33736	0.612357	0.612357
GOTERM_BP_DIRECT	GO:0051310~metaphase plate congression	3	1.546392	0.00679	CENPE, KIF2C, NDC80	176	11	15177	23.51808	0.686366	0.686366
GOTERM_CC_DIRECT	GO:0000775~chromosome, centromeric region	3	1.546392	0.130372	CENPE, KIF2C, NDC80	185	56	16400	4.749035	1	0.991416

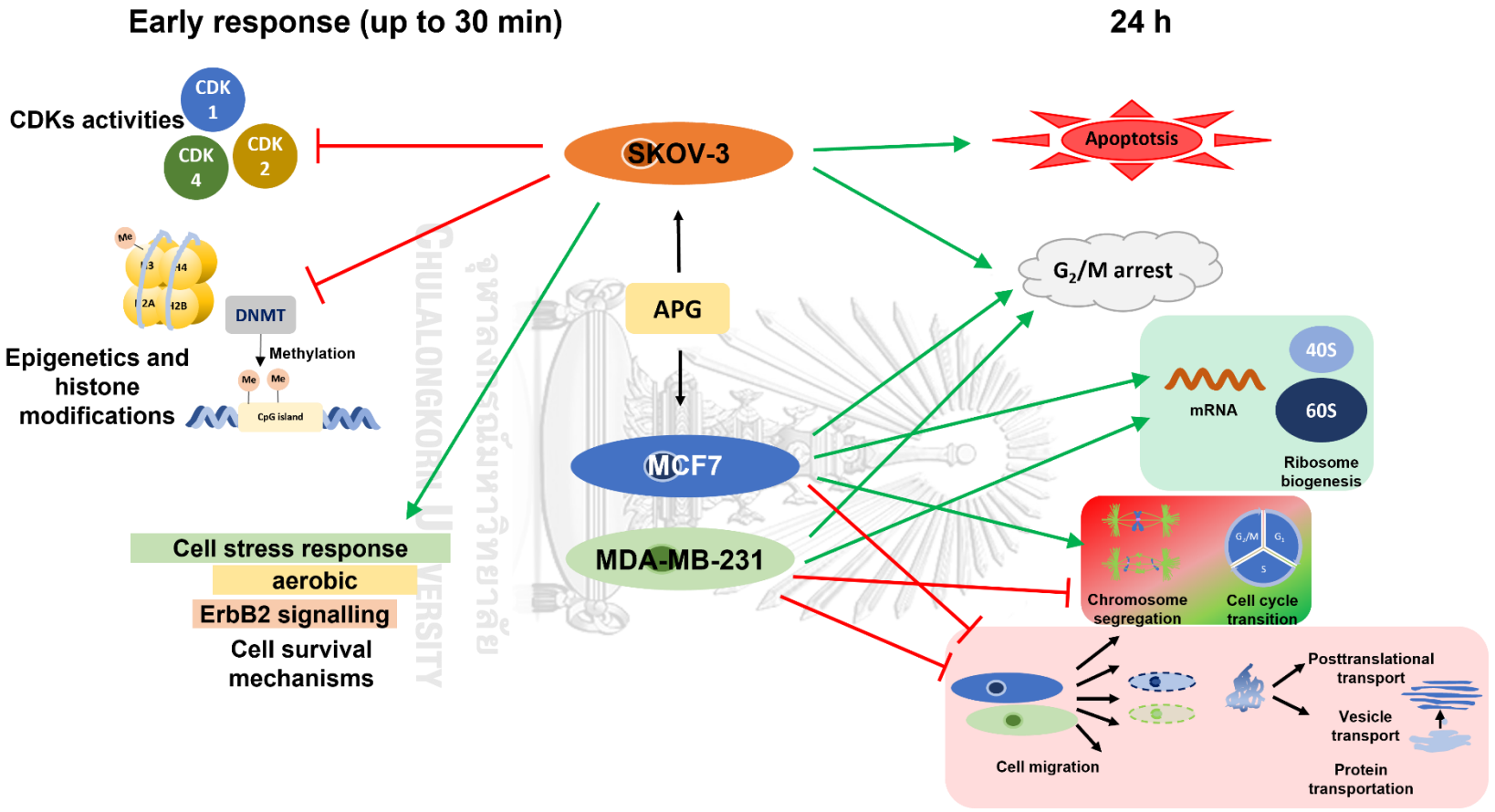

Figure 4.13 Summary graphic of the findings from antiproliferative effect and phosphoproteomics studies of apigenin together with public domain data analysis.

4.4 Discussion

The results from KSEA analysis highlighted that the activation of MAPK and HER2 (ERBB2) signalling pathway, which under normal circumstances are associated with cell survival and proliferation, occurred rapidly after treatment of APG. This result was observed previously in our phosphoproteomics GSEA result that upregulation of activation of MAPKK activity, regulation of ErbB2 signalling pathway, and epithelial cell proliferation was shown at 30 minutes (Fig. 3.13B the first, third, and fifth row of the first column). A previous study reported that APG treatment for 24 h in HER2-overexpressing breast cancer cell lines led to degradation of HER2 by competing with GRP94 to form complexes that protected Her2 from polyubiquitination and thus disrupting the HER2 signalling through PI3K/Akt pathway involved in cell proliferation and differentiation (309). SKOV-3 is reported to be a HER2-overexpressing cell line (310) and might react to APG treatment in a similar fashion as in these breast cancer studies. The activation of HER2 signalling might appear to be associated with an early cell survival mechanism against the stress from APG treatment. This event might reduce along the course of the treatment by the APG-induced degradation of HER2 protein.

Suppression of cyclin-dependent kinases, CDK1, CDK2, and CDK4, suggests a direct role of APG on cell progression arrest activity that results in G_2/M arrest in SKOV-3 cell line. This finding is correlated to the literature analysis (Fig. 4.4) that the inhibition of CDK expression level and activity occurred in several cell lines from different origins and is associated with the antiproliferative activity of APG that causes cell cycle arrest on either G_1 or G_2/M phase. Moreover, as SKOV-3 was arrested at G_2/M phase that is regulated by the activity of CDK1 and 2, it is interesting that CDK4 activity is also suppressed by APG.

An interesting set of kinases that are enhanced in their activity was pyruvate dehydrogenase kinases (PDK1 and PDK2), which inhibit pyruvate dehydrogenase activity by phosphorylation of pyruvate dehydrogenase complex (PDC) subunit E1α at Ser232, Ser293,

and Ser300 that interfere with the complex formation and catalytic activity of the enzyme (311). The hyperphosphorylation of these phosphosites at 30 minutes was illustrated in Figure 4.14. The consequences of this event affected the energy metabolism inside the cells by preventing acetyl-CoA biosynthesis from pyruvate and the TCA cycle afterwards meanwhile increasing aerobic glycolysis, which benefits the proliferation of cancer cells through providing precursors for several biosynthesis and electron carriers for redox reaction that reduce reactive oxygen species occurrences. This phenomenon was firstly discovered by Otto Warburg in 1924 (312) and has been named the Warburg effect. Interestingly, pyruvate kinase M2, which converts phosphoenolpyruvate to pyruvate, was inhibited in activity and expression level in colon cancer cells by APG at 24 hours (313). Observation in public domain data appeared that reduction of PDKs expression was found at 24 hours on both cell lines and GSEA results from MDA-MB-231 revealed a significant decrease in acetyl-CoA biosynthesis. According to the TF results, we found that FOXK2, which has been reported for involvement with aerobic glycolysis through upregulation of enzymatic machinery (314), was significantly hypophosphorylated at Ser398 at 30 minutes and upregulated in the MCF7 cell line. FOXK2 is Forkhead box protein K2 that was recently discovered a role in insulin signalling response and mitochondria biogenesis and knockdown of this TF resulted in induction of apoptosis, suppression of the cell cycle progression, and reduction of lipid metabolism via deregulating of its target gene expressions (315). Nonetheless, information regarding phosphosites of FOXK2 at Ser398 is still limited but a previous phosphoproteomics study has reported hypophosphorylation of this site associated with ErbB-dependent signalling in early breast cancer development (316). Therefore, the enhancement of ErbB2 signalling at 30 minutes was likely associated with perturbation of glucose metabolism in response to APG. Further experimentation is required to validate this.

JUN is activated by c-Jun N-terminal kinase (JNK) at Ser63 and Ser73 via a stress signalling pathway (317). Our KSEA result displayed enhancement of MAPK8 and MAPK9,

also known as JNK1 and JNK2, at 30 minutes that associated with hyperphosphorylation of JUN Ser63 at the same time point. Notably, previous studies had reported that APG had less effect on JNK signalling, possibly due to its protective effect, and specifically activated p38 MAPK and ERK1/2 signalling pathway (318-320). Moreover, phosphorylation of STAT at Ser727 that was observed to be enhanced at 30 minutes, was required for the activities of STAT1 and was associated with stress response by p38 MAPK signalling (321). According to KSEA result, MAPK14, known as MAP kinase p38α, increased in its activity at 30 minutes as well as JNKs and this kinase is one of the four p38 MAP kinases that governed STAT1 Ser727 sites. In parallel to STAT1 Ser727, hyperphosphorylation of STAT3 Ser727, which was regulated by protein kinase C-delta and JNKs (322, 323), was observed in the same manner. Surprisingly, other studies reported that APG suppressed STAT1 and STAT3 activity through inhibition of related signalling and kinases (324-326) although the detection of the phosphosites expression was taken at a later stage of treatment. In summary, APG treatment inhibits the cell cycle regulator kinases activity and suppresses energy metabolism, meanwhile it activates the stress response pathway at an early exposure time point in SKOV-3 cell line through JNK and p38 MAPK signalling pathway which results in the activation of ERBB2 signalling to improve survival.

Antiproliferative activity of APG in MCF7 and MDA-MB-231 appears to be mediated through different mechanisms although both cells were arrested at G_2/M phase. While direct downregulation of genes involved with cell cycle transition can be observed in the MDA-MB-231 dataset, in the MCF7 dataset these genes appear to be upregulated. In contrast, SKOV-3 cells showed downregulation of these genes at the protein level (139, 141, 287). There are several limitations in a direct comparison of MCF7/MDA-MB-231 and the SKOV-3 cell lines. First, gene expression was evaluated at 24h after exposure; second, mRNA levels are known to be impacted by APG through interference with mRNA maturation and splicing (327); and third, posttranslational modifications that could lead to inactivation or

degradation, and directly inhibit the enzymatic activity of these proteins by competing with substrates, coenzymes, and cofactors.

Interestingly, from the GSEA results of phosphoproteomics data, a decrease in the regulation of epigenetics and chromatin organisation was observed at the early time point in the SKOV-3 cell line. This might be associated with the upregulation of genes relating to transcription, ribosome biogenesis, and translation in APG-treated MCF-7 and MDA-MB-231 breast cancer cell lines at 24 hours from the public domain data. Especially, demethylation that related to DNA and histone methylation was increased at 30 minutes according to the GSEA result in this study. A main methyl donor source for one carbon metabolic process associated with DNA methylation is folate (328). Regarding the clustering result of upregulated genes in MCF-7 (Table 4.6), one-carbon metabolism involved with folate was reported and might relate to methyl group scavenging and metabolism after APG exposure. Future studies can be focused on methylation associated with the antiproliferative activity of APG by depleting methyl donors from the media in exposure with APG, which can be further extended to observe the global changes of DNA methylation by high-throughput bisulfite genomic sequencing and histone modifications through Chromatin immunoprecipitation sequencing (ChIP-Seq). Within the KSEA result, aerobic glycolysis was likely increased from the observation of inhibition of PDC activity via phosphorylation of PDHA1 at Ser232, Ser293, and Ser300 by PDK1 and PDK2. As mentioned above, studies had discovered that APG prevented pyruvate biosynthesis by inhibiting PKM2 (313), inhibited lactate dehydrogenase activity (329, 330) that have a critical role in glycolysis associated with cancer survivability and progression. At high concentrations this even leads to mitochondrial dysfunction in several cell lines (331-333). These events captured an interesting question on how APG impacts energy metabolism in SKOV-3 cell line and further experiments following the metabolite changes in energy-related scope would offer a better understanding of the disruption of the energy metabolic process after APG exposure.

Taken together, APG expressed its antiproliferative activity through distinctive signalling upon cancer cell types leading to similar outcomes by suppression of cell progression, induction of apoptosis, and preventing metastatic activity.

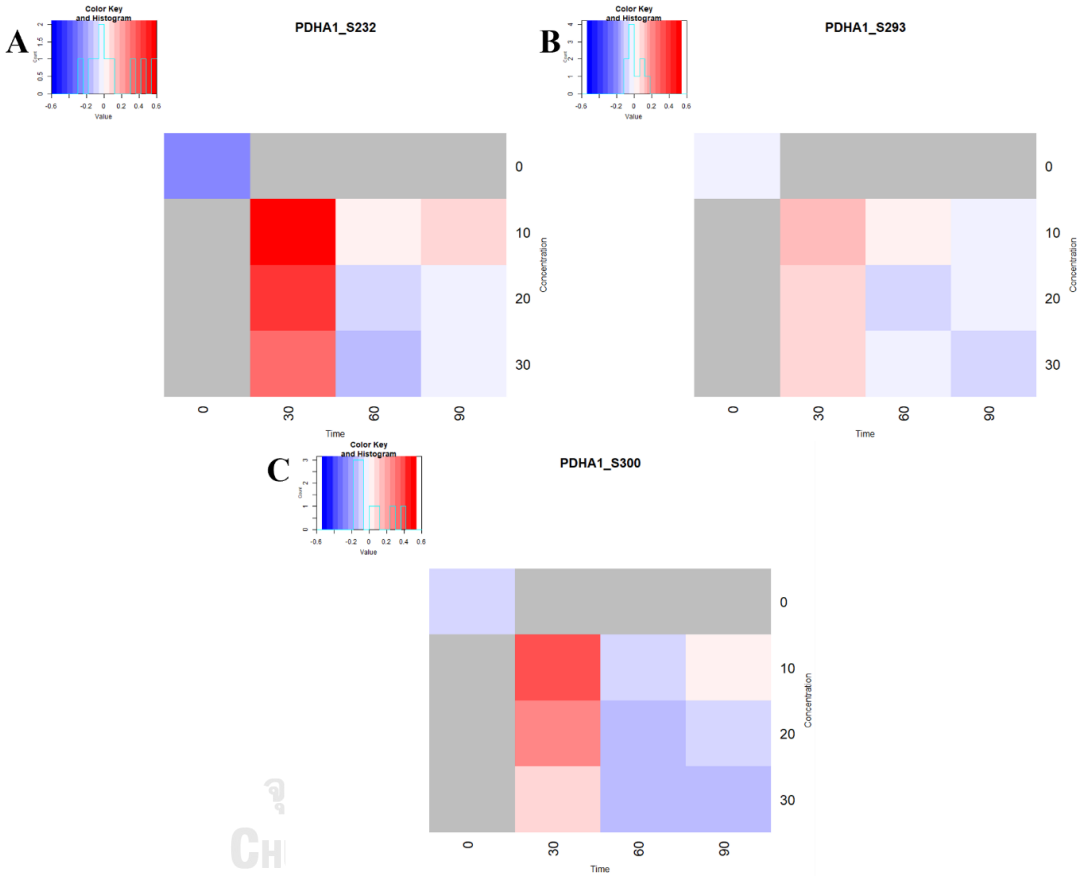

Figure 4.14 Heatmap of significant phosphosites on mitochondrial pyruvate dehydrogenase E1 component subunit alpha.

(A) phospho-PDHA Ser232, (B) phospho-PDHA Ser293, and (C) phospho-PDHA Ser300. X-axis indicated concentration while Y-axis indicated time. Colour represented phosphorylation status where red is hyperphosphorylated and blue is hypophosphorylated.

CHAPTER 5
DISCUSSION

Natural products have been applied into our daily life as crude extracts and purified compounds in the forms of dietary supplements, cosmetics, and other consumables. The increasing demand for natural or organic products including bee products has grown immensely due to a proportion of individuals who desires a better life quality and believes that these products are environmentally safer and nontoxic (334). Nevertheless, their effectiveness and safety remain to be questioned. An example of a well-known natural product that had been reported for no effective outcome is *Gingko biloba*. It has been found in Eastern Asian traditional medicine as a herbal treatment for preventing memory loss. Several *in vitro* and *in vivo* studies showed that the leaves extracts from *G. biloba* expressed neuroprotective effect and enhanced neurogenesis (335-337). However, in a randomised controlled trial, the participant group that received the treatment of 120-mg *G. biloba* extract appeared to have no difference in comparison to the placebo group (338). Bioavailability and pharmacokinetics of the extracts are a concerning issue and possibly explain this observation thus a better drug delivery and controlled release system could address this issue. Moreover, awareness regarding the toxicity of natural products has been recently raised on either natural compounds alone or synergistic with other agents (339) though there were limited numbers of adverse effect reports with mainly no lethal or severe symptoms (340).

APG and α-MG were found as constituent compounds of food and extracts for example wheat, vegetable, mangosteen drinks, and alcoholic beverages (341-343). Nonetheless, the amount and concentration of the compounds in those products were much lower than the effective dose for the treatment of ailments. Studies in mice models found that both compounds exhibit various activities such as protection against renal perfusion and neuroinflammation, antioxidation, antiviral, and anti-tumour activity with oral administration or intraperitoneal injection (344-349). However, a systematic review in human studies has

shown that oral uptake of APG was reported to reach only 30% bioavailability and 1-5 μM of circulating concentration with oral administration, which at this amount is not effective for the treatment of human gastrointestinal diseases and cancers (350). While there were no clinical or randomised controlled trial studies in humans, pharmacokinetics studies of α-MG administration in mice appeared that α-MG had poor adsorption activity by oral administration, the absorption of α-MG in mangosteen extract was higher than purified α-MG, and the tissue distribution of α-MG was associated with constituents of the extract and administration routes (83, 351). Regarding the safety of APG and α-MG, APG is considered to have low cytotoxicity although an overdose of APG could lead to muscle relaxation and sedation (352) whereas α-MG exposure at a high amount leads to cytotoxicity and lethal dose in animal models. A study in Wistar rats showed that oral administration of α-MG with more than 500mg/kg/day caused chronic liver degenerative and kidney disease (353). In addition, a lethal dose of intraperitoneal administration of pure α-MG was observed at more than 50mg/kg of mice (351). Moreover, α-MG exposure in zebrafish embryos affected the development of the embryo and liver, which might reflect the consideration of usage of α-MG during pregnancy (354). Furthermore, APG and α-MG had proved to express synergistic effects in treatment with several drugs and chemical agents by sensitizing the targets thus allowing possibilities of using available drugs to treat drug-resistant cancers cells (123, 355, 356). In addition to the synergistic effect, both compounds also exhibited a protective effect that could prevent and alleviate the adverse effects from the ailment treatments at an appropriate concentration and exposure length of time (357, 358). APG had been proven to protect against kidney injury caused by doxorubicin treatment (359) and oxidative stress by nickel oxide nanoparticles that could apply for multiple purposes (360) in rodent models. Taken together, the usage of APG and α-MG as medicinal agents for treatment or combination effects for a better outcome or protection for adverse effects should be

considered about the bioavailability and pharmacokinetics of the compounds that can be improved through advanced drug delivery system.

Drug discovery from natural products has re-emerged due to the availability of high throughput technology (361). Drug delivery systems had been developed to enhance the effectiveness of the drugs while preventing undesired consequences during or after the medication promoting a succession of the treatment and well-being of the patients. Since there are advances in the establishment of nanoparticle drug delivery systems, several systems including combinatorial therapeutic regiments have been applied in both compounds to enhance solubility, control the releasing sites and time, increase the compound bioavailability, extend the circulation time, and decrease the adverse effect (362, 363). This concept in combining with precision medicine knowledge to target specific cells has been shown recently to be successful with APG and α-MG treatments in *in vivo* studies enhancing anti-cancer activity (364, 365) and preventing amyloid-beta aggregation that leads to Alzheimer's disease (366) by mixing nanocarrier molecules with specific counterpart molecules or ligands of targeted receptors and the compounds. These approaches opened up opportunities and solved the prolonged controversy of a compound which reported to contain interesting bioactivities *in vitro* but had been limited in its application due to low water solubilities like α-MG, low permeability, and high conversion and excretion rate.

Personalised or precision medicine has been coming of the age in the treatment of several diseases, especially oncology. This medication technique is associated with specialised diagnostics and analysis of omics data of a person's biological status in determining disease subpopulation or subgroups in order to directly treat the main cause or target of the disease (367). In 1998, this concept was turned into the first drug named trastuzumab that was introduced for the treatment of HER2-overexpressing breast cancer (368). As mentioned earlier, several cancers have gained resistance to pharmacological treatment through known and unknown mechanisms that lead to more sophistication in

medication of the recurrence cancer (369). However, the limitations of this healthcare approach are patient accessibility due to the high cost and availability of specific drugs for the treatment. Hence, herbal medicine alone or in cotreatment with conventional anticancer agents could be an option to solve these limitations (370). As described above, APG and α-MG express synergistic effects with anticancer agents through sensitizing the resistant population of the cancer cells to be susceptible to the drug treatment. Recent advances in next generation sequencing, bioinformatics tools, and cell culture technology allow this hypothesis to happen by reducing the time and cost to spend on diagnostics for drug targets and providing an experimental platform for testing the drug response efficiency of cotreatment using patient-derived cancer organoids that are more closely related to the illness than cancer cell lines (371). Nonetheless, this idea remains to be proved in clinical trials for effectiveness and safety.

Altogether, the study of bioactivities from the extracts of bee products to purified compounds studies had led us to this study in discovering antiproliferation effect of APG and α-MG in breast and ovarian cancer cell lines. Then, further investigation of APG effect on cellular signalling pathway provided an interesting concept of how APG reshaped the phosphoprotein network in SKOV-3 at the early phase to achieve the anticancer scheme. Many interesting compounds from natural products are still in discovery for their bioactivities and could benefit human well-being. However, there is still a lot of experiments to be done before these compounds could be used and with a help of recent technology the age of using them in the treatment or co-treatment of cancers and other diseases could be happening not so long in the future.

APPENDICES

Appendix A: Boxplots and PCA plots of various normalization approaches on reporter ion intensity from the first replicate

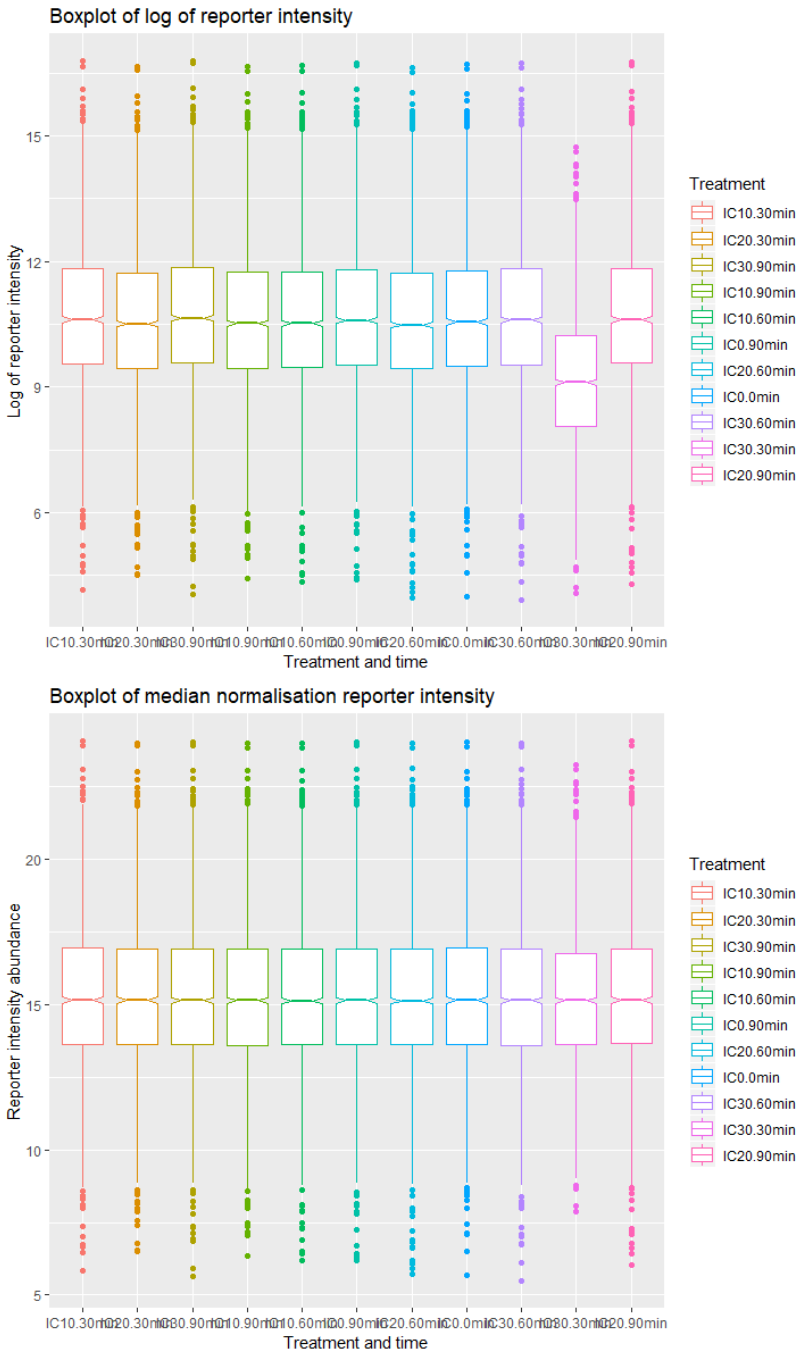

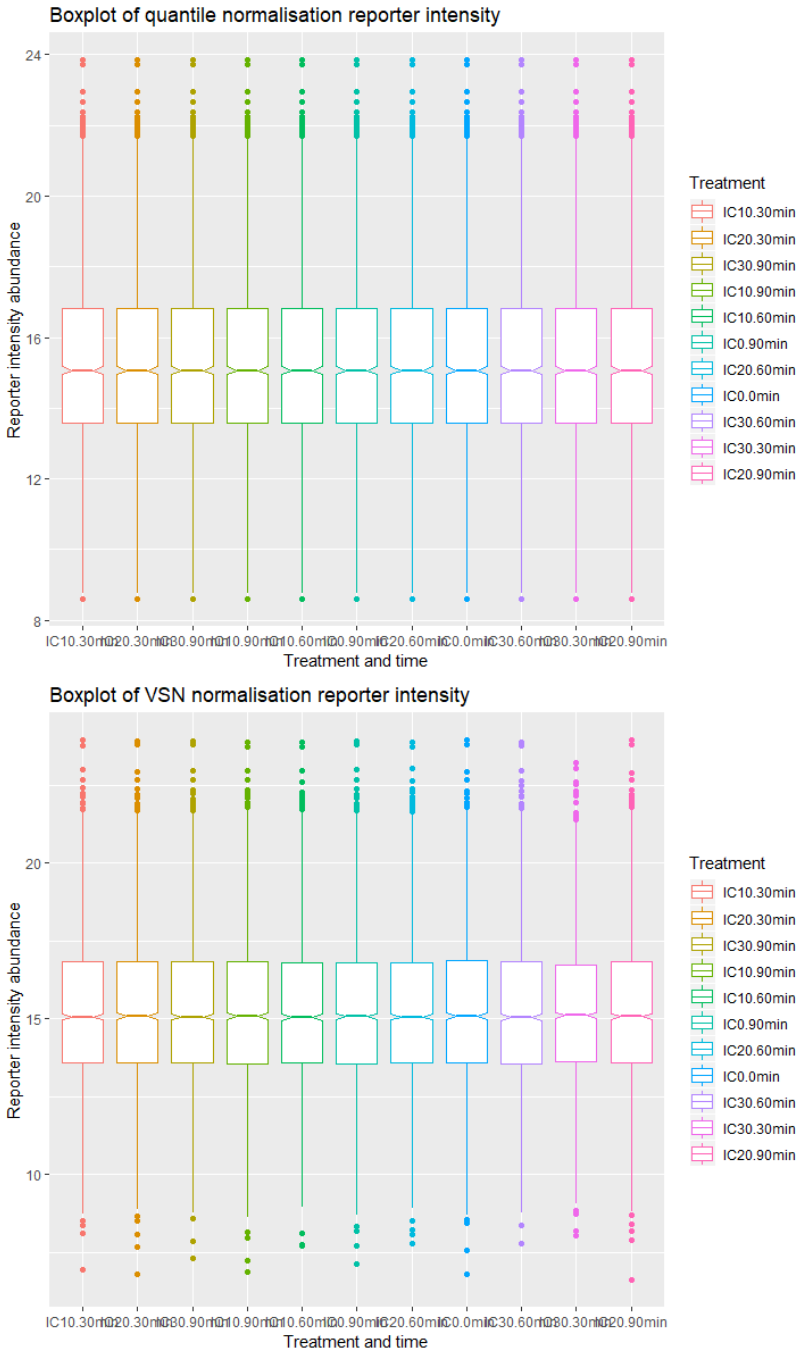

Figure A1 Boxplots of log-transformed, median sweeping normalisation, quantile normalisation, and variance stabilising normalisation.

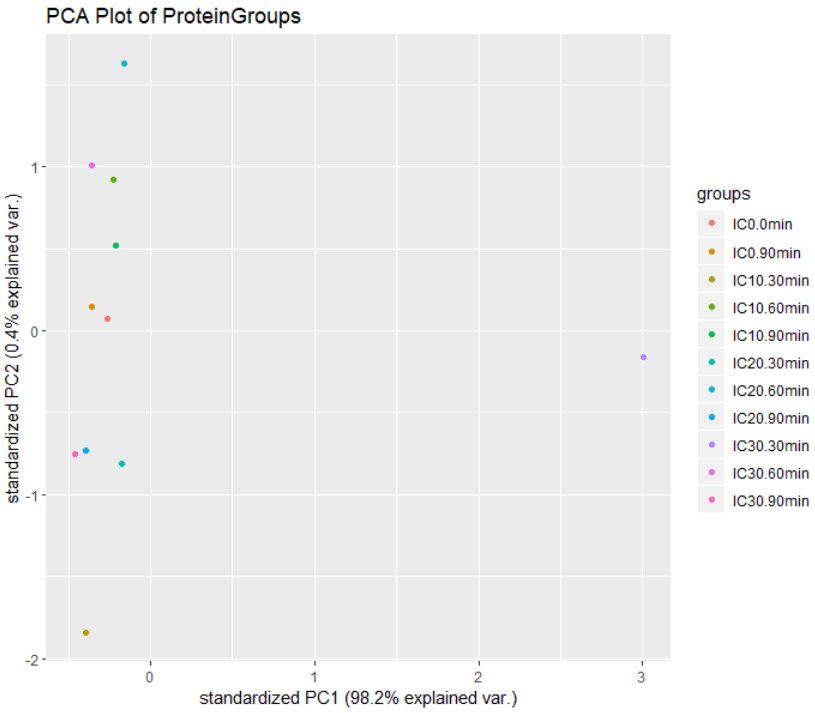
PCA Plot of ProteinGroups
standardized PC2 (0.4% explained var.)
standardized PC1 (98.2% explained var.)
groups
IC0.0min
IC0.90min
IC10.30min
IC10.60min
IC10.90min
IC20.30min
IC20.60min
IC20.90min
IC30.30min
IC30.60min
IC30.90min

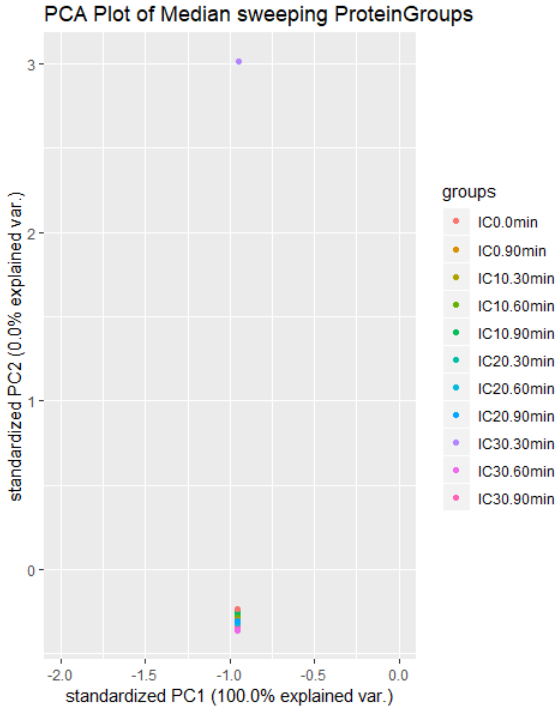
PCA Plot of Median sweeping ProteinGroups
standardized PC2 (0.0% explained var.)
standardized PC1 (100.0% explained var.)
groups
IC0.0min
IC0.90min
IC10.30min
IC10.60min
IC10.90min
IC20.30min
IC20.60min
IC20.90min
IC30.30min
IC30.60min
IC30.90min

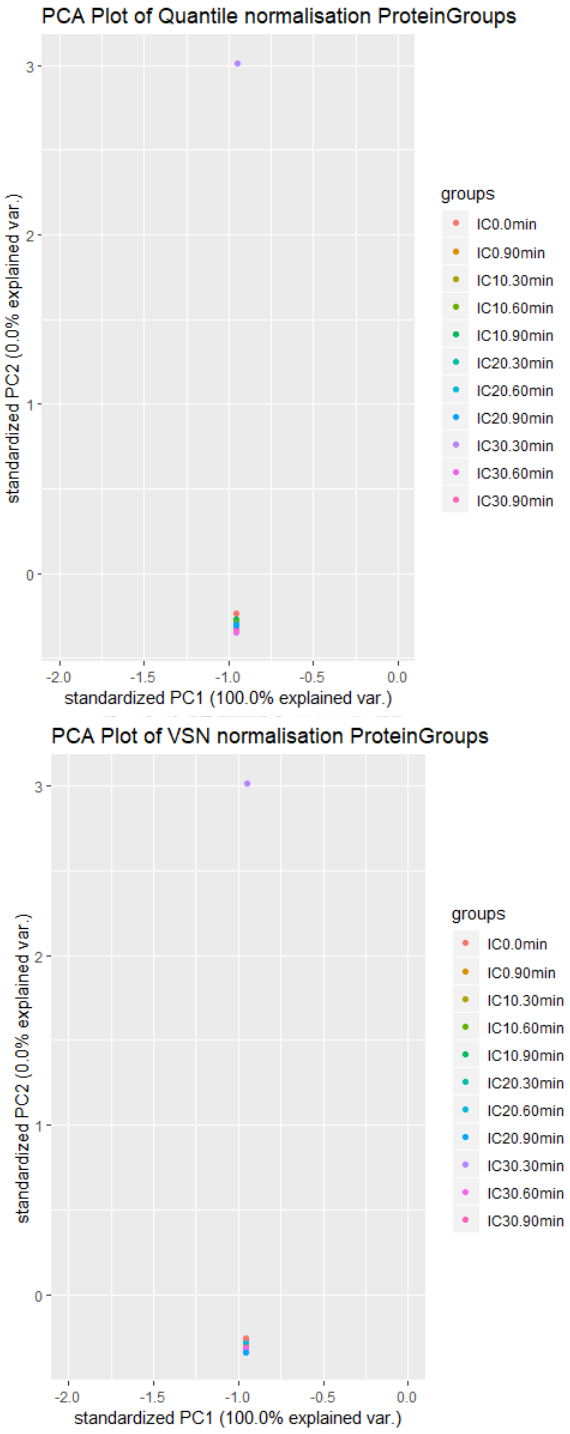

Figure A2 PCA plots of log-transformed, median sweeping normalisation, quantile normalisation, and variance stabilising normalisation.

Appendix B: DAVID functional annotation analysis of the significances from whole data analysis

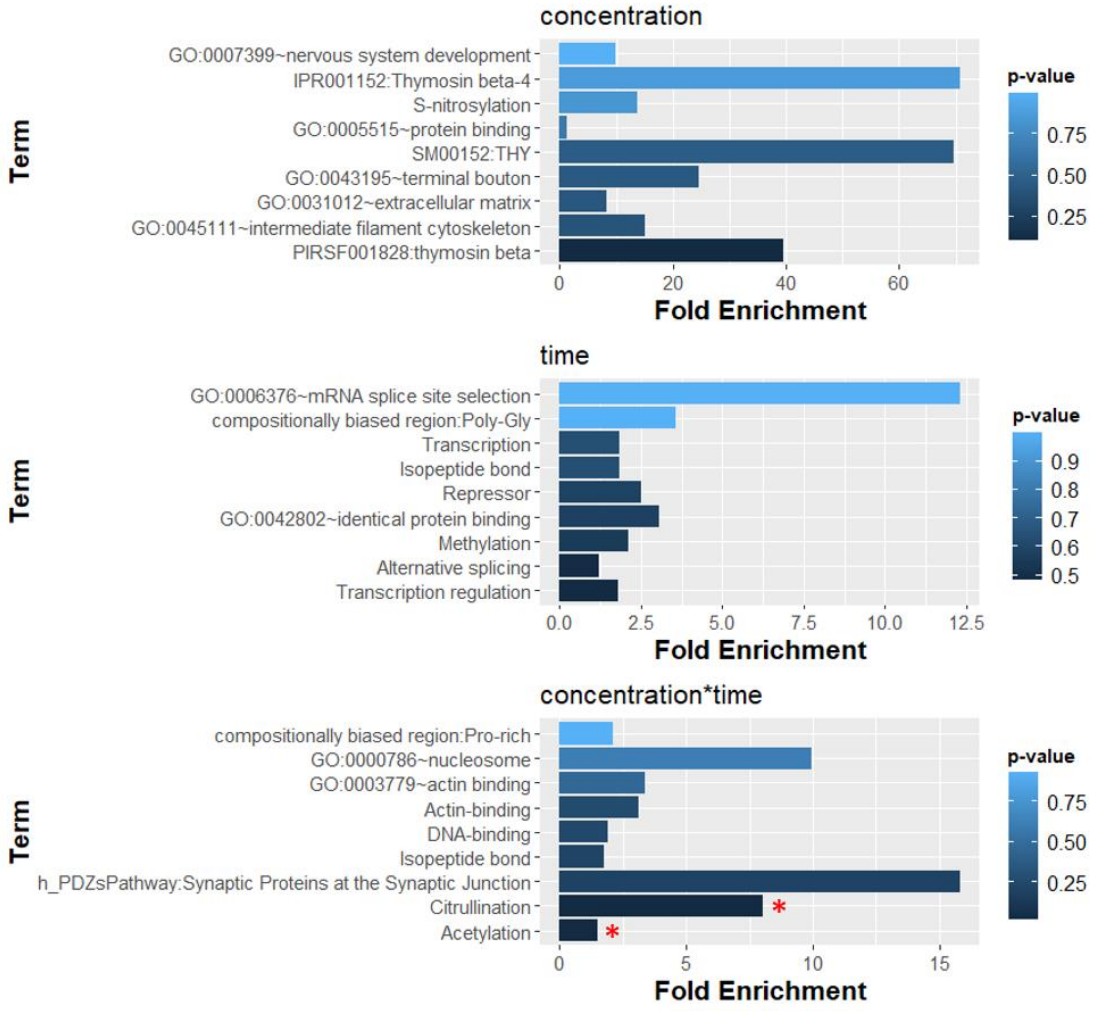

Figure B1 Boxplot of top 10 terms found from DAVID functional annotation analysis

Table B1. Significant clustering group from DAVID results of significant terms from time factor list of complete data analysis

ANNOTATION CLUSTER 1		ENRICHMENT SCORE: 1.8283378688095935									
CATEGORY	Term	Count	%	PValue	Genes	List Total	Pop Hits	Pop Total	Fold Enrichment	Benjamini	FDR
UP_KEYWORDS	Citrullination	7	9.589041	1.31E-04	P10412, Q9H6F5, P16402, Q8IYB3, P42166, Q9BQG0, Q71DI3	73	22	1844	8.03736	0.018251	0.154207
GOTERM_CC_DIRECT	GO:0000786~nucleosome	4	5.479452	0.005842	P10412, O75367, P16402, Q71DI3	71	10	1768	9.960563	0.608352	6.829883
GOTERM_MF_DIRECT	GO:0031490~chromatin DNA binding	4	5.479452	0.01592	P10412, O75367, P16402, Q7LBC6	70	14	1738	7.093878	0.480019	17.66668
GOTERM_BP_DIRECT	GO:0006334~nucleosome assembly	4	5.479452	0.063478	P10412, O75367, P16402, Q71DI3	67	24	1697	4.221393	0.999654	60.96197
GOTERM_BP_DIRECT	GO:0000122~negative regulation of transcription from RNA polymerase II promoter	9	12.32877	0.106891	P10412, O75367, Q9Y618, P26358, P67809, P51608, P16402, Q71DI3, Q96RK0	67	125	1697	1.823642	0.997767	80.2381
UP_KEYWORDS	Chromosome	7	9.589041	0.129991	P10412, O75367, O75151, P16402, P42166, Q71DI3, Q96KR1	73	89	1844	1.986763	0.805282	80.70024

Appendix C: Figure C Dot plots of enriched term from significant phosphosites.

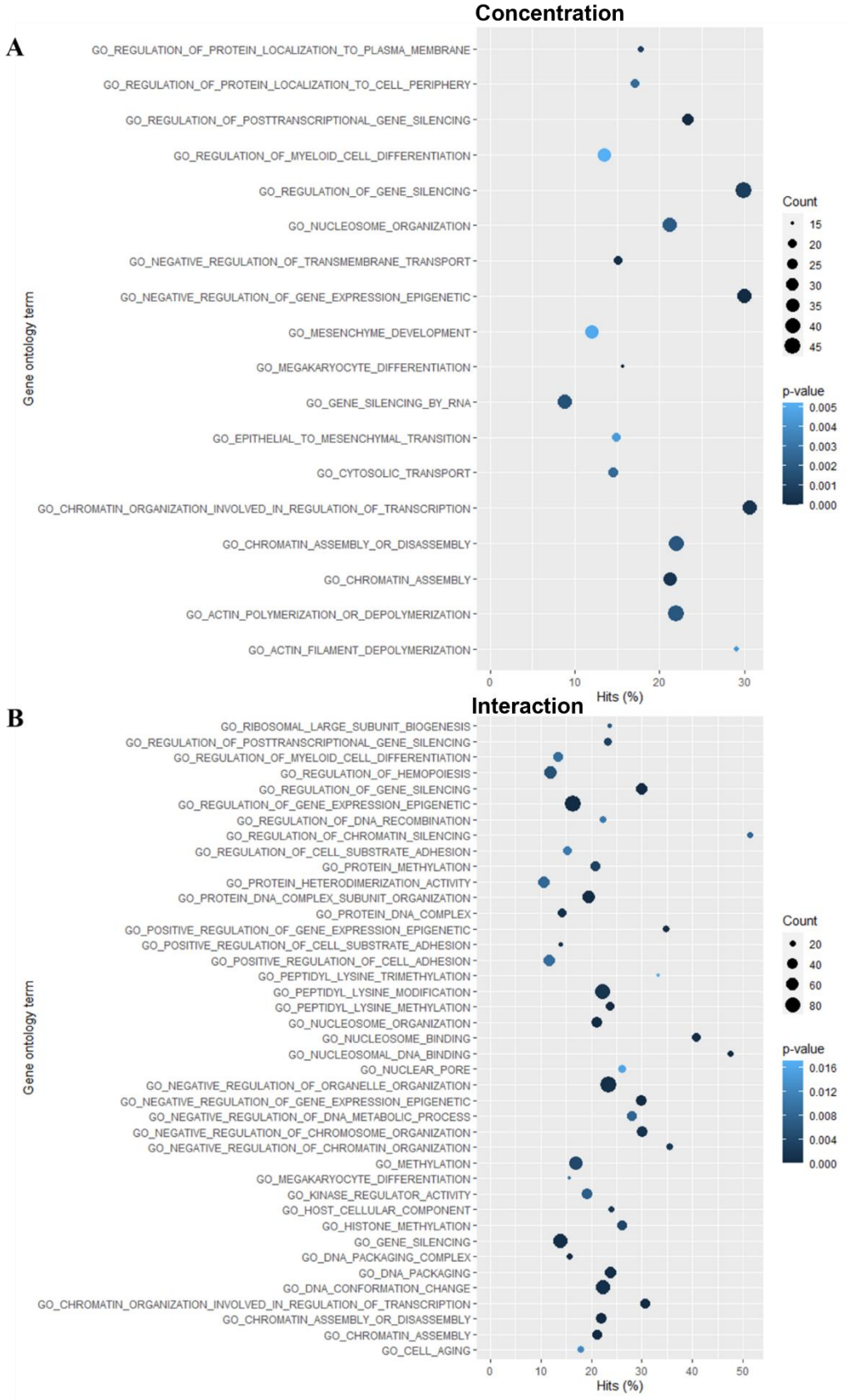

Appendix D: CDK1-associated methylation-related phosphosites of 30 minutes NetworKIN map from concentration (Table D1) and time (Table D2) list

Table D1. CDK1-associated methylation-related phosphosites of 30 minutes NetworKIN map from concentration list

Protein ID	Entry name	Protein names	Gene names	Length	significant phosphosites	NetworKIN score	coefficient value
Q9BYG3	MK67I_HUMAN	MKI67 FHA domain-interacting nucleolar phosphoprotein (Nucleolar phosphoprotein Nopp34) (Nucleolar protein interacting with the FHA domain of pKI-67) (hNIFK)	NIFK MKI67IP NOPP34	293	T223	2.32935	29.25318
Q15149	PLEC_HUMAN	Plectin (PCN) (PLTN) (Hemidesmosomal protein 1) (HD1) (Plectin-1)	PLEC PLEC1	4684	S1435	18.85644	-26.6674
P16949	STMN1_HUMAN	Stathmin (Leukemia-associated phosphoprotein p18) (Metablastin) (Oncoprotein 18) (Op18) (Phosphoprotein p19) (pp19) (Prosolin) (Protein Pr22) (pp17)	STMN1 C1orf215 LAP18 OP18	149	S25	17.82557	-22.1163
P42166	LAP2A_HUMAN	Lamina-associated polypeptide 2, isoform alpha (Thymopoietin isoform alpha) (TP alpha) (Thymopoietin-related peptide isoform alpha) (TPRP isoform alpha) [Cleaved into: Thymopoietin (TP) (Splenin); Thymopentin (TP5)]	TMPO LAP2	694	S351	6.1784	-27.2246
P19338	NUCL_HUMAN	Nucleolin (Protein C23)	NCL	710	T121	15.55237	38.08027
P02545	LMNA_HUMAN	Prelamin-A/C [Cleaved into: Lamin-A/C (70 kDa lamin) (Renal carcinoma antigen NY-REN-32)]	LMNA LMN1	664	S414	6.610232	-74.2745
P21333	FLNA_HUMAN	Filamin-A (FLN-A) (Actin-binding protein 280) (ABP-280) (Alpha-filamin) (Endothelial actin-binding protein) (Filamin-1) (Non-muscle filamin)	FLNA FLN FLN1	2647	S1533	2.42719	-35.7645
Q12888	TP53B_HUMAN	TP53-binding protein 1 (53BP1) (p53-binding protein 1) (p53BP1)	TP53BP1	1972	S366	7.427128	-21.9601
P17096	HMGA1_HUMAN	High mobility group protein HMG-I/HMG-Y (HMG-I(Y)) (High mobility group AT-hook protein 1) (High mobility group protein A1) (High mobility group protein R)	HMGA1 HMGIY	107	T53	20.46458768	29.18440647
					T78	20.46458768	22.34517821
Q9H8Y8	GORS2_HUMAN	Golgi reassembly-stacking protein 2 (GRS2) (Golgi phosphoprotein 6) (GOLPH6) (Golgi reassembly-stacking protein of 55 kDa) (GRASP55) (p59)	GORASP2 GOLPH6	452	T433	3.749519	-104.577

Table D2. CDK1-associated methylation-related phosphosites of 30 minutes NetworKIN map from time list

Protein ID	Entry name	Protein names	Gene names	Length	significant phosphosites	NetworKIN score	coefficient value
Q9BYG3	MK67I_HUMAN	MKI67 FHA domain-interacting nucleolar phosphoprotein (Nucleolar phosphoprotein Nopp34) (Nucleolar protein interacting with the FHA domain of pKI-67) (hNIFK)	NIFK MKI67IP NOPP34	293	T223	2.32935	-51.6499
Q15149	PLEC_HUMAN	Plectin (PCN) (PLTN) (Hemidesmosomal protein 1) (HD1) (Plectin-1)	PLEC PLEC1	4684	S4613	12.92775	-65.0985
P16949	STMN1_HUMAN	Stathmin (Leukemia-associated phosphoprotein p18) (Metablastin) (Oncoprotein 18) (Op18) (Phosphoprotein p19) (pp19) (Prosolin) (Protein Pr22) (pp17)	STMN1 C1orf215 LAP18 OP18	149	S25	17.82557	111.0953
P19338	NUCL_HUMAN	Nucleolin (Protein C23)	NCL	710	T121	15.55237	-25.639
P02545	LMNA_HUMAN	Prelamin-A/C [Cleaved into: Lamin-A/C (70 kDa lamin) (Renal carcinoma antigen NY-REN-32)]	LMNA LMN1	664	S414	6.610232	-45.4167
Q12888	TP53B_HUMAN	TP53-binding protein 1 (53BP1) (p53-binding protein 1) (p53BP1)	TP53BP1	1972	S366	7.427128	28.87632
P17096	HMGA1_HUMAN	High mobility group protein HMG-I/HMG-Y (HMG-I(Y)) (High mobility group AT-hook protein 1) (High mobility group protein A1) (High mobility group protein R)	HMGA1 HMGIY	107	T53	20.46458768	-35.45980869
					T78	20.46458768	-40.26003116
Q9H8Y8	GORS2_HUMAN	Golgi reassembly-stacking protein 2 (GRS2) (Golgi phosphoprotein 6) (GOLPH6) (Golgi reassembly-stacking protein of 55 kDa) (GRASP55) (p59)	GORASP2 GOLPH6	452	T433	3.749519	102.9277

Appendix E: Heatmap of interesting phosphosites from phosphoproteomics analysis. X-axis indicated time while Y-axis indicated inhibition concentration used in the experiment. The phosphorylation changes were indicated in spectrum from hypophosphorylation in blue to hyperphosphorylation in red.

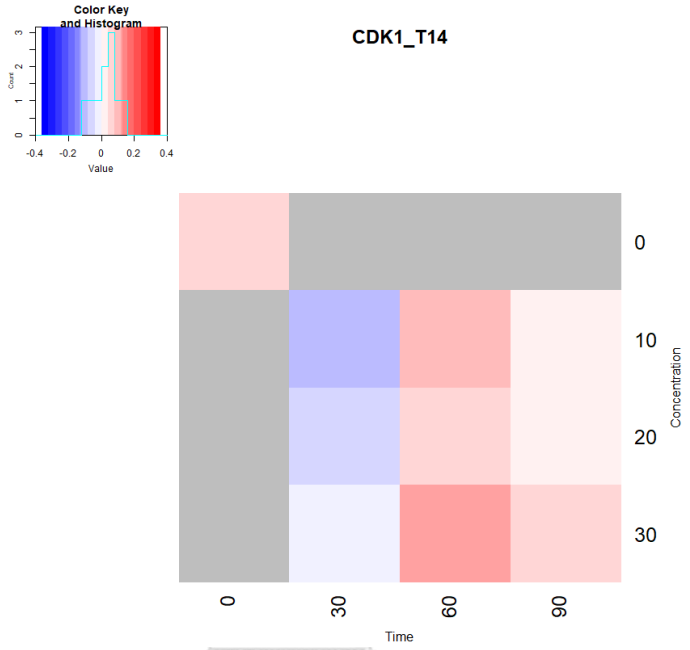

(1) phospho-CDK1-Thr14

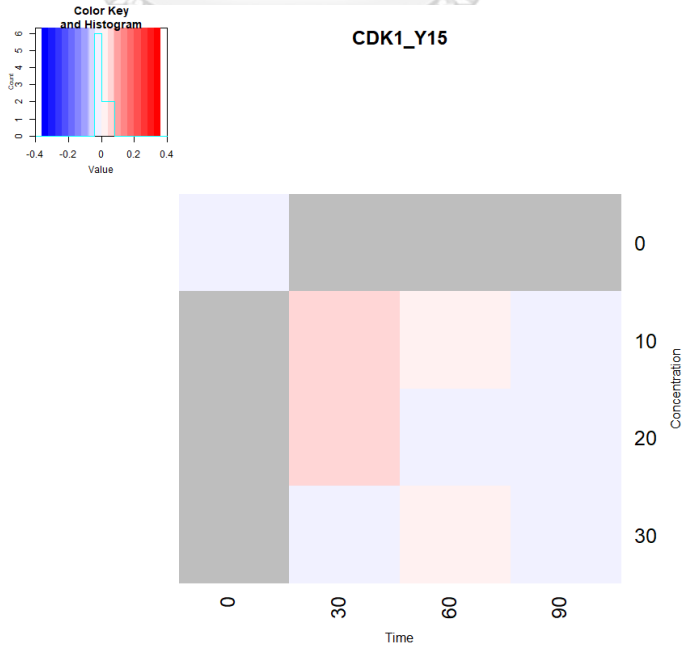

(2) phospho-CDK1-Tyr15

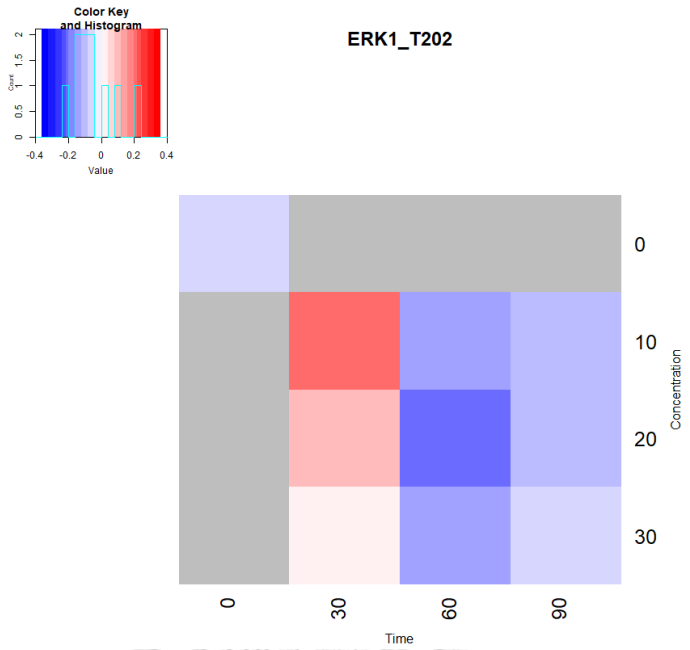

(3) phospho-Erk1-Thr202

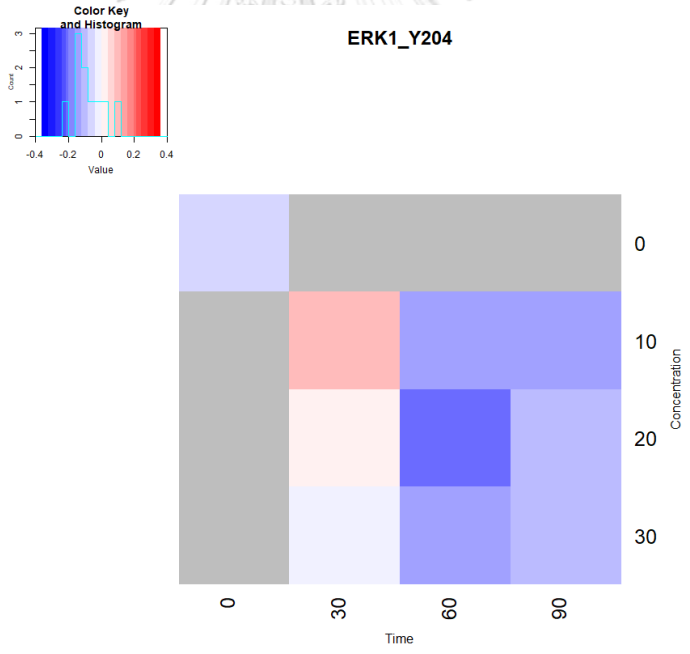

(4) phospho-Erk1-Tyr204

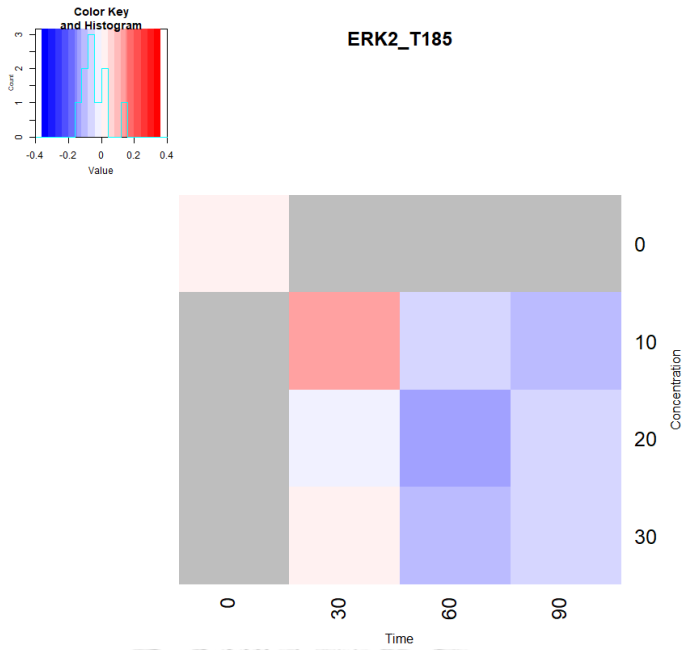

(5) phospho-Erk2-Thr185

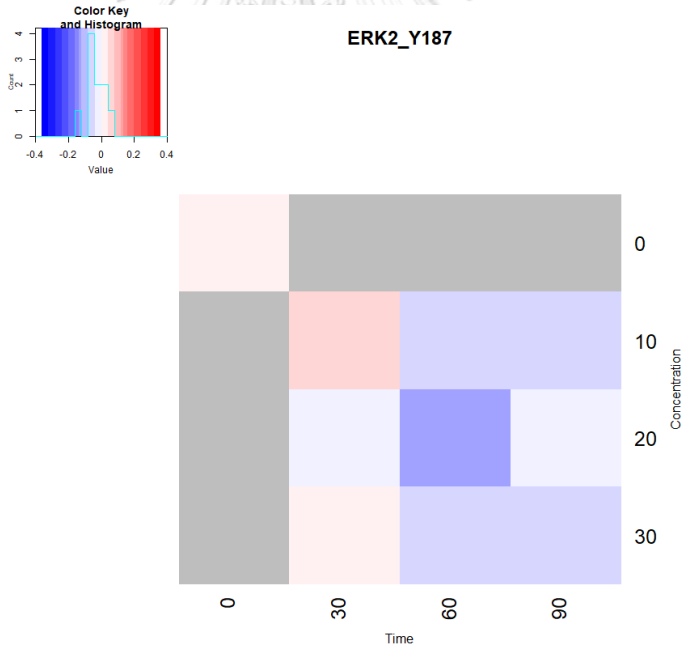

(6) phospho-Erk2-Tyr187

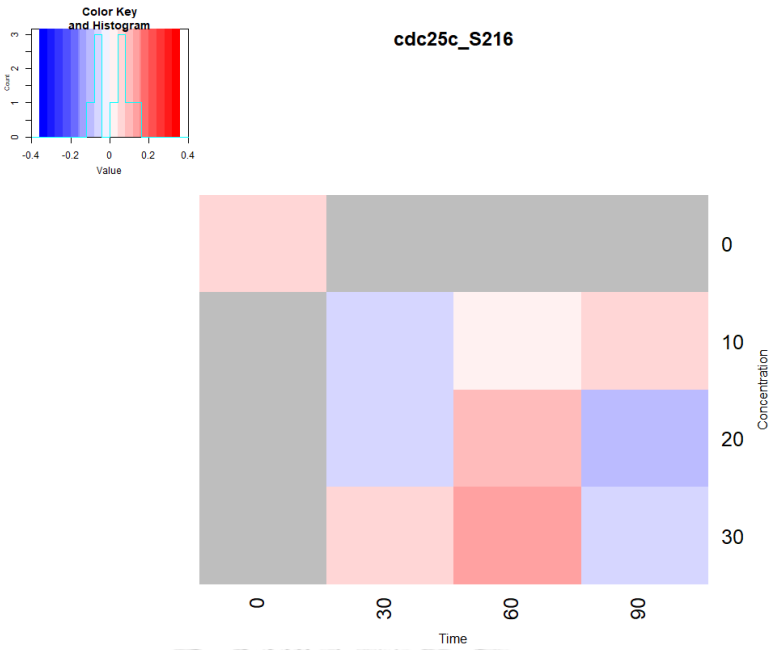

(7) phospho-Cdc25C-Ser216

Appendix F: Heatmaps of expression profiles of possible TF-targeted significant genes from MCF7 dataset.

X-axis indicated treatments. The first four columns were control while the last four were APG. Y-axis is genes. Colour indicated expression level where red was upregulated genes and blue was downregulated genes.

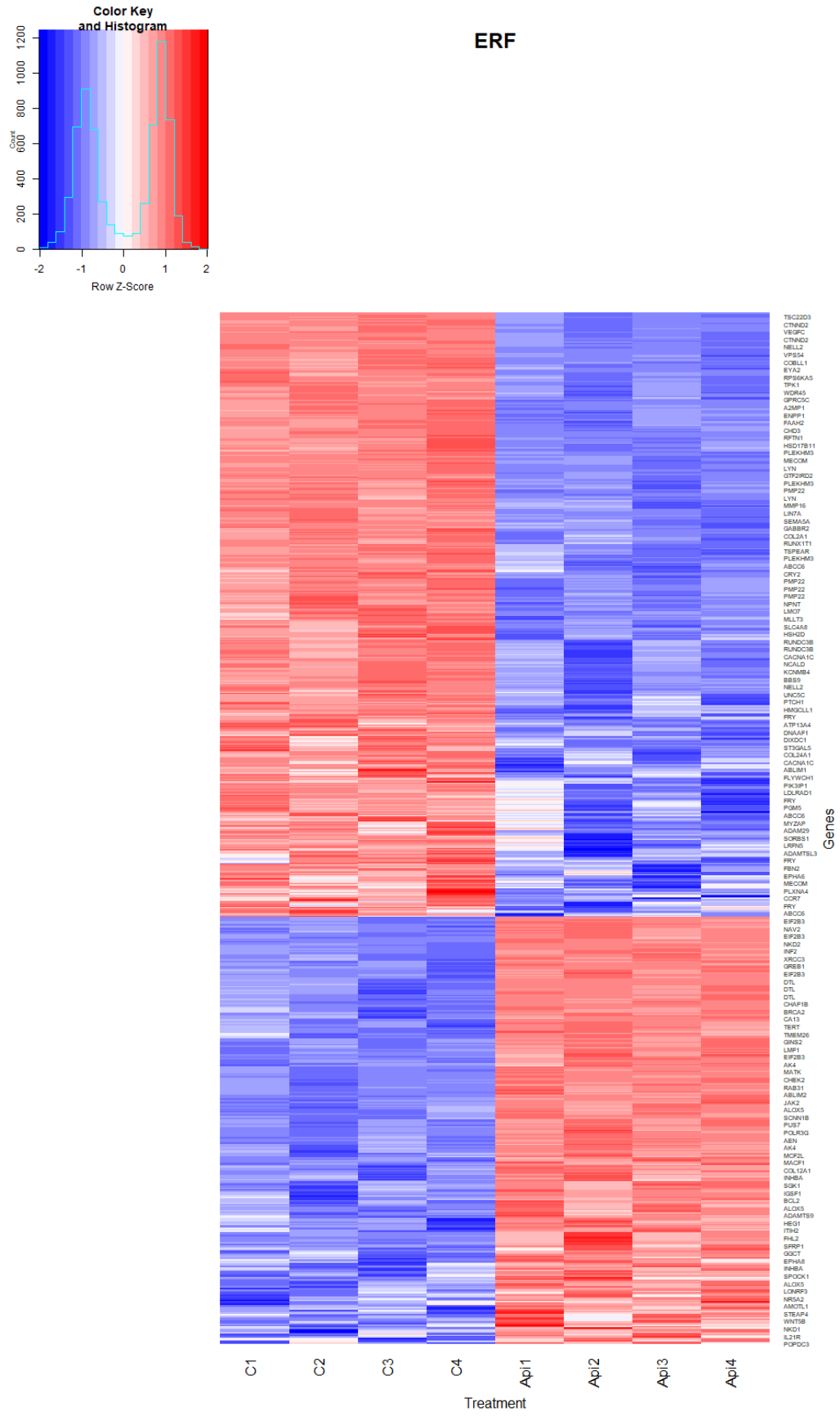
Color Key
and Histogram
Count
0
200
400
600
800
1000
1200
-2
-1
0
1
2
Row Z-Score
ERF
Genes
C1
C2
C3
C4
Api1
Api2
Api3
Api4
Treatment

(1) ERF

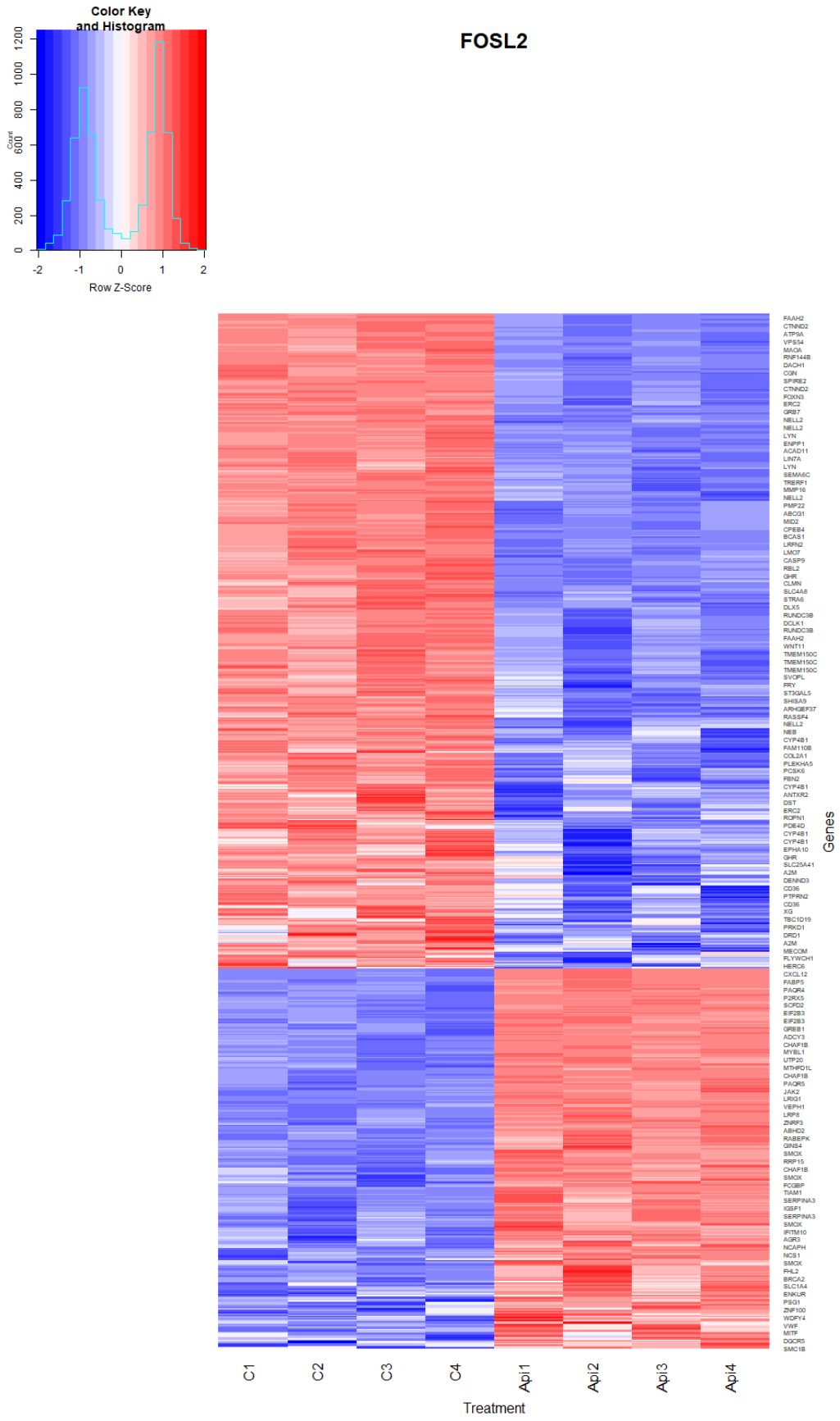
Color Key
and Histogram
Count
0
200
400
600
800
1000
1200
-2
-1
0
1
2
Row Z-Score
FOSL2
Genes
C1
C2
C3
C4
Api1
Api2
Api3
Api4
Treatment

(2) FOSL2

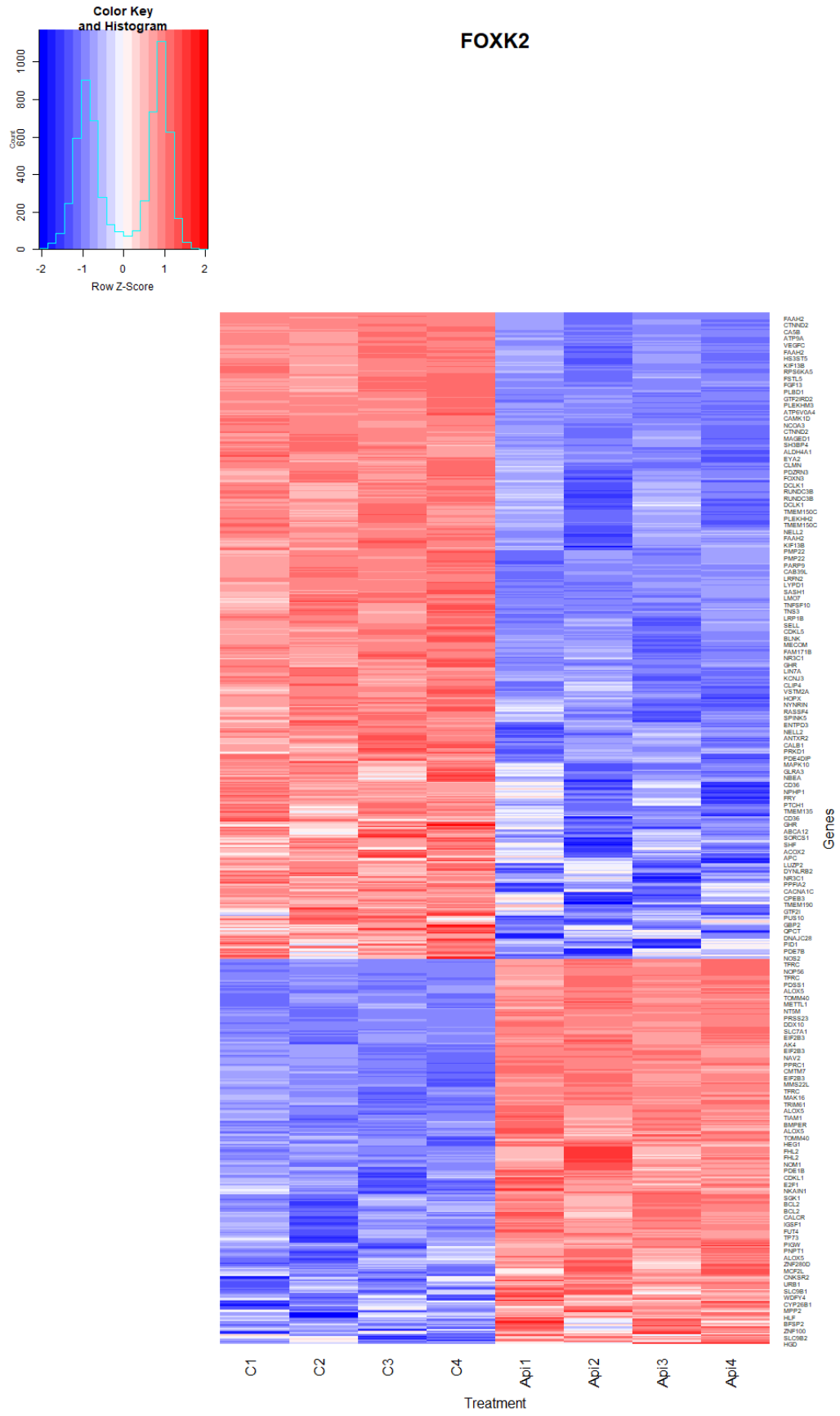
Color Key
and Histogram
Count
0
200
400
600
800
1000
-2
-1
0
1
2
Row Z-Score
FOXK2
Genes
C1
C2
C3
C4
Api1
Api2
Api3
Api4
Treatment

(3) FOXK2

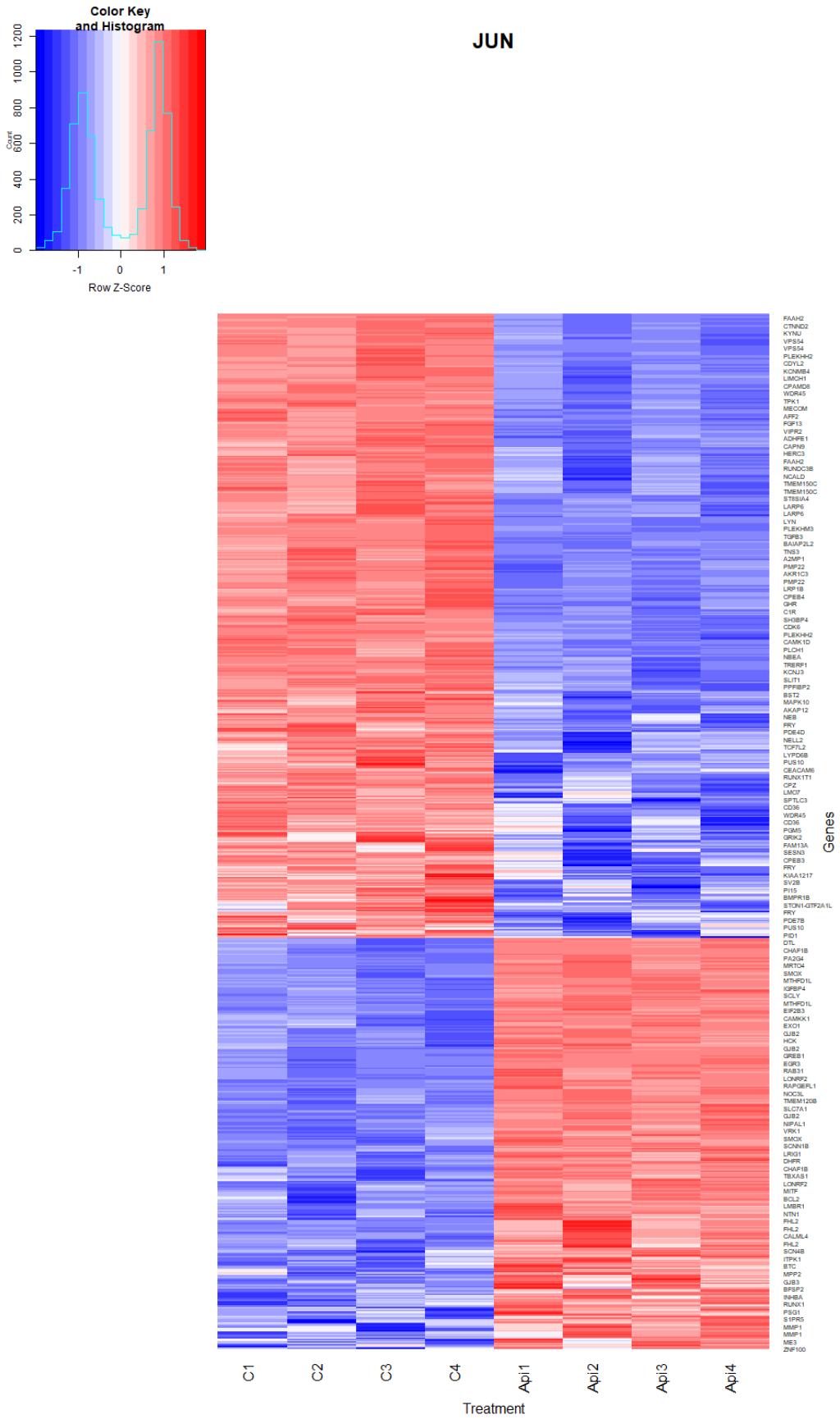
Color Key
and Histogram
Count
0
200
400
600
800
1000
1200
-1
0
1
Row Z-Score
JUN
Genes
C1
C2
C3
C4
Api1
Api2
Api3
Api4
Treatment

(4) JUN

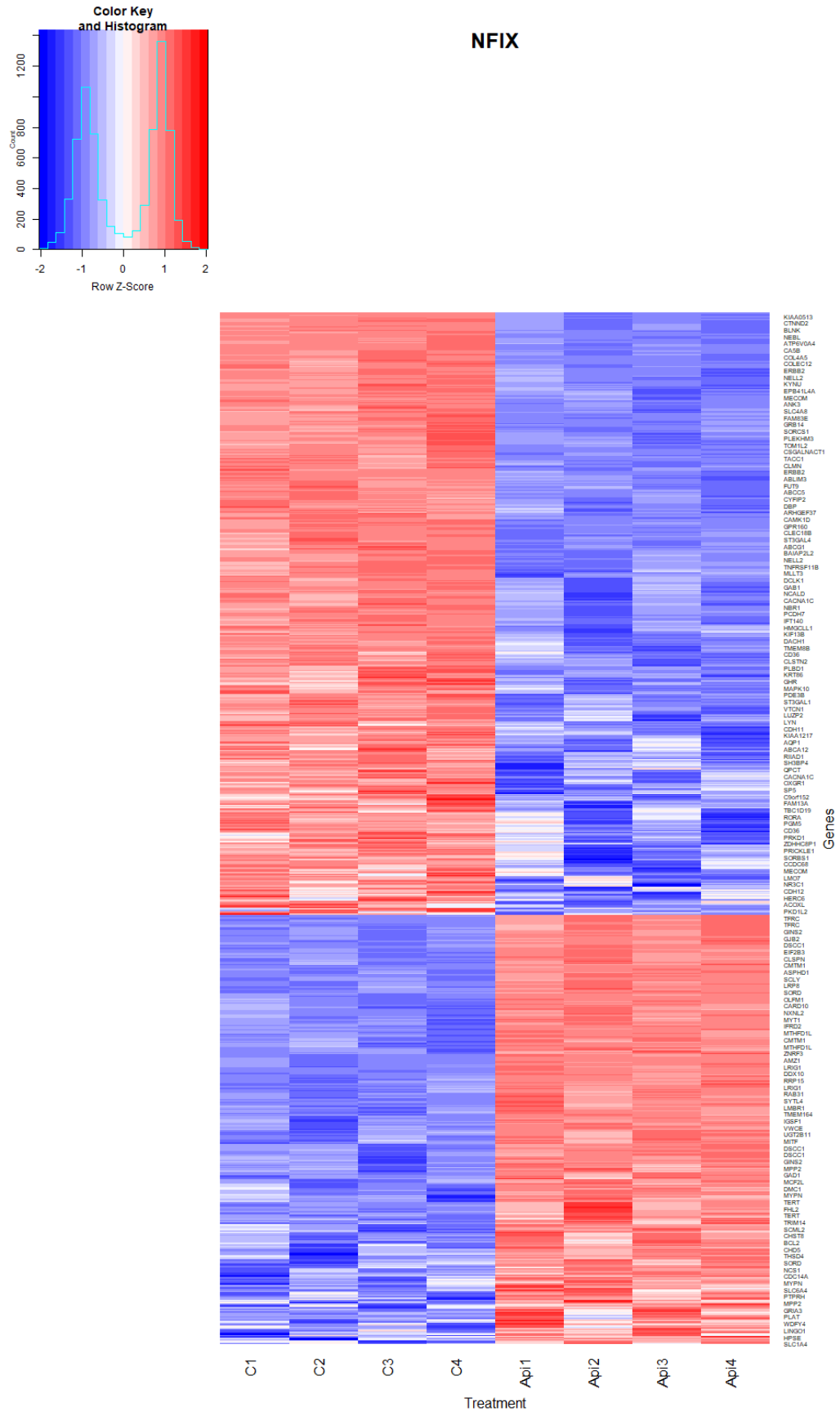
Color Key
and Histogram
Count
0
200
400
600
800
1200
-2
-1
0
1
2
Row Z-Score
NFIX
Genes
C1
C2
C3
C4
Api1
Api2
Api3
Api4
Treatment

(5) NFIX

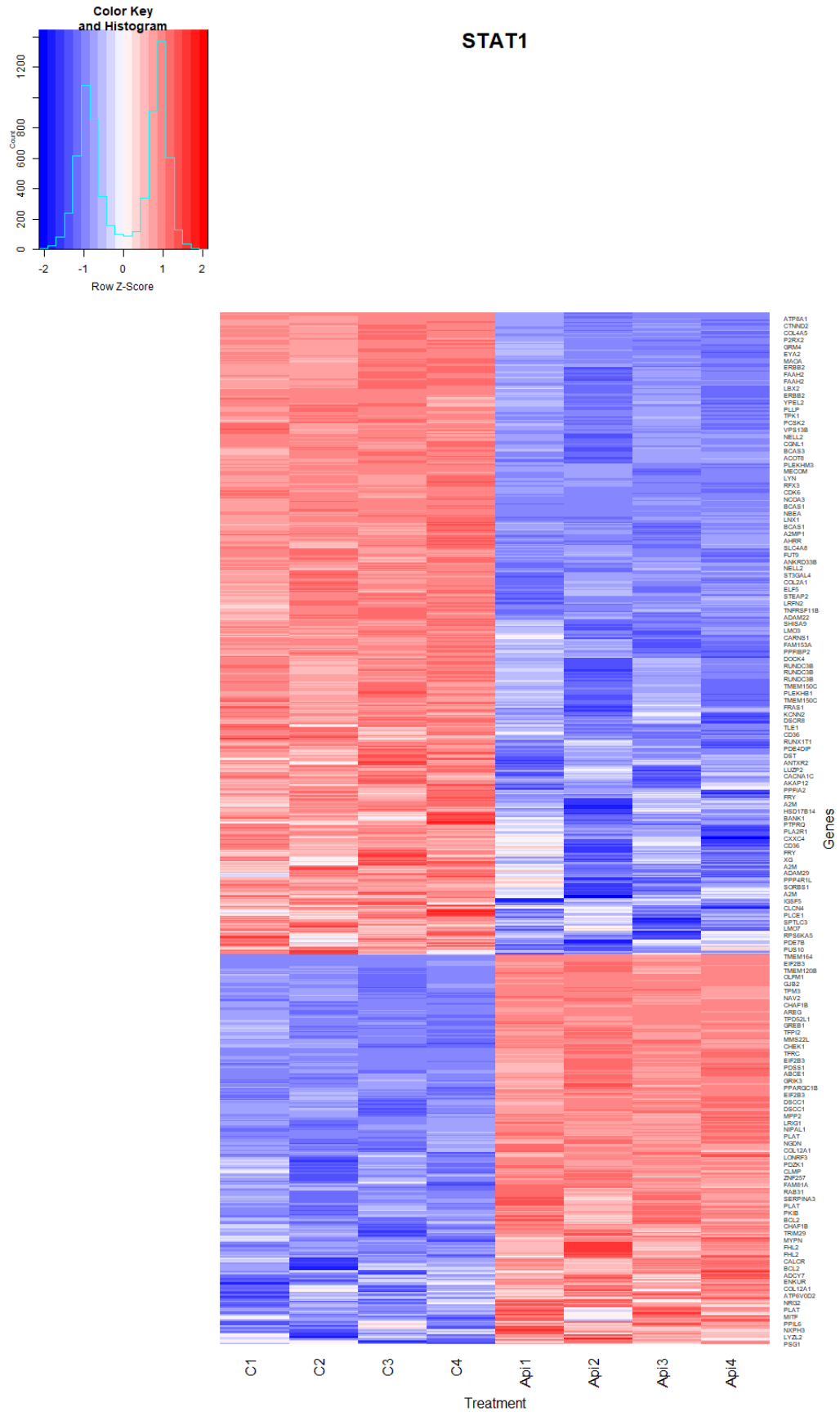
Color Key
and Histogram
Count
0
200
400
600
800
1200
-2
-1
0
1
2
Row Z-Score
STAT1
Genes
C1
C2
C3
C4
Api1
Api2
Api3
Api4
Treatment

(6) STAT1

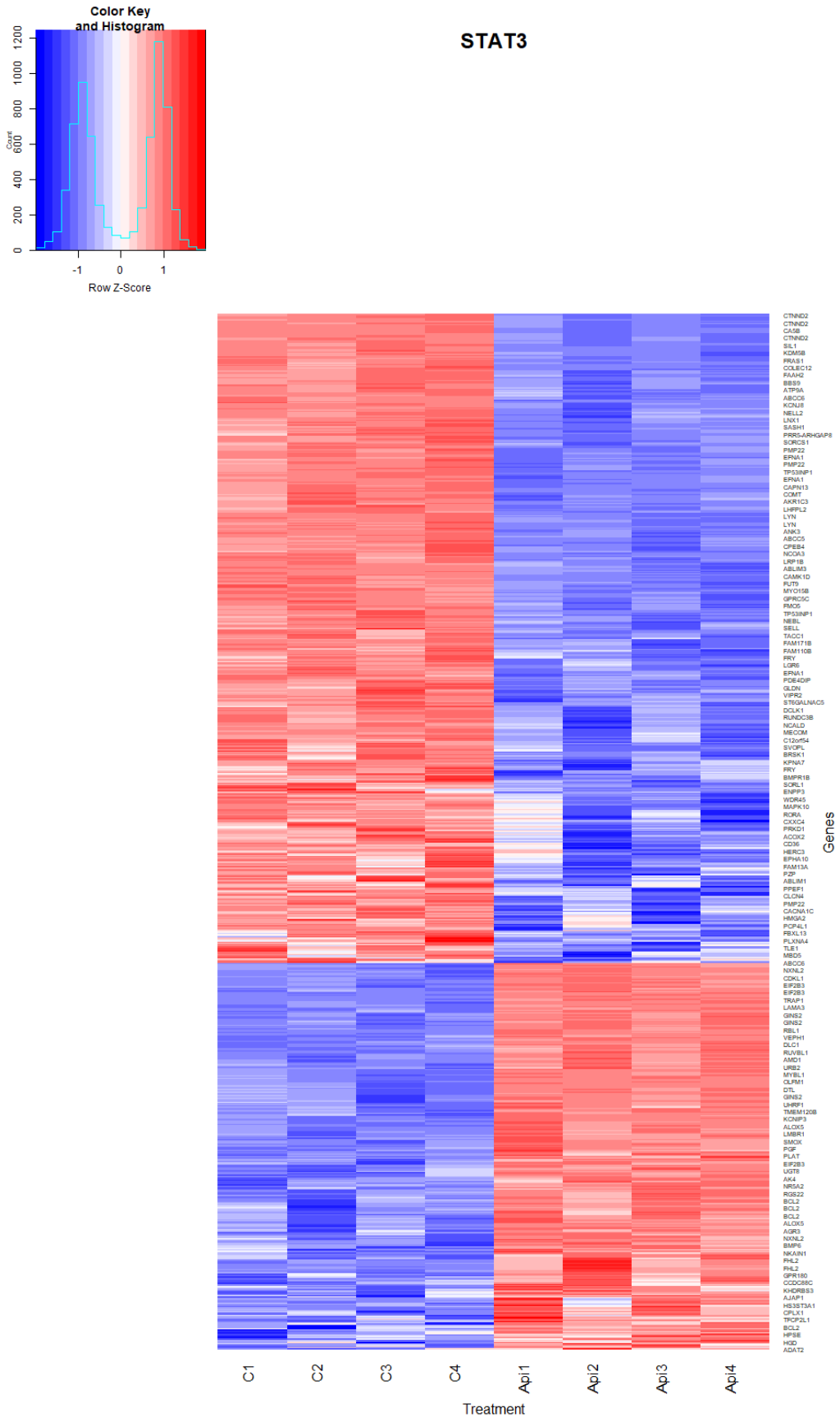
Color Key
and Histogram
Count
0
200
400
600
800
1000
1200
-1
0
1
Row Z-Score
STAT3
Genes
C1
C2
C3
C4
Api1
Api2
Api3
Api4
Treatment

(7) STAT3

Appendix G: Heatmaps of expression profiles of possible TF-targeted significant genes from MDA-MB-231 dataset.

X-axis indicated treatments. The first four columns were control while the last four were APG. Y-axis is genes. Colour indicated expression level where red was upregulated genes and blue was downregulated genes.

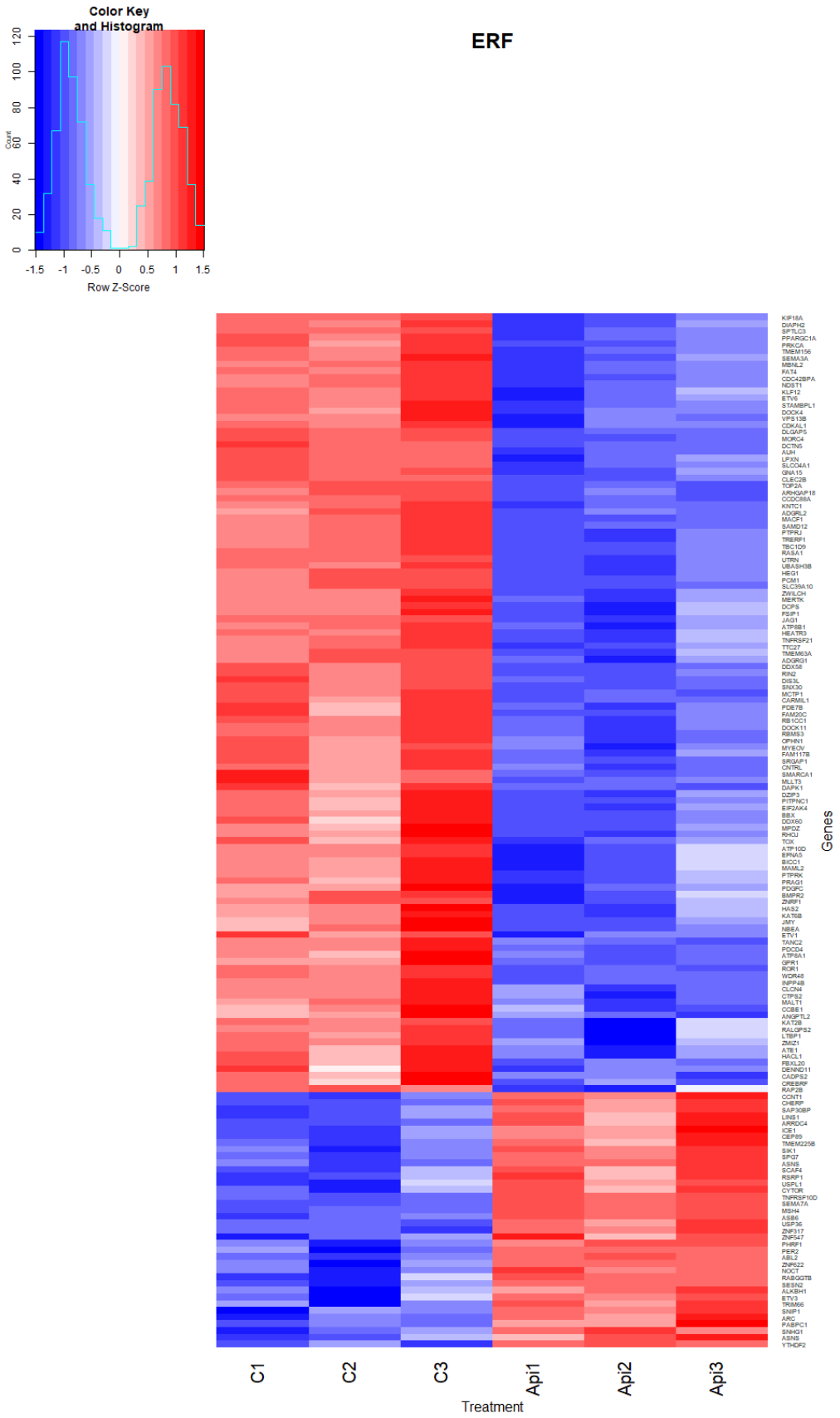
Color Key
and Histogram
Count
Row Z-Score
ERF
Genes
C1
C2
C3
Api1
Api2
Api3
Treatment

(1) ERF

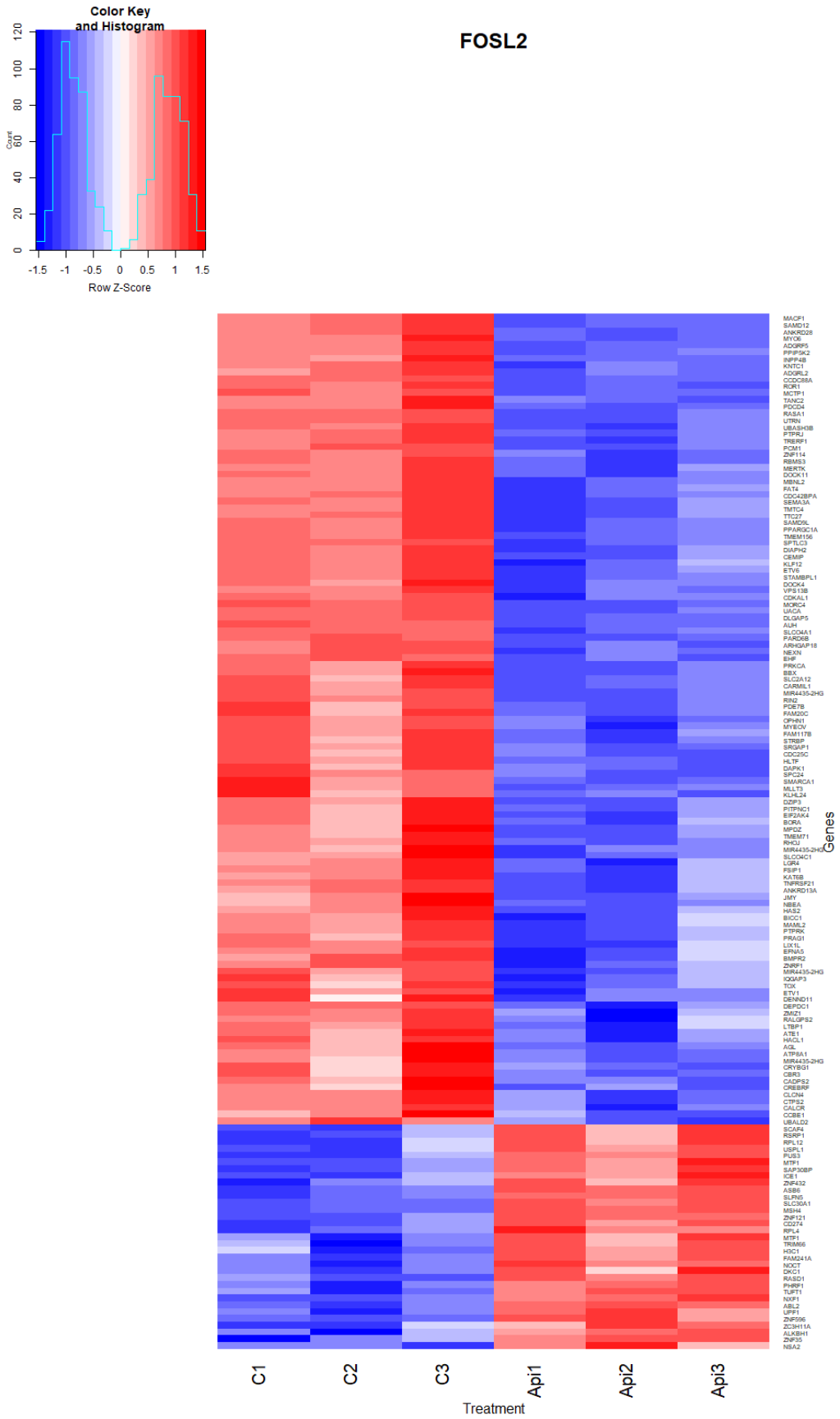
Color Key
and Histogram
Count
0
20
40
60
80
100
120
-1.5
-1
-0.5
0
0.5
1
1.5
Row Z-Score
FOSL2
Genes
C1
C2
C3
Api1
Api2
Api3
Treatment

(2) FOSL2

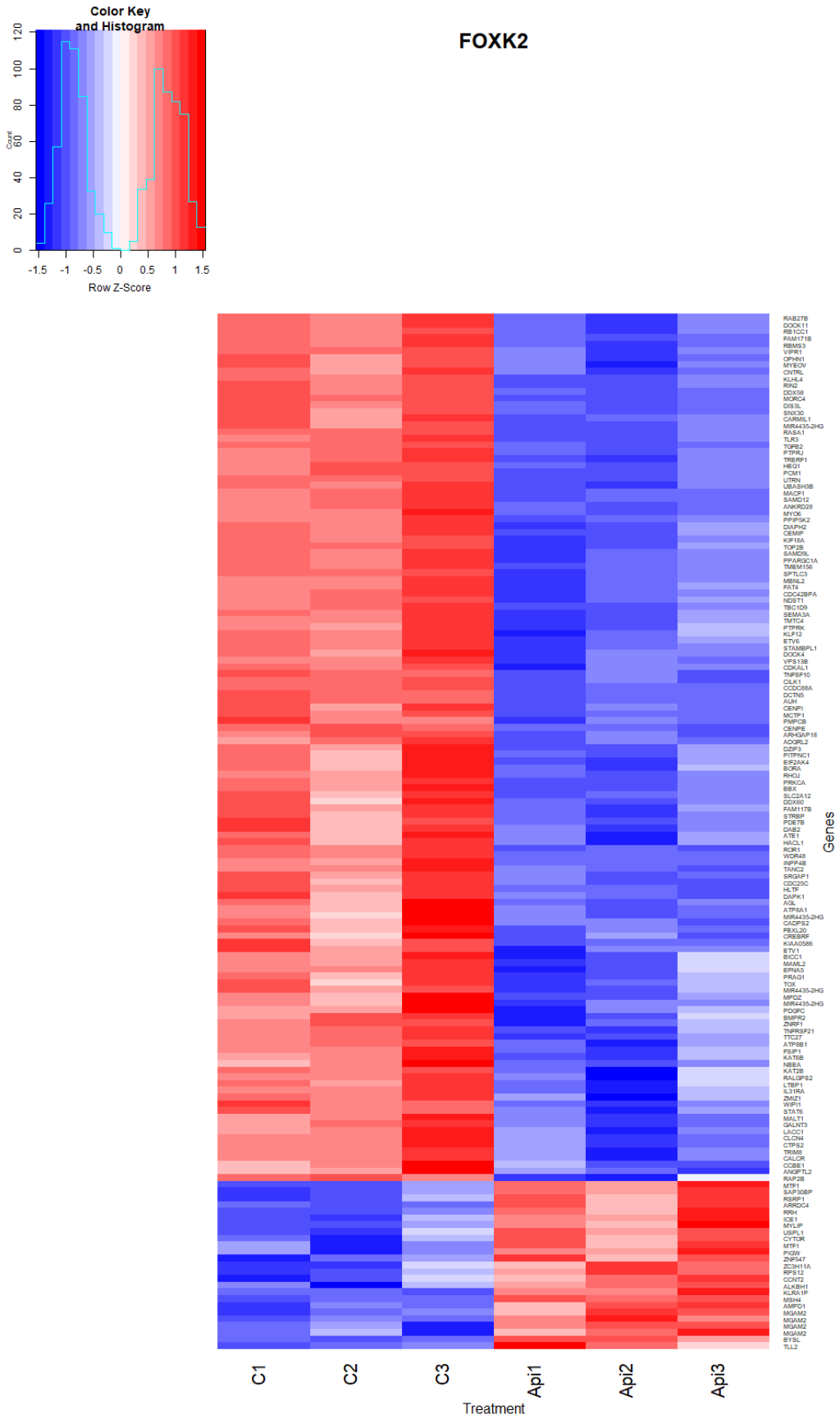
Color Key
and Histogram
Count
Row Z-Score
FOXK2
Genes
C1
C2
C3
Api1
Api2
Api3
Treatment

(3) FOXK2

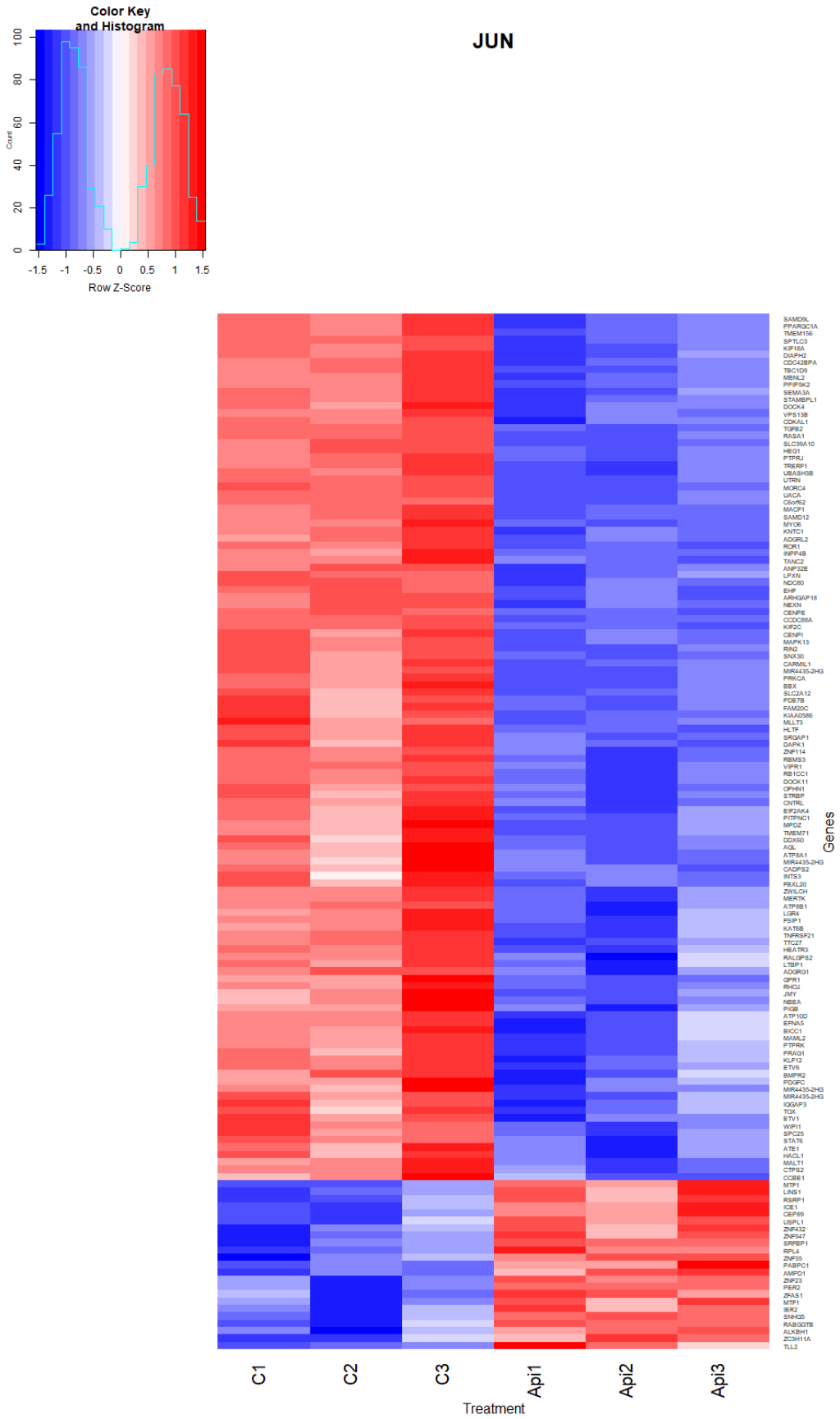
Color Key
and Histogram
Count
0
20
40
60
80
100
-1.5
-1
-0.5
0
0.5
1
1.5
Row Z-Score
JUN
Genes
C1
C2
C3
Api1
Api2
Api3
Treatment

(4) JUN

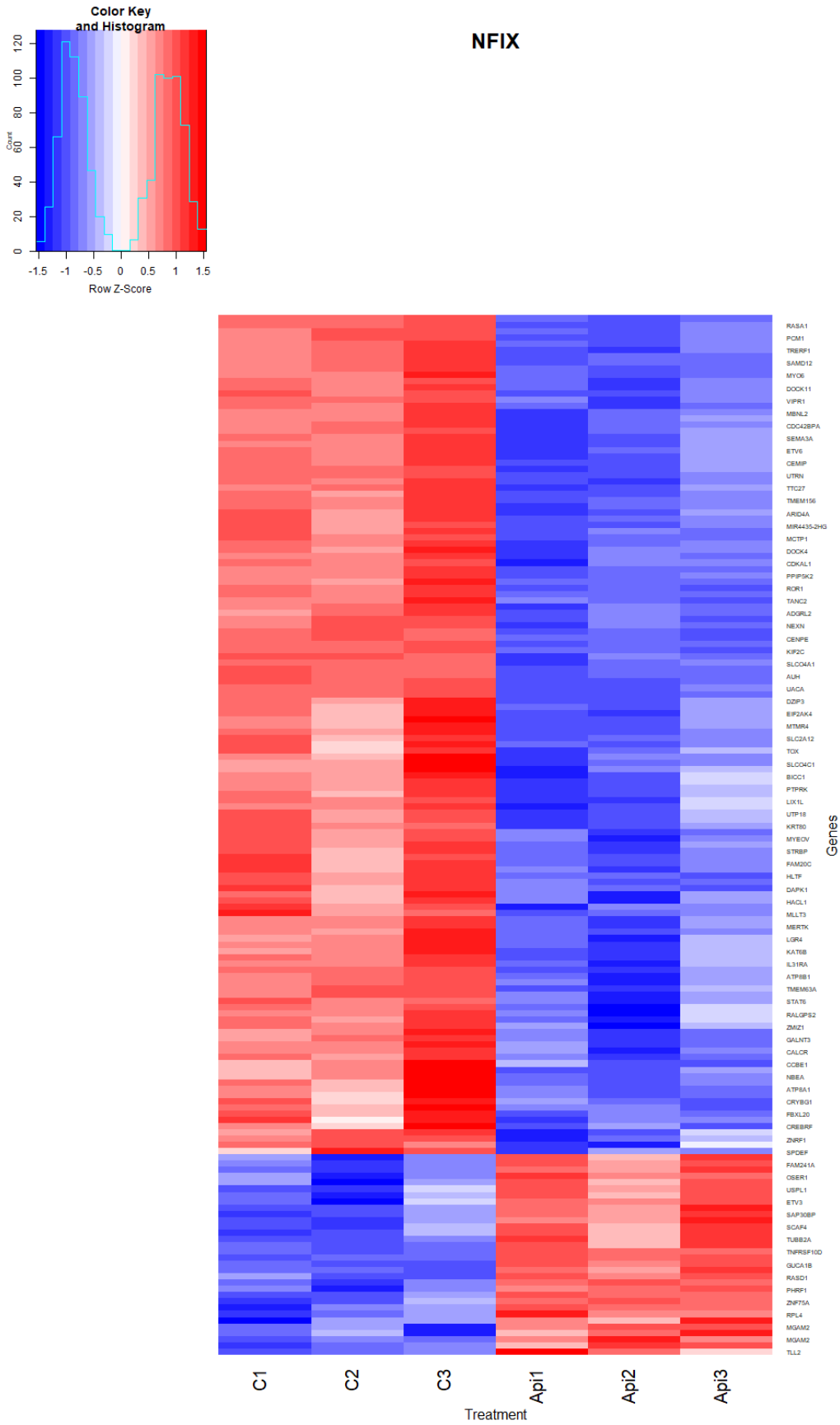
Color Key
and Histogram
Count
0
20
40
60
80
100
120
-1.5
-1
-0.5
0
0.5
1
1.5
Row Z-Score
NFIX
RASA1
PCM1
TRERF1
SAMD12
MYO6
DOCK11
VIPR1
MBNL2
CDC42BPA
SEMA3A
ETV6
CEMIP
UTRN
TTC27
TMEM156
ARID4A
MIR4435-2HG
MCTP1
DOCK4
CDKAL1
PPIP5K2
ROR1
TANC2
ADGRL2
NEXN
CENPE
KIF2C
SLCO4A1
AUH
UACA
DZIP3
EIF2AK4
MTMR4
SLC2A12
TOX
SLCO4C1
BICC1
PTPRK
LIX1L
UTP18
KRT80
MYEOV
STRBP
FAM20C
HLTF
DAPK1
HACL1
MLLT3
MERTK
LGR4
KAT6B
IL31RA
ATP8B1
TMEM63A
STAT6
RALGPS2
ZMIZ1
GALNT3
CALCR
CCBE1
NBEA
ATP8A1
CRYBG1
FBXL20
CREBRF
ZNRF1
SPDEF
FAM241A
OSER1
USPL1
ETV3
SAP30BP
SCAF4
TUBB2A
TNFRSF10D
GUCA1B
RASD1
PHRF1
ZNF75A
RPL4
MGAM2
MGAM2
TLL2
Genes
C1
C2
C3
Api1
Api2
Api3
Treatment

(5) NFIX

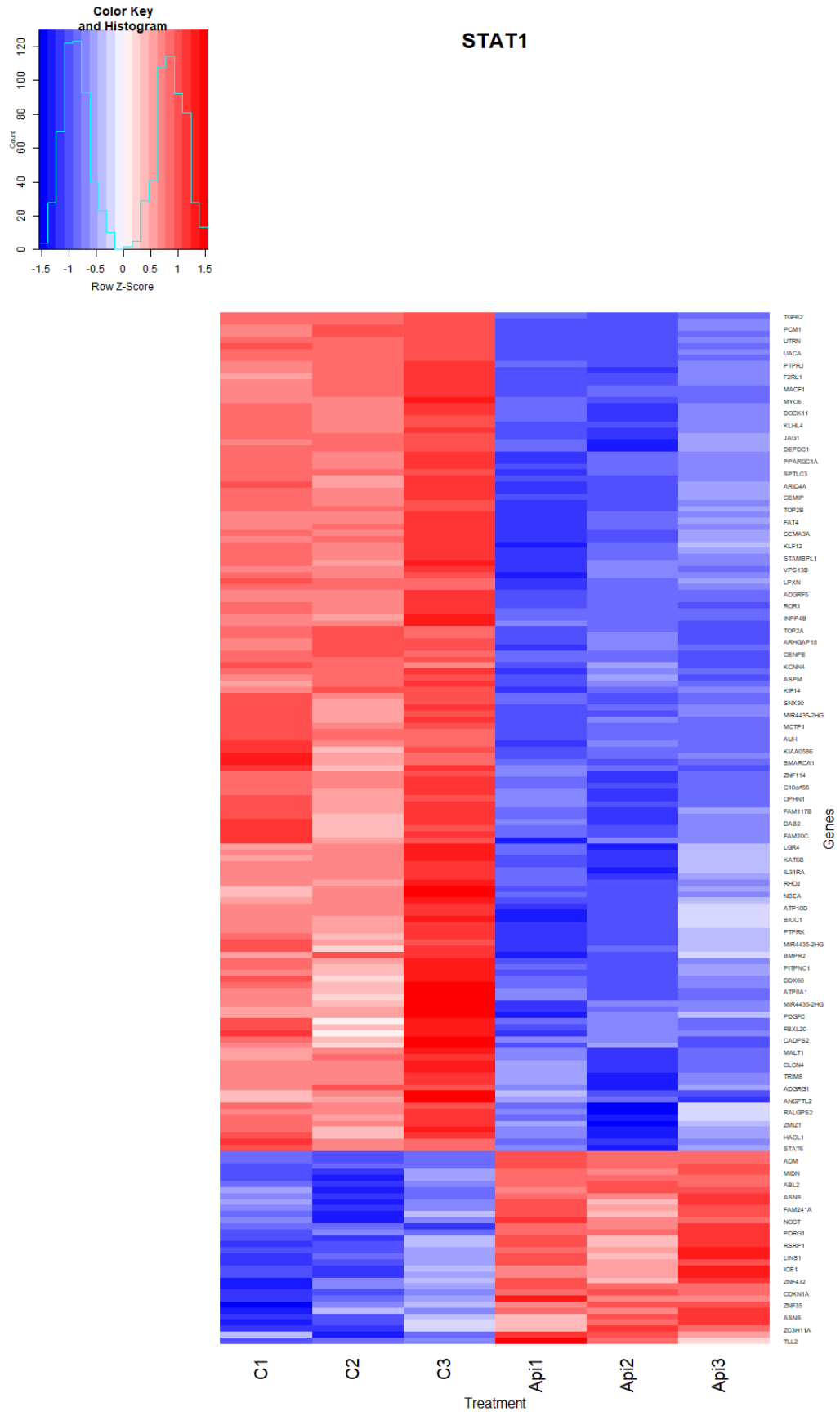
Color Key
and Histogram
Count
0
20
40
60
80
100
120
-1.5
-1
-0.5
0
0.5
1
1.5
Row Z-Score
STAT1
TGFB2
PCM1
UTRN
UACA
PTPRJ
F2RL1
MACF1
MYO6
DOCK11
KLHL4
JAG1
DEPDC1
PPARGC1A
SPTLC3
ARID4A
CEMIP
TOP2B
FAT4
SEMA3A
KLF12
STAMBPL1
VPS13B
LPXN
ADGRF5
ROR1
INPP4B
TOP2A
ARHGAP18
CENPE
KCNN4
ASPM
KIF14
SNX30
MIR4435-2HG
MCTP1
AUH
KIAA0586
SMARCA1
ZNF114
C10orf55
OPHN1
FAM117B
DAB2
FAM20C
LGR4
KAT6B
IL31RA
RHOJ
NBEA
ATP10D
BICC1
PTPRK
MIR4435-2HG
BMPR2
PITPNC1
DDX60
ATP8A1
MIR4435-2HG
PDGFC
FBXL20
CADPS2
MALT1
CLCN4
TRIM8
ADGRG1
ANGPTL2
RALGPS2
ZMIZ1
HACL1
STAT6
ADM
MIDN
ABL2
ASNS
FAM241A
NOCT
PDRG1
RSRP1
LIN51
ICE1
ZNF432
CDKN1A
ZNF35
ASNS
ZC3H11A
TLL2
Genes
C1
C2
C3
Api1
Api2
Api3
Treatment

(6) STAT1

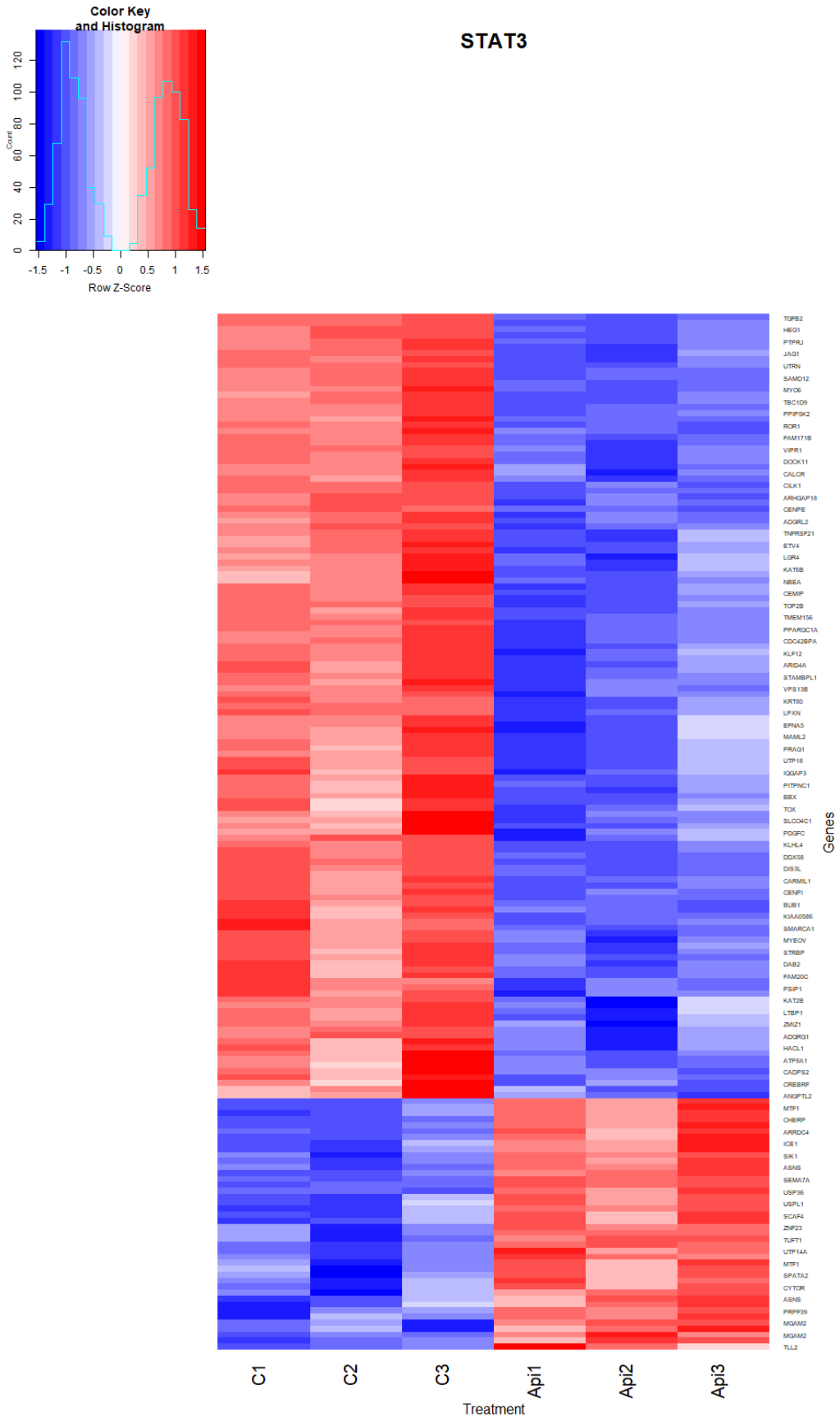
Color Key
and Histogram
Count
0
20
40
60
80
100
120
-1.5
-1
-0.5
0
0.5
1
1.5
Row Z-Score
STAT3
TGFB2
HEG1
PTPRJ
JAG1
UTRN
SAMD12
MYO6
TBC1D9
PPIP5K2
ROR1
FAM171B
VIPR1
DOCK11
CALCR
CILK1
ARHGAP18
CENPE
ADGRL2
TNFRSF21
ETV4
LGR4
KAT6B
NBEA
CEMIP
TOP2B
TMEM156
PPARGC1A
CDC42BPA
KLF12
ARID4A
STAMBPL1
VPS13B
KRT80
LPXN
EPNA5
MAML2
PRAG1
UTP18
IQGAP3
PITPNC1
BBX
TOX
SLCO4C1
PDGFC
KLHL4
DDX58
DIS3L
CARMIL1
CENPI
BUB1
KIAA0586
SMARCA1
MYEOV
STRBP
DAB2
FAM20C
PSIP1
KAT2B
LTBP1
ZMIZ1
ADGRG1
HACL1
ATP8A1
CADPS2
CREBRF
ANGPTL2
MTF1
CHERP
ARRDC4
ICE1
SIK1
ASNS
SEMA7A
USP36
USPL1
SCAF4
ZNF23
TUFT1
UTP14A
MTF1
SPATA2
CYTOR
ASNS
PRPF39
MGAM2
MGAM2
TLL2
Genes
C1
C2
C3
Api1
Api2
Api3
Treatment

(7) STAT3

REFERENCES

1. Jastrow M. The Medicine of the Babylonians and Assyrians. Proc R Soc Med. 1914;7(Sect Hist Med):109-76.
2. Petrovska BB. Historical review of medicinal plants' usage. Pharmacogn Rev. 2012;6(11):1-5.
3. Mahomoodally MF. Traditional Medicines in Africa: An Appraisal of Ten Potent African Medicinal Plants. Evidence-Based Complementary and Alternative Medicine. 2013;2013:617459.
4. Pan S-Y, Litscher G, Gao S-H, Zhou S-F, Yu Z-L, Chen H-Q, et al. Historical Perspective of Traditional Indigenous Medical Practices: The Current Renaissance and Conservation of Herbal Resources. Evidence-Based Complementary and Alternative Medicine. 2014;2014:525340.
5. Lee K-H, Morris-Natschke S, Qian K, Dong Y, Yang X, Zhou T, et al. Recent Progress of Research on Herbal Products Used in Traditional Chinese Medicine: the Herbs belonging to The Divine Husbandman's Herbal Foundation Canon (神農本草經 Shén Nóng Běn Cǎo Jīng). Journal of Traditional and Complementary Medicine. 2012;2(1):6-26.
6. Welz AN, Emberger-Klein A, Menrad K. Why people use herbal medicine: insights from a focus-group study in Germany. BMC Complementary and Alternative Medicine. 2018;18(1):92.
7. Karan V, Neetika S, Maninder K. Current Perspective in the International Trade of Medicinal Plants Material: An Update. Current Pharmaceutical Design. 2016;22(27):4288-336.
8. Information and Communiction Technology Center MoC, Thailand. Trade report of Thailand http://tradereport.moc.go.th/TradeThai.aspx2021 [Available from: http://tradereport.moc.go.th/.
9. Zhu F, Wongsiri S. A Brief Introduction to Apitherapy Health Care. Journal of Thai Traditional and Alternative Medicine. 2008;6(3):303-12.
10. Trumbeckaite S, Dauksiene J, Bernatoniene J, Janulis V. Knowledge, Attitudes, and Usage of Apitherapy for Disease Prevention and Treatment among Undergraduate Pharmacy Students in Lithuania. Evidence-Based Complementary and Alternative Medicine. 2015;2015:172502.
11. Roffet-Salque M, Regert M, Evershed RP, Outram AK, Cramp LJE, Decavallas O, et al. Widespread exploitation of the honeybee by early Neolithic farmers. Nature. 2015;527:226.
12. Suppasat T, Roan Smith D, Deowanish S, Siriwat Wongsiri. Matrilineal origins of Apis mellifera in Thailand. Apidologie. 2007;38(4):323-34.
13. Peršurić Ž, Pavelić SK. Bioactives from Bee Products and Accompanying Extracellular Vesicles as Novel Bioactive Components for Wound Healing. Molecules. 2021;26(12):3770.
14. Cornara L, Biagi M, Xiao J, Burlando B. Therapeutic Properties of Bioactive Compounds from Different Honeybee Products. Frontiers in Pharmacology. 2017;8(412).
15. Subramanian R, Umesh Hebbar H, Rastogi NK. Processing of Honey: A Review. International Journal of Food Properties. 2007;10(1):127-43.

16. Kwakman PHS, Velde AAt, de Boer L, Speijer D, Christina Vandenbroucke-Grauls MJ, Zaat SAJ. How honey kills bacteria. The FASEB Journal. 2010;24(7):2576-82.
17. Jantakee K, Tragoolpua Y. Activities of different types of Thai honey on pathogenic bacteria causing skin diseases, tyrosinase enzyme and generating free radicals. Biological Research. 2015;48(1):4.
18. Combarros-Fuertes P, Fresno JM, Estevinho MM, Sousa-Pimenta M, Tornadijo ME, Estevinho LM. Honey: Another Alternative in the Fight against Antibiotic-Resistant Bacteria? Antibiotics. 2020;9(11):774.
19. Nolan VC, Harrison J, Cox JAG. Dissecting the Antimicrobial Composition of Honey. Antibiotics. 2019;8(4):251.
20. Rabie E, Serem JC, Oberholzer HM, Gaspar ARM, Bester MJ. How methylglyoxal kills bacteria: An ultrastructural study. Ultrastructural Pathology. 2016;40(2):107-11.
21. McLoone P, Warnock M, Fyfe L. Honey: A realistic antimicrobial for disorders of the skin. Journal of Microbiology, Immunology and Infection. 2016;49(2):161-7.
22. Majtan J, Kumar P, Majtan T, Walls AF, Klaudiny J. Effect of honey and its major royal jelly protein 1 on cytokine and MMP-9 mRNA transcripts in human keratinocytes. Experimental Dermatology. 2010;19(8):e73-e9.
23. Kassi E, Chinou I, Spilioti E, Tsiapara A, Graikou K, Karabournioti S, et al. A monoterpene, unique component of thyme honeys, induces apoptosis in prostate cancer cells via inhibition of NF-κB activity and IL-6 secretion. Phytomedicine. 2014;21(11):1483-9.
24. Guo J, Wang Z, Chen Y, Cao J, Tian W, Ma B, et al. Active components and biological functions of royal jelly. Journal of Functional Foods. 2021;82:104514.
25. Pirk CWW. Honeybee Evolution: Royal Jelly Proteins Help Queen Larvae to Stay on Top. Current Biology. 2018;28(8):R350-R1.
26. Fujita T, Kozuka-Hata H, Ao-Kondo H, Kunieda T, Oyama M, Kubo T. Proteomic Analysis of the Royal Jelly and Characterization of the Functions of its Derivation Glands in the Honeybee. Journal of Proteome Research. 2013;12(1):404-11.
27. Fratini F, Cilia G, Mancini S, Felicioli A. Royal Jelly: An ancient remedy with remarkable antibacterial properties. Microbiological Research. 2016;192:130-41.
28. Makino J, Ogasawara R, Kamiya T, Hara H, Mitsugi Y, Yamaguchi E, et al. Royal Jelly Constituents Increase the Expression of Extracellular Superoxide Dismutase through Histone Acetylation in Monocytic THP-1 Cells. Journal of Natural Products. 2016;79(4):1137-43.
29. Kashima Y, Kanematsu S, Asai S, Kusada M, Watanabe S, Kawashima T, et al. Identification of a Novel Hypocholesterolemic Protein, Major Royal Jelly Protein 1, Derived from Royal Jelly. PLOS ONE. 2014;9(8):e105073.
30. Takikawa M, Kumagai A, Hirata H, Soga M, Yamashita Y, Ueda M, et al. 10-Hydroxy-2-decenoic acid, a unique medium-chain fatty acid, activates 5'-AMP-activated protein kinase in L6 myotubes and mice. Molecular Nutrition & Food Research. 2013;57(10):1794-802.

31. Park HM, Hwang E, Lee KG, Han SM, Cho Y, Kim SY. Royal jelly protects against ultraviolet B-induced photoaging in human skin fibroblasts via enhancing collagen production. J Med Food. 2011;14(9):899-906.
32. Zhang S, Liu Y, Ye Y, Wang X-R, Lin L-T, Xiao L-Y, et al. Bee venom therapy: Potential mechanisms and therapeutic applications. Toxicon. 2018;148:64-73.
33. Abd El-Wahed AA, Khalifa SAM, Sheikh BY, Farag MA, Saeed A, Larik FA, et al. Chapter 13 - Bee Venom Composition: From Chemistry to Biological Activity. In: Atta ur R, editor. Studies in Natural Products Chemistry. 60: Elsevier; 2019. p. 459-84.
34. Lee G, Bae H. Anti-Inflammatory Applications of Melittin, a Major Component of Bee Venom: Detailed Mechanism of Action and Adverse Effects. Molecules. 2016;21(5):616.
35. Lim HN, Baek SB, Jung HJ. Bee Venom and Its Peptide Component Melittin Suppress Growth and Migration of Melanoma Cells via Inhibition of PI3K/AKT/mTOR and MAPK Pathways. Molecules. 2019;24(5):929.
36. Alvarez-Fischer D, Noelker C, Vulinović F, Grünewald A, Chevarin C, Klein C, et al. Bee Venom and Its Component Apamin as Neuroprotective Agents in a Parkinson Disease Mouse Model. PLOS ONE. 2013;8(4):e61700.
37. Baek H, Lee C-j, Choi DB, Kim N-s, Kim Y-S, Ye YJ, et al. Bee venom phospholipase A2 ameliorates Alzheimer's disease pathology in Aβ vaccination treatment without inducing neuro-inflammation in a 3xTg-AD mouse model. Scientific Reports. 2018;8(1):17369.
38. Jung K-H, Baek H, Kang M, Kim N, Lee SY, Bae H. Bee Venom Phospholipase A2 Ameliorates House Dust Mite Extract Induced Atopic Dermatitis Like Skin Lesions in Mice. Toxins. 2017;9(2):68.
39. Athikomkulchai S, Awale S, Ruangrungsi N, Ruchirawat S, Kadota S. Chemical constituents of Thai propolis. Fitoterapia. 2013;88:96-100.
40. Fesen MR, Pommier Y, Leteurtre F, Hiroguchi S, Yung J, Kohn KW. Inhibition of HIV-1 integrase by flavones, caffeic acid phenethyl ester (CAPE) and related compounds. Biochemical Pharmacology. 1994;48(3):595-608.
41. Zhang T, Li Y, Lai J-P, Douglas SD, Metzger DS, O'Brien CP, et al. Alcohol potentiates hepatitis C virus replicon expression. Hepatology. 2003;38(1):57-65.
42. Kumar V, Dhanjal JK, Kaul SC, Wadhwa R, Sundar D. Withanone and caffeic acid phenethyl ester are predicted to interact with main protease (Mpro) of SARS-CoV-2 and inhibit its activity. Journal of Biomolecular Structure and Dynamics. 2021;39(11):3842-54.
43. Speciale A, Costanzo R, Puglisi S, Musumeci R, Catania MR, Caccamo F, et al. Antibacterial Activity of Propolis and Its Active Principles Alone and in Combination with Macrolides, Beta-lactams and Fluoroquinolones Against Microorganisms Responsible for Respiratory Infections. Journal of Chemotherapy. 2006;18(2):164-71.
44. Olgierd B, Kamila Ż, Anna B, Emilia M. The Pluripotent Activities of Caffeic Acid Phenethyl Ester. Molecules. 2021;26(5):1335.
45. Wu J, Omene C, Karkoszka J, Bosland M, Eckard J, Klein CB, et al. Caffeic acid phenethyl ester (CAPE), derived from a honeybee product propolis, exhibits a

diversity of anti-tumor effects in pre-clinical models of human breast cancer. Cancer Letters. 2011;308(1):43-53.
46. Beserra FP, Gushiken LFS, Hussni MF, Ribeiro VP, Bonamin F, Jackson CJ, et al. Artepillin C as an outstanding phenolic compound of Brazilian green propolis for disease treatment: A review on pharmacological aspects. Phytotherapy Research. 2021;35(5):2274-86.
47. Shimizu K, Das SK, Hashimoto T, Sowa Y, Yoshida T, Sakai T, et al. Artepillin C in Brazilian propolis induces G0/G1 arrest via stimulation of Cip1/p21 expression in human colon cancer cells. Molecular Carcinogenesis. 2005;44(4):293-9.
48. Pang S, Yee M, Saba Y, Chino T. Artepillin C as a targeting survivin molecule in oral squamous cell carcinoma cells in vitro: A preliminary study. Journal of Oral Pathology & Medicine. 2018;47(1):48-52.
49. Thakur M, Nanda V. Composition and functionality of bee pollen: A review. Trends in Food Science & Technology. 2020;98:82-106.
50. Abbas T, Dutta A. p21 in cancer: intricate networks and multiple activities. Nature Reviews Cancer. 2009;9(6):400-14.
51. Schmidt M, Rohe A, Platzer C, Najjar A, Erdmann F, Sippl W. Regulation of G2/M Transition by Inhibition of WEE1 and PKMYT1 Kinases. Molecules. 2017;22(12):2045.
52. Boutros R, Dozier C, Ducommun B. The when and wheres of CDC25 phosphatases. Current Opinion in Cell Biology. 2006;18(2):185-91.
53. Pucci B, Kasten M, Giordano A. Cell Cycle and Apoptosis. Neoplasia. 2000;2(4):291-9.
54. Tournier C, Hess P, Yang DD, Xu J, Turner TK, Nimnual A, et al. Requirement of JNK for Stress- Induced Activation of the Cytochrome c-Mediated Death Pathway. Science. 2000;288(5467):870-4.
55. Saraste A, Pulkki K. Morphologic and biochemical hallmarks of apoptosis. Cardiovascular Research. 2000;45(3):528-37.
56. Luo M, Lu Z, Sun H, Yuan K, Zhang Q, Meng S, et al. Nuclear entry of active caspase-3 is facilitated by its p3-recognition-based specific cleavage activity. Cell Research. 2010;20(2):211-22.
57. Julien O, Wells JA. Caspases and their substrates. Cell Death & Differentiation. 2017;24(8):1380-9.
58. Guicciardi ME, Gores GJ. Life and death by death receptors. FASEB journal : official publication of the Federation of American Societies for Experimental Biology. 2009;23(6):1625-37.
59. Chang L, Kamata H, Solinas G, Luo JL, Maeda S, Venuprasad K, et al. The E3 ubiquitin ligase itch couples JNK activation to TNFalpha-induced cell death by inducing c-FLIP(L) turnover. Cell. 2006;124(3):601-13.
60. Green DR, Kroemer G. The Pathophysiology of Mitochondrial Cell Death. Science. 2004;305(5684):626-9.
61. Aubrey BJ, Kelly GL, Janic A, Herold MJ, Strasser A. How does p53 induce apoptosis and how does this relate to p53-mediated tumour suppression? Cell Death & Differentiation. 2018;25(1):104-13.
62. Westphal D, Kluck RM, Dewson G. Building blocks of the apoptotic pore: how Bax and Bak are activated and oligomerize during apoptosis. Cell Death & Differentiation. 2014;21(2):196-205.

63. Cregan SP, Dawson VL, Slack RS. Role of AIF in caspase-dependent and caspase-independent cell death. Oncogene. 2004;23(16):2785-96.
64. Susin SA, Daugas E, Ravagnan L, Samejima K, Zamzami N, Loeffler M, et al. Two distinct pathways leading to nuclear apoptosis. J Exp Med. 2000;192(4):571-80.
65. Degterev A, Huang Z, Boyce M, Li Y, Jagtap P, Mizushima N, et al. Chemical inhibitor of nonapoptotic cell death with therapeutic potential for ischemic brain injury. Nature Chemical Biology. 2005;1(2):112-9.
66. Gong Y, Fan Z, Luo G, Yang C, Huang Q, Fan K, et al. The role of necroptosis in cancer biology and therapy. Molecular Cancer. 2019;18(1):100.
67. Zhang J, Webster JD, Dugger DL, Goncharov T, Roose-Girma M, Hung J, et al. Ubiquitin Ligases cIAP1 and cIAP2 Limit Cell Death to Prevent Inflammation. Cell Reports. 2019;27(9):2679-89.e3.
68. Vandenabeele P, Galluzzi L, Vanden Berghe T, Kroemer G. Molecular mechanisms of necroptosis: an ordered cellular explosion. Nature Reviews Molecular Cell Biology. 2010;11(10):700-14.
69. Glick D, Barth S, Macleod KF. Autophagy: cellular and molecular mechanisms. The Journal of Pathology. 2010;221(1):3-12.
70. Denton D, Kumar S. Autophagy-dependent cell death. Cell Death & Differentiation. 2019;26(4):605-16.
71. Papinski D, Kraft C. Regulation of Autophagy By Signaling Through the Atg1/ULK1 Complex. Journal of Molecular Biology. 2016;428(9, Part A):1725-41.
72. Wang B, Li R, Wu S, Liu X, Ren J, Li J, et al. Breast Cancer Resistance to Cyclin-Dependent Kinases 4/6 Inhibitors: Intricacy of the Molecular Mechanisms. Front Oncol. 2021;11:651541.
73. Costea T, Vlad OC, Miclea L-C, Ganea C, Szöllősi J, Mocanu M-M. Alleviation of Multidrug Resistance by Flavonoid and Non-Flavonoid Compounds in Breast, Lung, Colorectal and Prostate Cancer. International Journal of Molecular Sciences. 2020;21(2):401.
74. Lokhov P. Improving cellular cancer vaccines. Nature Precedings. 2010.
75. Zhang C, Hu Y, Xiao W, Tian Z. Chimeric antigen receptor- and natural killer cell receptor-engineered innate killer cells in cancer immunotherapy. Cellular & Molecular Immunology. 2021.
76. Nugitrangson P, Puthong S, Iempridee T, Pimtong W, Pornpakakul S, Chanchao C. In vitro and in vivo characterization of the anticancer activity of Thai stingless bee (Tetragonula laeviceps) cerumen. Experimental Biology and Medicine. 2016;241(2):166-76.
77. Pedraza-Chaverri J, Cárdenas-Rodríguez N, Orozco-Ibarra M, Pérez-Rojas JM. Medicinal properties of mangosteen (Garcinia mangostana). Food and Chemical Toxicology. 2008;46(10):3227-39.
78. Pothitirat W, Chomnawang MT, Supabphol R, Gritsanapan W. Comparison of bioactive compounds content, free radical scavenging and anti-acne inducing bacteria activities of extracts from the mangosteen fruit rind at two stages of maturity. Fitoterapia. 2009;80(7):442-7.
79. Yates P, Stout GH. The Structure of Mangostin1. Journal of the American Chemical Society. 1958;80(7):1691-700.

80. Ee GC, Daud S, Izzaddin SA, Rahmani M. Garcinia mangostana: a source of potential anti-cancer lead compounds against CEM-SS cell line. J Asian Nat Prod Res. 2008;10(5-6):475-9.
81. Azebaze AG, Menasria F, Noumi LG, Nguemfo EL, Tchamfo MF, Nkengfack AE, et al. Xanthones from the seeds of Allanblackia monticola and their apoptotic and antiproliferative activities. Planta Med. 2009;75(3):243-8.
82. Chairungsrilerd N, Takeuchi K, Ohizumi Y, Nozoe S, Ohta T. Mangostanol, a prenyl xanthone from Garcinia mangostana. Phytochemistry. 1996;43(5):1099-102.
83. Li L, Brunner I, Han A-R, Hamburger M, Kinghorn AD, Frye R, et al. Pharmacokinetics of α-mangostin in rats after intravenous and oral application. Molecular Nutrition & Food Research. 2011;55(S1):S67-S74.
84. Wathoni N, Rusdin A, Motoyama K, Joni IM, Lesmana R, Muchtaridi M. Nanoparticle Drug Delivery Systems for α-Mangostin. Nanotechnol Sci Appl. 2020;13:23-36.
85. Matsumoto K, Akao Y, Kobayashi E, Ohguchi K, Ito T, Tanaka T, et al. Induction of Apoptosis by Xanthones from Mangosteen in Human Leukemia Cell Lines. Journal of Natural Products. 2003;66(8):1124-7.
86. Matsumoto K, Akao Y, Yi H, Ohguchi K, Ito T, Tanaka T, et al. Preferential target is mitochondria in α-mangostin-induced apoptosis in human leukemia HL60 cells. Bioorganic & Medicinal Chemistry. 2004;12(22):5799-806.
87. Matsumoto K, Akao Y, Ohguchi K, Ito T, Tanaka T, Iinuma M, et al. Xanthones induce cell-cycle arrest and apoptosis in human colon cancer DLD-1 cells. Bioorganic & Medicinal Chemistry. 2005;13(21):6064-9.
88. Nakagawa Y, Iinuma M, Naoe T, Nozawa Y, Akao Y. Characterized mechanism of α-mangostin-induced cell death: Caspase-independent apoptosis with release of endonuclease-G from mitochondria and increased miR-143 expression in human colorectal cancer DLD-1 cells. Bioorganic & Medicinal Chemistry. 2007;15(16):5620-8.
89. Kaomongkolgit R, Chaisomboon N, Pavasant P. Apoptotic effect of alpha-mangostin on head and neck squamous carcinoma cells. Archives of Oral Biology. 2011;56(5):483-90.
90. Kaomongkolgit R. Alpha-mangostin suppresses MMP-2 and MMP-9 expression in head and neck squamous carcinoma cells. Odontology. 2013;101(2):227-32.
91. Krajarng A, Nakamura Y, Suksamrarn S, Watanapokasin R. α-Mangostin Induces Apoptosis in Human Chondrosarcoma Cells through Downregulation of ERK/JNK and Akt Signaling Pathway. Journal of Agricultural and Food Chemistry. 2011;59(10):5746-54.
92. Watanapokasin R, Jarinthanan F, Nakamura Y, Sawasjirakij N, Jaratrungtawee A, Suksamrarn S. Effects of α-mangostin on apoptosis induction of human colon cancer. World J Gastroenterol. 2011;17(16):2086-95.
93. Hsieh SC, Huang MH, Cheng CW, Hung JH, Yang SF, Hsieh YH. α-Mangostin induces mitochondrial dependent apoptosis in human hepatoma SK-Hep-1 cells through inhibition of p38 MAPK pathway. Apoptosis. 2013;18(12):1548-60.
94. Shibata MA, Iinuma M, Morimoto J, Kurose H, Akamatsu K, Okuno Y, et al. α-Mangostin extracted from the pericarp of the mangosteen (Garcinia mangostana Linn) reduces tumor growth and lymph node metastasis in an immunocompetent

xenograft model of metastatic mammary cancer carrying a p53 mutation. BMC Med. 2011;9:69.
95. Johnson JJ, Petiwala SM, Syed DN, Rasmussen JT, Adhami VM, Siddiqui IA, et al. α-Mangostin, a xanthone from mangosteen fruit, promotes cell cycle arrest in prostate cancer and decreases xenograft tumor growth. Carcinogenesis. 2011;33(2):413-9.
96. Kurose H, Shibata M-A, Iinuma M, Otsuki Y. Alterations in Cell Cycle and Induction of Apoptotic Cell Death in Breast Cancer Cells Treated with α-Mangostin Extracted from Mangosteen Pericarp. Journal of Biomedicine and Biotechnology. 2012;2012:672428.
97. Soda M, Endo S, Matsunaga T, Zhao H-T, El-Kabbani O, Iinuma M, et al. Inhibition of Human Aldose Reductase-Like Protein (AKR1B10) by α- and γ-Mangostins, Major Components of Pericarps of Mangosteen. Biological and Pharmaceutical Bulletin. 2012;35(11):2075-80.
98. Chung YT, Matkowskyj KA, Li H, Bai H, Zhang W, Tsao M-S, et al. Overexpression and oncogenic function of aldo-keto reductase family 1B10 (AKR1B10) in pancreatic carcinoma. Modern Pathology. 2012;25(5):758-66.
99. Mizushina Y, Kuriyama I, Nakahara T, Kawashima Y, Yoshida H. Inhibitory effects of α-mangostin on mammalian DNA polymerase, topoisomerase, and human cancer cell proliferation. Food and Chemical Toxicology. 2013;59:793-800.
100. Won Y-S, Lee J-H, Kwon S-J, Kim J-Y, Park K-H, Lee M-K, et al. α-Mangostin-induced apoptosis is mediated by estrogen receptor α in human breast cancer cells. Food and Chemical Toxicology. 2014;66:158-65.
101. Shan T, Cui XJ, Li W, Lin WR, Lu HW, Li YM, et al. α-Mangostin suppresses human gastric adenocarcinoma cells in vitro via blockade of Stat3 signaling pathway. Acta Pharmacol Sin. 2014;35(8):1065-73.
102. Zhang H, Tan YP, Zhao L, Wang L, Fu NJ, Zheng SP, et al. Anticancer activity of dietary xanthone α-mangostin against hepatocellular carcinoma by inhibition of STAT3 signaling via stabilization of SHP1. Cell Death Dis. 2020;11(1):63.
103. Li P, Tian W, Ma X. Alpha-mangostin inhibits intracellular fatty acid synthase and induces apoptosis in breast cancer cells. Molecular Cancer. 2014;13(1):138.
104. Kim HJ, Fei X, Cho SC, Choi BY, Ahn HC, Lee K, et al. Discovery of α-mangostin as a novel competitive inhibitor against mutant isocitrate dehydrogenase-1. Bioorg Med Chem Lett. 2015;25(23):5625-31.
105. Wu CP, Hsiao SH, Murakami M, Lu YJ, Li YQ, Huang YH, et al. Alpha-Mangostin Reverses Multidrug Resistance by Attenuating the Function of the Multidrug Resistance-Linked ABCG2 Transporter. Mol Pharm. 2017;14(8):2805-14.
106. Martínez-Abundis E, García N, Correa F, Hernández-Reséndiz S, Pedraza-Chaverri J, Zazueta C. Effects of α-mangostin on mitochondrial energetic metabolism. Mitochondrion. 2010;10(2):151-7.
107. Nabandith V, Suzui M, Morioka T, Kaneshiro T, Kinjo T, Matsumoto K, et al. Inhibitory effects of crude alpha-mangostin, a xanthone derivative, on two different categories of colon preneoplastic lesions induced by 1, 2-dimethylhydrazine in the rat. Asian Pac J Cancer Prev. 2004;5(4):433-8.
108. Chitchumroonchokchai C, Thomas-Ahner JM, Li J, Riedl KM, Nontakham J, Suksumrarn S, et al. Anti-tumorigenicity of dietary α-mangostin in an HT-29 colon

cell xenograft model and the tissue distribution of xanthones and their phase II metabolites. Molecular Nutrition & Food Research. 2013;57(2):203-11.
109. Hung S-H, Shen K-H, Wu C-H, Liu C-L, Shih Y-W. α-Mangostin Suppresses PC-3 Human Prostate Carcinoma Cell Metastasis by Inhibiting Matrix Metalloproteinase-2/9 and Urokinase-Plasminogen Expression through the JNK Signaling Pathway. Journal of Agricultural and Food Chemistry. 2009;57(4):1291-8.
110. Hafeez BB, Mustafa A, Fischer JW, Singh A, Zhong W, Shekhani MO, et al. α-Mangostin: a dietary antioxidant derived from the pericarp of Garcinia mangostana L. inhibits pancreatic tumor growth in xenograft mouse model. Antioxid Redox Signal. 2014;21(5):682-99.
111. Lee Y-B, Ko K-C, Shi M-D, Liao Y-C, Chiang T-A, Wu P-F, et al. α-Mangostin, A Novel Dietary Xanthone, Suppresses TPA-Mediated MMP-2 and MMP-9 Expressions through the ERK Signaling Pathway in MCF-7 Human Breast Adenocarcinoma Cells. Journal of Food Science. 2010;75(1):H13-H23.
112. Shih Y-W, Chien S-T, Chen P-S, Lee J-H, Wu S-H, Yin L-T. α-Mangostin Suppresses Phorbol 12-myristate 13-acetate-Induced MMP-2/MMP-9 Expressions via αvβ3 Integrin/FAK/ERK and NF-κB Signaling Pathway in Human Lung Adenocarcinoma A549 Cells. Cell Biochemistry and Biophysics. 2010;58(1):31-44.
113. Yuan J, Wu Y, Lu G. α-Mangostin suppresses lipopolysaccharide-induced invasion by inhibiting matrix metalloproteinase-2/9 and increasing E-cadherin expression through extracellular signal-regulated kinase signaling in pancreatic cancer cells. Oncol Lett. 2013;5(6):1958-64.
114. Xu Q, Ma J, Lei J, Duan W, Sheng L, Chen X, et al. α-Mangostin suppresses the viability and epithelial-mesenchymal transition of pancreatic cancer cells by downregulating the PI3K/Akt pathway. Biomed Res Int. 2014;2014:546353.
115. Ma Y, Yu W, Shrivastava A, Srivastava RK, Shankar S. Inhibition of pancreatic cancer stem cell characteristics by α-Mangostin: Molecular mechanisms involving Sonic hedgehog and Nanog. J Cell Mol Med. 2019;23(4):2719-30.
116. Chao AC, Hsu Y-L, Liu C-K, Kuo P-L. α-Mangostin, a Dietary Xanthone, Induces Autophagic Cell Death by Activating the AMP-Activated Protein Kinase Pathway in Glioblastoma Cells. Journal of Agricultural and Food Chemistry. 2011;59(5):2086-96.
117. Kim S-J, Hong E-H, Lee B-R, Park M-H, Kim J-W, Pyun AR, et al. α-Mangostin Reduced ER Stress-mediated Tumor Growth through Autophagy Activation. Immune Netw. 2012;12(6):253-60.
118. Li G, Petiwala SM, Nonn L, Johnson JJ. Inhibition of CHOP accentuates the apoptotic effect of α-mangostin from the mangosteen fruit (Garcinia mangostana) in 22Rv1 prostate cancer cells. Biochem Biophys Res Commun. 2014;453(1):75-80.
119. Bhagwat S, Haytowitz DB, Holden JM. USDA database for the flavonoid content of selected foods, release 3. 2011.
120. Ali F, Rahul, Naz F, Jyoti S, Siddique YH. Health functionality of apigenin: A review. International Journal of Food Properties. 2017;20(6):1197-238.
121. Ma X-Q, Zhuang C, Wang B-C, Huang Y-F, Chen Q, Lin N. Cocrystal of Apigenin with Higher Solubility, Enhanced Oral Bioavailability, and Anti-inflammatory Effect. Crystal Growth & Design. 2019;19(10):5531-7.
122. Kazi M, Alhajri A, Alshehri SM, Elzayat EM, Al Meanazel OT, Shakeel F, et al. Enhancing Oral Bioavailability of Apigenin Using a Bioactive Self-

Nanoemulsifying Drug Delivery System (Bio-SNEDDS): In Vitro, In Vivo and Stability Evaluations. Pharmaceutics. 2020;12(8).
123. Yan X, Qi M, Li P, Zhan Y, Shao H. Apigenin in cancer therapy: anti-cancer effects and mechanisms of action. Cell & Bioscience. 2017;7(1).
124. Birt DF, Walker B, Tibbels MG, Bresnick E. Anti-mutagenesis and anti-promotion by apigenin, robinetin and indole-3-carbinol. Carcinogenesis. 1986;7(6):959-63.
125. Hirano T, Oka K, Akiba M. Antiproliferative effects of synthetic and naturally occurring flavonoids on tumor cells of the human breast carcinoma cell line, ZR-75-1. Res Commun Chem Pathol Pharmacol. 1989;64(1):69-78.
126. Sato F, Matsukawa Y, Matsumoto K, Nishino H, Sakai T. Apigenin Induces Morphological Differentiation and G2-M Arrest in Rat Neuronal Cells. Biochemical and Biophysical Research Communications. 1994;204(2):578-84.
127. Plaumann B, Fritsche M, Rimpler H, Brandner G, Hess RD. Flavonoids activate wild-type p53. Oncogene. 1996;13(8):1605-14.
128. Boege F, Straub T, Kehr A, Boesenberg C, Christiansen K, Andersen A, et al. Selected novel flavones inhibit the DNA binding or the DNA religation step of eukaryotic topoisomerase I. J Biol Chem. 1996;271(4):2262-70.
129. Constantinou A, Mehta R, Runyan C, Rao K, Vaughan A, Moon R. Flavonoids as DNA topoisomerase antagonists and poisons: structure-activity relationships. J Nat Prod. 1995;58(2):217-25.
130. Lepley DM, Li B, Birt DF, Pelling JC. The chemopreventive flavonoid apigenin induces G2/M arrest in keratinocytes. Carcinogenesis. 1996;17(11):2367-75.
131. Lepley DM, Pelling JC. Induction of p21/WAF1 and G1 cell-cycle arrest by the chemopreventive agent apigenin. Molecular Carcinogenesis. 1997;19(2):74-82.
132. Gupta S, Afaq F, Mukhtar H. Involvement of nuclear factor-kappa B, Bax and Bcl-2 in induction of cell cycle arrest and apoptosis by apigenin in human prostate carcinoma cells. Oncogene. 2002;21(23):3727-38.
133. Shukla S, Gupta S. Molecular mechanisms for apigenin-induced cell-cycle arrest and apoptosis of hormone refractory human prostate carcinoma DU145 cells. Molecular Carcinogenesis. 2004;39(2):114-26.
134. Shukla S, Gupta S. Molecular targets for apigenin-induced cell cycle arrest and apoptosis in prostate cancer cell xenograft. Molecular Cancer Therapeutics. 2006;5(4):843-52.
135. Shukla S, Gupta S. Apigenin-induced cell cycle arrest is mediated by modulation of MAPK, PI3K-Akt, and loss of cyclin D1 associated retinoblastoma dephosphorylation in human prostate cancer cells. Cell Cycle. 2007;6(9):1102-14.
136. Patki M, Chari V, Sivakumaran S, Gonit M, Trumbly R, Ratnam M. The ETS Domain Transcription Factor ELK1 Directs a Critical Component of Growth Signaling by the Androgen Receptor in Prostate Cancer Cells *. Journal of Biological Chemistry. 2013;288(16):11047-65.
137. Pandey M, Kaur P, Shukla S, Abbas A, Fu P, Gupta S. Plant flavone apigenin inhibits HDAC and remodels chromatin to induce growth arrest and apoptosis in human prostate cancer cells: In vitro and in vivo study. Molecular Carcinogenesis. 2012;51(12):952-62.
138. Casagrande F, Darbon J-M. Effects of structurally related flavonoids on cell cycle progression of human melanoma cells: regulation of cyclin-dependent kinases

CDK2 and CDK111Abbreviations: CDK, cyclin-dependent kinase; CKI, CDK inhibitor; PI 3-kinase, phosphatidylinositol 3-kinase; PKC, protein kinase C; DTT, dithiothreitol; RIPA, radioimmunoprecipitation assay buffer. Biochemical Pharmacology. 2001;61(10):1205-15.
139. Yin F, Giuliano AE, Law RE, Van Herle AJ. Apigenin inhibits growth and induces G2/M arrest by modulating cyclin-CDK regulators and ERK MAP kinase activation in breast carcinoma cells. Anticancer Res. 2001;21(1A):413-20.
140. Ruela-de-Sousa RR, Fuhler GM, Blom N, Ferreira CV, Aoyama H, Peppelenbosch MP. Cytotoxicity of apigenin on leukemia cell lines: implications for prevention and therapy. Cell Death & Disease. 2010;1(1):e19-e.
141. Tseng T-H, Chien M-H, Lin W-L, Wen Y-C, Chow J-M, Chen C-K, et al. Inhibition of MDA-MB-231 breast cancer cell proliferation and tumor growth by apigenin through induction of G2/M arrest and histone H3 acetylation-mediated p21WAF1/CIP1 expression. Environmental Toxicology. 2017;32(2):434-44.
142. Meng S, Zhu Y, Li JF, Wang X, Liang Z, Li SQ, et al. Apigenin inhibits renal cell carcinoma cell proliferation. Oncotarget. 2017;8(12):19834-42.
143. Shi M-D, Shiao C-K, Lee Y-C, Shih Y-W. Apigenin, a dietary flavonoid, inhibits proliferation of human bladder cancer T-24 cells via blocking cell cycle progression and inducing apoptosis. Cancer Cell International. 2015;15(1):33.
144. Shukla S, Fu P, Gupta S. Apigenin induces apoptosis by targeting inhibitor of apoptosis proteins and Ku70–Bax interaction in prostate cancer. Apoptosis. 2014;19(5):883-94.
145. Wang B, Zhao X-H. Apigenin induces both intrinsic and extrinsic pathways of apoptosis in human colon carcinoma HCT-116 cells. Oncol Rep. 2017;37(2):1132-40.
146. Chan L-P, Chou T-H, Ding H-Y, Chen P-R, Chiang F-Y, Kuo P-L, et al. Apigenin induces apoptosis via tumor necrosis factor receptor- and Bcl-2-mediated pathway and enhances susceptibility of head and neck squamous cell carcinoma to 5-fluorouracil and cisplatin. Biochimica et Biophysica Acta (BBA) - General Subjects. 2012;1820(7):1081-91.
147. Zhang L, Cheng X, Gao Y, Zheng J, Xu Q, Sun Y, et al. Apigenin induces autophagic cell death in human papillary thyroid carcinoma BCPAP cells. Food Funct. 2015;6(11):3464-72.
148. Lee Y, Sung B, Kang YJ, Kim DH, Jang J-Y, Hwang SY, et al. Apigenin-induced apoptosis is enhanced by inhibition of autophagy formation in HCT116 human colon cancer cells. Int J Oncol. 2014;44(5):1599-606.
149. Lindenmeyer F, Li H, Menashi S, Soria C, Lu H. Apigenin Acts on the Tumor Cell Invasion Process and Regulates Protease Production. Nutrition and Cancer. 2001;39(1):139-47.
150. Spoerlein C, Mahal K, Schmidt H, Schobert R. Effects of chrysin, apigenin, genistein and their homoleptic copper(II) complexes on the growth and metastatic potential of cancer cells. Journal of Inorganic Biochemistry. 2013;127:107-15.
151. Seo HS, Ku JM, Choi HS, Woo JK, Jang BH, Go H, et al. Apigenin induces caspase-dependent apoptosis by inhibiting signal transducer and activator of transcription 3 signaling in HER2-overexpressing SKBR3 breast cancer cells. Mol Med Rep. 2015;12(2):2977-84.
152. Alms GR, Sanz P, Carlson M, Haystead TAJ. Reg1p targets protein phosphatase 1 to dephosphorylate hexokinase II in Saccharomyces cerevisiae:

characterizing the effects of a phosphatase subunit on the yeast proteome. The EMBO Journal. 1999;18(15):4157-68.
153. Ahn NG, Resing KA. Toward the phosphoproteome. Nature Biotechnology. 2001;19(4):317-8.
154. Riley NM, Coon JJ. Phosphoproteomics in the Age of Rapid and Deep Proteome Profiling. Analytical Chemistry. 2016;88(1):74-94.
155. Hogrebe A, von Stechow L, Bekker-Jensen DB, Weinert BT, Kelstrup CD, Olsen JV. Benchmarking common quantification strategies for large-scale phosphoproteomics. Nature Communications. 2018;9(1):1045.
156. Locard-Paulet M, Bouyssié D, Froment C, Burlet-Schiltz O, Jensen LJ. Comparing 22 Popular Phosphoproteomics Pipelines for Peptide Identification and Site Localization. Journal of Proteome Research. 2020;19(3):1338-45.
157. Safaei J, Maňuch J, Gupta A, Stacho L, Pelech S. Prediction of 492 human protein kinase substrate specificities. Proteome Science. 2011;9(1):S6.
158. Cheng F, Jia P, Wang Q, Zhao Z. Quantitative network mapping of the human kinome interactome reveals new clues for rational kinase inhibitor discovery and individualized cancer therapy. Oncotarget. 2014;5(11).
159. Hornbeck PV, Kornhauser JM, Tkachev S, Zhang B, Skrzypek E, Murray B, et al. PhosphoSitePlus: a comprehensive resource for investigating the structure and function of experimentally determined post-translational modifications in man and mouse. Nucleic Acids Research. 2011;40(D1):D261-D70.
160. Dinkel H, Chica C, Via A, Gould CM, Jensen LJ, Gibson TJ, et al. Phospho.ELM: a database of phosphorylation sites—update 2011. Nucleic Acids Research. 2010;39(suppl_1):D261-D7.
161. Linding R, Jensen LJ, Pasculescu A, Olhovsky M, Colwill K, Bork P, et al. NetworKIN: a resource for exploring cellular phosphorylation networks. Nucleic Acids Research. 2007;36(suppl_1):D695-D9.
162. Gao J, Thelen JJ, Dunker AK, Xu D. Musite, a Tool for Global Prediction of General and Kinase-specific Phosphorylation Sites *. Molecular & Cellular Proteomics. 2010;9(12):2586-600.
163. Song C, Ye M, Liu Z, Cheng H, Jiang X, Han G, et al. Systematic Analysis of Protein Phosphorylation Networks From Phosphoproteomic Data *. Molecular & Cellular Proteomics. 2012;11(10):1070-83.
164. Wiredja DD, Koyutürk M, Chance MR. The KSEA App: a web-based tool for kinase activity inference from quantitative phosphoproteomics. Bioinformatics. 2017;33(21):3489-91.
165. Lachmann A, Ma'ayan A. KEA: kinase enrichment analysis. Bioinformatics. 2009;25(5):684-6.
166. Sung H, Ferlay J, Siegel RL, Laversanne M, Soerjomataram I, Jemal A, et al. Global Cancer Statistics 2020: GLOBOCAN Estimates of Incidence and Mortality Worldwide for 36 Cancers in 185 Countries. CA: A Cancer Journal for Clinicians. 2021;71(3):209-49.
167. de Melo Gagliato D, Jardim DL, Marchesi MS, Hortobagyi GN. Mechanisms of resistance and sensitivity to anti-HER2 therapies in HER2+ breast cancer. Oncotarget. 2016;7(39):64431-46.

168. Ventriglia J, Paciolla I, Pisano C, Cecere SC, Di Napoli M, Tambaro R, et al. Immunotherapy in ovarian, endometrial and cervical cancer: State of the art and future perspectives. Cancer Treatment Reviews. 2017;59:109-16.
169. Mason JK, Thompson LU. Flaxseed and its lignan and oil components: can they play a role in reducing the risk of and improving the treatment of breast cancer? Appl Physiol Nutr Metab. 2014;39(6):663-78.
170. Rahman N, Jeon M, Song HY, Kim YS. Cryptotanshinone, a compound of Salvia miltiorrhiza inhibits pre-adipocytes differentiation by regulation of adipogenesis-related genes expression via STAT3 signaling. Phytomedicine. 2016;23(1):58-67.
171. Wu J, Meng L, Long M, Ruan Y, Li X, Huang Y, et al. Inhibition of breast cancer cell growth by the Pteris semipinnata extract ent-11α-hydroxy-15-oxo-kaur-16-en-19-oic-acid. Oncology letters. 2017;14(6):6809-14.
172. Sayeed MA, Bracci M, Ciarapica V, Malavolta M, Provinciali M, Pieragostini E, et al. Allyl Isothiocyanate Exhibits No Anticancer Activity in MDA-MB-231 Breast Cancer Cells. Int J Mol Sci. 2018;19(1).
173. Zhang Y, Chen S, Wei C, Rankin GO, Rojanasakul Y, Ren N, et al. Dietary Compound Proanthocyanidins from Chinese bayberry (Myrica rubra Sieb. et Zucc.) leaves inhibit angiogenesis and regulate cell cycle of cisplatin-resistant ovarian cancer cells via targeting Akt pathway. J Funct Foods. 2018;40:573-81.
174. Zhang Q, Dong J, Cui J, Huang G, Meng Q, Li S. Cytotoxicity of Synthesized 1,4-Naphthoquinone Oxime Derivatives on Selected Human Cancer Cell Lines. Chem Pharm Bull (Tokyo). 2018;66(6):612-9.
175. Puglisi MP, Bradaric MJ, Pontikis J, Cabai J, Weyna T, Tednes P, et al. Novel primary amine diazeniumdiolates-Chemical and biological characterization. Drug Dev Res. 2018;79(3):136-43.
176. Tsai SY, Chung PC, Owaga EE, Tsai IJ, Wang PY, Tsai JI, et al. Alpha-mangostin from mangosteen (Garcinia mangostana Linn.) pericarp extract reduces high fat-diet induced hepatic steatosis in rats by regulating mitochondria function and apoptosis. Nutr Metab (Lond). 2016;13:88.
177. Sándor Z, Mottaghipisheh J, Veres K, Hohmann J, Bencsik T, Horváth A, et al. Evidence Supports Tradition: The in Vitro Effects of Roman Chamomile on Smooth Muscles. Front Pharmacol. 2018;9:323.
178. Chantarudee A, Phuwapraisirisan P, Kimura K, Okuyama M, Mori H, Kimura A, et al. Chemical constituents and free radical scavenging activity of corn pollen collected from Apis mellifera hives compared to floral corn pollen at Nan, Thailand. BMC Complement Altern Med. 2012;12:45.
179. Sivaranjani M, Srinivasan R, Aravindraja C, Karutha Pandian S, Veera Ravi A. Inhibitory effect of α-mangostin on Acinetobacter baumannii biofilms - an in vitro study. Biofouling. 2018;34(5):579-93.
180. Chen G, Li Y, Wang W, Deng L. Bioactivity and pharmacological properties of α-mangostin from the mangosteen fruit: a review. Expert Opin Ther Pat. 2018;28(5):415-27.
181. Kumar KS, Sabu V, Sindhu G, Rauf AA, Helen A. Isolation, identification and characterization of apigenin from Justicia gendarussa and its anti-inflammatory activity. Int Immunopharmacol. 2018;59:157-67.

182. Abu Bakar FI, Abu Bakar MF, Rahmat A, Abdullah N, Sabran SF, Endrini S. Anti-gout Potential of Malaysian Medicinal Plants. Front Pharmacol. 2018;9:261.
183. Tang AQ, Cao XC, Tian L, He L, Liu F. Apigenin inhibits the self-renewal capacity of human ovarian cancer SKOV3derived sphere-forming cells. Mol Med Rep. 2015;11(3):2221-6.
184. Suh YA, Jo SY, Lee HY, Lee C. Inhibition of IL-6/STAT3 axis and targeting Axl and Tyro3 receptor tyrosine kinases by apigenin circumvent taxol resistance in ovarian cancer cells. Int J Oncol. 2015;46(3):1405-11.
185. Niu W, Chen F, Wang J, Qian J, Yan S. Antitumor effect of sikokianin C, a selective cystathionine β-synthase inhibitor, against human colon cancer in vitro and in vivo. Medchemcomm. 2018;9(1):113-20.
186. Fang A, Zhang Q, Fan H, Zhou Y, Yao Y, Zhang Y, et al. Discovery of human lactate dehydrogenase A (LDHA) inhibitors as anticancer agents to inhibit the proliferation of MG-63 osteosarcoma cells. Medchemcomm. 2017;8(8):1720-6.
187. Xu X, Rawling T, Roseblade A, Bishop R, Ung AT. Antiproliferative activities of alkaloid-like compounds. Medchemcomm. 2017;8(11):2105-14.
188. Koopman G, Reutelingsperger CP, Kuijten GA, Keehnen RM, Pals ST, van Oers MH. Annexin V for flow cytometric detection of phosphatidylserine expression on B cells undergoing apoptosis. Blood. 1994;84(5):1415-20.
189. Ko KP. Isoflavones: chemistry, analysis, functions and effects on health and cancer. Asian Pac J Cancer Prev. 2014;15(17):7001-10.
190. Easton DF, Bishop DT, Ford D, Crockford GP. Genetic linkage analysis in familial breast and ovarian cancer: results from 214 families. The Breast Cancer Linkage Consortium. Am J Hum Genet. 1993;52(4):678-701.
191. Yin L, Li J, Wei Y, Ma D, Sun Y, Sun Y. Primary ovarian small cell carcinoma of pulmonary type with coexisting endometrial carcinoma in a breast cancer patient receiving tamoxifen: A case report and literature review. Medicine (Baltimore). 2018;97(23):e10900.
192. Zhang L, Shin VY, Chai X, Zhang A, Chan TL, Ma ES, et al. Breast and ovarian cancer penetrance of BRCA1/2 mutations among Hong Kong women. Oncotarget. 2018;9(38):25025-33.
193. Reuter S, Gupta SC, Chaturvedi MM, Aggarwal BB. Oxidative stress, inflammation, and cancer: how are they linked? Free Radic Biol Med. 2010;49(11):1603-16.
194. Weinberg F, Chandel NS. Reactive oxygen species-dependent signaling regulates cancer. Cell Mol Life Sci. 2009;66(23):3663-73.
195. Chan DW, Liu VW, Tsao GS, Yao KM, Furukawa T, Chan KK, et al. Loss of MKP3 mediated by oxidative stress enhances tumorigenicity and chemoresistance of ovarian cancer cells. Carcinogenesis. 2008;29(9):1742-50.
196. Kang KA, Hyun JW. Oxidative Stress, Nrf2, and Epigenetic Modification Contribute to Anticancer Drug Resistance. Toxicol Res. 2017;33(1):1-5.
197. Fang Y, Su T, Qiu X, Mao P, Xu Y, Hu Z, et al. Protective effect of alpha-mangostin against oxidative stress induced-retinal cell death. Sci Rep. 2016;6:21018.
198. Mehlen P, Puisieux A. Metastasis: a question of life or death. Nature Reviews Cancer. 2006;6(6):449-58.
199. Chang CM, Wang ML, Lu KH, Yang YP, Juang CM, Wang PH, et al. Integrating the dysregulated inflammasome-based molecular functionome in the

malignant transformation of endometriosis-associated ovarian carcinoma. Oncotarget. 2018;9(3):3704-26.
200. Latz E, Xiao TS, Stutz A. Activation and regulation of the inflammasomes. Nature Reviews Immunology. 2013;13(6):397-411.
201. Man SM, Kanneganti TD. Regulation of inflammasome activation. Immunol Rev. 2015;265(1):6-21.
202. Barreiro-Iglesias A, Sobrido-Cameán D, Shifman MI. Retrograde Activation of the Extrinsic Apoptotic Pathway in Spinal-Projecting Neurons after a Complete Spinal Cord Injury in Lampreys. BioMed Research International. 2017;2017:5953674.
203. Hsu YN, Shyu HW, Hu TW, Yeh JP, Lin YW, Lee LY, et al. Anti-proliferative activity of biochanin A in human osteosarcoma cells via mitochondrial-involved apoptosis. Food Chem Toxicol. 2018;112:194-204.
204. Sano Y, Kogashiwa Y, Araki R, Enoki Y, Ikeda T, Yoda T, et al. Correlation of Inflammatory Markers, Survival, and COX2 Expression in Oral Cancer and Implications for Prognosis. Otolaryngol Head Neck Surg. 2018;158(4):667-76.
205. Perego S, Sansoni V, Banfi G, Lombardi G. Sodium butyrate has anti-proliferative, pro-differentiating, and immunomodulatory effects in osteosarcoma cells and counteracts the TNFα-induced low-grade inflammation. Int J Immunopathol Pharmacol. 2018;32:394632017752240.
206. Casili G, Campolo M, Paterniti I, Lanza M, Filippone A, Cuzzocrea S, et al. Dimethyl Fumarate Attenuates Neuroinflammation and Neurobehavioral Deficits Induced by Experimental Traumatic Brain Injury. J Neurotrauma. 2018;35(13):1437-51.
207. Papini A. Investigation of Morphological Features of Autophagy During Plant Programmed Cell Death. Methods Mol Biol. 2018;1743:9-19.
208. Yurdacan B, Egeli U, Eskiler GG, Eryilmaz IE, Cecener G, Tunca B. The role of usnic acid-induced apoptosis and autophagy in hepatocellular carcinoma. Hum Exp Toxicol. 2019;38(2):201-15.
209. Boehning AL, Essien SA, Underwood EL, Dash PK, Boehning D. Cell type-dependent effects of ellagic acid on cellular metabolism. Biomed Pharmacother. 2018;106:411-8.
210. Hu Y, Li X, An Y, Duan J, Yang XD. Selection of a novel CD19 aptamer for targeted delivery of doxorubicin to lymphoma cells. Oncotarget. 2018;9(42):26605-15.
211. Vallée A, Lecarpentier Y. Crosstalk Between Peroxisome Proliferator-Activated Receptor Gamma and the Canonical WNT/β-Catenin Pathway in Chronic Inflammation and Oxidative Stress During Carcinogenesis. Front Immunol. 2018;9:745.
212. O'Prey J, Brown J, Fleming J, Harrison PR. Effects of dietary flavonoids on major signal transduction pathways in human epithelial cells. Biochemical Pharmacology. 2003;66(11):2075-88.
213. Otake Y, Soundararajan S, Sengupta TK, Kio EA, Smith JC, Pineda-Roman M, et al. Overexpression of nucleolin in chronic lymphocytic leukemia cells induces stabilization of bcl2 mRNA. Blood. 2007;109(7):3069-75.

214. Shibata MA, Hamaoka H, Morimoto J, Kanayama T, Maemura K, Ito Y, et al. Synthetic α-mangostin dilaurate strongly suppresses wide-spectrum organ metastasis in a mouse model of mammary cancer. Cancer Sci. 2018;109(5):1660-71.
215. Xia Y, Sun J. Synergistic inhibition of cell proliferation by combined targeting with kinase inhibitors and dietary xanthone is a promising strategy for melanoma treatment. Clin Exp Dermatol. 2018;43(2):149-57.
216. Nurul SAS, Hazilawati H, Mohd RS, Mohd FHR, Noordin MM, Norhaizan ME. Subacute Oral Toxicity Assesment of Ethanol Extract of Mariposa christia vespertilionis Leaves in Male Sprague Dawley Rats. Toxicol Res. 2018;34(2):85-95.
217. Lee Y. Cancer Chemopreventive Potential of Procyanidin. Toxicol Res. 2017;33(4):273-82.
218. Mei J, Tian H, Huang H-S, Hsu C-F, Liou Y, Wu N, et al. Cellular models of development of ovarian high-grade serous carcinoma: A review of cell of origin and mechanisms of carcinogenesis. Cell Proliferation. 2021;54(5):e13029.
219. Shih I-M, Wang Y, Wang T-L. The Origin of Ovarian Cancer Species and Precancerous Landscape. The American Journal of Pathology. 2021;191(1):26-39.
220. Shi Y-Y, Meng X-T, Xu Y-N, Tian X-J. Role of FOXO protein's abnormal activation through PI3K/AKT pathway in platinum resistance of ovarian cancer. Journal of Obstetrics and Gynaecology Research. 2021;47(6):1946-57.
221. Elyashiv O, Wong YNS, Ledermann JA. Frontline Maintenance Treatment for Ovarian Cancer. Current Oncology Reports. 2021;23(8):97.
222. Damia G, Broggini M. Platinum Resistance in Ovarian Cancer: Role of DNA Repair. Cancers. 2019;11(1):119.
223. Pokhriyal R, Hariprasad R, Kumar L, Hariprasad G. Chemotherapy Resistance in Advanced Ovarian Cancer Patients. Biomarkers in Cancer. 2019;11:1179299X19860815.
224. Wang X, Yang Y, An Y, Fang G. The mechanism of anticancer action and potential clinical use of kaempferol in the treatment of breast cancer. Biomedicine & Pharmacotherapy. 2019;117:109086.
225. Qi J-h, Dong F-x. The relevant targets of anti-oxidative stress: a review. Journal of Drug Targeting. 2021;29(7):677-86.
226. Fan Q, Xu F, Liang B, Zou X. The Anti-Obesity Effect of Traditional Chinese Medicine on Lipid Metabolism. Frontiers in Pharmacology. 2021;12(1486).
227. Patel D, Shukla S, Gupta S. Apigenin and cancer chemoprevention: Progress, potential and promise (Review). Int J Oncol. 2007;30(1):233-45.
228. Salehi B, Venditti A, Sharifi-Rad M, Kręgiel D, Sharifi-Rad J, Durazzo A, et al. The Therapeutic Potential of Apigenin. International Journal of Molecular Sciences. 2019;20(6):1305.
229. Madunić J, Madunić IV, Gajski G, Popić J, Garaj-Vrhovac V. Apigenin: A dietary flavonoid with diverse anticancer properties. Cancer Letters. 2018;413:11-22.
230. Gupta SC, Kunnumakkara AB, Aggarwal S, Aggarwal BB. Inflammation, a Double-Edge Sword for Cancer and Other Age-Related Diseases. Frontiers in Immunology. 2018;9.
231. Shankar E, Goel A, Gupta K, Gupta S. Plant Flavone Apigenin: an Emerging Anticancer Agent. Current Pharmacology Reports. 2017;3(6):423-46.
232. Sung B, Chung HY, Kim ND. Role of Apigenin in Cancer Prevention via the Induction of Apoptosis and Autophagy. J Cancer Prev. 2016;21(4):216-26.

233. Vrhovac Madunić I, Madunić J, Antunović M, Paradžik M, Garaj-Vrhovac V, Breljak D, et al. Apigenin, a dietary flavonoid, induces apoptosis, DNA damage, and oxidative stress in human breast cancer MCF-7 and MDA MB-231 cells. Naunyn-Schmiedeberg's Archives of Pharmacology. 2018;391(5):537-50.
234. Hu XW, Meng D, Fang J. Apigenin inhibited migration and invasion of human ovarian cancer A2780 cells through focal adhesion kinase. Carcinogenesis. 2008;29(12):2369-76.
235. Li ZD, Hu XW, Wang YT, Fang J. Apigenin inhibits proliferation of ovarian cancer A2780 cells through Id1. FEBS Lett. 2009;583(12):1999-2003.
236. Ittiudomrak T, Puthong S, Roytrakul S, Chanchao C. alpha-Mangostin and Apigenin Induced Cell Cycle Arrest and Programmed Cell Death in SKOV-3 Ovarian Cancer Cells. Toxicol Res. 2019;35(2):167-79.
237. Nigg EA. Mitotic kinases as regulators of cell division and its checkpoints. Nature Reviews Molecular Cell Biology. 2001;2(1):21-32.
238. Vermeulen K, Van Bockstaele DR, Berneman ZN. The cell cycle: a review of regulation, deregulation and therapeutic targets in cancer. Cell Proliferation. 2003;36(3):131-49.
239. Sears RC, Nevins JR. Signaling Networks That Link Cell Proliferation and Cell Fate *. Journal of Biological Chemistry. 2002;277(14):11617-20.
240. VADLAKONDA L, Pasupuleti M, Reddanna P. Role of PI3K-AKT-mTOR and Wnt Signaling Pathways in Transition of G1-S Phase of Cell Cycle in Cancer Cells. Frontiers in Oncology. 2013;3(85).
241. Shobahah J, Xue S, Hu D, Zhao C, Wei M, Quan Y, et al. Quantitative phosphoproteome on the silkworm (Bombyx mori) cells infected with baculovirus. Virology Journal. 2017;14(1):117.
242. Subramanian A, Tamayo P, Mootha VK, Mukherjee S, Ebert BL, Gillette MA, et al. Gene set enrichment analysis: A knowledge-based approach for interpreting genome-wide expression profiles. Proceedings of the National Academy of Sciences. 2005;102(43):15545-50.
243. Horn H, Schoof EM, Kim J, Robin X, Miller ML, Diella F, et al. KinomeXplorer: an integrated platform for kinome biology studies. Nature Methods. 2014;11(6):603-4.
244. Wang P, Henning SM, Heber D. Limitations of MTT and MTS-Based Assays for Measurement of Antiproliferative Activity of Green Tea Polyphenols. PLOS ONE. 2010;5(4):e10202.
245. Kaur P, Shukla S, Gupta S. Plant flavonoid apigenin inactivates Akt to trigger apoptosis in human prostate cancer: an in vitro and in vivo study. Carcinogenesis. 2008;29(11):2210-7.
246. Bøgebo R, Horn H, Olsen JV, Gammeltoft S, Jensen LJ, Hansen JL, et al. Predicting Kinase Activity in Angiotensin Receptor Phosphoproteomes Based on Sequence-Motifs and Interactions. PLOS ONE. 2014;9(4):e94672.
247. Manning G, Whyte DB, Martinez R, Hunter T, Sudarsanam S. The Protein Kinase Complement of the Human Genome. Science. 2002;298(5600):1912-34.
248. Beurel E, Grieco SF, Jope RS. Glycogen synthase kinase-3 (GSK3): Regulation, actions, and diseases. Pharmacology & Therapeutics. 2015;148:114-31.
249. Pelzer AE, Bektic J, Haag P, Berger AP, Pycha A, Schäfer G, et al. The Expression of Transcription Factor Activating Transcription Factor 3 in the Human

Prostate and its Regulation by Androgen in Prostate Cancer. Journal of Urology. 2006;175(4):1517-22.
250. Hasim MS, Nessim C, Villeneuve PJ, Vanderhyden BC, Dimitroulakos J. Activating Transcription Factor 3 as a Novel Regulator of Chemotherapy Response in Breast Cancer. Transl Oncol. 2018;11(4):988-98.
251. Suk F-M, Lien G-S, Huang W-J, Chen C-N, Lu S-Y, Yang Y-C, et al. A Taiwanese Propolis Derivative Induces Apoptosis through Inducing Endoplasmic Reticular Stress and Activating Transcription Factor-3 in Human Hepatoma Cells. Evidence-Based Complementary and Alternative Medicine. 2013;2013:11.
252. Tang R, Hirsch P, Fava F, Lapusan S, Marzac C, Teyssandier I, et al. High Id1 expression is associated with poor prognosis in 237 patients with acute myeloid leukemia. Blood. 2009;114(14):2993-3000.
253. Paredes-Gonzalez X, Fuentes F, Su Z-Y, Kong A-NT. Apigenin Reactivates Nrf2 Anti-oxidative Stress Signaling in Mouse Skin Epidermal JB6 P + Cells Through Epigenetics Modifications. The AAPS Journal. 2014;16(4):727-35.
254. Kanwal R, Datt M, Liu X, Gupta S. Dietary Flavones as Dual Inhibitors of DNA Methyltransferases and Histone Methyltransferases. PLOS ONE. 2016;11(9):e0162956.
255. Iizumi Y, Oishi M, Taniguchi T, Goi W, Sowa Y, Sakai T. The Flavonoid Apigenin Downregulates CDK1 by Directly Targeting Ribosomal Protein S9. PLOS ONE. 2013;8(8):e73219.
256. Dash BC, El-Deiry WS. Phosphorylation of p21 in G₂/M Promotes Cyclin B-Cdc2 Kinase Activity. Molecular and Cellular Biology. 2005;25(8):3364-87.
257. Boehm EM, Gildenberg MS, Washington MT. Chapter Seven - The Many Roles of PCNA in Eukaryotic DNA Replication. In: Kaguni LS, Oliveira MT, editors. The Enzymes. 39: Academic Press; 2016. p. 231-54.
258. Lavoie G, St-Pierre Y. Phosphorylation of human DNMT1: Implication of cyclin-dependent kinases. Biochemical and Biophysical Research Communications. 2011;409(2):187-92.
259. Estève P-O, Zhang G, Ponnaluri VKC, Deepti K, Chin HG, Dai N, et al. Binding of 14-3-3 reader proteins to phosphorylated DNMT1 facilitates aberrant DNA methylation and gene expression. Nucleic Acids Research. 2015;44(4):1642-56.
260. Contreras A, Hale TK, Stenoien DL, Rosen JM, Mancini MA, Herrera RE. The Dynamic Mobility of Histone H1 Is Regulated by Cyclin/CDK Phosphorylation. Molecular and Cellular Biology. 2003;23(23):8626-36.
261. Franzen CA, Amargo E, Todorović V, Desai BV, Huda S, Mirzoeva S, et al. The Chemopreventive Bioflavonoid Apigenin Inhibits Prostate Cancer Cell Motility through the Focal Adhesion Kinase/Src Signaling Mechanism. Cancer Prevention Research. 2009;2(9):830-41.
262. Chan KT, Cortesio CL, Huttenlocher A. FAK alters invadopodia and focal adhesion composition and dynamics to regulate breast cancer invasion. J Cell Biol. 2009;185(2):357-70.
263. Small JV, Stradal T, Vignal E, Rottner K. The lamellipodium: where motility begins. Trends in Cell Biology. 2002;12(3):112-20.

264. Zhao J, Wei J, Mialki R, Zou C, Mallampalli RK, Zhao Y. Extracellular Signal-regulated Kinase (ERK) Regulates Cortactin Ubiquitination and Degradation in Lung Epithelial Cells *. Journal of Biological Chemistry. 2012;287(23):19105-14.
265. Dai J, Van Wie PG, Fai LY, Kim D, Wang L, Poyil P, et al. Downregulation of NEDD9 by apigenin suppresses migration, invasion, and metastasis of colorectal cancer cells. Toxicology and Applied Pharmacology. 2016;311:106-12.
266. Zhang R, Shi H, Ren F, Zhang M, Ji P, Wang W, et al. The aberrant upstream pathway regulations of CDK1 protein were implicated in the proliferation and apoptosis of ovarian cancer cells. Journal of Ovarian Research. 2017;10(1):60.
267. Ujiki MB, Ding X-Z, Salabat MR, Bentrem DJ, Golkar L, Milam B, et al. Apigenin inhibits pancreatic cancer cell proliferation through G2/M cell cycle arrest. Molecular Cancer. 2006;5(1):76.
268. Arango D, Parihar A, Villamena FA, Wang L, Freitas MA, Grotewold E, et al. Apigenin induces DNA damage through the PKCδ-dependent activation of ATM and H2AX causing down-regulation of genes involved in cell cycle control and DNA repair. Biochemical Pharmacology. 2012;84(12):1571-80.
269. Falck J, Mailand N, Syljuåsen RG, Bartek J, Lukas J. The ATM–Chk2–Cdc25A checkpoint pathway guards against radioresistant DNA synthesis. Nature. 2001;410(6830):842-7.
270. El-Deiry WS. The role of p53 in chemosensitivity and radiosensitivity. Oncogene. 2003;22(47):7486-95.
271. Iliakis G, Wang Y, Guan J, Wang H. DNA damage checkpoint control in cells exposed to ionizing radiation. Oncogene. 2003;22(37):5834-47.
272. Bulavin DV, Higashimoto Y, Demidenko ZN, Meek S, Graves P, Phillips C, et al. Dual phosphorylation controls Cdc25 phosphatases and mitotic entry. Nature Cell Biology. 2003;5(6):545-51.
273. Lundgren K, Walworth N, Booher R, Dembski M, Kirschner M, Beach D. mik1 and wee1 cooperate in the inhibitory tyrosine phosphorylation of cdc2. Cell. 1991;64(6):1111-22.
274. Korga-Plewko A, Michalczyk M, Adamczuk G, Humeniuk E, Ostrowska-Lesko M, Jozefczyk A, et al. Apigenin and Hesperidin Downregulate DNA Repair Genes in MCF-7 Breast Cancer Cells and Augment Doxorubicin Toxicity. Molecules. 2020;25(19):4421.
275. Song J, Parker L, Hormozi L, Tanouye MA. DNA topoisomerase I inhibitors ameliorate seizure-like behaviors and paralysis in a Drosophila model of epilepsy. Neuroscience. 2008;156(3):722-8.
276. Yan Y, Black CP, Cowan KH. Irradiation-induced G2/M checkpoint response requires ERK1/2 activation. Oncogene. 2007;26(32):4689-98.
277. Lu Z, Xu S. ERK1/2 MAP kinases in cell survival and apoptosis. IUBMB Life. 2006;58(11):621-31.
278. Zhang Q, Zhao X-H, Wang Z-J. Cytotoxicity of flavones and flavonols to a human esophageal squamous cell carcinoma cell line (KYSE-510) by induction of G2/M arrest and apoptosis. Toxicology in Vitro. 2009;23(5):797-807.
279. Kreis NN, Louwen F, Yuan J. Less understood issues: p21Cip1 in mitosis and its therapeutic potential. Oncogene. 2015;34(14):1758-67.

280. de la Fuente van Bentem S, Mentzen WI, de la Fuente A, Hirt H. Towards functional phosphoproteomics by mapping differential phosphorylation events in signaling networks. PROTEOMICS. 2008;8(21):4453-65.
281. Zhou H, Albuquerque C, Liang J, Suhandynata RT, Weng S. Quantitative phosphoproteomics. Cell Cycle. 2010;9(17):3479-84.
282. Mischnik M, Sacco F, Cox J, Schneider H-C, Schäfer M, Hendlich M, et al. IKAP: A heuristic framework for inference of kinase activities from Phosphoproteomics data. Bioinformatics. 2015;32(3):424-31.
283. Yang P, Patrick E, Humphrey SJ, Ghazanfar S, James DE, Jothi R, et al. KinasePA: Phosphoproteomics data annotation using hypothesis driven kinase perturbation analysis. PROTEOMICS. 2016;16(13):1868-71.
284. Hornbeck PV, Zhang B, Murray B, Kornhauser JM, Latham V, Skrzypek E. PhosphoSitePlus, 2014: mutations, PTMs and recalibrations. Nucleic Acids Research. 2014;43(D1):D512-D20.
285. Yang C-Y, Chang C-H, Yu Y-L, Lin T-CE, Lee S-A, Yen C-C, et al. PhosphoPOINT: a comprehensive human kinase interactome and phospho-protein database. Bioinformatics. 2008;24(16):i14-i20.
286. Chavez KJ, Garimella SV, Lipkowitz S. Triple negative breast cancer cell lines: one tool in the search for better treatment of triple negative breast cancer. Breast Dis. 2010;32(1-2):35-48.
287. Lin C-H, Chang C-Y, Lee K-R, Lin H-J, Chen T-H, Wan L. Flavones inhibit breast cancer proliferation through the Akt/FOXO3a signaling pathway. BMC Cancer. 2015;15(1):958.
288. Lecomte S, Demay F, Pham TH, Moulis S, Efstathiou T, Chalmel F, et al. Deciphering the Molecular Mechanisms Sustaining the Estrogenic Activity of the Two Major Dietary Compounds Zearalenone and Apigenin in ER-Positive Breast Cancer Cell Lines. Nutrients. 2019;11(2):237.
289. Bauer D, Mazzio E, Soliman KFA. Whole Transcriptomic Analysis of Apigenin on TNFα Immuno-activated MDA-MB-231 Breast Cancer Cells. Cancer Genomics - Proteomics. 2019;16(6):421-31.
290. Bauer D, Mazzio E, Hilliard A, Oriaku ET, Soliman KFA. Effect of apigenin on whole transcriptome profile of TNFα-activated MDA-MB-468 triple negative breast cancer cells. Oncol Lett. 2020;19(3):2123-32.
291. Lambert SA, Jolma A, Campitelli LF, Das PK, Yin Y, Albu M, et al. The Human Transcription Factors. Cell. 2018;172(4):650-65.
292. Fornes O, Castro-Mondragon JA, Khan A, van der Lee R, Zhang X, Richmond PA, et al. JASPAR 2020: update of the open-access database of transcription factor binding profiles. Nucleic Acids Research. 2019;48(D1):D87-D92.
293. Grant CE, Bailey TL, Noble WS. FIMO: scanning for occurrences of a given motif. Bioinformatics. 2011;27(7):1017-8.
294. Bailey TL, Johnson J, Grant CE, Noble WS. The MEME Suite. Nucleic Acids Research. 2015;43(W1):W39-W49.
295. Clements EG, Mohammad HP, Leadem BR, Easwaran H, Cai Y, Van Neste L, et al. DNMT1 modulates gene expression without its catalytic activity partially through its interactions with histone-modifying enzymes. Nucleic Acids Research. 2012;40(10):4334-46.

296. Liu Y, Ao X, Jia Z, Bai X-Y, Xu Z, Hu G, et al. FOXK2 Transcription Factor Suppresses ERα-positive Breast Cancer Cell Growth Through Down-Regulating the Stability of ERα via mechanism involving BRCA1/BARD1. Scientific Reports. 2015;5(1):8796.
297. Schummer P, Kuphal S, Vardimon L, Bosserhoff AK, Kappelmann M. Specific c-Jun target genes in malignant melanoma. Cancer Biology & Therapy. 2016;17(5):486-97.
298. Satoh J-i, Tabunoki H. A Comprehensive Profile of ChIP-Seq-Based STAT1 Target Genes Suggests the Complexity of STAT1-Mediated Gene Regulatory Mechanisms. Gene Regulation and Systems Biology. 2013;7:GRSB.S11433.
299. Carpenter RL, Lo H-W. STAT3 Target Genes Relevant to Human Cancers. Cancers. 2014;6(2):897-925.
300. Davis CA, Hitz BC, Sloan CA, Chan ET, Davidson JM, Gabdank I, et al. The Encyclopedia of DNA elements (ENCODE): data portal update. Nucleic Acids Research. 2017;46(D1):D794-D801.
301. Li Y, Cheng X, Chen C, Huijuan W, Zhao H, Liu W, et al. Apigenin, a flavonoid constituent derived from P. villosa, inhibits hepatocellular carcinoma cell growth by CyclinD1/CDK4 regulation via p38 MAPK-p21 signaling. Pathology - Research and Practice. 2020;216(1):152701.
302. Shukla S, Bhaskaran N, Babcook MA, Fu P, MacLennan GT, Gupta S. Apigenin inhibits prostate cancer progression in TRAMP mice via targeting PI3K/Akt/FoxO pathway. Carcinogenesis. 2013;35(2):452-60.
303. Shukla S, Kanwal R, Shankar E, Datt M, Chance MR, Fu P, et al. Apigenin blocks IKKα activation and suppresses prostate cancer progression. Oncotarget. 2015;6(31).
304. Wang W, Heideman L, Chung CS, Pelling JC, Koehler KJ, Birt DF. Cell-Cycle Arrest at G2/M and Growth Inhibition by Apigenin in Human Colon Carcinoma Cell Lines. Molecular Carcinogenesis. 2000;28(2):102-10.
305. Maggioni D, Garavello W, Rigolio R, Pignataro L, Gaini R, Nicolini G. Apigenin impairs oral squamous cell carcinoma growth in vitro inducing cell cycle arrest and apoptosis. Int J Oncol. 2013;43(5):1675-82.
306. Jayasooriya RGPT, Kang S-H, Kang C-H, Choi YH, Moon D-O, Hyun J-W, et al. Apigenin decreases cell viability and telomerase activity in human leukemia cell lines. Food and Chemical Toxicology. 2012;50(8):2605-11.
307. Banerjee K, Mandal M. Oxidative stress triggered by naturally occurring flavone apigenin results in senescence and chemotherapeutic effect in human colorectal cancer cells. Redox Biology. 2015;5:153-62.
308. Chiang L-C, Ng LT, Lin IC, Kuo P-L, Lin C-C. Anti-proliferative effect of apigenin and its apoptotic induction in human Hep G2 cells. Cancer Letters. 2006;237(2):207-14.
309. Way T-D, Kao M-C, Lin J-K. Apigenin Induces Apoptosis through Proteasomal Degradation of HER2/neu in HER2/neu-overexpressing Breast Cancer Cells via the Phosphatidylinositol 3-Kinase/Akt-dependent Pathway *. Journal of Biological Chemistry. 2004;279(6):4479-89.
310. Yu L, Wang Y, Yao Y, Li W, Lai Q, Li J, et al. Eradication of Growth of HER2-Positive Ovarian Cancer With Trastuzumab-DM1, an Antibody-Cytotoxic

Drug Conjugate in Mouse Xenograft Model. International Journal of Gynecologic Cancer. 2014;24(7):1158-64.
311. Woolbright BL, Rajendran G, Harris RA, Taylor JA. Metabolic Flexibility in Cancer: Targeting the Pyruvate Dehydrogenase Kinase:Pyruvate Dehydrogenase Axis. Molecular Cancer Therapeutics. 2019;18(10):1673-81.
312. Warburg O. Über den Stoffwechsel der Carcinomzelle. Naturwissenschaften. 1924;12(50):1131-7.
313. Shan S, Shi J, Yang P, Jia B, Wu H, Zhang X, et al. Apigenin Restrains Colon Cancer Cell Proliferation via Targeted Blocking of Pyruvate Kinase M2-Dependent Glycolysis. Journal of Agricultural and Food Chemistry. 2017;65(37):8136-44.
314. Sukonina V, Ma H, Zhang W, Bartesaghi S, Subhash S, Heglind M, et al. FOXK1 and FOXK2 regulate aerobic glycolysis. Nature. 2019;566(7743):279-83.
315. Sakaguchi M, Cai W, Wang C-H, Cederquist CT, Damasio M, Homan EP, et al. FoxK1 and FoxK2 in insulin regulation of cellular and mitochondrial metabolism. Nature Communications. 2019;10(1):1582.
316. Worthington J, Spain G, Timms JF. Effects of ErbB2 Overexpression on the Proteome and ErbB Ligand-specific Phosphosignaling in Mammary Luminal Epithelial Cells *. Molecular & Cellular Proteomics. 2017;16(4):608-21.
317. Davis RJ. Signal Transduction by the JNK Group of MAP Kinases. Cell. 2000;103(2):239-52.
318. Chen C-C, Chow M-P, Huang W-C, Lin Y-C, Chang Y-J. Flavonoids Inhibit Tumor Necrosis Factor-α-Induced Up-Regulation of Intercellular Adhesion Molecule-1 (ICAM-1) in Respiratory Epithelial Cells through Activator Protein-1 and Nuclear Factor-κB: Structure-Activity Relationships. Molecular Pharmacology. 2004;66(3):683-93.
319. Van Dross R, Xue Y, Knudson A, Pelling JC. The Chemopreventive Bioflavonoid Apigenin Modulates Signal Transduction Pathways in Keratinocyte and Colon Carcinoma Cell Lines. The Journal of Nutrition. 2003;133(11):3800S-4S.
320. Lin M, Lu S-s, Wang A-x, Qi X-y, Zhao D, Wang Z-h, et al. Apigenin attenuates dopamine-induced apoptosis in melanocytes via oxidative stress-related p38, c-Jun NH2-terminal kinase and Akt signaling. Journal of Dermatological Science. 2011;63(1):10-6.
321. Kovarik P, Stoiber D, Eyers PA, Menghini R, Neininger A, Gaestel M, et al. Stress-induced phosphorylation of STAT1 at Ser727 requires p38 mitogen-activated protein kinase whereas IFN-γ uses a different signaling pathway. Proceedings of the National Academy of Sciences. 1999;96(24):13956-61.
322. Miyazaki T, Bub JD, Iwamoto Y. c-Jun NH2-terminal kinase mediates leptin-stimulated androgen-independent prostate cancer cell proliferation via signal transducer and activator of transcription 3 and Akt. Biochimica et Biophysica Acta (BBA) - Molecular Basis of Disease. 2008;1782(10):593-604.
323. Gartsbein M, Alt A, Hashimoto K, Nakajima K, Kuroki T, Tennenbaum T. The role of protein kinase C δ activation and STAT3 Ser727 phosphorylation in insulin-induced keratinocyte proliferation. Journal of Cell Science. 2006;119(3):470-81.

324. Rezai-Zadeh K, Ehrhart J, Bai Y, Sanberg PR, Bickford P, Tan J, et al. Apigenin and luteolin modulate microglial activation via inhibition of STAT1-induced CD40 expression. Journal of Neuroinflammation. 2008;5(1):41.
325. Seo HS, Ku JM, Choi HS, Woo JK, Lee BH, Kim DS, et al. Apigenin overcomes drug resistance by blocking the signal transducer and activator of transcription 3 signaling in breast cancer cells. Oncol Rep. 2017;38(2):715-24.
326. Lim H, Park H, Kim HP. Effects of Flavonoids on Matrix Metalloproteinase-13 Expression of Interleukin-1<I>β</I>–Treated Articular Chondrocytes and Their Cellular Mechanisms: Inhibition of c-Fos/AP-1 and JAK/STAT Signaling Pathways. Journal of Pharmacological Sciences. 2011;116(2):221-31.
327. Kurata M, Fujiwara N, Fujita K-i, Yamanaka Y, Seno S, Kobayashi H, et al. Food-Derived Compounds Apigenin and Luteolin Modulate mRNA Splicing of Introns with Weak Splice Sites. iScience. 2019;22:336-52.
328. Crider KS, Yang TP, Berry RJ, Bailey LB. Folate and DNA Methylation: A Review of Molecular Mechanisms and the Evidence for Folate's Role. Advances in Nutrition. 2012;3(1):21-38.
329. Ren X, Liu M, Tang M, Tan L, Fu C, Wu Q, et al. Evaluation of Apigenin Inhibiting Lactate Dehydrogenase Activity Based on CdTe Quantum Dots Fluorescence. J Biomed Nanotechnol. 2021;17(9):1806-11.
330. Mahajan UB, Chandrayan G, Patil CR, Arya DS, Suchal K, Agrawal YO, et al. The Protective Effect of Apigenin on Myocardial Injury in Diabetic Rats mediating Activation of the PPAR-γ Pathway. International Journal of Molecular Sciences. 2017;18(4):756.
331. Enayatollah S, Hamid RR, Ahmad S, Zhaleh M, Jalal P. Selective Toxicity of Apigenin on Cancerous Hepatocytes by Directly Targeting their Mitochondria. Anti-Cancer Agents in Medicinal Chemistry. 2016;16(12):1576-86.
332. Park S, Lim W, Bazer FW, Song G. Apigenin induces ROS-dependent apoptosis and ER stress in human endometriosis cells. Journal of Cellular Physiology. 2018;233(4):3055-65.
333. Ghițu A, Schwiebs A, Radeke HH, Avram S, Zupko I, Bor A, et al. A Comprehensive Assessment of Apigenin as an Antiproliferative, Proapoptotic, Antiangiogenic and Immunomodulatory Phytocompound. Nutrients. 2019;11(4):858.
334. Gundala RR, Singh A. What motivates consumers to buy organic foods? Results of an empirical study in the United States. PLOS ONE. 2021;16(9):e0257288.
335. Chen L, Zhang C, Han Y, Meng X, Zhang Y, Chu H, et al. Gingko biloba Extract (EGb) Inhibits Oxidative Stress in Neuro 2A Cells Overexpressing APPsw. BioMed Research International. 2019;2019:7034983.
336. Yu D, Zhang P, Li J, Liu T, Zhang Y, Wang Q, et al. Neuroprotective effects of Ginkgo biloba dropping pills in Parkinson's disease. Journal of Pharmaceutical Analysis. 2021;11(2):220-31.
337. Ge W, Ren C, Xing L, Guan L, Zhang C, Sun X, et al. Ginkgo biloba extract improves cognitive function and increases neurogenesis by reducing Aβ pathology in 5×FAD mice. Am J Transl Res. 2021;13(3):1471-82.
338. DeKosky ST, Williamson JD, Fitzpatrick AL, Kronmal RA, Ives DG, Saxton JA, et al. Ginkgo biloba for Prevention of Dementia: A Randomized Controlled Trial. JAMA. 2008;300(19):2253-62.

339. Gaston TE, Mendrick DL, Paine MF, Roe AL, Yeung CK. “Natural” is not synonymous with “Safe”: Toxicity of natural products alone and in combination with pharmaceutical agents. Regulatory Toxicology and Pharmacology. 2020;113:104642.
340. Carla P, Ana SF. Adverse Effects of Natural Products: A Brief Pre-Systematic Review. Current Nutraceuticals. 2021;2(1):14-20.
341. Cardenas H, Arango D, Nicholas C, Duarte S, Nuovo GJ, He W, et al. Dietary Apigenin Exerts Immune-Regulatory Activity in Vivo by Reducing NF-κB Activity, Halting Leukocyte Infiltration and Restoring Normal Metabolic Function. International Journal of Molecular Sciences. 2016;17(3):323.
342. Chang C-C, Chen C-W, Owaga E, Lee W-T, Liu T-N, Hsieh R-H. Mangosteen Concentrate Drink Supplementation Promotes Antioxidant Status and Lactate Clearance in Rats after Exercise. Nutrients. 2020;12(5):1447.
343. Bin Q, Peterson DG. Identification of bitter compounds in whole wheat bread crumb. Food Chemistry. 2016;203:8-15.
344. Pang Q, Zhao Y, Chen X, Zhao K, Zhai Q, Tu F. Apigenin Protects the Brain against Ischemia/Reperfusion Injury via Caveolin-1/VEGF In Vitro and In Vivo. Oxidative Medicine and Cellular Longevity. 2018;2018:7017204.
345. Sarigul Sezenoz A, Akkoyun I, Helvacioglu F, Haberal N, Dagdeviren A, Bacanli D, et al. Antiproliferative and Mitochondrial Protective Effects of Apigenin in an Oxygen-Induced Retinopathy In Vivo Mouse Model. J Ocul Pharmacol Ther. 2021.
346. Wang X, Wang W, Wang J-Z, Yang C, Liang C-Z. Effect of apigenin on apoptosis induced by renal ischemia/reperfusion injury in vivo and in vitro. Renal Failure. 2018;40(1):498-505.
347. Im AR, Kim Y-M, Chin Y-W, Chae S. Protective effects of compounds from Garcinia mangostana L. (mangosteen) against UVB damage in HaCaT cells and hairless mice. Int J Mol Med. 2017;40(6):1941-9.
348. Patil P, Agrawal M, Almelkar S, Jeengar MK, More A, Alagarasu K, et al. In vitro and in vivo studies reveal α-Mangostin, a xanthonoid from Garcinia mangostana, as a promising natural antiviral compound against chikungunya virus. Virology Journal. 2021;18(1):47.
349. Guan H, Li J, Tan X, Luo S, Liu Y, Meng Y, et al. Natural Xanthone α-Mangostin Inhibits LPS-Induced Microglial Inflammatory Responses and Memory Impairment by Blocking the TAK1/NF-κB Signaling Pathway. Molecular Nutrition & Food Research. 2020;64(14):2000096.
350. DeRango-Adem EF, Blay J. Does Oral Apigenin Have Real Potential for a Therapeutic Effect in the Context of Human Gastrointestinal and Other Cancers? Frontiers in Pharmacology. 2021;12(1196).
351. Choi YH, Han SY, Kim Y-J, Kim Y-M, Chin Y-W. Absorption, tissue distribution, tissue metabolism and safety of α-mangostin in mangosteen extract using mouse models. Food and Chemical Toxicology. 2014;66:140-6.
352. Ross JA, Kasum CM. DIETARY FLAVONOIDS: Bioavailability, Metabolic Effects, and Safety. Annual Review of Nutrition. 2002;22(1):19-34.
353. Chivapat S, Chavalittumrong P, Wongsinkongman P, Phisalpong C, Rungsipipat A. Chronic Toxicity Study of Garcinia mangostana Linn. pericarp Extract. The Thai Journal of Veterinary Medicine. 2011;41(1):45-54.

354. Pimtong W, Kitipaspallop W, Chun H-S, Kim W-K. Effects of α-mangostin on embryonic development and liver development in zebrafish. Molecular & Cellular Toxicology. 2020;16(4):469-76.
355. Fukuda M, Sakashita H, Hayashi H, Shiono J, Miyake G, Komine Y, et al. Synergism between α-mangostin and TRAIL induces apoptosis in squamous cell carcinoma of the oral cavity through the mitochondrial pathway. Oncol Rep. 2017;38(6):3439-46.
356. Pérez-Rojas JM, González-Macías R, González-Cortes J, Jurado R, Pedraza-Chaverri J, García-López P. Synergic Effect of α-Mangostin on the Cytotoxicity of Cisplatin in a Cervical Cancer Model. Oxidative Medicine and Cellular Longevity. 2016;2016:7981397.
357. Zuo J, Yin Q, Wang L, Zhang W, Fan Y, Zhou Y-Y, et al. Mangosteen ethanol extract alleviated the severity of collagen-induced arthritis in rats and produced synergistic effects with methotrexate. Pharmaceutical Biology. 2018;56(1):455-64.
358. Kashyap P, Shikha D, Thakur M, Aneja A. Functionality of apigenin as a potent antioxidant with emphasis on bioavailability, metabolism, action mechanism and in vitro and in vivo studies: A review. Journal of Food Biochemistry.n/a(n/a):e13950.
359. Wu Q, Li W, Zhao J, Sun W, Yang Q, Chen C, et al. Apigenin ameliorates doxorubicin-induced renal injury via inhibition of oxidative stress and inflammation. Biomedicine & Pharmacotherapy. 2021;137:111308.
360. Ali AA-M, Mansour AB, Attia SA. The potential protective role of apigenin against oxidative damage induced by nickel oxide nanoparticles in liver and kidney of male Wistar rat, Rattus norvegicus. Environmental Science and Pollution Research. 2021;28(22):27577-92.
361. Atanasov AG, Zotchev SB, Dirsch VM, Orhan IE, Banach M, Rollinger JM, et al. Natural products in drug discovery: advances and opportunities. Nature Reviews Drug Discovery. 2021;20(3):200-16.
362. Wathoni N, Rusdin A, Motoyama K, Joni IM, Lesmana R, Muchtaridi M. Nanoparticle Drug Delivery Systems for alpha-Mangostin. Nanotechnol Sci Appl. 2020;13:23-36.
363. Pápay Z, Balogh E, Zariwala M, Somavarapu S, Antal I. Drug delivery approaches for apigenin: A review. In: Stacks NM, editor. Apigenin and Naringenin: Natural Sources, Pharmacology and Role in Cancer Prevention: Nova science; 2015. p. 1-20.
364. Samprasit W, Opanasopit P, Chamsai B. Mucoadhesive chitosan and thiolated chitosan nanoparticles containing alpha mangostin for possible Colon-targeted delivery. Pharmaceutical Development and Technology. 2021;26(3):362-72.
365. Jangdey MS, Kaur CD, Saraf S. Efficacy of Concanavalin-A conjugated nanotransfersomal gel of apigenin for enhanced targeted delivery of UV induced skin malignant melanoma. Artificial Cells, Nanomedicine, and Biotechnology. 2019;47(1):904-16.
366. Song Q, Song H, Xu J, Huang J, Hu M, Gu X, et al. Biomimetic ApoE-Reconstituted High Density Lipoprotein Nanocarrier for Blood–Brain Barrier Penetration and Amyloid Beta-Targeting Drug Delivery. Molecular Pharmaceutics. 2016;13(11):3976-87.

367. Ashley EA. Towards precision medicine. Nature Reviews Genetics. 2016;17(9):507-22.
368. Jørgensen JT. Twenty Years with Personalized Medicine: Past, Present, and Future of Individualized Pharmacotherapy. The Oncologist. 2019;24(7):e432-e40.
369. Vasan N, Baselga J, Hyman DM. A view on drug resistance in cancer. Nature. 2019;575(7782):299-309.
370. Wang Z, Liu X, Ho RLKY, Lam CWK, Chow MSS. Precision or Personalized Medicine for Cancer Chemotherapy: Is there a Role for Herbal Medicine. Molecules. 2016;21(7):889.
371. Hartl D, de Luca V, Kostikova A, Laramie J, Kennedy S, Ferrero E, et al. Translational precision medicine: an industry perspective. Journal of Translational Medicine. 2021;19(1):245.

VITA

NAME	Teeranai Ittiudomrak
DATE OF BIRTH	24 February 1987
PLACE OF BIRTH	Bangkok, Thailand
INSTITUTIONS ATTENDED	B.Sc.(Biotechnology), Thammasat University M.Sc.(Immunology), Mahidol University
HOME ADDRESS	2016/54 Chan23/1, Chan Rd, Chongnonsi, Yannawa, Bangkok, Thailand, 10120
PUBLICATION	Ittiudomrak T, Puthong S, Palaga T, Roytrakul S, Chanchao C. alpha-Mangostin and apigenin induced the necrotic death of BT474 breast cancer cells with autophagy and inflammation. Asian Pacific Journal of Tropical Biomedicine. 2018;8(11):519-26. Ittiudomrak T, Puthong S, Roytrakul S, Chanchao C. alpha-Mangostin and Apigenin Induced Cell Cycle Arrest and Programmed Cell Death in SKOV-3 Ovarian Cancer Cells. Toxicol Res. 2019;35(2):167-79.
AWARD RECEIVED	Young Scientist and Technologist Programme (YSTP), NSTDA, Thailand, 2008-2009 Thailand Graduate Institute of Science and Technology (TGIST), NSTDA, Thailand, 2010-2012 The 100th Anniversary Chulalongkorn University Fund for Doctoral Scholarship, Chulalongkorn University, Thailand, 2015-2018 Overseas Research Experience Scholarship for Graduate Student, Chulalongkorn University, Thailand, 2018-2019